NUCLEAR ENERGY RESEARCH INITIATIVE (NERI)

SUMMARY REPORT

FEASIBILITY OF RECYCLING PLUTONIUM AND MINOR ACTINIDES IN LIGHT WATER REACTORS USING HYDRIDE FUEL

Grant No. DE-FC07-06ID14736

NERI Project No. 2006-065

March 2006 through December 2008

Submitted by:

Lead Organization:
University of California, Berkeley
Ehud Greenspan

Collaborating Organizations:
Massachusetts Institute of Technology
Neil Todreas

Argonne National Laboratory
Temitope Taiwo

Submitted on:
March 10, 2009

Participating Organizations and Researchers

E. Greenspan (PI), **F. Ganda, M. Fratoni, D. Olander, K. Terrani and M. Balooch**
Department of Nuclear Engineering
University of California
Berkeley, CA 94720
gehud@nuc.berkeley.edu

N. Todreas (co-PI), **P. Ferroni**
Department of Nuclear Engineering
Massachusetts Institute of Technology
Cambridge, MA 02139
todreas@mit.edu

T. Taiwo(co-PI)
Argonne National Laboratory
9700 S. Cass Ave., Argonne, IL 60439
taiwo@anl.gov

ACKNOWLEDGMENT

This report is based upon work supported by the U S. Department of Energy under Award No. DE-FC07-06ID14736

DISCLAIMER

Table of Contents

Executive Summary

The objective of this DOE NERI program sponsored project was to assess the feasibility of improving the plutonium (Pu) and minor actinide (MA) recycling capabilities of pressurized water reactors (PWRs) by using hydride instead of oxide fuels. There are four general parts to this assessment:

1) Identifying promising hydride fuel assembly designs for recycling Pu and MAs in PWRs
2) Performing a comprehensive systems analysis that compares the fuel cycle characteristics of Pu and MA recycling in PWRs using the promising hydride fuel assembly designs identified in Part 1 versus using oxide fuel assembly designs
3) Conducting a thermal-hydraulic and safety analysis to evaluate the power attainable from hydride fuelled cores and assess the likelihood of licensing hydride fuel assembly designs
4) Assessing the compatibility of hydride fuel with cladding materials and water under typical PWR operating conditions

Following is a summary of the work performed and of the results obtained

Neutronics

A Pu-containing hydride fuel (PuH_2-U-$ZrH_{1.6}$ with 45 weight % U) assembly design (referred to as PUZH) was compared with two oxide fuel assembly designs that were proposed to overcome the positive void coefficient of reactivity – CORAIL and MOX-UE. The CORAIL design offers ~30% natural uranium and Separating Working Unit (SWU) saving over conventional UO_2 fuelled cores, but it provides for Pu stabilization rather than net destruction (a complete Pu drawdown from the YMR would require ~300 CORAIL cores, three times the current LWR fleet). It was found that a PWR loaded with these PUZH fuel assemblies will incinerate in the first recycle twice as much TRU (primarily Pu) as it will do when loaded with MOX fuel assemblies when both core designs are loaded with same amount of TRU and operate at the same power level for the same time. This PUZH core will also be less expensive, since it uses depleted uranium versus significantly larger quantities of enriched uranium required for the equivalent MOX-UE core. Additionally, the PUZH fuel design has a lower power peaking factor than the MOX-UE and, particularly, CORAIL fuel assemblies.

An assessment of the feasibility of enhancing the fractional plutonium destruction using hydride fuels with varying amounts of thorium and uranium was undertaken as well. These fuels are of the form ThH_2-$ZrH_{1.6}$-PuH_2 and U-$ZrH_{1.6}$-PuH_2. It was found that the fertile free hydride fuel (of the form PuH_2-$ZrH_{1.6}$), while offering the higher TRU destruction fraction of all the systems analyzed, also allows multi-recycling of Pu in PWRs an unlimited number of times when uniformly loaded in all fuel assemblies in the core. This unique feature of hydride fuels is due to the incorporation of a significant fraction of the hydrogen moderator in the fuel, thereby reducing the effect of spectrum hardening due to coolant voiding accidents; the large void reactivity coefficient remains negative. The fractional transmutation of PuH_2-$ZrH_{1.6}$ was found 64% at the first recycle and gradually decreases to about 20% towards the equilibrium recycle. The Fuel Temperature Coefficient of Reactivity (FTC) was found positive in the third batch of the first

recycle of PuH_2-$ZrH_{1.6}$ fuel. However, addition of relatively small amount of either depleted U or Th or using hydride fuel with D instead of H for the first recycle only can alleviate this problem.

An inert-matrix oxide fuel – PuO_2-ZrO_2, counterpart to the inert matrix hydride fuel PuH_2-$ZrH_{1.6}$ was investigated as well. Although the TRU destruction fraction at first recycle is almost as high as that of PuH_2-$ZrH_{1.6}$ fuel, the maximum possible number of recycles of the oxide fuel is limited, by positive reactivity effect of large core voiding, to 10 despite of the fact that the leakage effect due to large core voiding was found significantly larger for oxide as compared to hydride fueled cores.

The feasibility of recycling Pu+MA in hydride fuels was also assessed. It was found that hydride fuels allow multi recycling of Pu+Np at least 6 times, before getting a positive large void reactivity feedback. This corresponds to approximately 86 years of recycling campaign. A number of approaches where investigated for making the large voiding reactivity coefficients of NpH_2-PuH_2-$ZrH_{1.6}$ fuelled cores negative beyond the 6^{th} recycle. The most effective approach identified is enlarging the fuel rod radius while conserving the lattice pitch. This approach might, however, penalize the maximum attainable power unless an increase in the coolant pressure drop across the core is allowed. It was also found that if it is desired to recycle all the TRU in PWRs using hydride fuel, the number of possible recycles is limited to 3; the limit is imposed by a positive large void reactivity feedback.

A preliminary system analysis was performed to compare the fuel cycle characteristics of Pu multi-recycling in PWRs using the PuH_2-$ZrH_{1.6}$ hydride fuel assembly design versus Pu recycling in PWRs using several of the promising oxide fuel assemblies. If desired to transmute plutonium in a 2-tier system (i.e. recycle once in thermal reactors for Pu inventory reduction and subsequently recycle all the leftover TRU in fast reactors), the number of cores required for single recycling of the entire Pu inventory originally planned to be disposed of at the YMR would be ~70 for conventional MOX fuel versus ~100 in case of inert matrix hydride or oxide fuel. However, the inert matrixes would provide the greatest inventory reduction in one pass leaving only 30% of the loaded plutonium inventory while the conventional MOX would leave 77% of the initial plutonium mass. Inert matrixes would also leave a substantially more proliferation resistant discharged stream. Between oxide and hydride inert matrixes, it was found that hydride leaves a more proliferation resistant discharged stream while no substantial difference in other characteristics was observed. It is also noted that inert matrixes are most likely the cheapest Pu recycling options, since they allow reaching the desirable cycle length in PWRs with a smaller Pu loading, thereby providing the largest amount of electricity generated per unit of reprocessed LWR spent fuel. Using CORAIL fuel assemblies is not a practical option for the purpose of using all the Pu inventory originally planned for storage at the YMR; ~300 CORAIL cores would be required for this purpose.

Another system analysis performed is an evaluation of the repository impact of Pu multi-recycling in different fuel types. The following characteristics, normalized per ton of Pu transmuted and measured at the end of the transmutation campaign, were intercompared: (1) total radioactivity of the TRU stream; (2) total neutron emission; (3) total decay heat; (4) total gamma decay heat; (5) total toxicity in air; (6) total toxicity in water; and (7) total mass of ^{237}Np and its precursors (i.e. ^{241}Am and ^{245}Cm). It was found that all these measures of repository impact, except for the mass of neptunium and its precursors, are slightly higher for PuO_2-ZrO_2 than for PuH_2-$ZrH_{1.6}$ fuel. It was also observed that the radioactivity is higher for larger number of cores

operating in parallel for a smaller number of recycles, while all the other measures decrease with the use of larger number of parallel cores.

The proliferation resistance was evaluated through the estimate of the following parameters (normalized per ton of Pu transmuted) at the reprocessing plant: (1) total inventory of plutonium to be handled at the reprocessing plant; (2) Pu fissile fraction; (3) neutron emission per gram of plutonium and TRU; (4) specific decay heat for Pu and TRU. The total inventory of plutonium to be handled in the reprocessing plant is quite similar in the case of PuO_2-ZrO_2 and PuH_2-$ZrH_{1.6}$. However, the plutonium fissile fraction at the reprocessing facility, as well as the neutron emission per gram of plutonium, shows that the PuH_2-$ZrH_{1.6}$ stream appears more proliferation resistant than that of PuO_2-ZrO_2 for the first 9-10 recycles. The neutron emission per gram of TRU and the specific decay heat are similar for the two fuel types. It is concluded that multi-recycling in PuH_2-$ZrH_{1.6}$ is more resistant to proliferation than multi-recycling in PuO_2-ZrO_2.

Based on costs estimates for fuel fabrication, reprocessing and fuel and waste disposal, it was found that the final cost of PuH_2-$ZrH_{1.6}$ would only be ~1.2% lower than that of PuO_2-ZrO_2, not enough to justify the choice of this fuel based on this cost.

Another analysis performed compared a couple of systems at equilibrium: (1) A fleet of enriched uranium fuelled PWRs operating in the once-through fuel cycle supported by a smaller fleet of PWRs operating with Pu-recycling PuH_2-$ZrH_{1.6}$ fuelled cores so that the total TRU inventory in the combined fleets is capped. (2) A fleet of PWRs designed to have CORAIL fuel assemblies. It is assumed that the initial Pu feed comes from the LWR spent fuel that has been accumulated already. It was found that, at equilibrium, the CORAIL system requires less natural uranium and SWU and has a smaller repository impact than the coupled LWR+PUZH. This comparison did not account for the amount of MA accumulated in the fuel discharged from the once-through LWRs left over after the extraction of the Pu used for the initial loading into the CORAIL fuel assemblies.

Thermal-hydraulics

The objective of the thermal hydraulic analysis was to compare the behavior of a PUZH-fueled PWR core with that of geometrically identical cores, but loaded with different assemblies, both during normal operation and during accident scenarios. These assemblies have the same geometry, but differ either because of the type of fuel with which they are loaded or because of the fuel arrangement in the lattice. The assemblies analyzed are the following: (1) an all-UO_2-assembly: the reference assembly; it uses UO_2 fuel pins only; (2) a CONFU-assembly: heterogeneous assembly made of standard UO_2 fuel pins and pins made of recycled transuranics in an inert matrix; (3) a CORAIL-assembly: heterogeneous assembly made of enriched UO_2 pins and MOX pins; and (4) a PUZH-assembly: homogeneous assembly containing U-Pu-Th-$ZrH_{1.6}$ as fuel.

The steady state thermal-hydraulic analysis concluded that, under the constraint of the same safety limits for all the core types, a PUZH-core can operate at the same power level as the reference all-UO_2 core while PWR cores loaded with either CONFU or CORAIL fuel assemblies can only operate at about 80% of that power. This is due to the flatter pin-by-pin radial power distribution characterizing the PUZH assembly.

Transient analyses were performed for three accident scenarios: Large Break Loss Of Coolant Accident (LBLOCA), Main Steam Line Break (MSLB) and Complete Loss Of Forced Flow Accident (CLOFA). For all three scenarios, the PUZH-core was found to perform better than the other two core types aimed at Pu/MA incineration, i.e. CONFU- and CORAIL-core. Particularly:

- The peak cladding temperature for PUZH-core during LBLOCA was found to be about 300 K lower than that of all-UO_2-, CONFU- and CORAIL-cores. This is mainly due to the lower operating temperature characterizing the highly conductive PUZH fuel relative to UO_2-based fuels.
- Unlike all-UO_2-, CONFU- and CORAIL-cores, PUZH-core showed no return to criticality in the event of a MSLB. This is due to the moderator temperature coefficient (MTC) of PUZH-core, which was found to be the least negative among the cores analyzed.
- In the event of a CLOFA, the PUZH-core was found to reach a Minimum Critical Heat Flux Ratio (MCHFR) larger than that of the CONFU- and CORAIL-cores, and similar to that of the all-UO_2-core. This is due both to a larger pre-accident MCHFR – resulting from the flatter pin-by-pin power distribution characterizing the PUZH-assembly, than CONFU and CORAIL, and to the larger (negative) value of the MTC/β ratio (which controls the reactivity insertion upon coolant temperature variation) that caused a more rapid reduction in power upon the accident.

Materials

The primary objective of the material analysis, as originally defined, was to investigate the compatibility of hydride fuel with Zircaloy clad and with water under typical PWR operating conditions. For this purpose we have located a damaged unused TRIGA fuel at the University of California campuses at both Irvine and Davis and received DOE agreement to transfer the fuel element from Davis to Berkeley. Unfortunately, we encountered numerous administrative hurdles first by DOE and later by Davis and Berkeley and did not succeed getting the fuel to this date. Consequently, we have modified the plan for the material analysis.

Two uranium-thorium-zirconium alloys were arc-melted and then hydrided to form fuels with the nominal composition of $(UTh_4Zr_{10})H_{1.9}$ and $(U_4Th_2Zr_9)H_{1.5}$. Based on the analysis of these fuel samples it appears that uranium-thorium-zirconium hydride fuels are superior to TRIGA fuel (that does not have thorium) for power reactor use since the hydride matrix is more stable with respect to dehydriding. Also, higher heavy metal densities can be achieved in fuels containing thorium. Extensive study of the effects of irradiation on these fuels under typical light water reactor conditions is necessary in order to adequately understand their performance compared to TRIGA fuel and oxide fuels. An experiment intended for doing so at the ATR reactor an INL has been planned.

Steady state and transient behavior of hydride fuel under PWR operating conditions were investigated, taking into account the dependence of the fuel properties on the spatially varying temperature and hydrogen concentration. The steady state temperature, hydrogen concentration, and stress distributions across the hydride fuel were calculated for various linear heat generation rates (LHGR). The extent of hydrogen radial redistribution across the fuel, driven by the temperature gradient, is found more severe as the LHGR increases. Strains in the fuel occur from

thermal and hydrogen concentration gradients, with the latter being the dominant contributor. Axial and azimuthal stresses are found both compressive at the fuel surface and tensile at the fuel centerline. The fuel fracture criterion needs to be determined through finite element analysis.

The transient response of hydride fuel to a reactivity insertion accident scenario was studied by artificially pulsing power in a square wave. The thermal response of the fuel to the changing power level is found very rapid – on the order of few seconds. This is due to the small fuel rod diameter and large thermal diffusivity of hydride fuel. There is no discernable alteration in the hydrogen spatial distribution during the transient, since the characteristic hydrogen diffusion time for these length scales is many orders of magnitude larger than the power transient durations. Surprisingly, the stress across the fuel is actually reduced during the power pulse. The temperature-induced stresses counteract the hydrogen-induced stresses, so the fuel is in its most relaxed state during this stage of the transient. The fuel experiences maximum stress when the temperature gradients diminish but the hydrogen displacement remains at the pre-transient distribution.

In helium-bonded hydride fuel rods the flux of hydrogen atoms out of the fuel is found very small during both steady state and transient operation. This is because the net rate of (desorption – adsorption) quickly becomes zero when the equilibrium hydrogen partial pressure is established in the gas plenum. The pressure buildup inside the cladding and the total fraction of hydrogen lost from the solid fuel to the gas plenum are negligible even at very high fuel surface temperatures. The extent of dehydriding is expected to be even less for liquid metal bonded fuels. For the purpose of safety analyses assuming instantaneous equilibrium conditions is judged to be a conservative and relatively accurate assumption.

Zirconium is an effective getter of hydrogen and can readily undergo hydriding. However the fuel rod could be engineered such that the kinetics of hydrogen transfer from the fuel to the clad is limited and effectively becomes insignificant during the lifetime of the fuel inside the reactor. One such engineered approach we conceived is to substitute a liquid metal alloy for helium as the fuel – clad bonding material. A ternary alloy of lead-tin-bismuth (Pb-33wt%Sn-33wt%Bi) is proposed for this purpose. This alloy is chemically compatible with both the fuel and the clad. Also hydrogen solubility in any of the components of the alloy is very limited at the fuel operating temperatures. An investigation of the compatibility of the liquid metal bonded hydride fuel with the cladding was initiated but has not been concluded by the time of the issuing of this report.

An additional experimental study just recently initiated is to investigate the compatibility of hydride fuel with high temperature steam that may occur in case of a severe accident that causes the clad to rupture.

The experimental data available in the open literature on the swelling of hydride fuel and on the fission gas released from hydride fuel is very limited. Moreover, there is no data available at all on the feasibility of using liquid metal bonding instead of helium for hydride fuel. An irradiation test of a liquid-metal bonded hydride fuel specimen in the ATR irradiation test reactor at the Idaho National Laboratory was planned in order to improve the knowhow about hydride fuel performance under power reactor irradiation conditions and investigate all the practicality and effectiveness of the liquid metal bonding. We are now waiting for the ATR approval of this irradiation test proposal.

Recommendation for future work

The most important future undertaking is a study of the compatibility of hydride fuel with Zircaloy clad and with high temperature and high pressure water and steam. Reliable experimental data on the irradiation behavior of hydride fuel and, particularly, its irradiation induced swelling and fission gas release need also be obtained. Establishing the feasibility of using liquid metal instead of helium bonding is highly desirable along with an investigation of the protection of the clad from hydriding such liquid metal bonding mayn provide. Estimation of the commercial scale fabrication cost of hydride fuel is essential for evaluating the economic viability of hydride fuel applications in LWR. Practical processes for recycling hydride fuel need be developed as well.

More comprehensive system analyses that will address a number of promising scenarios, including scenarios involving a combination of recycling campaign in LWR using hydride fuel and recycling the leftover TRU – mostly MA, in fast spectrum reactors are also recommended. A comprehensive comparison of the feasibility and performance of inert matrix hydride versus oxide fuels is also desirable. Use of hydride fuel for recycling Pu and, possibly also MA in BWR need also be explored; our previous study indicated that hydride fuels enable to eliminate water rods and partial-length fuel rods and to reduce the water gaps between fuel bundles thus providing a substantial increase – possibly close to 30%, in the core power density. Based on our present study for PWR cores it is to be expected that, along with the power density increase, hydride fuel will also enable improvement in the transmutation capability of BWRs.

1. Introduction

1.1 About use of hydride fuels in LWRs

A comprehensive three-year feasibility study completed in 2006 under NERI Award No DE-FG07-02SF22615 [1] has established that, based on neutronics, thermal-hydraulics, fuel performance and safety analyses hydride fuel can safely operate in PWRs and BWRs without restricting the linear heat generation rate of these reactors relative to that attainable with oxide fuel. A detailed summary of the analysis performed and of the results obtained will be published later this year as a special issue of Nuclear Engineering and Design [2-14]. Briefly, the study identified a couple of particularly promising applications of hydride fuel in both PWRs and BWRs:

(a) Eliminating dedicated water moderator volumes in BWR cores[1] by loading hydride fuel rods thus enabling to significantly increase the cooled fuel rods surface area as well as the coolant flow cross section area in a given volume fuel bundle while significantly reducing the heterogeneity of BWR fuel bundles thus achieving flatter pin-by-pin power distribution. The net result is a possibility to significantly increase the core power density – on the order of 30% and, possibly, more, while greatly simplifying the fuel bundle design.

(b) Recycling plutonium in PWRs more effectively than is possible with oxide fuel by virtue of a couple of unique features of hydride fuel – reduced inventory of ^{238}U and increased inventory of hydrogen. As a result of these features, the amount of Pu that needs to be loaded into the hydride core to provide the reference cycle length is only 75% that is needed for MOX cores, and the hydride core neutron spectrum is softer. Due to these characteristics, the hydride fuelled core achieves nearly double the average discharge burnup – about 103 vs. 50 GWD/MTHM of MOX. The total Pu inventory in the discharged PUZH fuel is only 43% of the initially loaded inventory versus 73 % in the discharged MOX fuel. The net amount of Pu consumed per cycle is 60% larger with PUZH versus MOX fuel. The corresponding fissile Pu to total Pu ratio is 44% versus 63%. The corresponding ratio of minor actinides (MA) to Pu concentration at discharge is 13.25% versus 6.76%. The total neutron source strength at discharge of PUZH fuel is 1250 n/s per gram of Pu and 5.25×10^5 n/s per gram of TRU versus, respectively, 796 n/s and 2.23×10^5 n/s for MOX fuel. The decay heat levels are 2.35 w/gTRU for PUZH and 1.19 w/gTRU for MOX fuel. Nevertheless, the decay heat and radiation levels per PUZH fuel assembly discharged are smaller than for MOX fuel assembly.

1.2 Hydride fuels considered

The primary hydride fuel considering in this project is uranium-zirconium hydride similar to that developed by General Atomics (GA) for TRIGA reactors [15]. The U-Zr hydride composition used for the TRIGA fuel has, typically, 1.6 hydrogen atoms per Zr atom, i.e., it is U-$ZrH_{1.6}$. The Medium Enriched Uranium (MEU) fuel developed by General Atomics for TRIGA reactors contains 45 $^{w}/_{o}$ uranium of up to 20$^{w}/_{o}$ ^{235}U [15]. This corresponds to U/Zr atom ratio of 0.31. The U-Zr hydride fuel considered throughout this project has the same elemental composition. The uranium enrichment is a design variable. This fuel has been in use for more than 40 years in

[1] Including water rods, possibly also replacing partial length by full length fuel rods, and minimizing the water gap width in-between fuel bundles.

many reactors around the world both in constant power and pulsed power operating conditions. It has an impressive record of safety.

The design limits set for the high power TRIGA core [16] are fuel temperatures of 750°C at steady-state and 1050°C under transients. Although these temperatures are significantly lower than the maximum permissible operating temperatures of UO_2 fuel, the thermal conductivity of hydride fuel is ~5 times higher than that of oxide fuel. Consequently, U-$ZrH_{1.6}$ fuel can safely operate at linear heat rates that even exceed those of commercial LWR. TRIGA fuel burnup also significantly exceeds typical LWR oxide fuel burnup.

In high power TRIGA reactor [16] the fuel-average linear heat generation rate (LHGR) is 37kW/m while the peak LHR is 74 kW/m. The corresponding peak steady-state fuel temperature is 550°C. For comparison, the average LHGR of oxide fueled PWR is 19 kW/m. The TRIGA fuel discharge burnup is ~120 GWD/tHM versus <60 GWD/tHM of oxide fuel in PWR. The specific power of the TRIGA fuel is 76 W/gHM versus ~36 W/gHM of the PWR. The water in TRIGA reactors is at a significantly lower temperature than in LWR's. Hence, the LHGR hydride fuel could operate at in a PWR is significantly lower than in the TRIGA reactor. Nevertheless, the detailed analyses performed in the previous study [1-14] established that U-$ZrH_{1.6}$ fuel can safely operate in both PWR and BWR cores at, at least, as high a LHGR as attainable with oxide fuel.

Relative to uranium dioxide fuel, U-$ZrH_{1.6}$ fuel has a number of possible drawbacks:

(a) The nominal specific density of U-$ZrH_{1.6}$ at room temperature is 8.256 g/cm^3 and the maximum practical U weight % is 45. This makes the atomic density of uranium in U-$ZrH_{1.6}$ only about 40% that in UO_2 fuel. For Pu and MA recycling, though, the relatively low U loading is likely to be an asset rather than a disadvantage, as discussed in Section 2 of this report – it reduces the inventory of Pu that needs to be loaded per core and increases the fraction of the Pu that is consumed in one cycle. Moreover, the nominal density of a U-ThH_2 fuel having 25 $^w/_o$ U is 10.865 g/cm^3 making the HM density in Th-hydride fuel nearly 12% higher than the U density in UO_2! This might enable increasing the PWR cycle length beyond that attainable using oxide fuel using same loading of fissile material.

(b) Zircaloy may not be a compatible clad material for hydride fuel, as the hydrogen of the fuel may hydride it. Nevertheless, half-a-dozen of approaches have been proposed for protecting the Zy clad using a hydrogen permeation barrier [3] including the following: (i) Form a thin oxide layer (~ 40 μm) over the hydride fuel pellets; it may retain the hydrogen up to 800°C and will probably avoid fuel-cladding chemical reaction. (ii) Fill the fuel-clad gap with a liquid metal. In addition to providing a hydrogen permeation barrier, the LM will significantly reduce the gap-resistance to heat transfer and will enable to accommodate significant pellet swelling with burnup without penalizing the fuel temperature. The feasibility of using LM bonding for LWR UO_2 fuel so as to improve the heat transfer from the fuel to the clad and thus reduce the peak fuel temperature, delay onset of fission gas release, avoids PCI and prevents Zy clad secondary hydriding due to clad failure has recently been established by Olander et al. [3]. The LM is a low melting temperature (~120°C) alloy of Pb, Sn and Bi at 33 weight % each.

The feasibility of such barriers needs to be carefully studied. The "default" approach is to use SS clad. Experiments done at General Atomics with hydride fuel proved that [15] "high-temperature strength and ductility of the stainless steel or Alloy 800 fuel cladding provides total clad integrity at temperatures as high as 950°C". Whereas for low enrichment uranium

fuel use of SS clad will significantly penalize the neutron economy relative the Zy clad, the penalty for Pu bearing fuel is smaller, due to the higher absorption cross section of Pu.

(c) If, due to a very severe accident, the hydride fuel temperature will significantly exceed $1000^{o}C$ for a prolonged period of time, hydrogen could diffuse out from the fuel into the fission gas plenum. If the gas pressure buildup will be excessive, it may pose a safety hazard. Assessment of this hazard and its probability need yet to be performed.

(d) Hydride fuel may not be compatible with water coolant at PWR and/or BWR operating conditions. Experiments performed at GA showed that there was no chemical reaction when a very hot ($1200^{o}C$) pellet of U-$ZrH_{1.6}$ was dropped into a container of water. A safety concern may be steam – fuel interaction in case of a breach in the clad. Based on the experience with TRIGA fuel, steam – fuel interaction is not likely to be of safety concern. Nevertheless, due to the higher operating temperatures and pressures of LWR's, there may be a compatibility issue.

Several types of hydride fuels have been considered for this study in addition to U-$ZrH_{1.6}$; they are members of a family of a composite hydride fuel that can be denoted as U-$(Th_nPu_mZr_j)H_x$; the subscripts n, m, and j are the atomic proportions of the metals with respect to uranium whereas the subscript x denotes the atomic ratio of H to the total metals excluding the U. The uranium forms a separate metallic phase because its hydride (UH_3) is unstable at the reactor operating temperatures. The other constituents make a mixed-metal hydride $(Th_nPu_mZr_j)H_x$. The hydrogen density in these fuels is comparable to that in the water of PWR. Even though the experience with and data-base for thorium hydride and plutonium hydride fuels is small as compared with that of zirconium hydride fuel, these fuels are expected perform comparably, if not superior to $ZrH_{1.6}$ fuel. According to Simnad [17], the developer of the U-$ZrH_{1.6}$ TRIGA fuel, U-ThH_2 is even more stable than U-$ZrH_{1.6}$ fuel and can operate at higher temperatures. Plutonium also forms a very stable hydride; the equilibrium hydrogen pressure is 1 atm at $883^{o}C$ for ThH_2, $810^{o}C$ for $ZrH_{1.6}$, and about $870^{o}C$ for PuH_2 [17]. Uranium-thorium-zirconium hydride fuel was developed and characterized by Yamawaki et al. [18, 19].

1.3 Study objectives

The objective of this DOE NERI program sponsored project is to more thoroughly assess the feasibility of improving the plutonium (Pu) and minor actinide (MA) recycling capabilities of pressurized water reactors (PWRs) by using hydride instead of oxide fuels. There are four general parts to this assessment:

(a) Identifying promising hydride fuel assembly designs for multi-recycling of Pu and MAs in PWRs

(b) Performing a comprehensive systems analysis that compares the fuel cycle characteristics of Pu and MA recycling in PWRs using the promising hydride fuel assembly designs identified in Part 1 versus using promising assembly designs proposed for recycling in oxide fuel

(c) Conducting a safety analysis to assess the likelihood of licensing hydride fuel assembly designs

(d) Assessing the compatibility of hydride fuel with cladding materials and water under typical PWR operating conditions

1.4 Scope of work

Whereas the previous project [1, 2, 12] preliminary considered a single recycling of Pu in U-$ZrH_{1.6}$ fuel, The present study considers multi-recycling of either Pu only, Pu and Np, or all the TRU discharged from LWRs. Moreover, whereas the previous project [1, 2, 12] considered a single, somewhat unrealistic MOX fuel recycling in a full core uniformly loaded with UO_2 plus PuO_2, the present study examines three of the most promising assembly designs proposed for recycling of oxide fuel – MOX-UE [20], CORAIL[20, 21] and CONFU [22, 23]; they enable full core loading and multi-recycling of plutonium and possibly also minor actinides. The transmutation characteristics of hydride fuel are also compared against those attainable using plutonium in fertile-free, or "inert matrix", oxide fuel [24]. Performance characteristics considered include transmutation effectiveness, proliferation resistance of the discharged fuel and fuel cycle economics.

There are three major parts to this study: neutronic and fuel cycle analyses, thermal-hydraulics and safety analysis and evaluation of hydride fuel material properties. The work performed and results obtained in these parts are described in, respectively, Chapters 2, 3 and 4 of this report.

1.5 References

1. E. Greenspan and the NERI project team, "Use of Solid Hydride Fuel for Improved LWR Core Designs," Final Summary Report for NERI Project # NE02-189, UCBNE Internal Report UCB-NE-5105, April 30, 2006.
2. E. Greenspan, N. Todreas, B. Petrovic, P. Diller, P. Ferroni, M. Fratoni, F. Ganda, H. Garkisch, F. Ginex, J. Malen, D. Olander, A. Romano, C. Shuffler and J. Trant, "Hydride Fuel for LWR's – Project Overview", to be published in special issue of Nuclear Engineering and Design, 2009.
3. D. Olander, H. Garkisch, B. Petrovic and E. Greenspan, "Hydride Fuel Materials Performance and Design Constraints", to be published in special issue of Nuclear Engineering and Design, 2009.
4. F. Ganda, E. Greenspan and B. Petrovic, "Reactor Physics Analysis for PWR Cores", to be published in special issue of Nuclear Engineering and Design, 2009.
5. C. Shuffler, J. Trant, J. Malen, N. Todreas, "Thermal Hydraulic Analysis for Grid Supported Pressurized Water Reactor Cores"
6. P. Diller, N. Todreas and P. Hejzlar, "Thermal Hydraulic Analysis for Wire Wrapped PWR Cores", to be published in special issue of Nuclear Engineering and Design, 2009.
7. A. Romano, C. Shuffler, H. Garkisch, D. Olander and N Todreas, "Fuel Performance Analysis for PWR Cores", to be published in special issue of Nuclear Engineering and Design, 2009.
8. C. Shuffler, J. Malen, P. Diller, F. Ganda, N. Todreas, E. Greenspan and B. Petrovic, "Economic analysis for PWRs", to be published in special issue of Nuclear Engineering and Design, 2009.
9. M. Fratoni, F. Ginex, F. Ganda and E. Greenspan, "Reactor Physics Analysis for BWR Cores", to be published in special issue of Nuclear Engineering and Design, 2009.

10. P. Ferroni, C. Handwerk and N. Todreas, “Steady State Thermal-Hydraulic Analysis of Hydride-fueled Grid-supported BWRs”, to be published in special issue of Nuclear Engineering and Design, 2009.
11. F. Ganda, C. Shuffler and E. Greenspan, E., “Economic analysis for BWRs”, to be published in special issue of Nuclear Engineering and Design, 2009.
12. F. Ganda and E. Greenspan, “Plutonium Recycling in Hydride Fueled PWR Cores”, to be published in special issue of Nuclear Engineering and Design, 2009.
13. J. Malen, N. Todreas, P. Hejzlar, P. Ferroni and A. Bergles, “Thermal Hydraulic Design of a Hydride-fueled Inverted PWR Core”, to be published in special issue of Nuclear Engineering and Design, 2009.
14. F. Ganda and E. Greenspan, “Analysis of reactivity coefficients of hydride fueled PWR cores,” to be published in Nuclear Science & Engineering, 2009.
15. M. T. Simnad, “The U-ZrH_x Alloy: its Properties and Use in TRIGA Fuel”, Nucl. Eng. Design, 64, p. 403-422, August 1981. Also General Atomic Report GA-A16029, 1980.
16. C. Iorgulis, M. Ciocanescu, M. Preda, and M. Mladin, “Neutronic Calculations Regarding the New LEU 6x6 Fuel Bundle for 14 MW TRIGA-SSR, in order to Increase the Reactor Power Up to 21 MW”, Int. Mtg. on Reduced Enrichment for Research and Test Reactors, Sao Paulo, Brazil, October 1998.
17. M.T. Simnad, “An Assessment of Thorium Hydride or Deutride as a Reactor Fuel Matrix”, Reprint from the archives of Prof. Mike Driscoll of MIT Nuclear Engineering Department. 1986. also M.T. Simnad, “Uranium Thorium Hydride Nuclear Fuel,” United States Patent No 4,493,809, May 27 1986.
18. T.Yamamoto, H. Suwarno, F. Ono, H. Kayano, and M. Yamawaki, “Preparation, Analysis and Irradiation of Hydrided U-Th-Zr Alloy Samples For a New Fuel,” J. Alloys Compds. 271-273, 702-726, 1998.
19. M. Yamawaki, et al., “Development of U-Th-Zr Alloy Hydrides as Alternative Thorium-Base Fuel and MA Burning Target Fuel,” Proc. Int. Conf. on Future Nuclear Systems, GLOBAL’99, Jackson Hole, Wy. 1999.
20. G. Youinou, and A.Vasile, “Plutonium Multirecycling in Standard PWRs Loaded with Evolutionary Fuels”, Nuclear Science and Engineering: 151, 25-45, 2005.
21. G. Youinou, A. Zaetta, A. Vasile, M. Delpech, M. Rohart, and J.L. Guillet, “Heterogeneous Assembly for Plutonium Multi-recycling in PWRs: The CORAIL Concept”, Proc. Global’ 01, Paris, France, 2001.
22. E. Shwageraus, P. Hejzlar and M. Kazimi, “Feasibility of Multi-recycling of Pu and MA in PWRs Using Combined Non-Fertile and UO_2 (CONFU) Fuel”, Proc. GLOBAL’03, New Orleans, LA, 2003.
23. E. Shwageraus, P. Hejzlar and M.S. Kazimi, “A Combined Nonfertile and UO_2 PWR Fuel Assembly for Actinide Waste Minimization Nuclear Technology”, Volume 149, Number 3, Pages 281-303, 2005.

24. C. Degueldre, H. Akie, P. Boczar, N. Chauvin, M. Meyer and V. Troyanov, “Inert Matrix Fuel Deployment for Reducing Plutonium Stockpile in Reactors,” Proc.GLOBAL’03, New Orleans, LA. , 2003.

2 Neutronic Analysis

This section is organized as follows:

- Section 2.1: Introduction;
- Section 2.2: Benchmark our Fuel Assembly Computational Capability;
- Section 2.3: Database Establishment: Identification of Promising PWR Fuel Assembly Designs and Comparison with Equivalent Hydrides;
- Section 2.4: Identification of the Most Promising Hydride Fuels (fertile free, thorium- and uranium-based) for Pu Multi-Recycling;
- Section 2.5: Pu+Np and "all TRu" Multi-Recycling in PWR Using Hydride Fuels;
- Section 2.6: Comparisons of Hydride Fueled Systems;
- Section 2.7: System Analysis;
- Section 2.8: Conclusions.

2.1 Introduction

The objective of the neutronic analysis is to assess the feasibility of multi-recycling plutonium and TRU in PWR using hydride rather than oxide fuel and to quantify the resulting transmutation effectiveness. The extra hydrogen in the fuel softens the neutron spectrum and thereby reduces the critical Pu concentration [1,2]. The fuel hydrogen also mitigates the adverse effect of large voiding on the core reactivity.

The study starts with the benchmarking our neutronic computational capabilities for heterogeneous, plutonium-containing (CORAIL [3,4]) and TRU-containing (CONFU [14]), fuel assemblies. Our verified computational capability is then applied to the comparison of the performance of the reference Pu-hydride (PUZH) fuel assembly with two oxide fuel assembly designs that were proposed to overcome the positive void coefficient of reactivity – CORAIL and MOX-UE [3,4]. Both of these design approaches use enriched uranium, either segregated or mixed with the Pu, to reduce the critical plutonium mass. These design approaches offer neither substantial natural uranium nor Separating Working Unit (SWU) saving over conventional UO_2 fuelled cores and they provide for Pu stabilization rather than net destruction. It will be shown that the PUZH fuel offers a larger fractional transmutation than the equivalent MOX-UE oxide fuel while using depleted uranium, because of its larger H/HM ratio.

A search for the hydride fuel composition that offers maximum fractional plutonium transmutation is then undertaken; the design variables are amounts of thorium and uranium. The three-constituent fuels examined are of the form ThH_2-$ZrH_{1.6}$-PuH_2 and U-$ZrH_{1.6}$-PuH_2; the volume fraction of the constituents vary. Also investigated is the possibility for multi-recycling plutonium, inferring that the use of hydrides could allow for a larger number of recycles than what would be possible with oxides. This is because the incorporation of a significant fraction of the hydrogen moderator in the fuel (a unique feature of hydride fuels), would mitigate the effect of spectrum hardening due to coolant voiding accidents, thereby allowing the large void reactivity coefficient to remain negative for a larger number of recycles. Finally, the study

evaluates the possibility of recycling in hydride fuels neptunium together with plutonium and Pu along with the entire MA stream.

The work is concluded with a system and economic analysis that compares the fuel cycle characteristics of Pu and MA recycling in PWR using the promising hydride fuel assembly designs identified in the previous part of the work versus Pu and MA recycling in PWRs using oxide, including inert matrix fuel assemblies.

2.2 Benchmark our Fuel Assembly Computational Capability

2.2.1 Computer codes and data libraries

The calculations presented throughout this work were performed mostly with the TRITON/NEWT sequence of SCALE 5.0 and 5.1 [5,6,7,8] applied to a single unit cell configuration using the ENDF/B-V derived 238 energy group libraries generated using the BONAMI and NITAWL modules for, respectively, the unresolved and resolved resonances. The ability of NEWT/TRITON to correctly predict the performance of plutonium bearing fuel was established by performing benchmark calculations with complex plutonium and TRU-bearing assembly designs (such as the CORAIL and CONFU assemblies). A summary of the results of those benchmarks are presented in this Section.

2.2.2 Benchmark of the CORAIL assembly

The CORAIL is a 17x17 PWR fuel assembly design having 264 fuel rods of which 84 are MOX pins and the remaining 180 are UO_2 pins using enriched uranium. The modeling of the CORAIL assembly is particularly challenging, both because of the presence of degraded plutonium and because of its strong heterogeneities, due to the positioning of MOX pins on the periphery and UO_2 pins in the center of the assembly, which in turn cause a strong flux gradient within the assembly. For this reason a benchmarking effort was initiated between ANL and CEA of France, using both deterministic and Monte Carlo codes [9]. In particular WIMS8 and MCNP4C where used at ANL, and APOLLO2 and TRIPOLI4 where used at CEA. Initially large discrepancies where found in the evaluated pin power distribution between WIMS8 and APOLLO2. These discrepancies where later largely resolved by using the $P_{ij} + S_n$ model in APOLLO2 [9].

For the purpose of validating our computational tool - TRITON/NEWT code and associated cross section libraries, part of SCALE 5.1 [8], against results of WIMS8 and APOLLO2, a benchmark was performed for the CORAIL assembly.

First a static calculation was performed at BOL, mainly comparing k_∞ and assembly pin power distribution. Afterwards a depletion calculation was performed and several parameters were compared including k_∞, pin power distribution and most importantly the concentration evolution of various actinides, averaged over the assembly. At this stage a significant disagreement was found in the burnup-dependent concentrations of some of the minor actinides, particularly of ^{242m}Am. Therefore an effort was initiated to understand the reason of this discrepancy. The afore-mentioned discrepancy was traced back to a difference in the branching ratio (BR) of the (n,γ) reaction of ^{241}Am. After changing the branching ratio in the SCALE libraries to the values used by WIMS8, the agreement on ^{242m}Am appeared satisfactory. Additionally the calculated concentrations of several other minor actinides benefited from this change, particularly of ^{242}Cm, because it is formed by β^- decay of ^{242}Am. This demonstrated that the reason of the discrepancy is not due to the cross section libraries, but to the branching ratio used by the codes.

For the most accurate results, the resolved resonance treatment should be done with CENTRM, a continuous energy transport module. Unfortunately, at the time of this work, CENTRM was not recommended by ORNL for reactor calculations at normal operating temperatures because of a

yet un-resolved issue with the absorption cross section of ^{238}U [10]. Therefore the recommended module for un-resolved resonance treatment remains NITAWL, based on the Nordheim method and available with ENDF/B-V based cross sections. Nevertheless we will show some results obtained with CENTRM before the cross section issue was found and made public.

The benchmark in [9] was performed for both 8 weight percent plutonium and 12 weight percent plutonium. We performed both benchmarks, but for compactness and clarity in this report we only show the results for the 8 weight percent plutonium design. The results accuracy for the 12 weight percent Pu design is similar.

2.2.3 CORAIL benchmark specification and computational methodology

The CORAIL benchmark geometric details are shown in Figure 2.1 and the atomic densities of each of the constituents are given in Table I for the fuel, and in Table II and Table III for the coolant densities in cold and hot conditions, respectively.

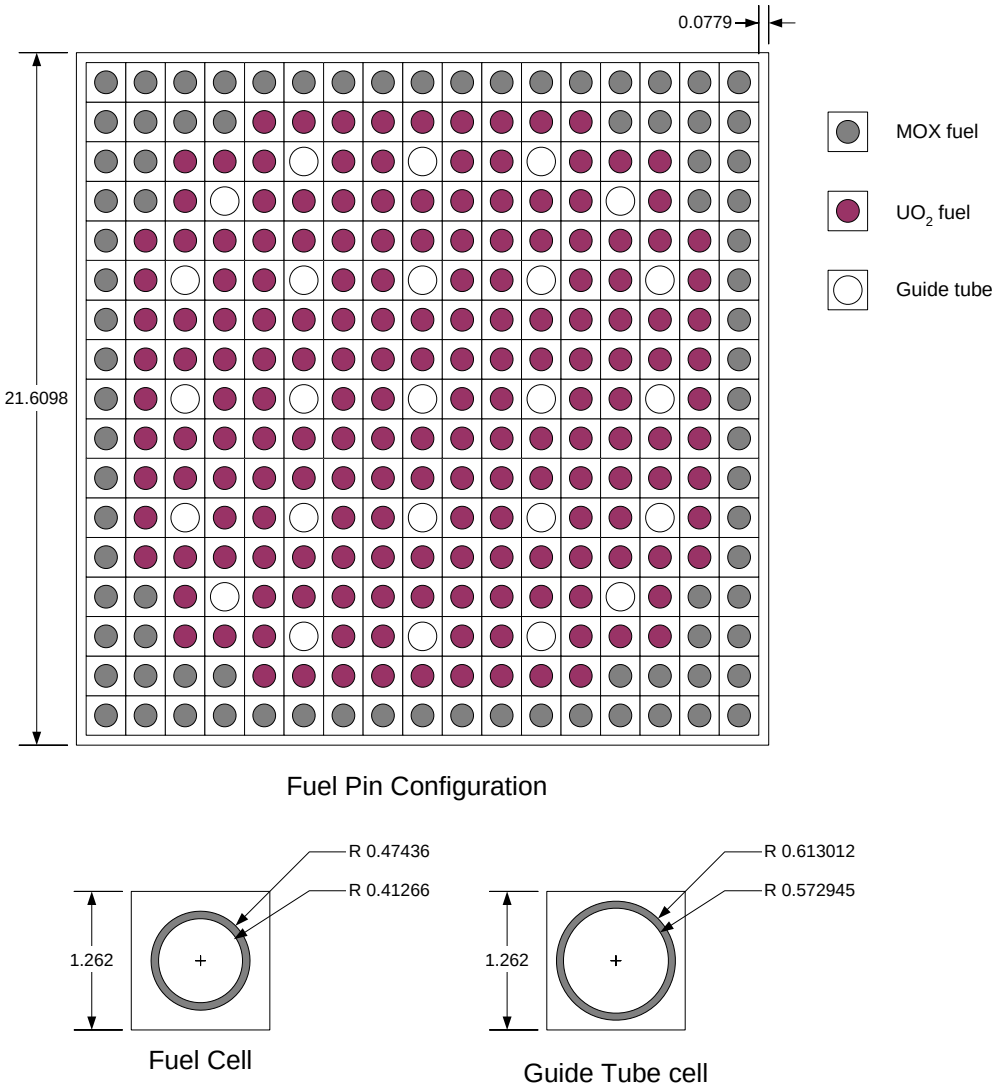

Figure 2.1 Geometric configuration of the CORAIL assembly (from [9])

The WIMS8 and APOLLO2 calculations used JEF2.2 derived cross section library whereas TRITON for this analysis used ENDF/B-V derived 44 group library; only the BOL static calculation was performed with the 238-groups library. The multi-group cross sections are calculated using BONAMI for treating the unresolved resonances with the Bondarenko method, and NITAWL to treat the resolved resonances using the Nordheim method. The depletion is performed by ORIGEN-S.

Figure 2.2 shows the TRITON/NEWT model of the CORAIL assembly. The model employed simulates the lower right quadrant of the assembly, with the water gap explicitly represented on the side of the MOX pins as was done with the WIMS8 and the MCNP4C models.

2.2.4 CORAIL benchmark results: k_∞ and pin power distribution evaluation at BOL

The BOL k_∞ results of the benchmarks calculated at ANL and CEA are given in Table 2.1. To adapt the calculations to the cross sections available in the Monte Carlo codes (MCNP and TRIPOLI), all the results are at room temperature (294 K). Our results with TRITON are therefore at 294 K as well; they are given in Table 2.2 together with the extent to which they differ from MCNP4C results calculated using ENDF/B-V.

Table 2.1 Benchmark Results of the BOL k_∞ from ANL and CEA

Methodology	Code	Library	k_∞	
			8% Pu	12% Pu
Monte-Carlo	MCNP4C	ENDF/B-VI release 2	1.28861 ± 0.00031	1.29541 ± 0.00031
		ENDF/B-VI release 5	1.28906 ± 0.00031	1.29609 ± 0.00031
		ENDF/B-V	1.28937 ± 0.00032	1.29505 ± 0.00029
		JEF-2.2	1.29409 ± 0.00031	1.29992 ± 0.00031
	TRIPOLI 4	JEF-2.2	1.29637 ± 0.00038	1.30187 ± 0.00039
Deterministic transport	WIMS8	JEF-2.2 (6)	1.28645	1.29185
		JEF-2.2 (28)	1.28633	1.29217
		JEF-2.2 (172)	1.28706	1.29263
	APOLLO2	JEF-2.2	1.29649	1.30212

Table 2.2 Results of the TRITON/NEWT Simulations at BOL

XS library	Condition	BOL k_∞	Difference (pcm) from MCNP4C (ANL)
ENDF/B-V 44 groups	Nominal cold	1.289124	-19.0791
ENDF/B-V 238 groups	Nominal cold	1.282912	-500.865
ENDF/B-V 44 groups [(a)]	Nominal cold	1.289145	-17.4504
ENDF/B-V 44 groups	Boron Branch cold	1.290805	N/A

[(a)] Using 38 different zones to evaluate the power distribution and to allow for pin-dependent depletion.

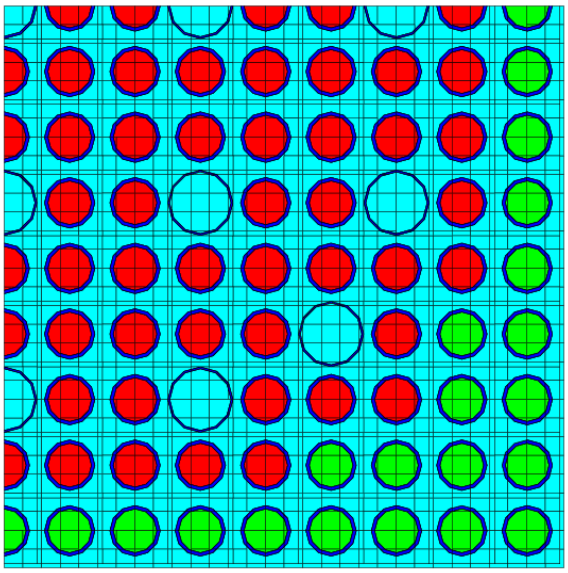

Figure 2.2 TRITON model of the CORAIL assembly: bottom-right quarter of the assembly: in red the UO_2 pins and in green the MOX pins. The water gap is modeled explicitly

The agreement with ANL MCNP on the multiplication factor is very satisfactory (less then 20 pcm and within a standard deviation) when the 44 group cross section library is used, but becomes less satisfactory when the 238 groups library is used. This is likely due to fortuitous compensation of errors.

Table 2.3 gives the normalized pin power distribution and the difference in percent between TRITON with 44 groups and ANL-MCNP4C, with cross sections derived from ENDF/B-VI. The agreement is satisfactory, showing a maximum discrepancy of 1.72 % and –1.48 %. The agreement is worse between the reported results of ANL and CEA, being as high as 2.8% between TRIPOLI and MCNP4C (using JEF2.2 and ENDF/B-VI respectively).

2.2.5 CORAIL benchmark results: k_∞ evolution with burnup

Figure 2.3 shows a comparison of the differences in k_∞ as a function of burnup for APOLLO2 and WIMS8 and for a number of cases to be presented in greater detail later. The difference between APOLLO2 and WIMS8 (blue line) is larger than the difference between TRITON and WIMS8; this is despite of the fact that both APOLLO2 and WIMS8 use JEF2.2 cross section libraries while TRITON/NEWT uses ENDF/B-V. The difference becomes even smaller when TRITON is compared with the average of WIMS and APOLLO. BR in the caption means "Branching Ratio" and involves changes in the branching ratio of the (n,γ) reaction of ^{241}Am, for reasons to be explained later in Section 2.2.7. Changes in this parameter do not alter substantially the calculated eigenvalues. The difference between TRITON and WIMS8 becomes larger than the difference between APOLLO2 and WIMS8 at larger burnups if CENTRM is used to create the multi-group cross sections (brown line with the circle marker).

Table 2.3 Normalized CORAIL pin power distribution at BOL: TRITON results and percent difference from ANL MCNP with ENDF/B-VI. The maximum and minimum discrepancies are 1.72 % and –1.48 % respectively (in red)

Triton							0.803
% diff	MCNP						0.04%
						0.809	0.796
						0.82%	0.64%
					0.767	0.901	0.825
					-0.78%	**1.72%**	0.30%
					0.911	1.024	0.888
					0.75%	0.67%	-0.32%
			1.068	1.074	0.992	0.814	0.978
			-1.02%	0.03%	-0.73%	0.73%	1.13%
			1.125	1.091		0.901	1.033
			-0.87%	-0.70%		-0.01%	1.51%
	1.092	1.145	1.070	1.043	1.029	0.879	1.041
	-1.10%	-0.90%	-1.05%	0.17%	-0.27%	0.28%	0.78%
1.103	1.101	1.146	1.078	1.044	1.040	0.886	1.056
-0.70%	**-1.48%**	-0.58%	-0.58%	-0.24%	-0.87%	0.48%	0.64%
1.161	1.153		1.128	1.099		0.932	1.060
0.23%	-0.89%		-1.11%	0.37%		0.10%	0.88%

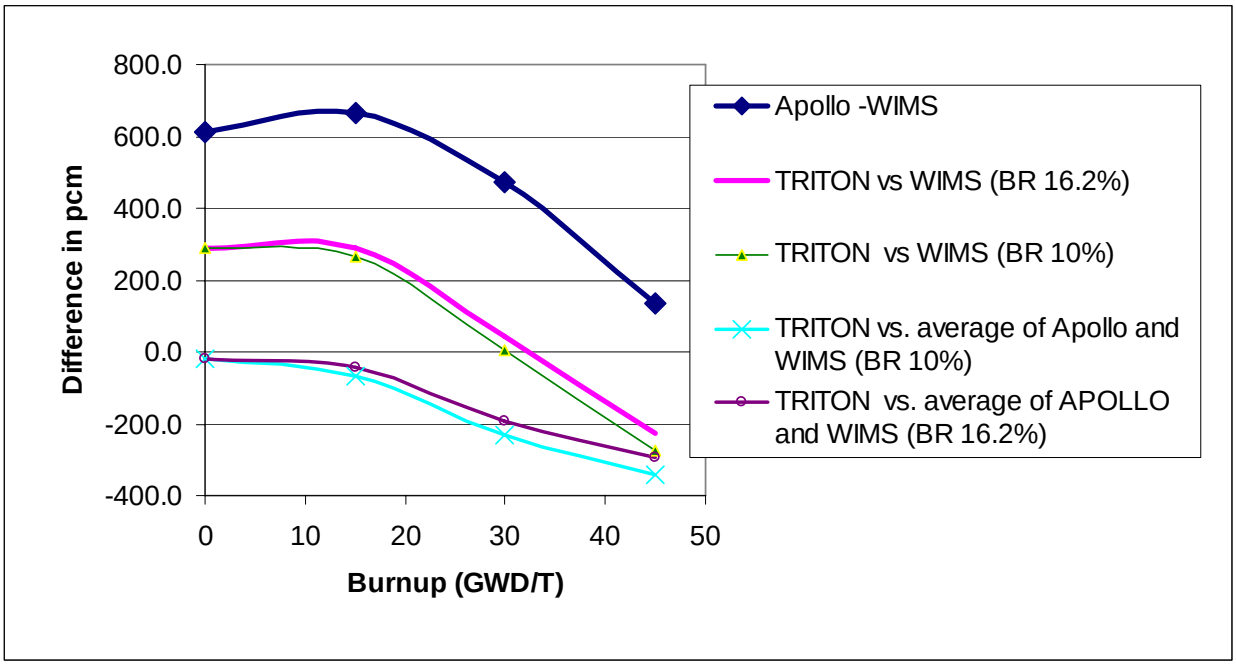

Figure 2.3 Evolution with burnup of the differences in the k_∞ (in pcm) between APOLLO and WIMS as compared to TRITON versus WIMS and TRITON versus the average of WIMS and APOLLO. From top to bottom: difference between APOLLO2 and WIMS8, between TRITON and WIMS8 with branching ratios of 16.2% and 10% in the (n,γ) reaction of 241Am, between the TRITON and the average of WIMS8 and APOLLO2 and between TRITON and WIMS8 when CENTRM is used instead of NITAWL.

2.2.6 CORAIL benchmark results: Pin-wise power distribution and actinides evolution with burnup

Pin-wise power distribution data are available in [9] at 0, 15, 30, 45 GWD/T for APOLLO2 and WIMS8. The disagreement between these and TRITON's is of the same order of magnitude (always less than 3% and mostly less than 2%) as the disagreement between WIMS and APOLLO − even though the latter two use the same cross sections; and is generally larger from the results of APOLLO than of WIMS8; this maybe reflecting the fact that both WIMS and TRITON model the water gap at the periphery of the assembly explicitly, while APOLLO does not.

Similarly, assembly-wise average actinides concentration data are available in [9] at 15, 30, 45 GWD/T for APOLLO2 and WIMS8. These were compared to those of TRITON. The discrepancy in concentration is reasonable for the major U isotopes, the Pu isotopes and ^{241}Am. The heavier minor actinides show less satisfactory agreement. Of particular concern is the discrepancy – exceeding 60% – in the ^{242m}Am concentration, which is even somewhat increased when using the continuous-energy spectrum averaging module CENTRM instead of NITAWL to generate the self-shielded cross sections. When CENTRM is used for cross section pre-processing, most of the actinides, with the exception of ^{238}U, ^{238}Pu, ^{241}Am, ^{242m}Am, ^{242}Cm and ^{244}Cm show an increase in accuracy as compared to when NITAWL is used.

2.2.7 Branching ratio of ^{241}Am

The large discrepancy observed in ^{242m}Am prompted us to investigate the effect of the branching ratio of the (n,γ) reaction of ^{241}Am. The branching ratio is energy dependent, therefore it needs to be evaluated by spectrum-weighting the energy-dependent branching ratio using Equation 2.1 (where $f_{\gamma 1}(E)$ is the energy dependent branching ratio).

$$\bar{f}_{\gamma 1} = \frac{\int_0^\infty f_{\gamma 1}(E)\sigma_c(E)\phi(E)dE}{\int_0^\infty \sigma_c(E)\phi(E)dE} \qquad (2.1)$$

We obtained from [11] the data in Figure 2.4, showing the branching ratio of the (n,γ) reaction of ^{241}Am to generate ^{242}Am (and ^{242m}Am) as a function of energy. All the most recent nuclear data files are in good agreement in the thermal region and, with the exception of JENDL-3.3, exhibit a similar behavior also in the epithermal region. The default SCALE 5.1 libraries of the depletion module ORIGEN-S have a branching ratio of 16.2% for the creation of ^{242m}Am from the (n,γ) reaction of ^{241}Am.

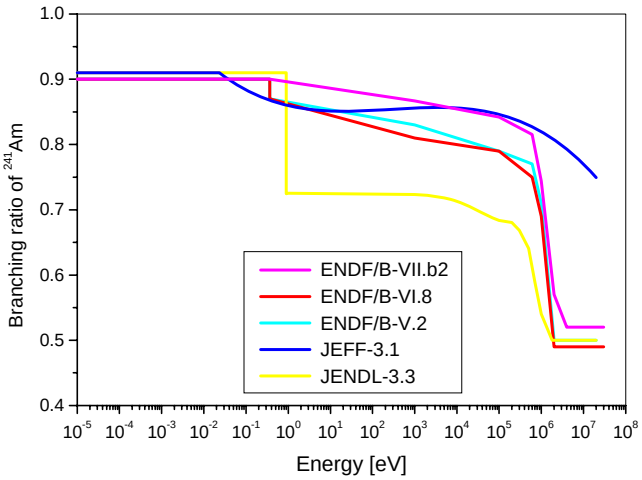

Figure 2.4 Branching ratio of ^{241}Am (n,γ) reaction

To estimate how accurate this number is with respect to the more recent evaluations, we performed a spectrum weighting on the typical spectra for few representative fuel types. Starting from the energy-dependence of the branching ratio shown in Figure 2.4 for the ENDF/B-VI (red line), we weighted it over the fluxes of a typical PWR with 5% enriched UO_2 and with MOX. Additionally we integrated over the CORAIL average fuel spectrum and over the average spectrum of PUZH fuel[1], which is softer than that of MOX fuel because of its larger hydrogen-to-Pu ratio in the fuel assembly.

The resulting evaluated branching ratios are compared in Table 2.4. All the resulting branching ratios are of the order of 10% to 11%, making the SCALE 5.1 default value of 16.2% clearly inadequate. Recently presented measurements at the CEA labs of Saclay and Cadarache of a branching ratio of 10.5% ±0.1% at 0.025 eV [12] further confirm our spectrum averaged results.

Table 2.4. Resulting evaluated branching ratios for different typical fuel types spectra

	PWR	MOX	PUZH	CORAIL
BR ^{242}Am	0.884	0.893	0.889	0.893
BR ^{242m}Am	0.116	0.107	0.111	0.107

2.2.8 Re-evaluation of the CORAIL benchmark with the modified branching ratio

WIMS8 in use at ANL uses a branching ratio of 10%, while APOLLO2 uses 11.5% for (n,γ) capture reaction of ^{241}Am. To test the importance of the branching ratio on the observed discrepancy of ^{242m}Am, we changed the branching ratio in the scale binary libraries to 10%, and re-performed the benchmark calculation.

Table 2.5 compares the calculated nuclei evolutions using the new libraries with a 10% branching ratio (on the right side) to the nuclei evolution in case of 16.2% branching ratio (on the

[1] PUZH is an acronym for a hydride fuel of the type U-PuH_2-$ZrH_{1.6}$, which has been studied extensively at UCB as an alternative for the disposition of plutonium in PWR.

left side). The disagreement on the ^{242m}Am evolution virtually disappears, confirming our assumption that the discrepancy found initially was mainly due to the difference in the branching ratio. The other differences are roughly similar, with the exception of ^{242}Cm, which is formed mainly by β^- decay of ^{242}Am. Large discrepancies in the number densities of heavier actinides, especially the curium isotopes are well known and documented in the literature: for example the reported uncertainties in the number densities of curium isotopes in the OECD-proposed benchmark A for Pu recycling in PWR, [10] are: 17%, 26%, 11% and 19% for respectively ^{242}Cm, ^{243}Cm, ^{244}Cm, ^{245}Cm. Except for ^{245}Cm these values exceed the discrepancies found between TRITON/NEWT and WIMS8.

Table 2.5. Percent difference in the assembly-average concentrations in TRITON as compared to WIMS for the case of NITAWL with 10% ^{241}Am branching ratio

	TRITON BR 16.2% versus WIMS8				TRITON BR 10% BR versus WIMS8		
	15 GWD/T	30 GWD/T	45 GWD/T		15 GWD/T	30 GWD/T	45 GWD/T
U-234	-2.50%	-8.60%	-4.00%		-5.40%	-5.70%	-5.70%
U-235	-2.10%	1.00%	-7.80%		-0.70%	-1.80%	-2.90%
U-236	7.80%	2.00%	4.80%		4.60%	4.20%	3.20%
U-238	0.00%	0.10%	-0.10%		0.00%	0.00%	0.00%
Pu-238	-0.50%	-1.50%	0.40%		-0.10%	0.00%	0.90%
Pu-239	0.50%	-2.20%	-4.10%		0.50%	-2.60%	-3.20%
Pu-240	-0.50%	-1.10%	-2.70%		-0.60%	-1.30%	-2.20%
Pu-241	1.10%	-1.10%	-1.50%		0.60%	-0.50%	-1.50%
Pu-242	1.80%	1.80%	5.00%		1.50%	2.60%	3.80%
Am-241	2.30%	1.50%	1.10%		2.10%	1.60%	1.60%
Am-242m	42.40%	61.20%	61.40%		-13.10%	-0.30%	0.30%
Am-243	4.00%	6.00%	16.70%		0.20%	9.10%	12.30%
Cm-242	-8.60%	-10.10%	-6.90%		-3.90%	-1.90%	-1.70%
Cm-243	18.20%	8.10%	14.00%		20.10%	20.80%	18.40%
Cm-244	-7.30%	-10.80%	5.80%		-13.90%	-5.00%	-1.50%
Cm-245	-26.60%	-35.40%	-23.20%		-34.20%	-29.40%	-29.50%

2.2.9 Benchmark of the reactivity coefficients of first recycle plutonium in CORAIL

To validate the accuracy of our reactivity coefficients calculations, we benchmarked our calculated Beginning-Of-Life (BOL) reactivity coefficients with those reported in reference [3] for the CORAIL fuel assembly. In the absence of enough details in reference [3], the fuel assembly geometry and material composition, density and temperature as specified for the CORAIL benchmark [9, 7] were used. The BOL soluble boron concentration assumed is 1700 ppm [3]. The BOL coolant temperature coefficient of reactivity, calculated for the temperature range from 583 K to 593 K, is -14 pcm/K. This value is in reasonable agreement with the -20 pcm/K reported in reference [3].

2.2.10 Benchmark of the CONFU fuel assembly

The CONFU assembly [14,15,16], has been proposed for multi-recycling of TRU in PWR. The TRITON/NEWT benchmark results, presented in this section, are compared against the

CASMO-4 results obtained at MIT. The characteristics compared are the evolution with burnup of k_∞, pin power distribution and the concentrations of the most important actinides.

The TRITON/NEWT model of the lower right quadrant of the CONFU fuel assembly is very similar to that of the CORAIL fuel assembly (Figure 2.2): the 84 peripheral pins are fertile free fuel containing minor actinides, while the 180 central pins are made of 4.2% enriched UO_2. The composition, in atoms/b-cm, of the two fuel types is given in Table 2.6. The density of the fertile free fuel is 5.526 g/cm^3, the density of the UO_2 fuel is 10.34 g/cm^3. The temperature of both fuel types is 900 K, that of the water is 580 K. The dimensions of the UO_2 and fertile free fuel rods are the same: the fuel radius is 0.4095 cm, the clad inner radius is 0.4178 cm and the clad outer radius is 0.475 cm. Control rod guide tubes' inner and outer radius are 0.5715 cm and 0.612 cm respectively. The assembly average power density is 104.5 kW/liter. The pitch is 1.26 cm while the assembly pitch is 21.5 cm.

Figure 2.5 shows the evolution of k_∞ with burnup as calculated with TRITON/NEWT and CASMO-4. The two curves are indistinguishable. The maximum discrepancies between the two codes prediction of the pin-wise power distribution are in the corner pin, which is showing a maximum discrepancy of 3.83%. The CONFU assembly-averaged isotopic evolution with burnup were compared for the most important actinides: ^{235}U, ^{236}U, ^{238}U, ^{238}Pu, ^{239}Pu, ^{240}Pu, ^{241}Pu, ^{242}Pu, ^{241}Am, ^{242m}Am and ^{244}Cm. The agreement between the TRITON and CASMO predictions is excellent for all the evaluated actinides with the exception of ^{242m}Am which shows a discrepancy of about 20%: CASMO predicts a higher concentration. As in the case of CORAIL, this is likely due to differences in the branching ratio of the (n,γ) reaction of ^{241}Am between TRITON and CASMO.

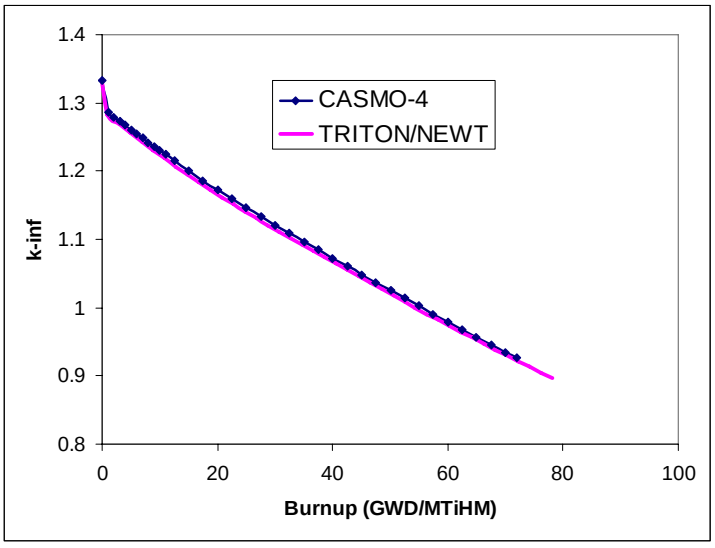

Figure 2.5 CONFU assembly k_∞ evolution with burnup as predicted by CASMO-4 and TRITON/NEWT

Table 2.6. Nuclei Density of the CONFU Fuel Assembly in atoms/b-cm

	Fertile free	UO_2
U-235	5.6835E-08	0.000981
U-238	7.797E-06	0.022086
Pu-239	0.00116425	
Pu-242	0.00011912	
Am-243	3.4713E-05	
Cm-244	1.1654E-05	
Y-89	0.00070454	
Zr	0.03332603	
U-234	1.7066E-09	7.88E-06
Np-237	0.0001601	
Pu-240	0.00054789	
Am-241	0.00011056	
Cm-242	0	
Cm-245	8.8965E-07	
Mg	0.01871896	
U-236	4.6944E-08	
Pu-238	6.6027E-05	
Pu-241	0.00016453	
Am-242	4.497E-07	
Cm-243	1.1791E-07	
Cm-246	1.3997E-07	
O-16	0.05447767	0.046117

2.2.11 Comparison of k_∞ estimated with an equivalent pin cell and an assembly calculation

Doing depletion analysis for a full fuel assembly and 238 energy groups is not practical with our TRITON/NEWT system due to excessive memory requirements. However, since the reference TRU-hydride fuel assembly features a uniform configuration, reactor physics characteristics, such as achievable burnup, actinide concentration evolution and reactivity coefficients can be estimated using a unit cell analysis, even at a high energy resolution through the use of the 238 energy group library. Other characteristics, such as the assembly power peaking factors and control rods worth, require a full 2-D assembly calculation. A unit cell model that will properly represent a fuel assembly has to account for the extra water present in the assembly in the control rods channels and the inter-assembly gap.

The pitch-to-diameter ratio (P/D) of the fuel pins in the reference assembly is 1.3261. When the extra water present in the control rod thimbles and in the inter-assembly gap is taken into account, the equivalent unit cell P/D is 1.393. All the unit cell results presented in this report were obtained from calculations performed with the 238-groups library of SCALE-5.1. Figure 2.6 shows on the left the evolution of k_∞ of the effective unit cell model loaded with plutonium hydride (PUZH) in comparison with that of the fuel assembly, and on the right the percent difference between the two lines.

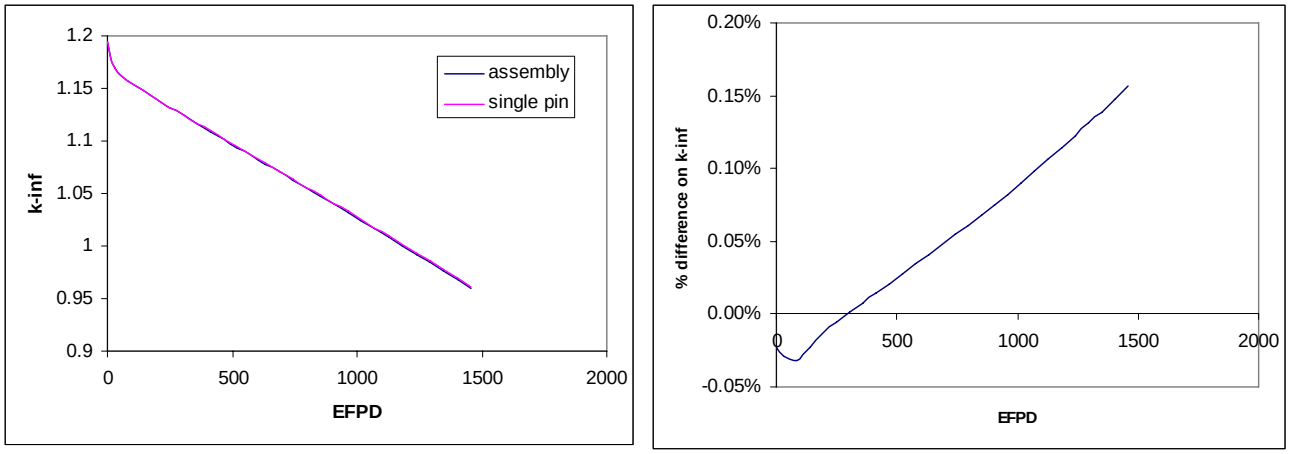

Figure 2.6 k_∞ evolution of the assembly and the equivalent unit cell for PUZH fuel with plutonium from first recycling (left) and Percent difference in the k_∞ evolutions (right)

2.2.12 Conclusions

The TRITON/NEWT sequence and associated cross section libraries of the SCALE 5.1 code package were found of satisfactory accuracy for modeling complex TRU-containing PWR fuel assemblies like the CORAIL and CONFU, provided that the ORIGEN default branching ratio for production of ^{242m}Am is changed to approximately 10-11%. A value of 10% for the branching ratio was found to provide good agreement with the calculated results of both APOLLO2 and WIMS8 in the case of CORAIL. In case of CONFU, the agreement between the TRITON and CASMO predictions is good for all the evaluated actinides with the exception of ^{242m}Am which shows a discrepancy of about 20%: CASMO, which likely uses a slightly different value for the branching ratio of ^{241}Am, predicts a higher concentration of ^{242m}Am.

Since the reference TRU-hydride fuel assembly features a uniform composition, integral reactor physics characteristics, such as achievable burnup, actinide concentration evolution and reactivity coefficients can be estimated using a unit cell analysis, even at a high energy resolution through the use of the 238 energy group library. Other characteristics, such as the assembly power peaking factors and control rods worth, require a full 2-D assembly calculation.

2.3 Database Establishment: Identification of Promising PWR Fuel Assembly Designs and Comparison with Equivalent Hydrides

In this section the Pu bearing oxide fueled PWR designs to be used as the reference are identified. CORAIL, MOX-UE [3] and CONFU [13,14,15] are the most promising among a number of oxide fuel assembly designs that were proposed to overcome the positive void coefficient that arises when the total plutonium inventory in PWR reaches ~12 $^{w}/_{o}$ (i.e. after 2 to 3 recyclings). All three design approaches use enriched uranium, either segregated or mixed with the Pu (or TRU), to reduce the required TRU mass.

These designs offer neither substantial natural uranium nor Separating Working Unit (SWU) saving over conventional UO_2 fuelled cores as they offer Pu (or TRU) stabilization rather than net destruction. The heterogeneous configurations (CORAIL and CONFU) feature relatively large pin-wise power peaking factor.

2.3.1 CORAIL characterization and comparison with PuH_2-U-ZrH_2 (PUZH) for first-recycle plutonium

The main purpose of the CORAIL assembly (described in detail in Section 2.2.3) is to safely allow for multi-recycling of plutonium in PWR [3]. The resulting heterogeneous system has been shown to be capable of stabilizing the plutonium inventory without requiring any modification to the control system of the core and without the insurgence of positive void reactivity feedback at the onset of a large core voiding [3]. Its drawbacks are the requirement of enriched uranium and a relatively high power peaking factor due to the heterogeneous configuration.

The CORAIL design is a rather effective plutonium burner, destroying about 40% of the initial plutonium loaded in the peripheral rods – thanks to the UO_2 rods surrounding the plutonium loaded ones [3]. However, because plutonium is loaded only in the peripheral rods – which are only 84/264 or less than a third – and the UO_2 rods create about the same amount of plutonium that is consumed in the peripheral ones, the assembly design ends up being a plutonium stabilizer. A proper comparison of the CORAIL assembly with a hydride fuel design can be done assuming an identical geometry and linear heat rate, but changing the fuel type. The performance of the two systems (CORAIL and homogeneous hydride) is compared with plutonium from the first recycling, called Pu-V1 in [3] and given in Table 2.7[2].

Table 2.7 The Plutonium Isotopic Composition for the First Recycling (from (Youinou, 2005))

	^{238}Pu	^{239}Pu	^{240}Pu	^{241}Pu	^{242}Pu	^{241}Am	Pu-fissile
Pu-V1	2.7%	56%	25.9%	7.4%	7.3%	0.7%	63.7%

For the first recycling the CORAIL assembly is loaded with 8 weight percent Pu-V1 in the peripheral 84 fuel rods and with 5.4% enriched UO_2 in the central 180 fuel rods. Table 2.8 gives the assembly average densities and the total amount of plutonium, ^{235}U and ^{238}U per assembly at BOL.

[2] Expected to be the average composition from LWR available in France around 2015.

Table 2.8. BOL Assembly-Average Densities (g/cc) and Masses (kg/assembly) of Plutonium, of ^{235}U and ^{238}U in the CORAIL Assembly

	g/cc	kg/assembly
Pu	0.2551	13.15
^{235}U	0.3276	16.89
^{238}U	8.2481	425.27

The first hydride fuel considered for this comparison is of the type U-PuH_2-$ZrH_{1.6}$, also known as PUZH; it has been studied extensively at UCB in a previous project [1, 17, 18 and 2]. The PUZH fuel used in this analysis has the same plutonium vector (Pu-V1) loaded in each rod, mixed with uranium depleted to 0.3% ^{235}U. The uranium atomic density is chosen identical to the one loaded as a maximum in TRIGA reactors (of $9.4137 \cdot 10^{-3}$ at/barn-cm, corresponding to 3.72 g/cc of metallic uranium). The amount of plutonium is then adjusted to match the CORAIL fuel cycle length of 1255 days, resulting in a density of 0.86 g/cc of plutonium. Zirconium hydride fills the remaining volume fraction of 72%. The overall fuel density is 8.6278 g/cc. Table 2.9 gives the assembly average densities and volume fractions of the fuel constituents. Table 2.10 gives the assembly average densities and total mass per assembly. The total content of plutonium is about 3.3 times higher than in the case of CORAIL, but the uranium total amount is about half. Moreover the CORAIL contains uranium with an average enrichment of 3.8%, while the PUZH assembly contains depleted uranium. Figure 2.7 shows the evolution of k_{inf} for the two fuel types: the PUZH fuel shows a flatter behavior.

Table 2.9. Assembly-Average Densities and Volume Fractions of the Fuel Constituents of the PUZH

	g/cc	Volume fraction
PuH_2	0.8678	8.34%
U	3.7211	19.53%
$ZrH_{1.6}$	4.0388	72.12%

Table 2.10. Assembly-Average Densities of the U and Pu in the PUZH Assembly

	g/cc	kg/assembly
Pu	0.8606	44.37
^{235}U	0.0110	0.57
^{238}U	3.7092	191.25

A useful measure of the transmutation capability of these fuel types is the residual inventory at discharge of plutonium plus minor actinides (or total TRU) as compared to the mass loaded. The CORAIL fuel at discharge contains 107.77% of the loaded TRU, while the PUZH fuel contains 68.24% of the originally loaded TRU. In other words the CORAIL stabilizes the plutonium inventory while the PUZH consumes 31.76% of the loaded TRU in one pass through the core.

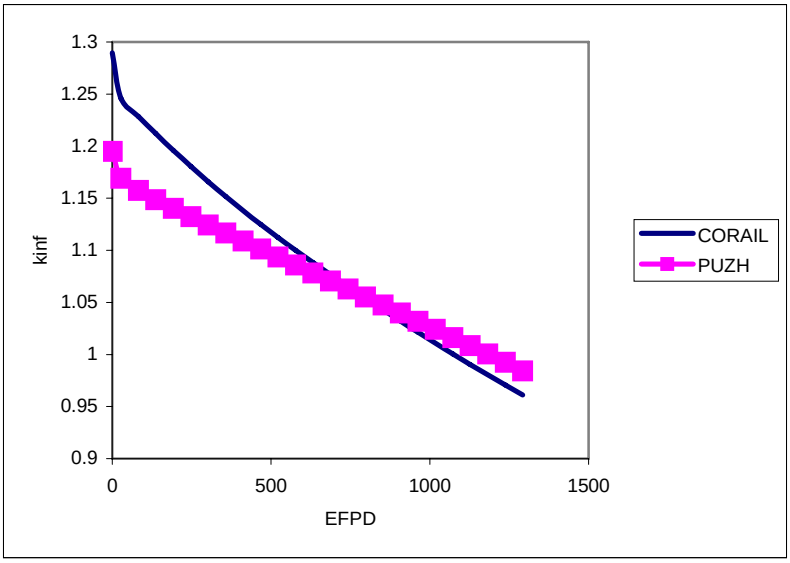

Figure 2.7: k_∞ evolution with fuel life (in EFPD) for CORAIL and PUZH first recycle

Table 2.11 and Table 2.12 give the detailed mass balances for, respectively, the CORAIL and PUZH at BOL and EOL. The amount of americium and curium in the discharged PUZH assembly is about three times higher than in the case of CORAIL. Additionally the residual plutonium in the PUZH is still about twice as much, reflecting the higher loading, despite the higher destruction fraction. The downloaded plutonium is more degraded in the PUZH assembly, having only 49.8% of fissile fraction, while in the CORAIL the fissile fraction is 58.68%.

Table 2.11. Nuclide Balance for the CORAIL Assembly with First Recycle Plutonium

	BOL (g/assembly)	EOL (g/assembly)
TOT U	442164	419309
TOT Np	0.00	248.95
TOT Pu	13057	13260
Fiss Pu/Pu	63.75%	58.68%
TOT Am	92.04	487.84
TOT Cm	0.00	193.87

Table 2.12. Nuclide Balance for the PUZH Assembly with First Recycle Plutonium

	BOL (g/assembly)	EOL (g/assembly)
TOT U	191820	184298
TOT Np	0.00	34.78
TOT Pu	44052	28257
Fiss Pu/Pu	63.75%	49.80%
TOT Am	312.34	1507.19
TOT Cm	0.00	553.69

2.3.2 MOX-UE characterization and comparison with PuH_2-U-$ZrH_{1.6}$ (PUZH) for first-recycle plutonium

The MOX-UE [3] (MOX with Enriched Uranium) design is a standard 17x17 fuel assembly containing 264 fuel rods and 25 guide tubes (24 control rods and 1 central instrumentation channel). Four assembly designs were analyzed, as in [3]; their plutonium content is 0% (or conventional UO_2 fuel), 4%, 8% and 12%. The uranium enrichment is consequently varied to achieve an assembly burnup of 60 GWd/t. The uranium enrichment, from [3] is 4.9% for the reference UO_2 core (no plutonium), 3.7% for 4% Pu, 2.3% for 8% Pu and 0.3% for 12% Pu. The geometry of the system, not described in [3], is assumed for consistency and ease of comparison to be the standard 17x17 PWR assembly design used for the PUZH and CORAIL assemblies. All fuel assemblies were designed to have the same cycle length at the same power level.

The mass balance for the different MOX-UE assembly designs is reported in Table 2.13 to Table 2.16 for, respectively, 0%, 4%, 8% and 12% plutonium. The TRU transmutation effectiveness is summarized in the last column of Table 2.17. The MOX-UE-4 assembly, that containing only plutonium and depleted uranium, has the best transmutation performance. The mass of loaded TRU (Pu and Am only) is 54 kg/assembly, and the total remaining TRU at EOL is 48 kg, giving a fractional TRU destruction of 16.35%. Smaller plutonium loading, and correspondingly larger ^{235}U loading, decrease the transmutation effectiveness.

The PUZH fuel assembly achieves the largest TRU fractional destruction of 31.6%. For comparison, a MOX-UE fuel assembly initially loaded with same amount of TRU gives a fractional transmutation of 15.6%. Design and performance data for this equivalent MOX-UE fuel assembly are given in the last line of Table 2.17; the data given was obtained by interpolated between the corresponding values of the MOX-UE-3 and MOX-UE-4 designs. The required plutonium weight fraction is 9.3, and the uranium enrichment need be 1.7%.

Table 2.13. Nuclide Balance for the MOX-UE-1 Assembly with 0% First Recycle Plutonium

	BOL (g/assembly)	EOL (g/assembly)
TOT U	475607	447107
TOT Np	0.00	324
TOT Pu	0.00	5654
Fiss Pu/Pu	N/A	70.58%
TOT Am	0.00	100.9
TOT Cm	0.00	35.2

Table 2.14. Nuclide Balance for the MOX-UE-2 Assembly with 4% First Recycle Plutonium

	BOL (g/assembly)	EOL (g/assembly)
TOT U	457500	438777
TOT Np	0.00	215.20
TOT Pu	18944	16198
Fiss Pu/Pu	63.75%	59.67%
TOT Am	134.32	748.25
TOT Cm	0.00	336.97

Table 2.15. Nuclide Balance for the MOX-UE-3 Assembly with 8% First Recycle Plutonium

	BOL (g/assembly)	EOL (g/assembly)
TOT U	439300	424061
TOT Np	0.00	159.36
TOT Pu	37963	30607
Fiss Pu/Pu	63.75%	58.04%
TOT Am	269.18	1253.15
TOT Cm	0.00	459.41

Table 2.16. Nuclide Balance for the MOX-UE-4 Assembly with 12% First Recycle Plutonium

	BOL (g/assembly)	EOL (g/assembly)
TOT U	421046	408444
TOT Np	0.00	83.15
TOT Pu	57055	45681
Fiss Pu/Pu	63.75%	57.54%
TOT Am	404.5	1734.2
TOT Cm	0.00	564.25

Table 2.17. Summary of the MOX-UE Fuel Assemblies Performance, as compared to PUZH and CORAIL; included also a MOX-UE with the same initial TRU mass as PUZH

	Pu (weight%)	Uranium enrichment (%)	Cycle length (EFPD)	TRU @ BOL (g/assembly)	TRU @ EOL (g/assembly)	TRU fractional destruction
MOX-UE 1	0	4.9	1226	0.0	6114	N/A
MOX-UE 2	4	3.7	1122	19078	174989	8.28%
MOX-UE 3	8	2.3	1164	38232	32479	15.05%
MOX-UE 4	12	0.3	1222	57459	48062	16.35%
CORAIL	N/A	N/A	1256	13149	141901	-7.92%
PUZH	18.78	0.3	1246	44365	30353	31.58%
MOX-UE eq*	9.3	1.7	N/A	44365	37449	15.59%

* Equivalent to PUZH in terms of amount of Pu loaded; data obtained by interpolating designs MOX-UE 3 and MOX-UE 4

It is concluded that the PUZH fuel offers twice as large fractional transmutation as the equivalent MOX-UE oxide fuel. That is, a PWR loaded with PUZH fuel assemblies will incinerate in the first recycle twice as much TRU (primarily Pu) as it will do when loaded with MOX-UE fuel assemblies when both core designs are loaded with same amount of TRU and operate at the same power level for the same time. The PUZH core is likely to be less expensive as it uses depleted uranium versus significantly larger quantities of 1.7% enriched uranium required for the equivalent MOX-UE core.

2.3.3 Power peaking factor of CORAIL, PUZH and MOX-UE

A drawback of the CORAIL design is a higher power peaking factor than in uniform-composition fuel assemblies. The CORAIL parameters for first recycling – fuel rod position,

number, uranium enrichment and plutonium weight fraction – were chosen to avoid a peaking factor higher than 1.2 at any point along the fuel life. This was in fact verified by our calculations.

Figure 2.8 shows the burnup-dependent pin-wise power peaking of the CORAIL, MOX-UE and PUZH fuel assemblies. It is observed that the PUZH fuel design has a lower power peaking factor than all the plutonium-bearing fuel assemblies analyzed along the entire fuel life (it is always less than 1.09). The MOX-UE-1 design, that is essentially a conventional UO_2 fuel assembly design, has a lower peaking factor. However, this fuel does not contain plutonium at BOL. The higher initial plutonium content in the MOX-UE fuel assemblies the higher becomes the peaking factor. For the equivalent amount of Pu as in the PUZH fuel assembly, the peaking factor of the MOX-UE fuel assembly is more than 1% point larger – approximately 1.096 versus 1.058 for the PUZH design at BOL.

The maximum peaking factor for the MOX-UE-1, MOX-UE-3 and PUZH fuel assembly designs – respectively 1.058, 1.096 and 1.083 – is in the same location; in the vicinity of a number of water-filled guide tubes. The lower peaking factor of the PUZH design is due to its enhanced moderation resulting from having hydrogen in the fuel, making it less sensitive to the extra moderation provided by the guide tubes water.

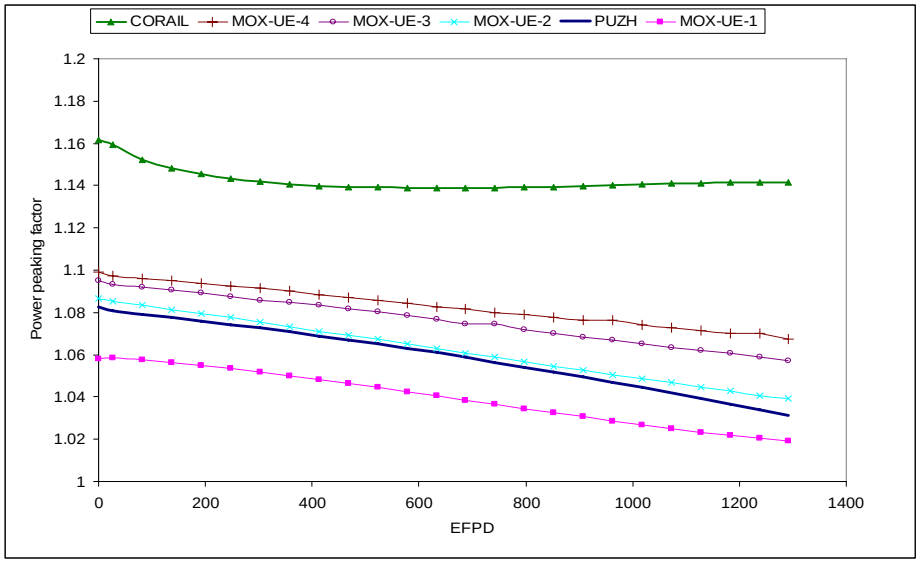

Figure 2.8 Pin-wise power peaking factor for the various fuel assemblies analyzed

2.3.4 Reactivity coefficients of CORAIL, MOX-UE and PUZH with 1st recycle Pu

This section summarizes the three-batch core average characteristics for the MOX-UE and PUZH, estimated from the results calculated for the equivalent unit cell using the methodology described in [19]. The results of the calculation of the reactivity coefficients of the CORAIL fuel assembly were presented in Section 2.2.9 in connection with the benchmarking.

The coefficients of reactivity – especially CTC and SVRC, are strongly dependent on the amount of soluble boron. An approach typically used at the level of unit cell and fuel assembly analysis is to assume a cycle average boron concentration. This assumption underestimates the necessary amount of soluble boron at BOC, leading to non-conservative estimates of the CTC and SVRC. Hence, time-dependent soluble boron concentration is calculated for our analysis.

For the PUZH fueled unit cell, the BOC needed amount of boron is 2758 ppm while at EOC no boron is left in the core (0 ppm). The EOC core average k_∞ is assumed 1.05, allowing for 5% neutron leakage probability from the finite core. All the reactivity coefficients of the PUZH fueled unit cell with plutonium from first recycling were found substantially negative, offering a margin of safety even without the use of burnable poisons to reduce the critical soluble boron.

Next consider the MOX-UE fueled unit cells. First their exact boron let-down curve has been estimated. It was found that the BOC required boron concentration is quite similar for the MOX-UE fuel types, as evidenced in the last column of Table 2.18; this is despite of the substantially different isotopic concentration.

Table 2.18. Summary of the MOX-UE Fuel Assemblies Performance, as Compared to PUZH; Included also a MOX-UE with the Same Initial TRU Mass as PUZH

	Pu $^{w}/_{o}$	U enrichment (%)	Cycle length (EFPD)	Fractional Pu destruction	Sol Bor at BOC (ppm)
MOX -UE 1	0	4.9	1494.8	N/A	2513.7
MOX -UE 2	4	3.7	1389.6	10.58%	2167.1
MOX -UE 3	8	2.3	1393.4	17.69%	2395.9
MOX -UE 4	12	0.3	1431.6	18.71%	2604.6
MOX-UE eq	9.3	1.7	N/A	18.32%	N/A
PUZH	10	0.3	1433.2	35.69%	2758.3

Figure 2.9 shows on the left the cycle-by-cycle LVRC for the MOX-UE fueled unit cells (MOX-UE-1 to MOX-UE-4) and on the right the corresponding core-average burnup-dependent LVRC. All other coefficients of reactivity were found negative). It is observed that only the MOX-UE-1 and MOX-UE-3 are acceptable over the entire desired burnup range without use of burnable poisons. MOX-UE-4 has a positive LVRC at BOC that is only slightly negative at EOC. From the trends in Figure 2.9 it appears that an increase in the fractional content of plutonium beyond the 12 $^{w}/_{o}$ value of MOX-UE-4 will results in positive values of core-averaged LVRC even at the EOC when there is no boron – an un-acceptable situation from the safety viewpoint. This result is consistent with the values reported in the literature [3], for which $12^{w}/_{o}$ plutonium loading (as in the case of MOX-UE-4) is the limit for a negative LVRC. For comparison, using PUZH fuel with depleted uranium as in the case of MOX-UE-4 enables attaining the same cycle length of the MOX-UE fueled systems while maintaining all the coefficients of reactivity, including the LVRC (in Figure 2.10), substantially negative. In addition, the fractional destruction of TRU in the PUZH fueled system is about twice that of the largest fractional transmutation attainable using MOX-UE fuel (Table 2.17 and Table 2.18).

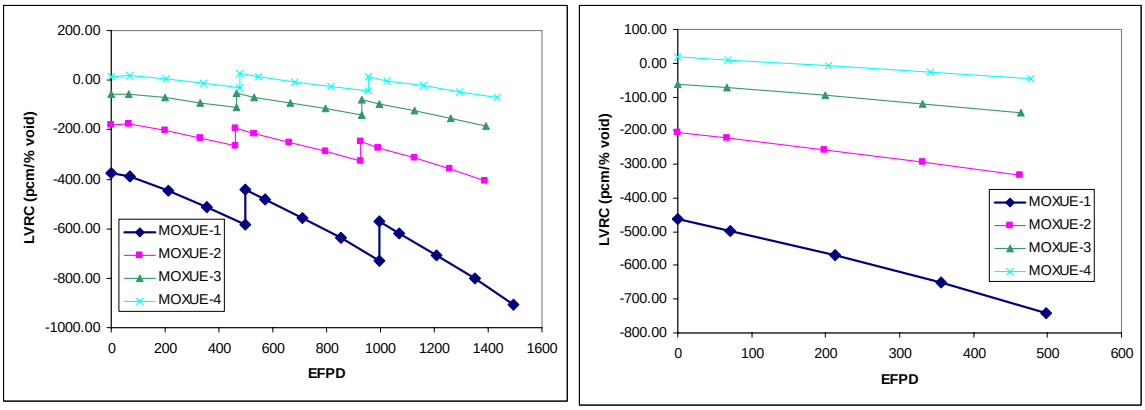

Figure 2.9 Large void coefficient of reactivity (LVRC) of MOX-UE fueled unit cell (left); core average (right)

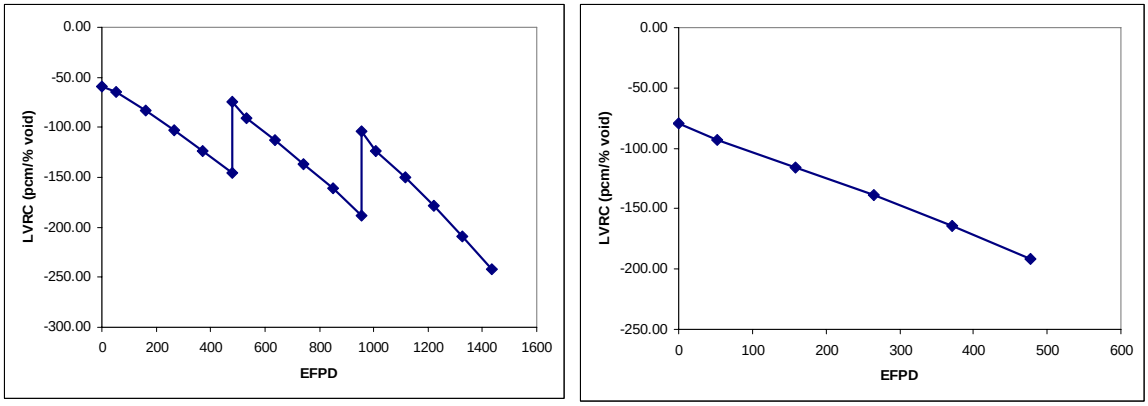

Figure 2.10 Large void coefficient of reactivity of PUZH fueled unit cell (left); core average (right)

2.4 Identification of the Most Promising Hydride Fuels (fertile free, thorium- and uranium-based) for Pu Multi-Recycling

2.4.1 Depletion performance for 1st Pu recycle of fertile-free hydride fuels and of hydride fuels with variable amounts of thorium

An assessment was undertaken of the feasibility of enhancing the fractional plutonium transmutation using thorium-based and fertile-free hydride fuels. These fuels are of the form ThH_2-$ZrH_{1.6}$-PuH_2, with Pu from first recycling. All the results pertain to the reference PWR unit cell dimensions (Table 2.19), and were obtained from effective unit cell analysis accounting for a 3-batch fuel management strategy using the methodology described in [19].

Table 2.19. Unit Cell Geometry and Specific Power

	Hydride Fuels	Oxide Fuels
Clad outside diameter	0.95 cm	0.95 cm
P/D	1.3261	1.3261
Fuel diameter	0.8192 cm	0.8205 cm
Clad inside diameter	0.8357 cm	0.8357 cm
Pitch	1.26 cm	1.26 cm
Specific power	76.715 W/giHM	36.138 W/giHM

The fuel composition is determined using the following procedure: Initially a plutonium amount is guessed with the intent of matching the fuel cycle length of about 1430 EFPD[3]. A certain fraction of the remaining fuel volume is assigned to ThH_2 and the balance to zirconium hydride ($ZrH_{1.6}$). Once the cycle length obtained in this way is known, the plutonium amount is increased or decreased to reach the desired cycle length and the remaining volume is split between the two hydrides (ThH_2 and $ZrH_{1.6}$) in the same ratio as before. This is repeated until convergence. This parametric study covered the entire ThH_2 to (ThH_2 + $ZrH_{1.6}$) volume fraction range from 0 $^{v}/_{o}$ to 100 $^{v}/_{o}$. The case having 0 $^{v}/_{o}$ ThH_2 is a fertile-free based hydride fuel. Table 2.20 gives the resulting composition of the unit cells examined, all featuring the same cycle length in EFPD. The required plutonium amount increases with the thorium content, going from 0.772 g/cm^3 for the case without thorium (PuH_2-$ZrH_{1.6}$) to 1.098 g/cm^3 for the case with no zirconium (ThH_2-PuH_2). Correspondingly, the density of the fuel increases from 5.956 g/cm^3 for the fertile free case to 9.595 g/cm^3 for the case without zirconium. Because of the strongly varying amount of heavy metal, the fuel burnup is highly varying – from 624.0 GWD/MTiHM for the fertile free case to 50.5 GWD/MTiHM for the case without zirconium.

[3] 1430 EFPD is the cycle length of the CORAIL, MOX-UE and PUZH fueled assemblies that use first recycle plutonium

Table 2.20: Properties of ThH_2 and Fertile-Free Hydride Fueled Unit Cells

ThH_2 $^v/_o$ of $ZrH_{1.6}$	0%	20%	30%	40%	50%	60%	70%	80%	100%
Pu density (g/cm^3)	0.772	0.783	0.808	0.839	0.876	0.917	0.960	1.005	1.098
Fuel density (g/cm^3)	5.956	6.683	7.052	7.422	7.790	8.157	8.521	8.882	9.595
HM density (g/cm^3)	0.766	2.519	3.407	4.296	5.181	6.062	6.936	7.803	9.513
Th density (g/cm^3)	0.0	1.742	2.606	3.463	4.312	5.153	5.984	6.806	8.424
Burnup (EFPD)	1427	1425	1428	1430	1433	1435	1436	1436	1434
Burnup (GWD/MTiHM)	624.0	189.4	140.3	111.5	92.6	79.3	69.3	61.6	50.5

Figure 2.11 shows that, for the same three batch cycle length, the burnup reactivity swing is reduced with an increase in the ThH_2 content. This is because the conversion ratio increases with the thorium volume fraction.

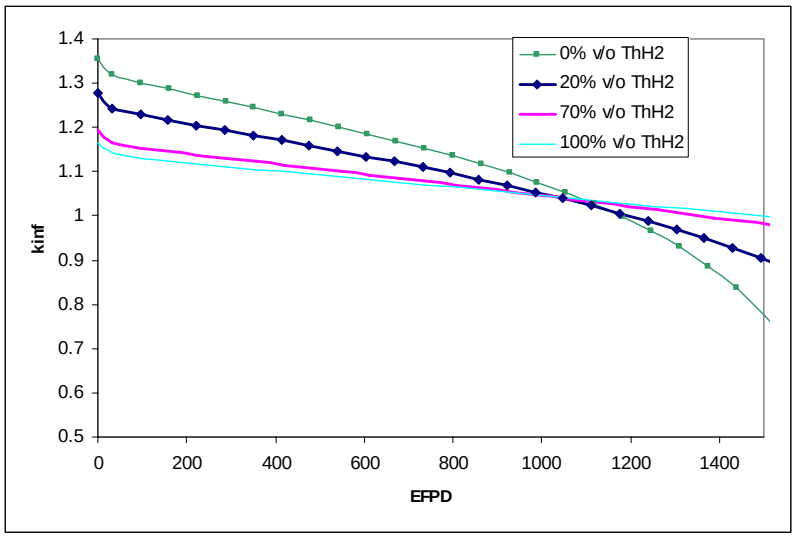

Figure 2.11 k_∞ evolution dependence on the ThH_2 volume fraction

The transmutation performance of the analyzed fuels is quantified by means of the TRU destruction fraction, defined as the ratio between the mass of TRU at discharge and the mass of the loaded TRU. Also of interest for proliferation concerns is the plutonium fissile fraction at discharge, defined as the ratio between the mass of ^{239}Pu and ^{241}Pu and the total mass of plutonium.

Figure 2.12 gives the TRU destruction fraction and the plutonium fissile fraction at discharge as a function of the ThH_2 volume fraction. The TRU destruction fraction decreases with the ThH_2 volume fraction, from a value of 63.89% for fertile free fuels to 35.85 % for ThH_2-PuH_2. This latter performance is similar to the one of PUZH (35.69%) and about double that of the highest performing MOX-UE (18.71%). Fertile free fuels (FFF), or almost fertile free fuels (AFFF) (i.e. those with a little amount of ThH_2) feature a TRU destruction fraction that is slightly less than double that of PUZH. The plutonium fissile fraction increases with the thorium content, from a low of 22.38% for the fertile free fuel to a maximum of 45.25% for ThH_2-PuH_2 fuel.

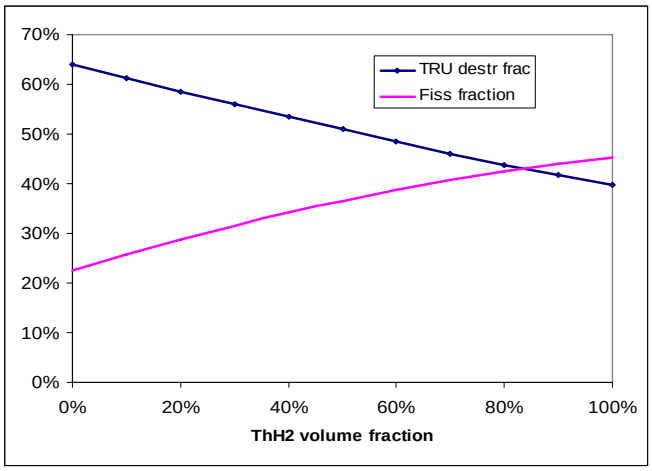

Figure 2.12. TRU destruction fraction and fissile fraction at discharge versus the ThH_2 $^v/_o$

2.4.2 TRU destruction fraction for 1st Pu recycle of PUZH and MOX with partial uranium loading

Both MOX and PUZH fuelled cores with Pu from first recycle (Table 2.7) and different fractions of uranium loading are analyzed in this section. The MOX fuel examined is of a more general composition than the "conventional" MOX – it may contain a certain amount of ZrO_2 to make up for the volume fraction of the fuel that is not fully loaded with uranium. The inert matrix oxide fuel PuO_2-ZrO_2 is evaluated as well to provide a fair comparison with the inert matrix hydride fuel PuH_2-$ZrH_{1.6}$.

Among the evaluated parameters are the attainable burnup, the mass balance of actinides throughout the recycling, the TRU destruction fraction, the plutonium fissile fraction, the initial conversion ratio (ICR), and the reactivity coefficients as a function of the fuel life, for the last recycle. Additionally, for both fuel types, a multi-recycling analysis was performed. As for the Th-containing hydrides described in the previous section, all the results pertain to the reference PWR unit cell dimensions and were obtained from effective unit cell analysis (Table 2.19).

The uranium used is depleted to 0.3% and the plutonium vector taken from the UO_2 fuelled LWR spent fuel (also referred to here as "from the repository") is that of Table 2.7. For both fuel types (i.e. PUZH and MOX) the fuel composition is determined in the following way: the uranium amount is given as a fixed parameter, indicated in the following as a fraction of the maximum uranium loadable in the specific fuel type, as explained in the next paragraph. For each fuel type the plutonium amount is guessed and the amount of zirconium (hydride or oxides) is calculated by filling the space not taken by either the uranium or the plutonium, each in the appropriate chemical form. The cycle length is calculated for this composition, and eventually the plutonium amount is adjusted to give the desired cycle length of 1430 Effective Full Power Days (EFPD).

The PUZH fuel analyzed in this study comprises of 5 different uranium loadings, referred to as percent of the maximum loading allowable in zirconium hydrides: U 0%, 25%, 50%, 75% and 100% of the maximum: 3.72 g/cm^3 – corresponding to the reference U-$ZrH_{1.6}$ fuel. The resulting fuel compositions for the various uranium amounts in case of PUZH for the first irradiation are given in Table 2.21.

Table 2.21. Properties of PUZH Fuels with Partially-Loaded Uranium

Characteristic	Fraction of uranium				
	0%	25%	50%	75%	100%
U density (g/cm^3)	0	0.9301	1.8601	2.7902	3.7203
Pu density (g/cm^3)	0.7337	0.7564	0.7791	0.8018	0.8245
HM density (g/cm^3)	0.7338	1.6865	2.6392	3.592	4.5448
fuel density (g/cm^3)	5.9415	6.6087	7.2759	7.9432	8.6104
H/HM	82.04	34.89	21.85	15.73	12.18
Burnup (GWD/MTiHM)	628.4	284.2	182.1	132.6	102.9
EFPD	1376.0	1430.1	1434.3	1420.9	1395.8

The amount of uranium in the MOX fuel is specified in g/cm^3 to match the amount present in the PUZH fuel with variable uranium concentration; these correspond to 0%, 11%, 22%, 34% and 45% of the maximum heavy-metal (HM) loadable in Pu-U-O_2[4]. Three additional cases are investigated, corresponding to 64%, 84% and 100% of the maximum loadable uranium, since the maximum amount of uranium that can be loaded in the PUZH fuel is a fraction of the mass that can be loaded in MOX.

MOX fuel, as opposed to PUZH, present the additional issue that, after the desired amount of uranium is specified and the required plutonium amount is calculated to reach the desired cycle length of 1430 EFPD, the sum of the desired uranium and of the required plutonium may exceed the available volume. If this is the case, the uranium amount is reduced to, together with the plutonium, fill the available space. The resulting mass of ZrO_2 would then obviously be zero. This particular situation is happening only for uranium loading close to the maximum possible. Practically, in our analysis, also along the multi-recycling, it happens only for the case labeled as MOX 100% uranium. The densities of the MOX fuels for the first recycling are shown in Table 2.22.

In the following each case for either PUZH or MOX is identified based on the percentage of uranium loaded, or by the first row of, respectively, Table 2.21 and Table 2.22. During multi-recycling, as the plutonium quality degrades, the Pu amount that is necessary to re-load increases. Additionally, if the uranium becomes, as a result of transmutation, non proliferation resistant (i.e. the ^{235}U content becomes greater than 20%), it is necessary to add some depleted uranium, effectively increasing the reloaded amount of uranium. All this can result in a slight deviation from the previous percentage value. Nevertheless, for sake of consistency, the cases will still be referred to by the initial uranium fractional loading.

[4] The exact mass depends on the maximum possible density of plutonium and uranium –10.96 g/cm^3 for 100% UO_2 or to 11.5 g/cm^3 for100% PuO_2. For the purpose of labeling the percentages of uranium are related to the density of 11.15 g/cm^3 corresponding to the case with 0% zirconium oxide and with enough plutonium from 1st recycling to match a cycle length of 1430 EFPD.

Table 2.22 MOX Fuel Composition for Each of the Cases Analyzed[5]

Density	U percent of maximum							
	0%	11.2%	22.4%	33.7%	44.9%	64.2%	83.6%	100.0%
U (g/cm^3)	0	0.930	1.860	2.790	3.720	5.322	6.924	8.286
Pu (g/cm^3)	0.767	0.798	0.838	0.878	0.920	0.990	1.057	1.105
HM (g/cm^3)	0.767	1.729	2.698	3.669	4.640	6.312	7.981	9.391
HM-O_2 (g/cm^3)	0.870	1.961	3.061	4.162	5.264	7.161	9.054	10.654
U_{PUZH} (g/cm^3)	0	0.930	1.860	2.790	3.720	N/A	N/A	N/A
Zr (g/cm^3)	2.738	2.429	2.117	1.805	1.492	0.954	0.418	0
ZrO_2 (g/cm^3)	3.698	3.281	2.859	2.438	2.016	1.289	0.564	0
Fuel (g/cm^3)	4.569	5.241	5.920	6.600	7.280	8.450	9.618	10.654

The depletion properties of PUZH and MOX fuel at the first recycle are summarized in Table 2.23. The TRU destruction fraction is defined as the fraction of TRU remaining at the reactor shutdown as a fraction of the plutonium loaded before irradiation.

Table 2.23 PUZH and MOX TRU Destruction Fraction and Pu Fissile Fraction at Discharge

U % of total in PUZH	0%	25%	50%	75%	100%
PUZH TRU destruction fraction	64.36%	54.13%	47.83%	42.39%	37.48%
MOX TRU destruction fraction	63.65%	49.76%	42.65%	37.11%	32.56%
PUZH fissile fraction at EOL	21.63%	32.87%	38.52%	42.74%	46.13%
MOX fissile fraction at EOL	24.50%	38.05%	43.39%	46.99%	49.65%

Figure 2.13 through Figure 2.15 compare the results obtained for variable uranium with those obtained with variable thorium concentration, presented in the previous section. Figure 2.13 shows a comparison of the TRU destruction fraction for the variable uranium and variable thorium bearing fuels, defined as a fraction of the maximum loadable[6]. It is found that the transmutation performance of MOX fuels is slightly worse than that of hydride-based fuels (both PUZH and TPZH, or Thorium-based PUZH), for each uranium loading except 0%, for which it is similar. The performance of uranium bearing hydride fuels appears similar but slightly worse than that of thorium bearing hydride fuels. The similarity of the 0% case of PUZH and TPZH is not coincidental, since they are the same fuel type (PuH_2-$ZrH_{1.6}$). On the other hand, the strong similarity of the 0% MOX could not have been expected as it pertains to a very different system – MOX with 0% U, that is, PuO_2-ZrO_2.

The picture is slightly different when comparing, in Figure 2.14, the TRU destruction performance as a function of H/HM for the three fuel types. For the same H/HM, the TPZH fuels outperform the uranium bearing PUZH fuels. MOX-based fuels have a lower fractional transmutation than TPZH but slightly higher than PUZH for the same H/HM, except for the largest H/HM, corresponding to the 0% U case.

[5] The MOX fuel is smeared to 95.5% of the theoretical density.

[6] The percent in the abscissa indicates the fraction of the maximum loadable amount of thorium in PuH_2-ThH_2-$ZrH_{1.6}$ for the case indicated as "TPZH", and of the maximum amount of uranium in U-$ZrH_{1.6}$-PuH_2 for the case indicated as "PUZH". For the case indicated as MOX, the percentage in the abscissa refers to the maximum amount loadable in U-$ZrH_{1.6}$-PuH_2, not to the maximum loadable in MOX, which is substantially higher. The cases with heavier loadings of uranium are omitted from these graphs, which have the purpose of comparing the TRU destruction fraction for the same amount of uranium in case of MOX and PUZH.

Figure 2.15 provides, yet, another comparison – as a function of the amount of plutonium initially loaded in the fuel, It is observed that for the same fractional destruction, PUZH fuels require a substantially lower amount of plutonium than either MOX or thorium bearing PUZH fuels.

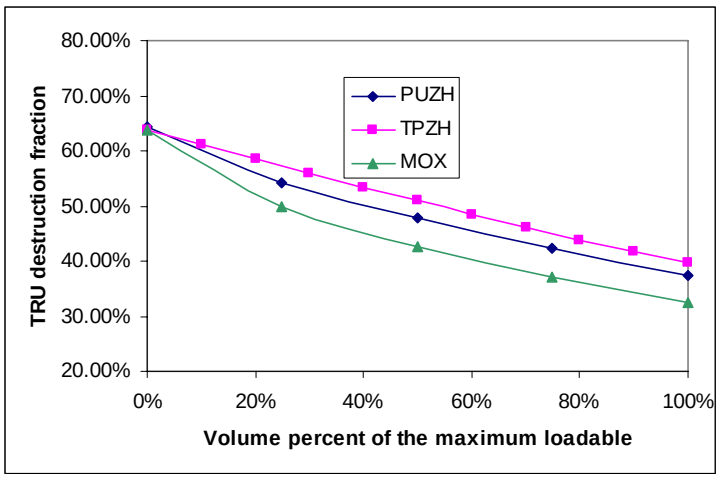

Figure 2.13 TRU fractional transmutation at discharge for variable uranium and variable thorium cases; First recycle

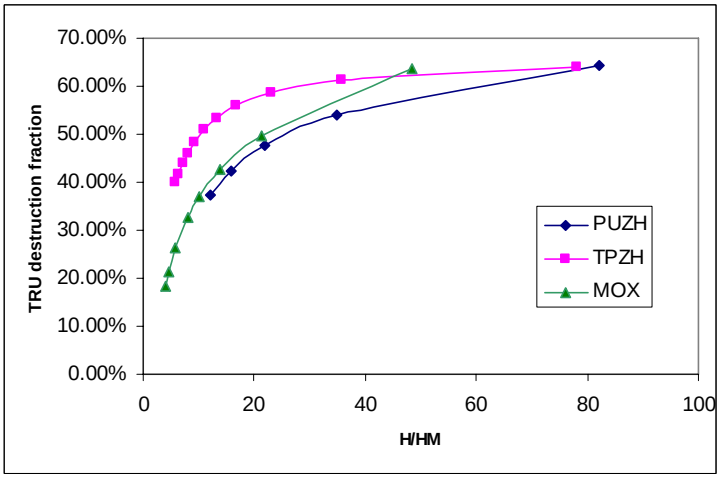

Figure 2.14 TRU fractional transmutation at discharge as a function of H/HM; First recycle

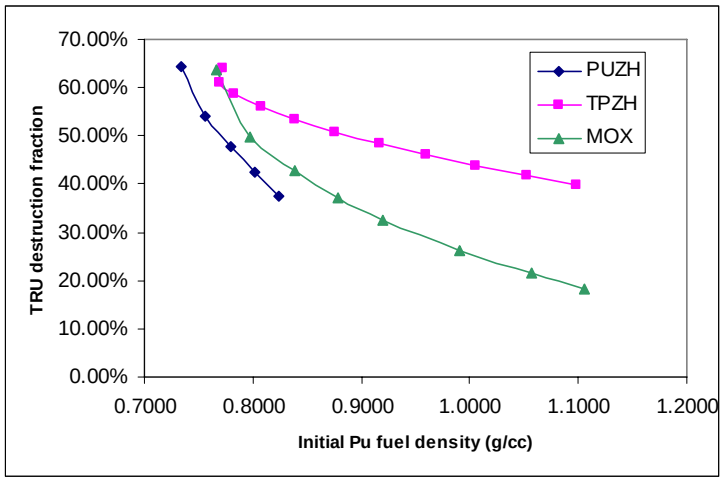

Figure 2.15. TRU fractional transmutation at discharge for the as a function of the initial plutonium loading in g/cm^3; First recycle

2.4.3 Reactivity coefficients for 1st Pu recycle in PUZH and MOX fuel with variable uranium loading

In this section the reactivity coefficients of PuH_2-$ZrH_{1.6}$(-ThH_2)-U and UO_2-PuO_2-ZrO_2 fuels with variable uranium loading are evaluated for the first recycle. The reactivity coefficients calculations start with an estimation of the required soluble boron, followed by burnup-dependent calculations of the reactivity coefficients with soluble boron.

For PUZH fuel with variable uranium loading the core average CTC with soluble boron is found positive since BOC for uranium loadings up to about 50% of the maximum possible. At EOC the core-average CTC are negative for all uranium loadings, indicating that without soluble boron all the geometries might be feasible. Similar findings apply to the SVRC. The LVRC is less restrictive – it is negative through the cycle for all the uranium loadings greater than or equal to 25%. Only the case of 0% U features positive LVRC through about the first 1/3 of the cycle. When the soluble boron concentration becomes sufficiently small, though, the LVRC becomes negative indicating that without soluble boron the LVRC is likely to be negative throughout the cycle. The core average FTC is found negative for the first recycle for a fractional uranium loading greater or equal to 25% of the maximum loadable in PUZH. However, with 0% uranium loading the FTC is found positive along the entire third batch, making the core-average FTC positive as well. Therefore this case will be practically feasible only up to a burnup level reached after the second batch. As an alternative approach, it was inferred, based on fuel hydrogen induced spectrum hardening considerations, that the substitution of D for H would eliminate the positive FTC that was found due to up-scattering by the fuel hydrogen atoms that shifts the thermal neutron peak to better overlap the 0.3 eV resonance of ^{239}Pu.

Figure 2.16 shows the burnup-dependent (left) and the core-average (right) FTC for H and D based Pu-Zr fuels. The cycle length is exactly the same in both cases (1430 EFPD). It is observed that the FTC is negative and slightly decreasing in the case of D-based fuel, and increasing in the case of H-based fuel. In this latter case the FTC starts more negative than in the D-based fuel at BOL and eventually becomes larger and substantially positive towards EOL; the core average is also positive.

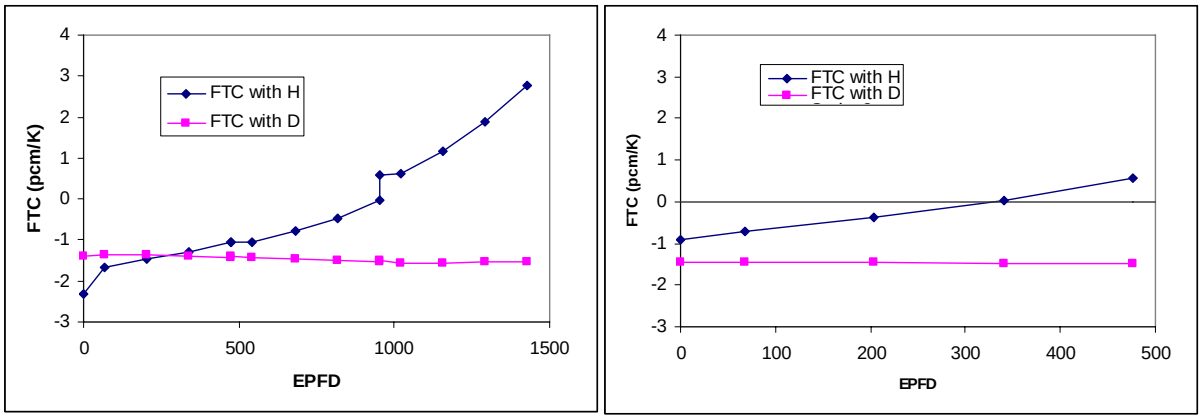

Figure 2.16 Burnup dependent FTC (pcm/K) for $ZrH_{1.6}$-PuH_2 and $ZrD_{1.6}$-PuD_2 fueled unit cells (left); core average (right)

Since the neutronic performances of the two fuels are similar (See Table 2.32), it is concluded that the use of deuterium-based fuel is a satisfactory approach for Pu first recycling in fertile-free hydride fuel. There is no need for D in the second and following recycles. An alternative design approach for the first recycle is to add approximately 25% uranium for the first recycle; there is no need of uranium for the following recycles.

The first recycle FTC of MOX fuel with variable uranium loading is negative and decreasing with time for all the cases. It becomes more negative as the uranium fraction increases from 0% to 33.7% after which it becomes insensitive to further increase in the uranium loading. The core averaged CTC and SVRC are negative throughout the first recycle for all cases except the 0% case, indicating that the first depletion cycle may have to be started with some uranium (at least 11.2% of the maximum) if soluble boron alone is used for reactivity compensation. More problematic for MOX fuels is the core average LVRC: it is positive with soluble boron at BOC for each of the cases analyzed. Cases with lower initial uranium loading have more positive BOC LVRC, but they also feature more negative values towards the end of the cycle.

Without soluble boron, all the CTC SVRC and LVRC are negative for all the uranium loadings, including the 0% case. Therefore it is concluded that, if a means of control other than soluble boron were to be used, also the case with 0% uranium can safely be used for the first recycle. Hopefully, use of burnable poisons will provide an acceptable solution.

2.4.4 Multi-recycling logic of PUZH and MOX fuel with variable uranium loading

Both the uranium and the plutonium are recycled during multi-recycles of PUZH and MOX fuels. The minimum amount of uranium to be loaded is decided beforehand. The first irradiation starts with depleted uranium (0.3%). All the uranium remaining after irradiation is re-cycled into the next cycle (minus the reprocessing losses of 0.1% [20]). If the recycled uranium is not enough to match the amount required, the balance is added using depleted uranium. If, on the other hand, the amount of downloaded uranium is larger than at the beginning of the irradiation – in other words if there was a net production of uranium, the entire amount is re-fabricated in the new fuel, after accounting for the processing losses. This latter situation happens only in the case

of 0% uranium, for both MOX and PUZH, where a small net production occurs during the multiple recycles.

As in the case of uranium, the entire amount of plutonium remaining after irradiation, minus the reprocessing losses of 0.1%, is recycled in the newly fabricated fuel. The total amount of plutonium is adjusted to meet the required cycle length of 1430 EFPD, for each of the cases and for each irradiation step, by adding fresh plutonium coming from the LWR spent fuel, the isotopic composition of which is shown in Table 2.7.

2.4.5 Uranium and plutonium mass balance along the recycling for PUZH fuel with variable uranium loading

The uranium loaded in each recycle for each of the 5 cases remains constant at the original value for all the cases except for the 0% uranium, which shows a slight increase. Additionally, the enrichment of the uranium has to remain below the limits imposed by proliferation concerns. Again, this is an issue only for the case of 0% uranium: the formation of relatively large quantities of ^{234}U in the first few re-cycles (see Figure 2.17 for the isotopic evolution of the uranium present in the fuel for the case of 0% uranium), leads to a formation of growing amounts of ^{235}U in the following re-cycles[7]. Therefore it is necessary to add a minimum amount of depleted uranium, determined re-cycle by re-cycle, to denature the mixture below the enrichment limit for proliferation purposes (20%).

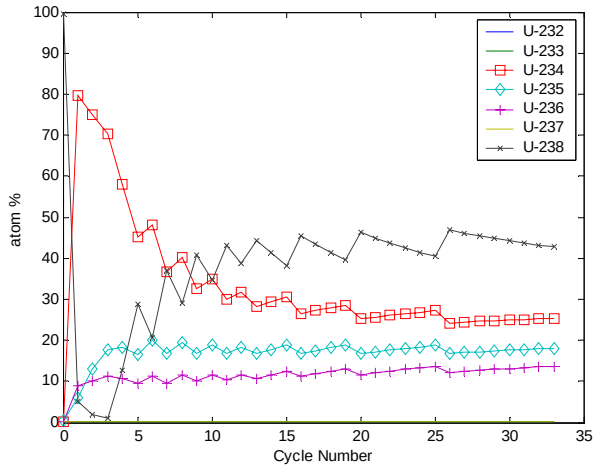

Figure 2.17 Uranium isotopic evolution, in atom percent, as a function of the recycle number for the case with 0% initial uranium loading; PUZH fuel

The total mass of plutonium loaded in the fuel, shown in Figure 2.18 (left), increases with the recycle number, reflecting degradation of its isotopic quality. Since the energy produced in each recycle is the same, the total mass of recycled plutonium (shown in Figure 2.18, right) increases

[7] The first recycle, indicated as step zero in the abscissa, has a nominal composition of the standard depleted uranium. This is somewhat arbitrary: the intention is to have 0 g/cm^3 of uranium. Nevertheless, in order for ORIGEN to properly update the isotopes, it is necessary to initialize the composition with negligible amounts of each isotope that is to be traced. The initialization values are set somewhat arbitrarily at the standard depleted uranium isotopic.

as well. It is observed that fuels with higher uranium loading require also a higher amount of plutonium loading, and discharge a higher amount of plutonium for recycling. On the other hand, the plutonium that is withdrawn from the repository, or the difference between the total loading and the recycled mass, decreases with the recycle number for each of the five cases examined. It can also be observed that the cases with lower uranium loading feature a smaller decrease in the withdrawal mass, maintaining their plutonium destruction capability more effectively with multiple recycles. This reflects the fact that the conversion ratio becomes smaller with lower uranium loading.

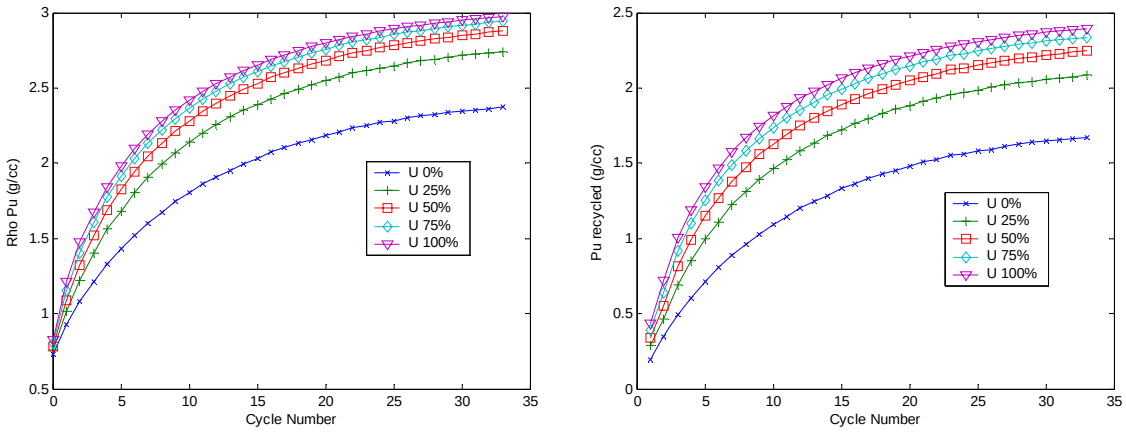

Figure 2.18 Plutonium loading (left) and recycled (right), in g/cm^3, as a function of the recycle number; PUZH fuel

2.4.6 Uranium and plutonium mass balances along the recycling for MOX fuel with variable uranium loading

In this section the MOX fuel with variable uranium loading is analyzed along the first 10 recycles. Even though an equilibrium composition is not completely reached, the recycling is stopped at the 10th recycle because the LVRC becomes positive for each of the MOX fuel types, both with and without soluble boron (see Section 2.4.12), even when accounting for the increased leakage due to large core voiding (See Section 2.4.13). Therefore, for safety concerns, no further recycling can be made. The total uranium loaded in each recycle for each of the 8 cases of MOX fuel remains constant at the original value for all the cases except for the 0% and 100% uranium, which show respectively a slight increase and a decrease. The decrease in the case of 100% uranium reflects the increase in the amount of plutonium required along the multi-recycling; since, by definition of 100% uranium, no spare volume is left, every increase in the plutonium has to be compensated by a reduced volume of uranium. Additionally, the enrichment of the uranium has to remain below the limits imposed by proliferation concerns. As in the case of PUZH, this is an issue only for the case of 0% uranium: the formation of relatively large quantities of ^{234}U in the first few recycles leads to a formation of growing amounts of ^{235}U in the following recycles. Therefore it is necessary to add a minimum amount of depleted uranium, determined recycle by recycle, to denature the mixture below the enrichment limit for proliferation purposes (20% ^{235}U).

The total mass of plutonium loaded in the fuel, shown in Figure 2.19 (left), increases with the recycle number, reflecting its degradation in isotopic quality. Since the energy produced in each recycle is the same, the total mass of recycled plutonium (shown in Figure 2.19, right) increases as well. It is observed that fuels with larger uranium loading require also a larger amount of plutonium loading and discharge a larger amount of plutonium for recycling. The plutonium that is withdrawn from the repository, or the difference between the total loading and the recycled mass, decreases with the recycle numbers for each of the five cases. It is also observed that the cases with lower uranium loading feature a smaller decrease in the withdrawal mass, maintaining their destruction properties more effectively than cases with larger uranium loadings with multiple recycles.

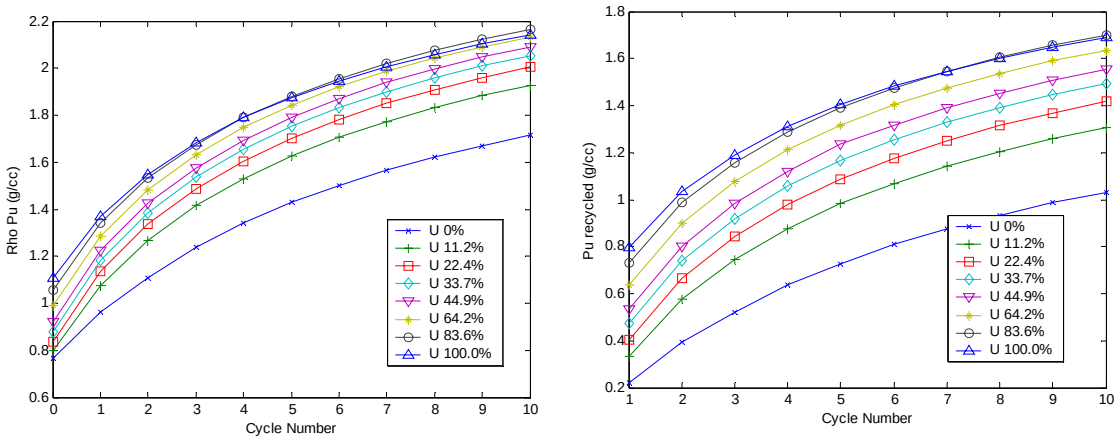

Figure 2.19 Plutonium loaded (left) and recycled (right), in g/cm^3, as a function of the recycle number; MOX fuel

2.4.7 TRU destruction fraction and plutonium fissile fraction at discharge for PUZH and MOX fuels with variable uranium loading

Figure 2.20 shows the TRU destruction fraction for PUZH and MOX fuels – both with variable uranium – as a function of the recycle number. The TRU destruction fraction is defined here to be one minus the ratio of the number of TRU atoms discharged to the number of plutonium atoms loaded. It is observed that, as expected, the TRU destruction fraction decreases with the uranium loadings because of an increase in the conversion ratio. A similar trend is observed for MOX and PUZH fuels.

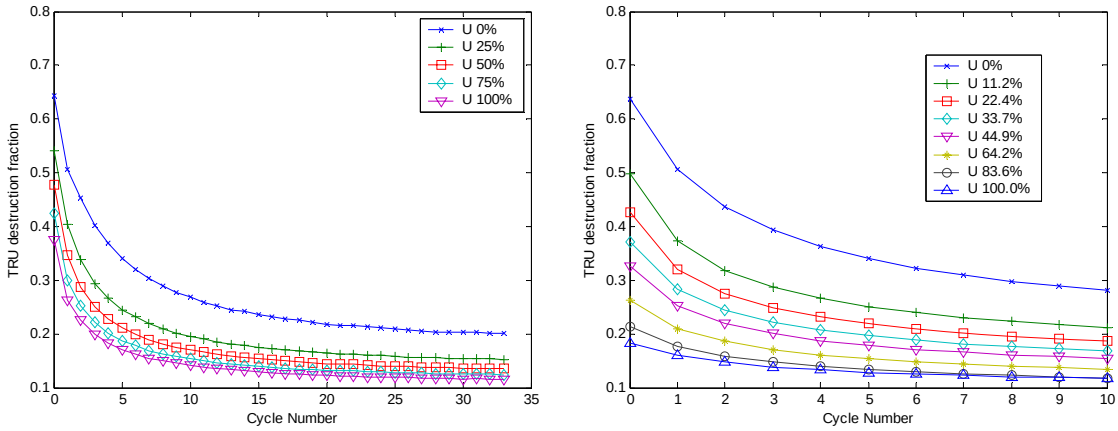

Figure 2.20 TRU destruction fraction as a function of the recycle number; PUZH fuel (left) and MOX fuel (right)

The TRU destruction fraction for low uranium content fuels compares favorably with critical fast reactor systems envisioned in [9] for multi-recycling of TRU - 18.6% TRU destruction fraction for fast critical systems and 29.2% for ATW, both at equilibrium. This is not quite a fair comparison as only Pu is recycled in the above considered PWR cores.

Figure 2.21 shows the plutonium fissile fraction at discharge for PUZH and MOX fuels as a function of the recycles. A different behavior is observed for different uranium loading -- decreasing for heavier uranium loading and increasing (or remaining flat in case of MOX) for the case with 0% initial uranium loading. Intermediate uranium loadings have mixed behavior in PUZH: for example the case of 25% uranium loading increases for the first three recycles and decreases thereafter.

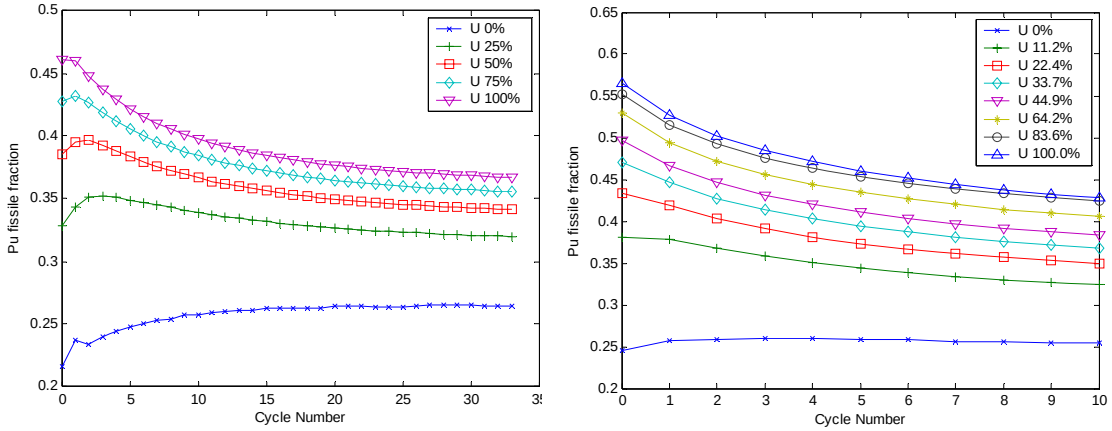

Figure 2.21 Plutonium fissile fraction at discharge as a function of the recycle number; PUZH fuel (left) and MOX fuel (right)

This peaking is a reflection of a similarly-peaking behavior in the concentration of ^{241}Pu at discharge, shown for PUZH in Figure 2.22. The inventories of the recharged ^{240}Pu and ^{241}Pu at each recycle in PUZH are shown in Figure 2.23.

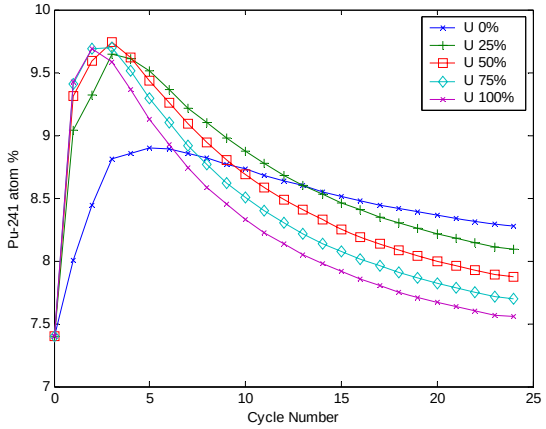

Figure 2.22 ^{241}Pu concentration at discharge as a function of the recycle number; PUZH fuel

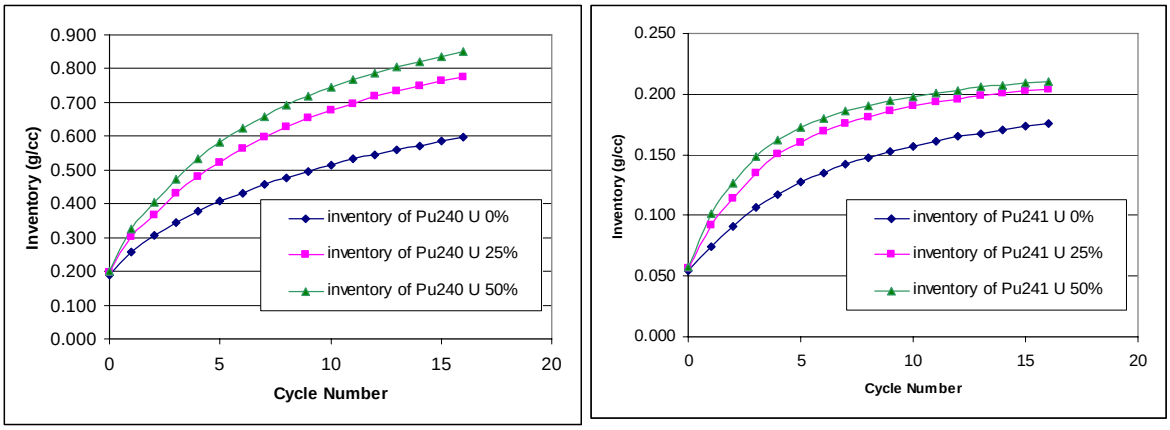

Figure 2.23 Inventory of ^{240}Pu (left) and ^{241}Pu (right) in the re-charged plutonium at each recycle; PUZH fuel

2.4.8 Initial conversion ratio of PUZH and MOX fuels with variable uranium loading

The Initial Conversion Ratio (ICR), calculated as:

$$ICR = \frac{\Phi\Sigma_{n,\gamma}^{U-238} + \Phi\Sigma_{n,\gamma}^{U-234} + \Phi\Sigma_{n,\gamma}^{Pu-238} + \Phi\Sigma_{n,\gamma}^{Pu-240} + \Phi\Sigma_{n,\gamma}^{Pu-242}}{\Phi\Sigma_{n,a}^{Pu-239} + \Phi\Sigma_{n,a}^{Pu-241} + \Phi\Sigma_{n,a}^{U-235} + \Phi\Sigma_{n,a}^{U-233} + \Phi\Sigma_{n,a}^{Pu-243} + \lambda^{Pu-243}N^{Pu-243} + \lambda^{Pu-241}N^{Pu-241}}$$

is plotted in Figure 2.24 for PUZH and MOX fuels as a function of recycles. ^{234}U, normally not accounted for in the calculation of ICR, is included here because of its relatively large importance in the case of 0% uranium loading (see Figure 2.17). For both PUZH and MOX the ICR increases with the recycles and is higher the higher is the uranium loading.

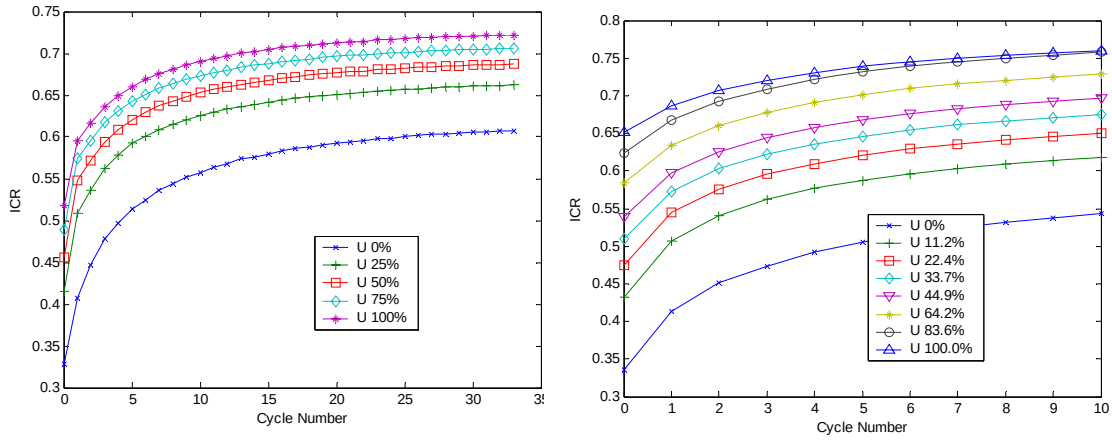

Figure 2.24 ICR as a function of recycle number, for different uranium loading; PUZH fuel (left) and MOX fuel (right)

2.4.9 One-group cross sections of fertile-free PUZH fuel at equilibrium (33rd recycle)

The BOL effective one-group cross sections and related neutronic characteristics of PUZH fuel at the beginning and end of the equilibrium recycle are summarized in, respectively, Table 2.24 and Table 2.25.The nuclei present in the system are ranked by the fractional absorption per fission neutron. The dominant role is played by the plutonium isotopes. The uranium isotopes have only a minor role because of their low concentration in this fuel. The average η value for this fuel is 1.21453 at BOC and 1.11067 at EOC.

Table 2.24 Total, Absorption, Fission Cross Sections, ν and η of PUZH at Beginning of Equilibrium Cycle

	Fraction of neutron absorbed per fission neutron(%)	Total XS (b)	Absorption XS (b)	Fission XS (b)	ν	η
^{239}Pu	42.12%	41.704	33.015	20.960	2.895	1.838
^{240}Pu	27.94%	31.178	19.896	0.700	3.135	0.110
^{241}Pu	15.03%	47.531	38.392	28.673	2.959	2.210
^{242}Pu	8.78%	16.630	5.687	0.555	3.182	0.310
^{238}Pu	1.74%	20.906	9.347	1.899	3.065	0.623
^{234}U	0.76%	28.025	16.409	0.633	2.655	0.102
H in H_2O	0.75%	11.983	0.010	0	N/A	0
Zr in $ZrH_{1.6}$	0.72%	6.917	0.032	0	N/A	0
^{235}U	0.56%	25.635	16.934	12.261	2.448	1.772
^{238}U	0.55%	21.378	6.973	0.139	2.826	0.056
Zr in Clad	0.34%	6.999	0.035	0	N/A	0
H in $ZrH_{1.6}$	0.27%	11.051	0.006	0	N/A	0
^{236}U	0.23%	22.208	9.183	0.386	2.588	0.109
^{16}O in H_2O	0.20%	3.432	0.005	0	N/A	0

Table 2.25 Total, Absorption, Fission Cross Sections, ν and η of PUZH at End of Equilibrium Cycle

	Fraction of neutron absorbed per fission neutron(%)	Total XS (b)	Absorption XS (b)	Fission XS (b)	ν	η
^{240}Pu	25.79%	34.590	23.062	0.689	3.134	0.094
^{239}Pu	24.73%	54.394	45.613	28.761	2.892	1.823
^{241}Pu	23.38%	56.160	46.981	34.844	2.958	2.194
^{242}Pu	9.10%	16.873	5.846	0.544	3.182	0.296
^{243}Am	4.40%	39.171	29.676	0.555	3.771	0.070
^{241}Am	2.37%	49.481	40.246	0.877	3.413	0.074
^{238}Pu	1.84%	22.803	11.093	1.939	3.058	0.534
H in H_2O	0.90%	12.227	0.011			
Zr in $ZrH_{1.6}$	0.79%	6.928	0.033			
^{103}Rh	0.74%	19.899	13.002			
^{244}Cm	0.74%	26.128	13.468	1.035	3.787	0.291
^{135}Xe	0.70%	43916.1	36718.7			
^{235}U	0.69%	28.246	19.504	14.423	2.446	1.809
^{131}Xe	0.61%	68.256	23.241			
^{149}Sm	0.61%	1247.8	1216.9			
^{234}U	0.58%	27.092	15.548	0.623	2.653	0.106
^{133}Cs	0.57%	17.380	9.295			
^{109}Ag	0.49%	41.666	32.162			
^{238}U	0.49%	21.551	7.001	0.135	2.828	0.055
^{152}Sm	0.47%	202.257	68.263			

2.4.10 Shutdown margin at equilibrium (33rd recycle) for fertile-free PUZH fuel

The control rods shutdown margin is evaluated for the equilibrium PUZH core (33rd recycle). The evaluation is done at BOL – when the reactivity of the fuel is maximal, both with and without soluble boron and with all the core constituents at cold (300 K) shutdown condition; the water density is correspondingly 1 g/cm^3. Conservatively, the concentrations of both Xe and Sm are set to zero; no credits are assumed for partially burned fuel batches. The calculations are done for a 2-D quarter assembly model using TRITON and 238 energy groups. Two types of control rods are investigated: B_4C and standard Ag-In-Cd (AIC).

The results are summarized in Table 2.26 where they are compared to those obtained for the reference UO_2 fueled core. It is found that the AIC control rods are not capable of keeping the cold shut-down PUZH fuelled core below the desired value of 0.95. However, with B_4C control rods k_∞ becomes 0.97038 and the corresponding k_{eff} is expected to be smaller than 0.95 even without any soluble boron in the coolant. The shutdown margin of a PUZH core that uses B_4C control rods (0.97038) is comparable to that of the reference UO_2 core that uses the reference AIC control rods (0.97419). If a larger shutdown margin is needed, the B_4C could be enriched with ^{10}B.

Table 2.26 BOL Control Rod Shutdown Margin With and Without Critical Soluble Boron; Equilibrium Recycle

	PUZH fuel		UO_2 fuel (reference)	
	k_∞ with soluble boron	k_∞ without soluble boron	k_∞ with soluble boron	k_∞ without soluble boron
no CR	1.09981	1.22860	1.12866	1.35481
AIC	0.97097	1.05076	0.85074	0.97419
B4C	0.89777	0.97038	0.75451	0.85589

2.4.11 Reactivity coefficients at equilibrium (33rd recycle) for PUZH fuel with variable uranium loading

At the 33rd recycle for PUZH fuel, the FTC are negative and flat for all the cases, more negative for higher uranium–containing systems. The CTC and SVRC, on the other hand, are positive at the beginning of each batch, making the core-averaged values positive as well. However, when the CTC and SVRC are evaluated without soluble boron, they remain negative throughout the entire cycle. All the systems feature a similar behavior, with a slight deviation only in case of 0% uranium.

A very different behavior is observed for LVRC. It is known [3] that the LVRC becomes positive in MOX systems for Pu loading higher than about 12 $^{w}/_{o}$ (corresponding to about 1.2 g/cm^3 of plutonium). This is also shown in Section 2.4.12 (Figure 2.27). This limits the number of feasible multi-recycles in MOX. In case of PUZH fuel, towards equilibrium, the lowest amount of plutonium is in 0% uranium and is about 2.4 g/cm^3. Nevertheless, it is observed in Figure 2.25 that its LVRC has negative values at the end of each of the batches and of the core-average as well. This suggests that the case with 0% uranium and little or no soluble boron will feature negative LVRC throughout the fuel life, making this fuel feasible.

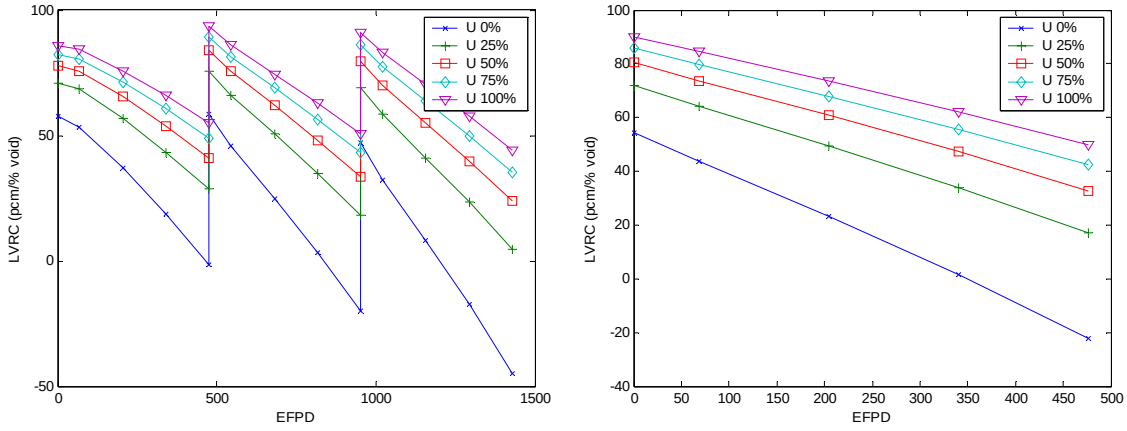

Figure 2.25 LVRC with soluble boron, as a function of burnup (left), core average value along the equilibrium recycle (right); PUZH fuel

Without soluble boron, the CTC and SVRC are both negative, as expected, and decreasing with burnup. The core average LVRC (in Figure 2.26) is positive for all the heavier uranium loading (25% to 100%), but is negative throughout the cycle for the case with 0% uranium. Therefore, if a method was devised to reduce enough the soluble boron necessary for controlling the excess

reactivity, such as the use of burnable poisons [2,25], the case with 0% uranium could be successfully and safely used to infinitely recycle plutonium in PWR.

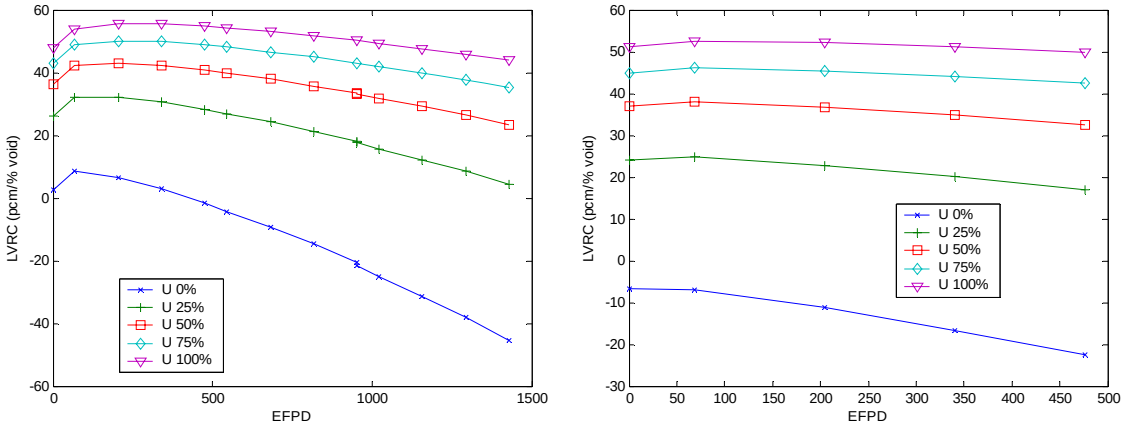

Figure 2.26 LVRC without soluble boron, as a function of burnup (left) and core average value along the equilibrium cycle (right); PUZH fuel

2.4.12 Reactivity coefficients at the 13th step for MOX fuel with variable uranium loading

Even though equilibrium cannot be reached in Pu multi-recycling in MOX, in this section the reactivity coefficients for MOX fuel with variable uranium loading at the 10th recycle to prove that this is, indeed, the maximum feasible recycle of MOX fuel.

The FTC are found negative and decreasing with burnup for all the cases. A slight uranium increase from the 0% to the 33.7% case causes a decrease in the value of the FTC along the cycle; a further increase in the uranium loading has significantly smaller effect on the core-average FTC.

The CTC and SVRC are positive at BOC but negative at EOC for all the cases, implying that without soluble boron they will both be negative throughout the cycle, which in fact has been verified.

On the other hand, the burnup-dependent and cycle-average LVRC, shown in Figure 2.27, are positive for all the cases examined at both BOC and EOC even when the soluble boron concentration is zero. It is concluded that recycle 10 with MOX fuel is not feasible based on spectral effect alone. It is shown in Section 2.4.13 that the 10th recycle in MOX is the last feasible recycle when accounting for the negative reactivity effect of the core leakage.

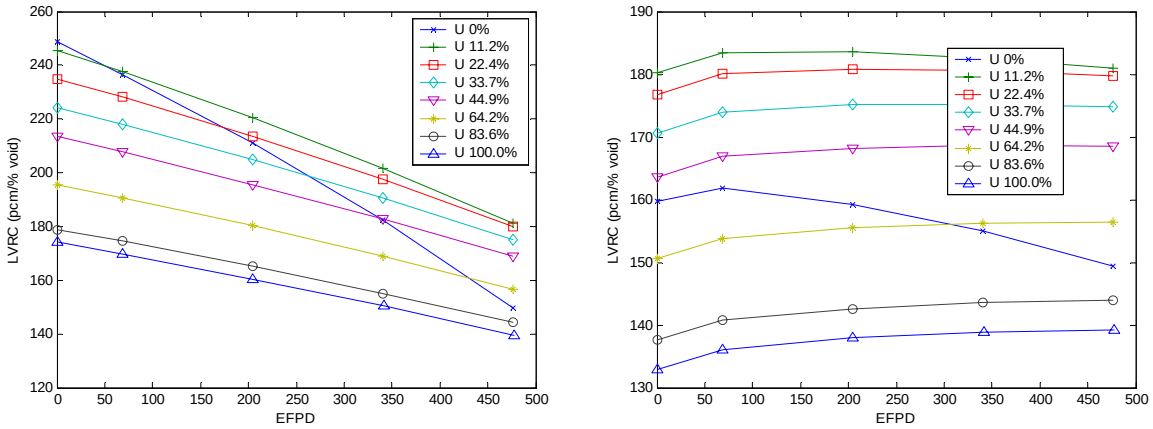

Figure 2.27 Core-average LVRC (pcm/%void) with soluble boron (left) and without soluble boron (right) at 13th recycle; MOX fuel

2.4.13 Reactivity of PuO_2-ZrO_2 fuel accounting for the leakage effect of core voiding

All the void reactivity effects reported above did not account for the voiding effect on the core leakage probability. Figure 2.28 shows the burnup-dependent, core-average void reactivity effect for an infinite lattice of unit cells fuelled with PuO_2-ZrO_2 (calculated using TRITON/NEWT) compared to the leakage effect (negative) of core voiding (also in pcm) as calculated with MCNP. It is observed that (1) the void reactivity becomes more negative with burnup, reflecting the lower inventory of plutonium; (2) the LVRC increases after about 60% void for all the burnups, and becomes positive at every burnup after around 90% void; this is due to spectrum hardening effects; (3) the negative leakage effect of voiding is substantially larger than the positive spectral effect, resulting in substantially negative reactivity coefficients.

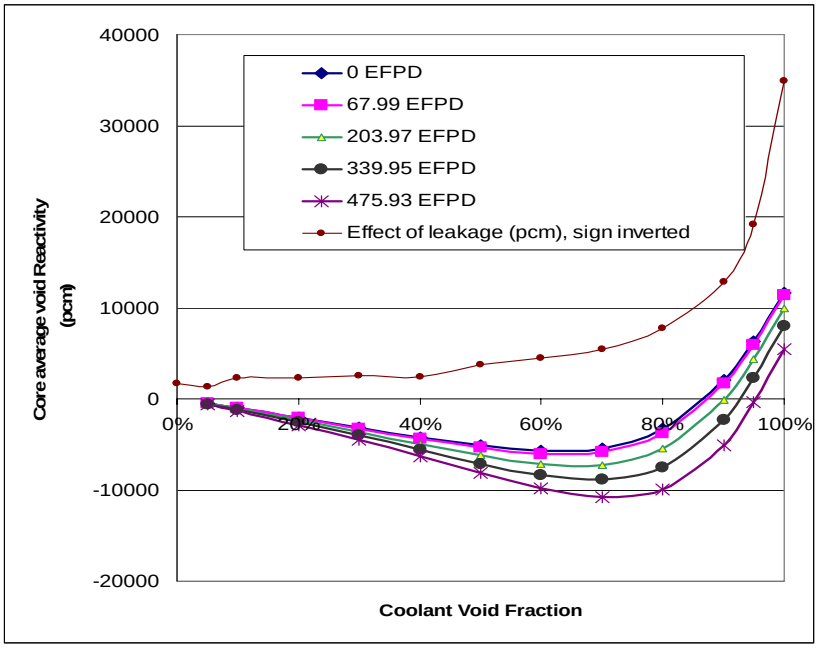

Figure 2.28 Core average void reactivity effect (LVRC) expressed in pcm, and compared to the leakage effect of core voiding (displayed as positive) as calculated by MCNP

Figure 2.29 shows the evolution of the BOL large void reactivity coefficients, for both 90% and 100% voiding, as a function of the recycle number for PuO_2-ZrO_2 fuel. The discrete points represent spectral effects as calculated by NEWT; they are all positive. The straight lines are the leakage effect of voiding the core as calculated with MCNP; they are all negative. It is found that for 100% void the spectral effects are overcompensated by the large leakage effect; it is larger than -30000 pcm while the spectral effect gets to slightly above +20000 pcm. On the other hand, at 90% voiding the spectral effect exceeds the leakage effect after about the 10th recycle. It is concluded that the maximum number of plutonium recycling in MOX is certainly less or equal to 10.

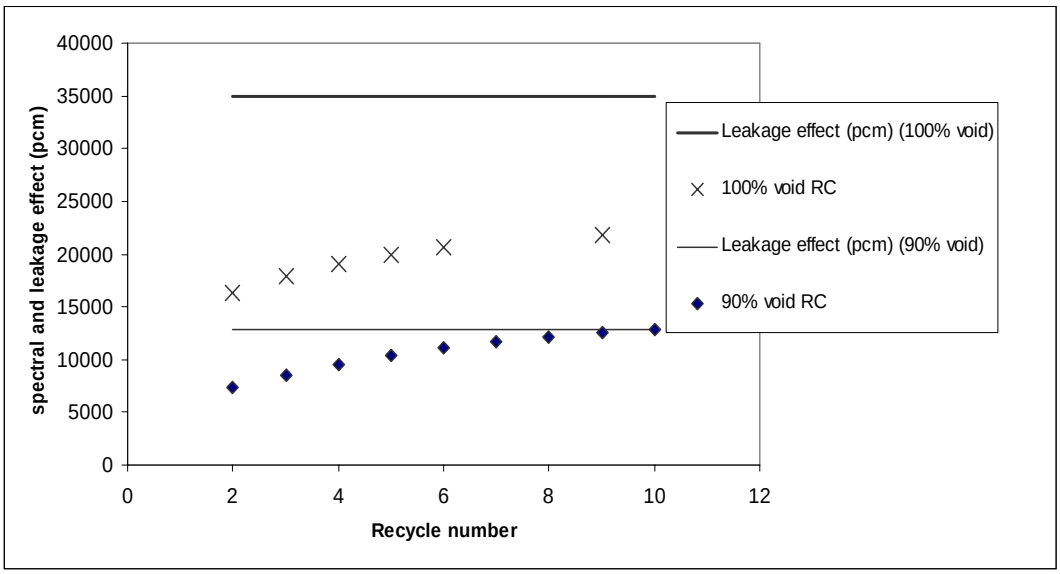

Figure 2.29 BOL LVRC for 90% and 100% void as a function of recycle. Discrete points are spectral effect (positive) while straight lines are leakage effect (negative)

2.4.14 Summary table for fertile-free PUZH fuel along the multi-recycling

Table 2.27 gives a summary, recycle by recycle, of selected characteristics of the fertile-free PUZH cores (i.e. PuH_2-$ZrH_{1.6}$) obtained from the plutonium multi-recycling calculations described in this chapter. It is observed that the amount of plutonium consumed per cycle (9th column) increases with the recycles although the fractional plutonium consumption per recycle decreases. Because of the increased plutonium loading with recycling, the specific power and discharge burnup keep decreasing. However, the TRU consumed per recycle or per unit of energy generated is practically constant at about 0.364 kg of TRU/MWt-yr.

Table 2.27 Summary Table for PUZH with Pu Recycling

Cycle #	Specific power (W/gHM)	Burnup (GWD/MT)	TRU destruction fraction	Fissile fraction	Pu loaded (g/cc)	U loaded (g/cc)	Pu recycled (g/cc)	Pu consumed (g/cc)	kgPu/MWt-yr	kgTRU/MWt-yr
0	456.7	628.4	64.36%	21.63%	0.734	0.000		0.539	0.410	0.359
1	359.1	508.2	50.69%	23.75%	0.931	0.001	0.195	0.585	0.446	0.375
2	308.1	442.1	45.39%	23.36%	1.083	0.004	0.346	0.590	0.450	0.371
3	275.3	391.4	40.23%	23.95%	1.209	0.006	0.492	0.605	0.462	0.373
4	250.3	357.9	36.83%	24.39%	1.327	0.010	0.604	0.613	0.468	0.372
5	231.3	330.6	34.08%	24.81%	1.430	0.016	0.714	0.626	0.477	0.372
6	217.5	311.0	32.07%	25.02%	1.520	0.018	0.805	0.634	0.484	0.370
7	205.3	293.2	30.28%	25.34%	1.602	0.027	0.886	0.640	0.489	0.371
8	196.5	281.0	29.01%	25.44%	1.675	0.028	0.962	0.647	0.493	0.369
9	187.8	268.5	27.75%	25.71%	1.745	0.038	1.028	0.651	0.497	0.369
10	181.8	259.9	26.85%	25.75%	1.803	0.038	1.093	0.657	0.501	0.368
11	175.3	250.7	25.94%	25.96%	1.861	0.047	1.147	0.660	0.503	0.368
12	171.0	244.5	25.28%	25.98%	1.910	0.047	1.202	0.664	0.506	0.364
13	166.7	236.5	24.47%	26.10%	1.951	0.056	1.246	0.666	0.508	0.367
14	163.1	233.2	24.12%	26.12%	1.996	0.056	1.285	0.665	0.507	0.367
15	160.1	228.5	23.63%	26.25%	2.034	0.056	1.331	0.672	0.513	0.366
16	156.4	223.6	23.15%	26.29%	2.073	0.066	1.362	0.672	0.513	0.366
17	154.2	220.4	22.80%	26.29%	2.104	0.066	1.400	0.676	0.515	0.366
18	152.2	217.6	22.51%	26.28%	2.132	0.066	1.428	0.678	0.517	0.366
19	150.5	215.1	22.25%	26.26%	2.158	0.066	1.455	0.680	0.519	0.365
20	147.8	211.3	21.87%	26.42%	2.187	0.077	1.478	0.680	0.519	0.365
21	146.4	209.3	21.66%	26.41%	2.209	0.077	1.507	0.682	0.520	0.367
22	144.8	208.2	21.54%	26.42%	2.234	0.077	1.528	0.683	0.521	0.365
23	143.9	205.7	21.28%	26.39%	2.249	0.077	1.551	0.688	0.525	0.368
24	142.5	205.5	21.26%	26.40%	2.272	0.077	1.561	0.686	0.523	0.365
25	141.9	202.9	20.98%	26.37%	2.282	0.077	1.585	0.692	0.528	0.364
26	140.2	200.4	20.74%	26.49%	2.300	0.088	1.590	0.686	0.524	0.362
27	139.3	198.4	20.54%	26.54%	2.314	0.088	1.613	0.687	0.524	0.362
28	138.6	197.5	20.43%	26.52%	2.326	0.088	1.626	0.687	0.524	0.364
29	138.0	197.3	20.41%	26.52%	2.338	0.088	1.639	0.687	0.524	0.364
30	137.4	196.6	20.33%	26.50%	2.348	0.088	1.651	0.690	0.526	0.364
31	136.9	195.8	20.25%	26.48%	2.356	0.088	1.658	0.691	0.527	0.364
32	136.5	195.1	20.18%	26.46%	2.364	0.088	1.665	0.691	0.527	0.364
33	136.1	194.6	20.12%	26.45%	2.372	0.088	1.673			

2.5 Pu+Np and "all TRu" Multi-Recycling in PWR Using Hydride Fuels

2.5.1 Pu and Np multi-recycling in hydride fuel with variable uranium loading: mass balances of U, Pu and Np

Due to proliferation concerns the AFCI program is considering co-recycling of neptunium with plutonium. This will greatly increase the ^{238}Pu concentration and make the Pu more proliferation resistant. The feasibility of multi-recycling Pu together with Np is investigated in this section. The fuel cycle scheme examined is shown in Figure 2.30. The Pu+Np composition fed to the system as makeup fuel is assumed that given in [20] – Table 1 col. b, based on "extended PWR benchmark with 10y cooling". In absence of more accurate information, it is assumed that Np forms a hydride of the type NpH_2; that it is stable at reactor operating conditions; and that it has the same density as PuH_2 (10.4 g/cm^3).

The amount of make-up Pu+Np that is loaded at each recycle is adjusted so as to achieve the desired cycle length (i.e. 1430 EFPD). As for the "Pu only systems", several cases were studied with a varying amount of uranium, from zero to the maximum loadable (i.e. 3.72 g/cm^3). The remaining fuel volume is taken by $ZrH_{1.6}$. The detailed fuel composition at first recycling is given in Table 2.28. It is observed that the required plutonium amount increases with the uranium amount, going from 0.7986 g/cm^3 for 0 g/cm^3 of U to 1.108 g/cm^3 for 3.72 g/cm^3 of U. Correspondingly, the neptunium amount increases from 0.061 g/cm^3 to 0.085 g/cm^3. The hydrogen density decreases with the increasing uranium amount.

The re-cycling has been done 13 times (corresponding to 14.3*13=186 years): even though equilibrium has not been reached, the recycling was stopped because the large void reactivity coefficient (also accounting for the leakage effect) becomes positive.

Table 2.28 Fuel Composition at First Recycle for the 6 Cases Analyzed with Varying Uranium Loading

Case #	1	2	3	4	5	6
Fuel density (g/cc)	6.0004	6.3421	6.6868	7.3804	8.0799	8.7821
U density (g/cc)	0	0.465	0.93	1.86	2.79	3.72
Pu density (g/cc)	0.7986	0.8255	0.8583	0.9320	1.0175	1.1084
Np density (g/cc)	0.0614	0.0635	0.0660	0.0717	0.0783	0.0853
Zr density (g/cc)	5.0438	4.8940	4.7409	4.4298	4.1121	3.7912
H density (g/cc)	0.0964	0.0940	0.0916	0.0868	0.0819	0.0771

The total amount of reloaded Pu is comprised of the amount of plutonium recycled and of the makeup plutonium (plutonium from LWR spent fuel), both given in Figure 2.31. Figure 2.32 gives similar information on the neptunium inventory. It is observed that cases with low uranium content require less plutonium and neptunium makeup for the first few recycles but larger amount of makeup after the 3rd to 4th recycle. This is due to the low conversion ratio of the low U-content cores.

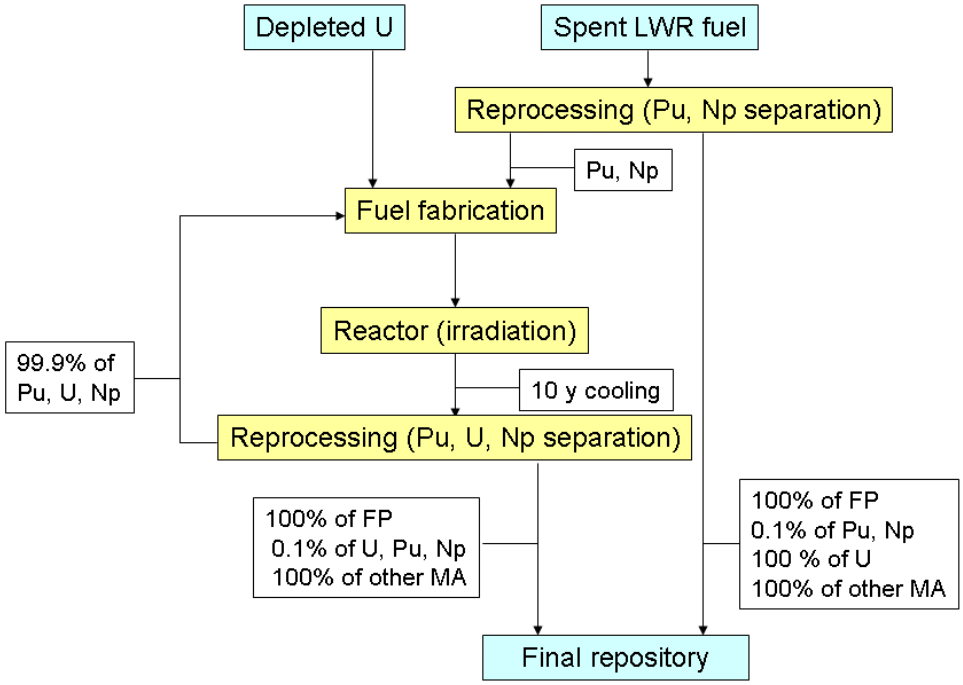

Figure 2.30 Fuel cycle scheme with plutonium and neptunium recycle

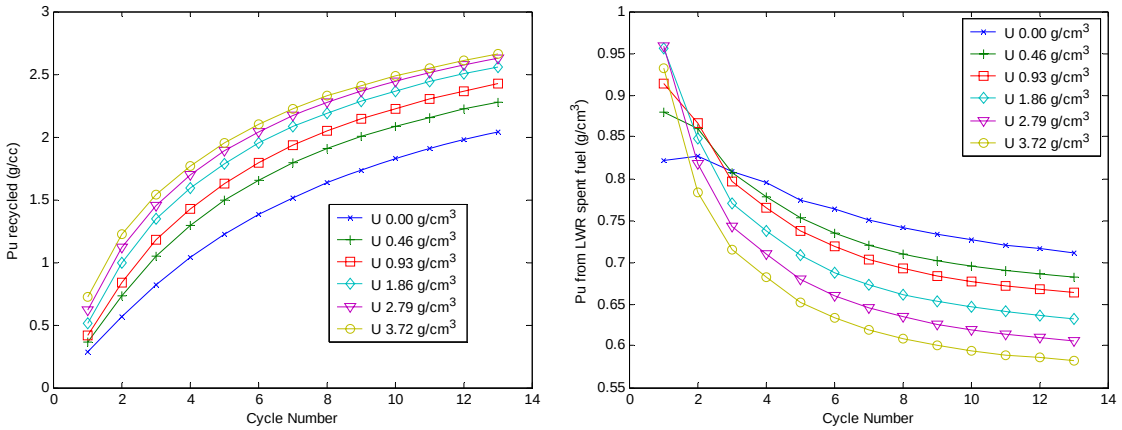

Figure 2.31 Required plutonium recycled density (g/cm^3) (left) and makeup plutonium density (g/cm^3) (right) as a function of the re-cycle number for NpH_2-U-PuH_2-$ZrH_{1.6}$

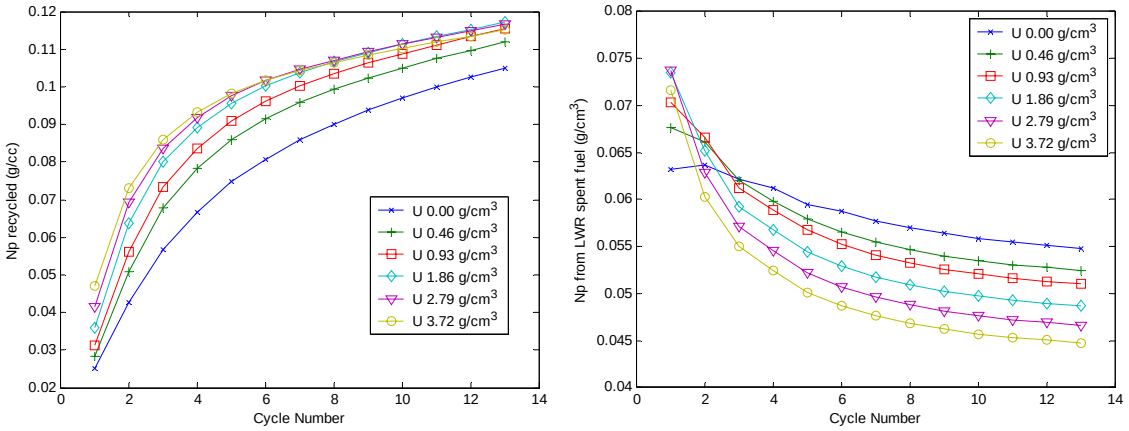

Figure 2.32 Required neptunium recycled density (g/cm^3) (left) and makeup plutonium density (g/cm^3) (right) as a function of the re-cycle number for NpH_2-U-PuH_2-$ZrH_{1.6}$

2.5.2 TRU destruction fraction of Pu+Np recycling in hydride fuel

The achievable burnup, the corresponding fuel residence time in the core, the TRU fractional destruction and the plutonium fissile fraction at discharge are given in Table 2.29 for the first recycle for NpH_2-U-PuH_2-$ZrH_{1.6}$ fuel. It is observed that the achievable burnup is the highest in the case without uranium – 556 GWD/MT. The corresponding TRU destruction fraction is 57%. In the second recycle these values drop to, respectively, 395.5 GWD/MT and 31.3%. These values are somewhat smaller than those obtained when recycling only plutonium (Section 2.4.2).

Table 2.29 Properties of NpH_2 U PuH_2 $ZrH_{1.6}$ Fuel at First Recycling

Case #	1	2	3	4	5	6
Burnup (GWD/MTiHM)	556.0	353.2	258.0	167.0	123.0	97.3
Fuel residence time (EFPD)	1430.7	1430.7	1431.1	1430.5	1430.3	1430.3
TRU destruction fraction	56.91%	49.03%	44.35%	37.31%	31.77%	27.32%
Pu fissile fraction at discharge	27.42%	34.91%	38.87%	44.23%	47.97%	50.69%

Figure 2.33 shows the evolution with recycling of the TRU destruction fraction and of the fissile Pu fraction at discharge. The latter is decreasing with the recycles for heavier uranium loaded cores but initially increases for low uranium loaded cores. Both effects are due to the increasing amount of makeup Pu that needs to be loaded as the recycling proceeds.

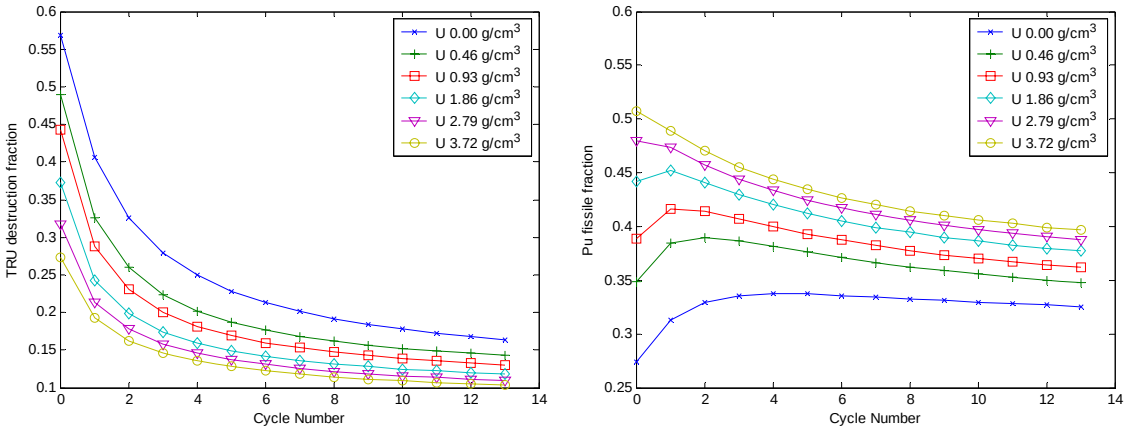

Figure 2.33 TRU destruction fraction (left) and Pu fissile fraction (right) as a function of the re-cycle number for NpH_2-U-PuH_2-$ZrH_{1.6}$ fuel

2.5.3 Reactivity coefficients of Pu+Np recycling in hydride fuel

For NpH_2-U-PuH_2-$ZrH_{1.6}$ at the 1st recycle, the core averaged FTC increases throughout the cycle for all uranium loadings, and is higher (i.e. less negative) for smaller uranium loading. The case with no initial uranium loading has a positive FTC after about 400 EFPD, corresponding to a fuel life of 1200 EFPD, or about 84% of the theoretically achievable life (1430 EFPD). However, the addition of about 0.25 g/cm^3 of U would be sufficient to reduce the FTC to negative values throughout the first cycle. Alternatively, the use of deuterium would have a similar effect as in the case of Pu only (see Section 2.4.3). All the other reactivity coefficients (i.e. CTC, SVRC and LVRC for either 90% voiding or 100% voiding (not corrected for leakage effect of voiding)) are negative and are decreasing throughout the cycle, for each of the uranium loadings.

The core averaged FTC and LVRC (90% and 100% void) for NpH_2-U-PuH_2-$ZrH_{1.6}$ at the 13th recycle have a quite different behavior than at the 1st recycle; the FTC is mostly flat throughout the cycle and substantially negative for each of the uranium loadings, including the case with no uranium. The case with no initial uranium features the smallest spectral effect for both 90% and 100% void; their value is +4050 pcm for 90% void and +7200 pcm for 100% void. Both values are larger than the negative effect of leakage. It is concluded that the 13th recycle is non feasible because of positive LVRC. All the other core-averaged reactivity coefficients are negative for each of the uranium loadings.

Consequently, a 3-D MCNP calculations were performed to estimate the neutron leakage probability from the PuH_2-NpH_2-$ZrH_{1.6}$ fuelled cores at recyclings <13. Figure 2.34 shows the evolution of the maximum core-average burnup-dependent large void spectral effect of the reactivity coefficient (positive) as a function of the recycle numbers as well as the leakage effect of voiding (negative) as calculated by MNCP.

It is found that the number of maximum recycling is limited to 6. It is imposed by the 100% voiding that is more constraining for this fuel than the 90% voiding.

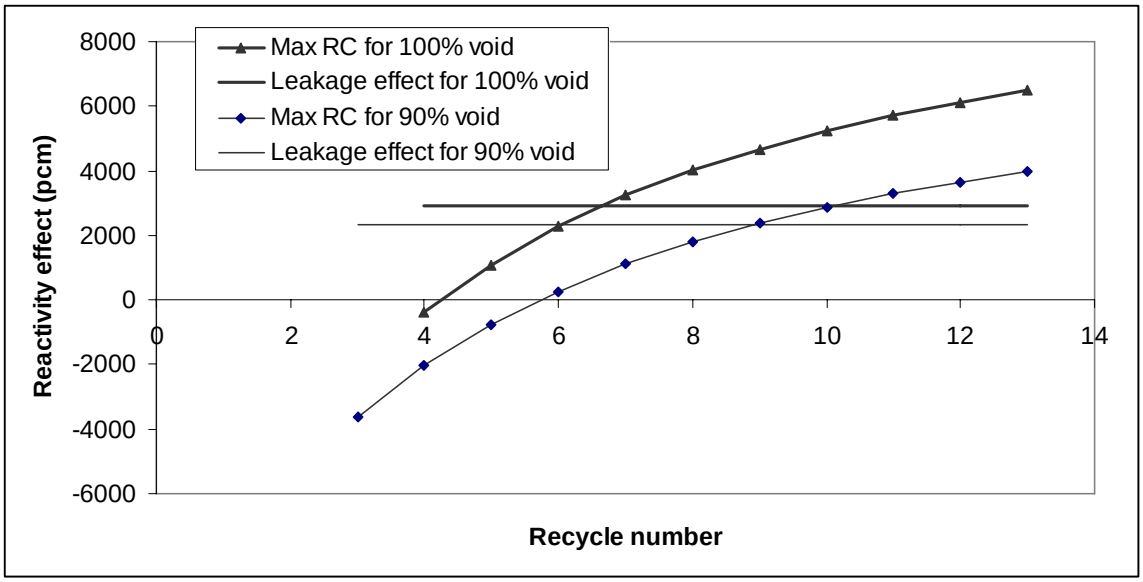

Figure 2.34 Evolution of the maximum core-average, burnup-dependent spectral component of the reactivity coefficient (positive) as a function of recycle at BOL, compared to the leakage effect (negative) of voiding as calculated by MCNP; NpH_2-PuH_2-$ZrH_{1.6}$ fuel

2.5.4 Ways to increase the number of acceptable recycles for NpH_2-PuH_2-$ZrH_{1.6}$ fuel

A number of approaches where investigated for making negative the large voiding reactivity coefficients beyond the 6th recycle for NpH_2-PuH_2-$ZrH_{1.6}$ fuel:

1. Add slightly enriched uranium;
2. Add burnup poisons (erbium);
3. Enlarge the fuel rod radius while keeping the same pitch.

Of these, only the latter was found effective in substantially extending the range of feasible number of recycles. The rationale for enlarging the fuel radius, while keeping the pitch at the original level, is that more of the moderation would be performed by the hydrogen in the fuel instead of the hydrogen in the water. This would not change substantially the neutronic behavior during normal operation, while it would allow for more hydrogen to remain in the system during large voiding.

It was found that an enlargement of the clad outside diameter from 0.95 cm to 1.03 cm would be sufficient to extend the feasible range to the 13th recycle. On the down side, this would penalize the maximum attainable power by up to 14% because of the larger friction losses associated with the reduction in the hydraulic diameter, unless an increase in the pressure drop is allowed.

2.5.5 Recycling of all the TRU in hydride fuel

The rationale of the fuel cycle scheme examined for the multi-recycling all the TRU in hydride fuel is similar to the one for recycling Pu only, described in Section 2.5.1. As for the Np+Pu evaluation, the TRU vector (shown in Table 2.30) used for the initial loading and for the makeup is taken from [20], Table 1 col. b, based on "extended PWR benchmark with 10y cooling". As for the case of recycling Np+Pu, because of the limited information on the physical properties of the hydrides, two assumptions were made:

1) The MA form hydrides of the form AmH_2, CmH_2 etc. that are stable at reactor operating conditions;
2) The MA-hydrides have a density equal to that of PuH_2 – 10.4 g/cm^3.

The fuel composition at BOL of the first recycles is shown in Table 2.31 for the six cases analyzed; they differ in the amount of uranium loading (from 0 to 3.72 g/cm^3). The TRU amount is adjusted to match the desired cycle length of 1430 EFPD; it increases from 0.894 g/cm^3 for no uranium to 1.754 g/cm^3 for the maximum uranium amount. Np, Am and Cm are all in amount proportional to the plutonium amount according to the values in Table 2.30.

Table 2.30 TRU Vector, from [20], Table 1 col. b, Based on "Extended PWR Benchmark with 10y Cooling"

Isotope	Fraction
U-235	0.002
U-236	0.002
U-238	0.325
NP-237	6.641
PU-238	2.749
PU-239	48.652
PU-240	22.98
PU-241	6.926
PU-242	5.033
AM-241	4.654
AM-242M	0.019
AM-243	1.472
CM-242	0.000
CM-243	0.005
CM-244	0.496
CM-245	0.038
CM-246	0.006

Table 2.31 Fuel Composition at First Recycles for the 6 Cases Analyzed with Varying Uranium Loading (all TRU-Recycling Hydrides)

Case #	1	2	3	4	5	6
U density (g/cc)	0.0	0.465	0.93	1.86	2.79	3.72
Fuel density (g/cc)	6.0808	6.4886	6.8939	7.6850	8.4402	9.1689
Pu density (g/cc)	0.8946	1.0427	1.1860	1.4363	1.6199	1.7540
Np density (g/cc)	0.0688	0.0802	0.0912	0.1105	0.1246	0.1349
Am density (g/cc)	0.0637	0.0742	0.0844	0.1022	0.1153	0.1248
Cm density (g/cc)	0.0056	0.0066	0.0075	0.0091	0.0102	0.0111
Zr density (g/cc)	4.9516	4.7261	4.5035	4.0807	3.6990	3.3477
H density (g/cc)	0.0962	0.0937	0.0911	0.0861	0.0811	0.0762

The TRU destruction fraction and the plutonium fissile fraction at discharge are shown in Figure 2.35 as a function of the recycle number for the MAH_2-U-PuH_2-$ZrH_{1.6}$ fuel. Although as high as 47% of the TRU loaded are fissioned in the first recycle when no uranium is added, the TRU fractional destruction reaches 10-15% for all the initial uranium loadings by the 3rd recycle. It is also observed that while the plutonium fissile fraction at discharge decreases steadily for the heavier uranium loadings, it has a peak similar to that of Pu only for the smaller U loadings.

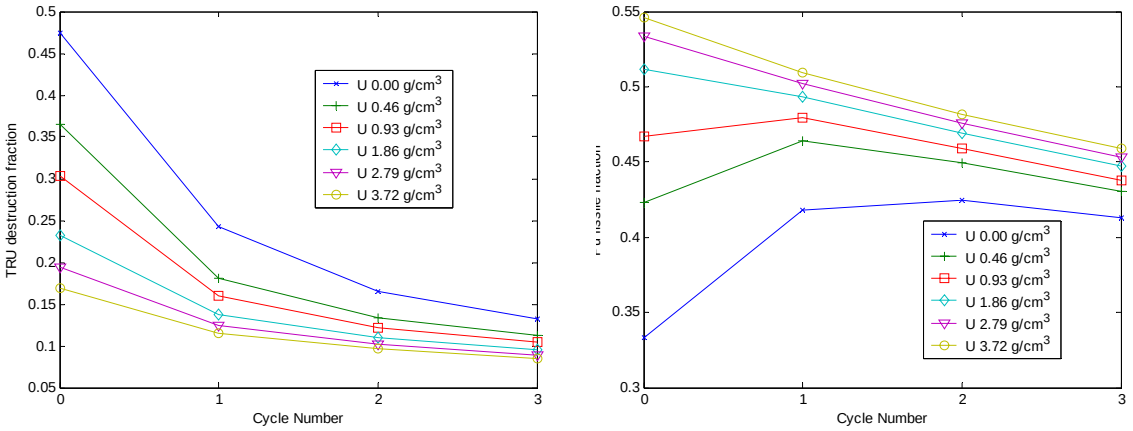

Figure 2.35 TRU destruction fraction (left) and Pu fissile fraction (right) as a function of the re-cycle number; MAH_2-U-PuH_2-$ZrH_{1.6}$ fuel

The reactivity coefficients for MAH_2-U-PuH_2-$ZrH_{1.6}$ fuel were evaluated at each recycle with and without soluble boron. At the 3rd recycle (the limit), only the FTC is negative and flat throughout the cycle, with the larger uranium loadings featuring a more negative FTC. All the other reactivity coefficients are positive and increasing throughout the cycle.

2.6 Comparisons of Hydride Fueled Systems

The purpose of this section is to directly compare the properties of hydride fuels (Pu only, Pu + Np, all TRU) at first recycle with variable uranium amounts, in terms of achievable burnup (Figure 2.36), maximum core average FTC (Figure 2.37), TRU destruction fraction and fissile fraction at discharge (Figure 2.38). It is observed that the maximum achievable burnup, as high as 628 GWD/MTiHM in case of recycling plutonium only, features a positive FTC before reaching EOL. Therefore, practically, the uranium content should be increased to about 0.5 g/cm^3, which would decrease the feasible burnup to less than 500 GWD/MTiHM. The addition of Np, on the other hand, would reduce the FTC to negative with just 0.2 g/cm^3 of U, while the feasible burnup would be reduced to about 500 GWD/MTiHM, making the addition of Np for the first few recyclings probably a preferred approach. The addition of the entire TRU vector makes the FTC negative throughout the entire cycle without the addition of uranium, even though the achievable burnup and the TRU destruction fractions are penalized. It will be interesting, therefore, to analyze the possibility of recycling Pu+Np+Am, which may feature a negative FTC without a need for uranium.

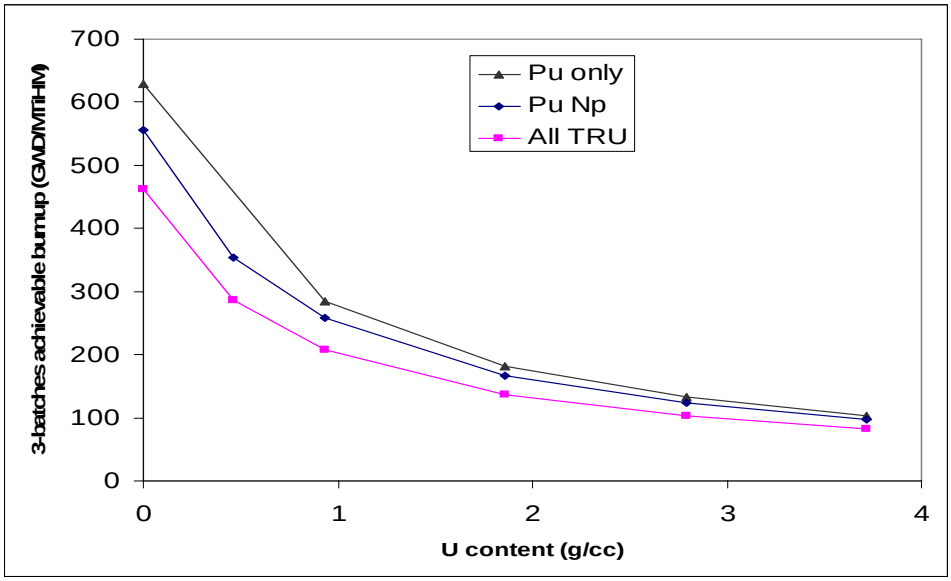

Figure 2.36 First recycle, three-batch achievable burnup (GWD/MTiHM) as a function of uranium loading, for recycling Pu only, Pu + Np or all TRU in hydride fuels

Table 2.32 provides a summary of selected neutronic properties of the TRU-bearing fuels studied at the 1st recycle. "MOX reference" is the standard MOX with 0% $ZrH_{1.6}$; "Pu D-hydride no U" and "Pu hydride 25% U_{max}" are added because they are possible approaches to make the sign of the FTC negative at the first recycle (as discussed in Section 2.4.3). All the presented fuels feature the same cycle length. Characteristics compared include burnup, U, Pu and MA amounts (for the elements and for the most important isotopes) at BOL and EOL; and incineration capability. Also compared are measures of repository impact ((Np and its precursors, total TRU inventory at discharge, decay and gamma heat) and measures of proliferation resistance (Fissile/total Pu, MA/Pu, neutron emission per g of Pu and of HM, and likewise for heat

emission). It is observed that fertile free, Pu-loaded MOX, hydride and deuteride, have similar characteristics in all the measures examined.

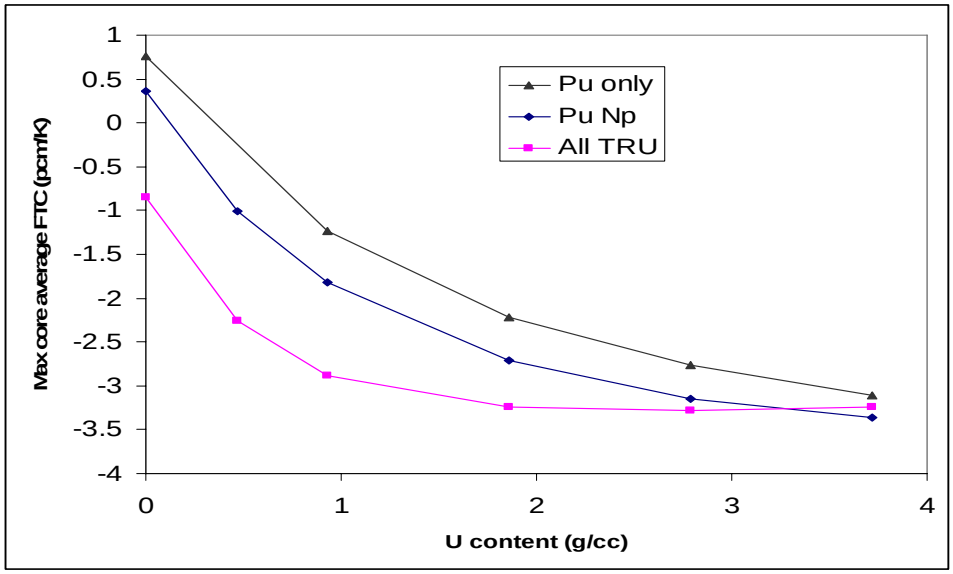

Figure 2.37 First recycle, maximum core-average FTC (pcm/K) as a function of uranium loading, for recycling Pu only, Pu + Np or all TRU in hydride fuels

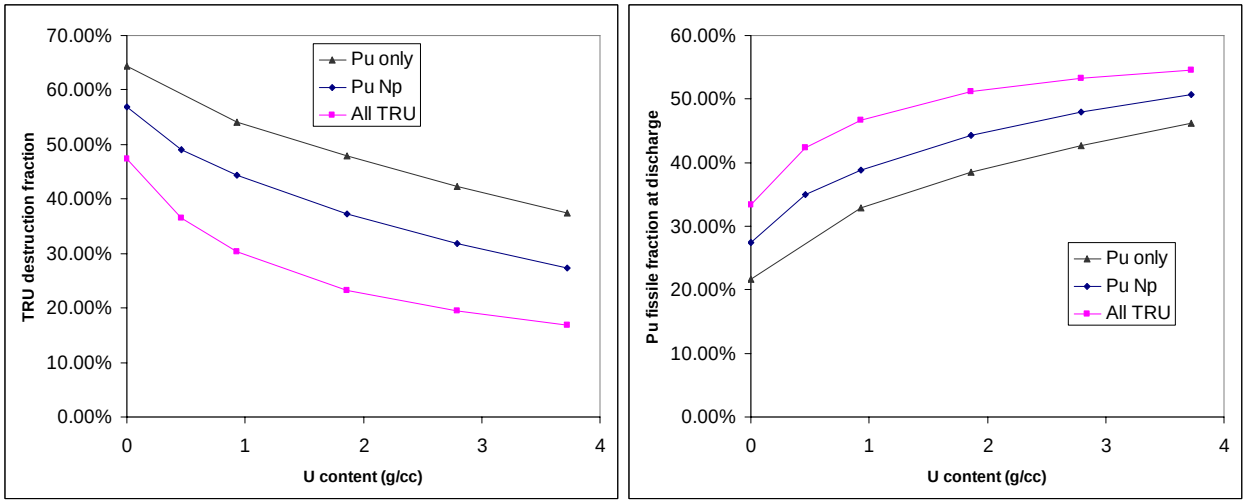

Figure 2.38 First recycle, TRU destruction fraction (left) and Pu fissile fraction at discharge (right) as a function of uranium loading, for recycling Pu only, Pu + Np, or all TRU in hydride fuels

Table 2.32 Summary of neutronic properties of selected TRU-bearing fuels at 1st recycle

Property	MOX reference	MOX no U	Pu hydride no U	Pu deutride no U	Pu+Np hydride	TRU hydride
Burnup (GWD/MtiHM)	51.4	622.1	627.9	620.1	555.9	462.4
Residence time (EFPD)	1426.4	1427.8	1429.0	1429.2	1430.7	1428.8
Initial Pu loading (g/cc)	1.0977	0.7617	0.7562	0.7658	0.7986	0.8945
Initial Pu loading (Pu w/o)	10.43	16.68	12.70	12.73	13.30	14.71
Initial U loading (g/cc)	8.1740	0	0	0	0	0
Initial Np loading (g/cc)	0	0	0	0	0.0614	0.0688
Initial Am loading (g/cc)	0	0	0	0	0	0.0637
Initial Cm loading (g/cc)	0	0	0	0	0	0.0057
At discharge						
U inventory (g/cc)	7.8894	0.0006	0.0006	0.0006	0.0011	0.0016
^{235}U	1.4E-02	1.1E-04	9.7E-05	1.1E-04	2.0E-04	2.7E-04
^{236}U	2.6E-03	7.1E-05	7.1E-05	7.2E-05	8.3E-05	9.4E-05
^{238}U	7.9E+00	7.0E-05	7.8E-05	7.1E-05	7.8E-05	7.9E-05
Pu inventory (g/cc)	0.85	0.23	0.23	0.24	0.31	0.44
Pu inventory/ initial Pu	77.36%	30.65%	30.31%	31.00%	38.42%	49.35%
^{238}Pu	0.842	0.577	0.574	0.590	1.549	2.322
^{239}Pu	0.572	0.029	0.022	0.028	0.055	0.118
^{240}Pu	0.910	0.404	0.382	0.401	0.475	0.601
^{241}Pu	1.537	0.787	0.719	0.794	0.922	1.215
^{242}Pu	1.027	1.484	1.635	1.535	1.754	1.621
% Pu incinerated/cycle	22.6%	69.4%	69.7%	69.0%	61.6%	50.7%
Fissile Pu/ Tot Pu	56.5%	24.5%	21.9%	24.3%	27.4%	33.3%
MA inventory (g/cc)	4.86E-02	4.57E-02	4.27E-02	4.47E-02	6.57E-02	1.04E-01
Th:	3.17E-09	1.51E-09	1.77E-09	1.56E-09	9.12E-05	9.16E-05
Pa:	6.89E-10	4.17E-10	3.73E-10	4.22E-10	3.33E-07	2.86E-07
Np:	1.75E-03	2.26E-05	2.22E-05	2.29E-05	2.47E-02	3.13E-02
Am:	3.30E-02	2.38E-02	2.47E-02	2.35E-02	2.48E-02	4.11E-02
Cm:	1.39E-02	2.19E-02	1.80E-02	2.12E-02	1.61E-02	3.17E-02
Bk:	1.02E-09	1.65E-08	4.14E-09	1.40E-08	2.92E-09	3.17E-08
^{237}Np+^{241}Am+^{245}Cm	1.53E-02	4.31E-03	3.72E-03	4.31E-03	3.02E-02	4.87E-02
Total TRU inventory	0.90	0.28	0.27	0.28	0.37	0.55
% TRU incinerated/cycle	18.2%	63.4%	64.0%	63.2%	56.7%	47.2%
MA/Pu at discharge (%)	5.7%	19.6%	18.6%	18.8%	21.4%	23.6%
Neutron source (n/s/cc)	1.38E+05	2.23E+05	1.89E+05	2.17E+05	1.70E+05	3.43E+05
Activity (Ci/cc)	40.06	59.33	57.74	58.26	50.97	60.71
Decay heat (w/cc)	0.27	0.37	0.37	0.37	0.38	0.82
Gamma Decay heat (w/cc)	3.07E-03	6.92E-03	6.73E-03	6.73E-03	5.39E-03	4.73E-03
Neutrons per g Pu (n/s)	635.81	1251.60	1314.42	1260.57	1280.53	1190.36
Neutrons per g HM (n/s)	1.57E+04	8.00E+05	6.95E+05	7.69E+05	4.55E+05	6.28E+05
Specific heat (w/g Pu)	0.05	0.26	0.26	0.25	0.21	0.17
Specific heat (w/g HM)	0.03	1.32	1.37	1.32	1.01	1.50

2.7 System Analysis

2.7.1 System analysis performance for reduction of accumulated Pu inventory

Plutonium stabilizing fuel assemblies, such as the CORAIL and MOX-UE, do not offer Pu inventory draw-down after the first recycle: for this reason we decided to compare the following two energy systems:

(1) A system comprised of conventional once-through UO_2 fuelled PWRs and PUZH fuelled PWRs; the ratio of the number of cores of the two types are adjusted so as to stabilize the amount of Pu in the combined system.
(2) A system consisting of PWRs having CORAIL cores only.

The most promising hydride fuel was identified to be PuH_2-$ZrH_{1.6}$ (called "PUZH" in the present Section) for its highest TRU transmutation performance and for its physical characteristics that allow for unlimited number of plutonium recycling in PWR. The best performing oxide fuel, in terms of TRU destruction fraction, was identified as PuO_2-ZrO_2 (called "MOX" in the present Section), which is the inert-matrix counterpart of the optimal hydride fuel. This latter does not allow indefinite multi-recycling (see Section 2.4.12); it nevertheless offers the fastest destruction of the accumulated plutonium inventory among the analyzed oxide fuels. These two optimal hydride and oxide fuel systems are compared in Sections 2.7.3, 2.7.4, 2.7.5 and 2.7.6 for their performance with respect to the reduction of the accumulated plutonium inventory in the Yucca Mountain Repository.

2.7.2 System analysis: comparison with CORAIL

The PUZH fuel core does not require any natural uranium (i.e. it can use depleted uranium as feed) and no SWU, while the CORAIL cores requires 7 kg of natural uranium and 5.4 SWU per kg of uranium used as fuel (because of the required enrichment). Since the PUZH fuel is a net plutonium destroyer, at equilibrium the PUZH core will be supported for its plutonium feed by 6.7 standard UO_2 LWR[8]. This is compared with 7.7 self-sufficient CORAIL assemblies: they will need 26% less natural uranium and SWU as compared to 6.7 PWR + 1 PUZH, and produce 50% less minor actinides.

It is therefore concluded that at equilibrium the CORAIL system requires less natural resources and has a smaller repository impact than the coupled LWR+PUZH. It is also noted that the CORAIL system would not be practical for a substantial Pu draw-down from the YMR, since the number of cores required to load the entire YMR Pu inventory would be ~300, three times larger than the current US operating fleet of commercial reactors.

2.7.3 Material balance

The 63,000 MTiHM of LWR spent fuel that is planned to be stored at the Yucca Mountain Repository (YMR) will contain about 750 MT of Pu and 61 MT of minor actinides. The present section estimates the level of reduction in TRU inventory that can be obtained by multi-recycling

[8] The resource consumptions of the typical UO_2 PWR (using 5% enriched uranium) are 10.3 kg of natural uranium and 7.92 SWU per kg of enriched uranium.

the accumulated mass of Pu in a given number of PWR cores, using either one of the systems defined in Section 2.7.1.

The analysis is performed by assuming a given number of hydride cores operating in parallel, and making the assumption that this number will not be varied during the recycling campaign. This determines the number of recycles necessary to consume the entire accumulated inventory of plutonium, and therefore the duration of the recycling campaign[9].

The number of cores that can be used for recycling the total Pu inventory vary from 1 (requiring a large number of recyclings) to 101 for PUZH and from 10 to 98 for MOX. In MOX the number of parallel cores used for recycling cannot be less than 10, since a smaller number of cores would require a larger number of recyclings than the 10 that are allowed in this fuel type before the large void coefficient of reactivity becomes positive (see Section 2.4.12). On the contrary, PUZH fuel can multi-recycle plutonium an un-limited number of times, allowing the entire recycling campaign to be operated even with as low as one core.

At the end of the recycling campaign, the leftover TRU stream will compose of:

1) The MA discharged from the PuH_2-$ZrH_{1.6}$ core at each multi-recycling step;
2) The plutonium left over after the PuH_2-$ZrH_{1.6}$ irradiation campaign will be ended.

There could be a further reduction in the plutonium leftover after the entire YMR inventory will have been drawn-down, by concentrating the plutonium leftover in different hydrides cores into fewer cores, to reach the inventory necessary for the desired cycle length. However, this option has not been studied in the present work.

Figure 2.39 shows the plutonium loaded and consumed at each recycle in PuH_2-$ZrH_{1.6}$ fuelled PWR core. It is observed that the amount of plutonium consumed at each recycle slightly increases with recycling while the amount of plutonium loaded at each recycle increases significantly with the recycling; this reflects the significant decrease in the fractional transmutation of Pu with the recycle number reported in Figure 2.20. The net result is a substantial increase in the amount of plutonium that accumulates in the system with increased number of recyclings. The amount of MA keeps accumulating as well.[10]

Figure 2.40 shows the TRU mixture remaining after the recycling campaign for the PUZH and for the optimal MOX as a function of the number of cores, expressed as a fraction of the initial mass of plutonium. It is observed that a larger number of cores (i.e. smaller number of required plutonium recycles) results in a smaller accumulation of MA, but also in a larger residual inventory of plutonium at discharge. The net effect, somewhat surprisingly, is that the total TRU mass after the recycles is relatively constant with the number of parallel cores; slightly smaller for smaller number of cores (and more recycles), at about 30-35% of the initial inventory. It is also observed that the residual TRU inventory is slightly higher for MOX cores than for PUZH cores.

[9] The total YMR plutonium inventory may not be an exact multiple of the consumption per cycle of a given hydride fleet (actually, in general it will not). For this reason, after the recycling campaign will be over, there will be a "left-over" plutonium amount stemming only from the simplifying assumption that the hydride fleet size will not be varied during the recycling campaign. This would make a comparison between different fleet sizes difficult. To obviate this problem, it is chosen to normalize all the results presented in this and following Sections per ton of TRU fissioned. It is also noted that the target amount of plutonium to be transmuted is likely not constant, because of the continued accumulation of plutonium from operating LWR, isotopic decay etc… Also for this reason, the normalization approach makes the presented results of more general validity.

[10] The number of fissions per recycle is constant, though.

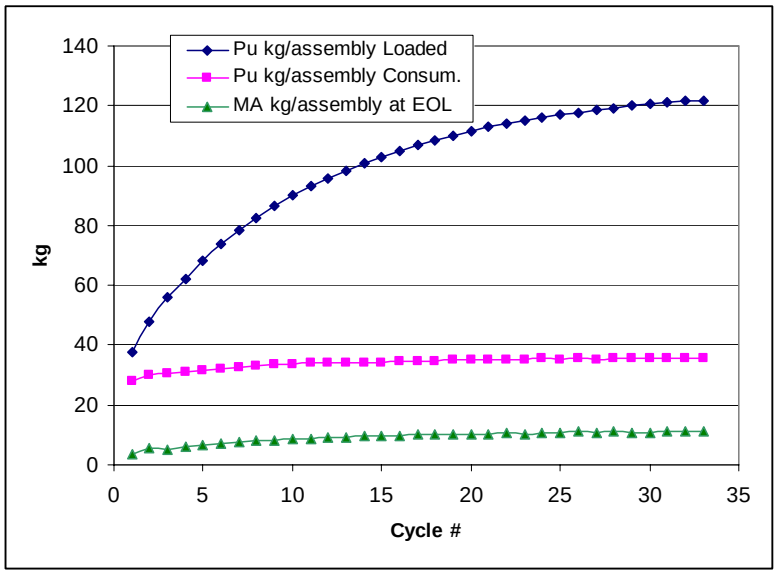

Figure 2.39 Plutonium (in kg/assembly) loaded and consumed at each recycle in PuH_2-$ZrH_{1.6}$, and MA (in kg/assembly) discharged at the end of each recycle

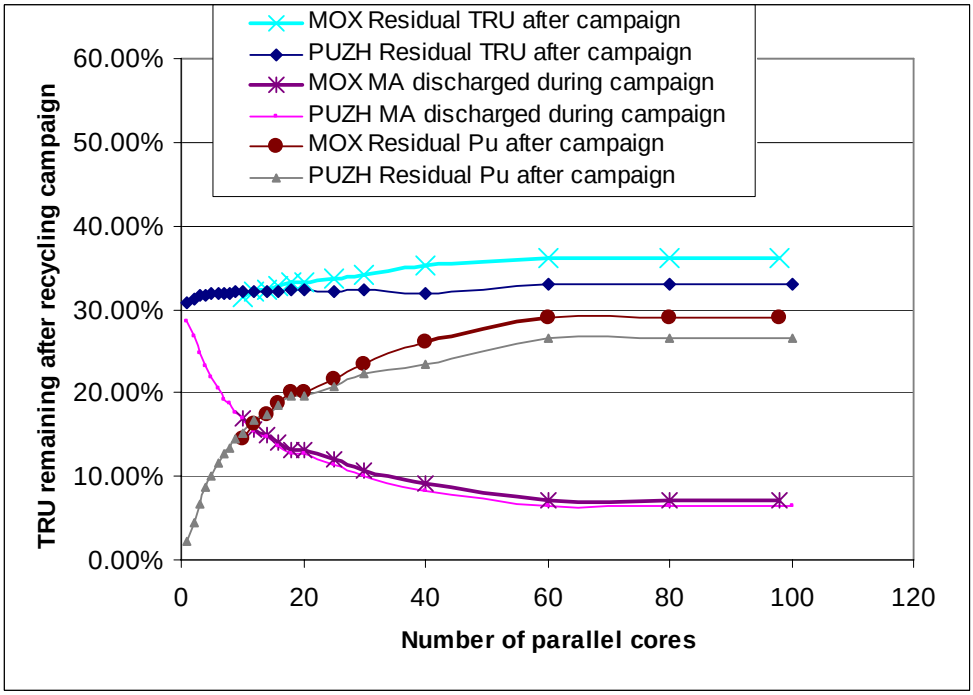

Figure 2.40 TRU mixture remaining after the recycling campaign for the optimal PUZH and for the optimal MOX, expressed as a fraction of the initial mass of Pu inventory, as a function of a variable number of cores[11].

[11] There could be a further reduction in the plutonium leftover after the entire YMR inventory will have been drawn-down, by concentrating the plutonium leftover in different hydrides cores into fewer cores, to reach the inventory necessary for the desired cycle length. However, this option has not been studied in the present work.

2.7.4 Repository impact

The repository impact[12] is evaluated through the estimate of the following normalized parameters at the end of the campaign, as a function of the total number of PUZH and MOX cores:

1) total radioactivity of the TRU stream (Ci/ton of initial Pu), in Figure 2.41 (left);
2) total neutron emission (n/s/ton of initial Pu), in Figure 2.41 (right);
3) total decay heat (W/ton of initial Pu), in Figure 2.42 (left);
4) total gamma decay heat (W/ton of initial Pu), in Figure 2.42 (right);
5) total toxicity in air ($m^3$of Air/ton of initial Pu), in Figure 2.43 (left);
6) total toxicity in water ($m^3$of H_2O/ton of initial Pu), in Figure 2.43 (right).
7) total mass of ^{237}Np and its precursors (i.e. ^{241}Am and ^{245}Cm) (ton/ton of initial Pu), in Figure 2.44.

It is observed that all these measures of repository impact, except for the mass of neptunium and its precursors as a fraction of total Pu transmuted, are slightly higher for MOX than for PUZH, more so for larger number of cores. It is also observed that the radioactivity is higher for larger number of cores, while all the other measures decrease with the use of higher number of parallel cores (i.e. with a smaller number of recyclings).

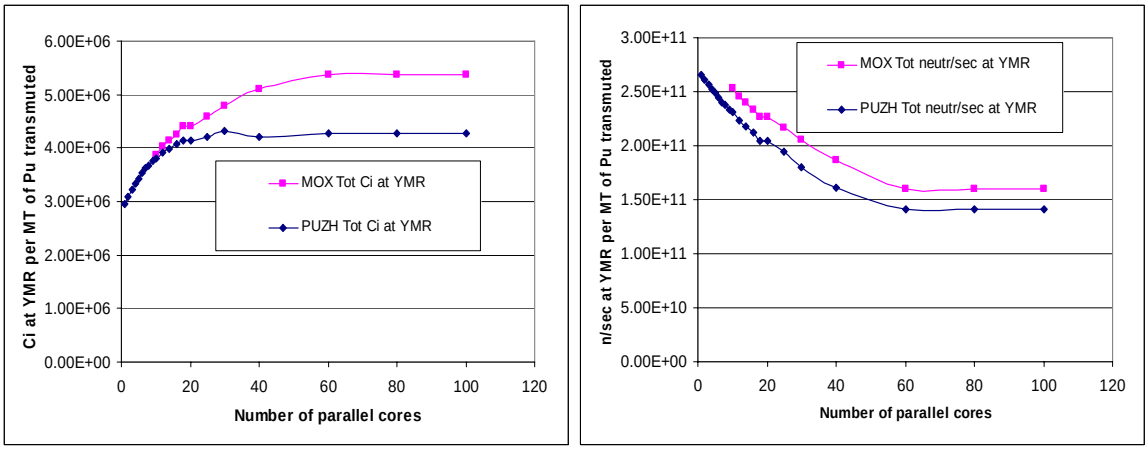

Figure 2.41 Total radioactivity (Ci/ton of initial Pu) (left) and neutron emission (n/s/ton of initial Pu) (right) sent to YMR after the end of the recycling campaign as a function of the number of parallel PUZH and MOX cores.

Table 2.33 shows the repository impact related characteristics of the residual stream after transmutation in either PUZH or MOX fuelled cores (in a selected number of parallel cores) as compared to those in the original LWR-derived Pu disposed at YMR (in column 1). All the values are normalized per ton of Pu transmuted[13]. It is observed that the total radioactivity decreases after transmutation, while all the other parameters increase.

[12] The measured parameters for the repository impact are evaluated at 10 years after discharge. Longer recycling campaigns allow more time for the TRU to decay before the end of the recycling campaign, resulting in smaller repository impact if measured at the end of the campaign itself. No account is taken for possibly longer reprocessing/disposal times.

[13] For LWR the values are normalized "per ton of Pu to be transmuted", or the total inventory of 750 MT

While this implies a heavier heat and toxicity load on the YMR after the transmutation campaign, it also shows a much greater proliferation resistance of the transmuted stream as compared to the original one, since the residual stream would has a small amount of highly degraded plutonium and a high neutron, gamma ray and heat emission would make the diversion and handling of the residual stream difficult (more information of this in Section 2.7.5).

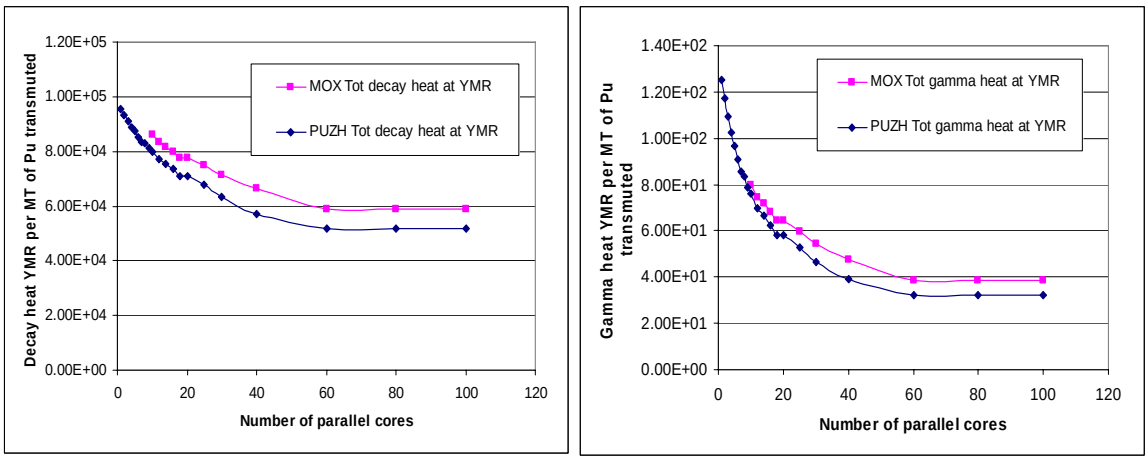

Figure 2.42 Total decay heat (W/ton of initial Pu) (left) and gamma decay heat (W/ton of initial Pu) (right) sent to YMR after the end of the recycling campaign as a function of the number of parallel PUZH and MOX cores

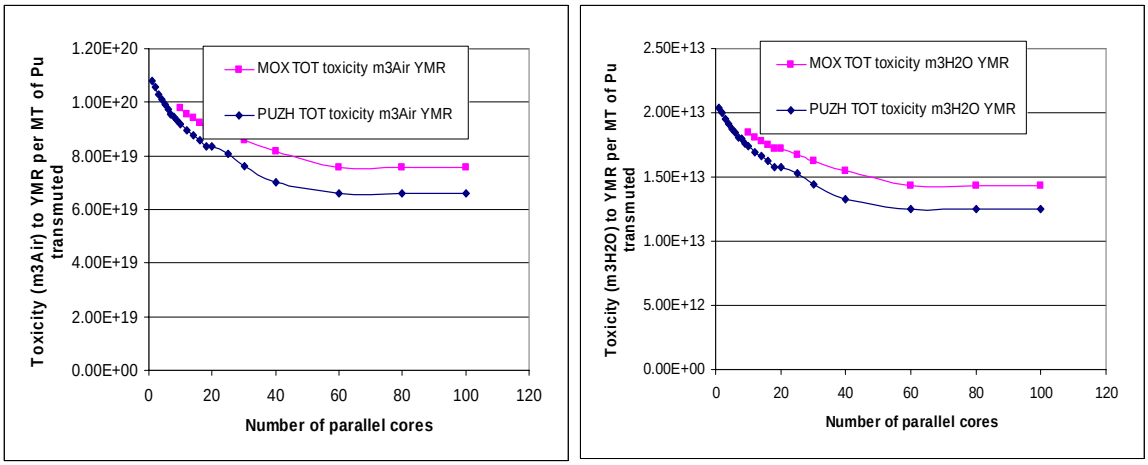

Figure 2.43 Total toxicity ($m^3$of Air/ton of initial Pu) (left) and ($m^3$of H_2O/ton of initial Pu) (right) and sent to YMR after the end of the recycling campaign as a function of the number of parallel PUZH and MOX cores

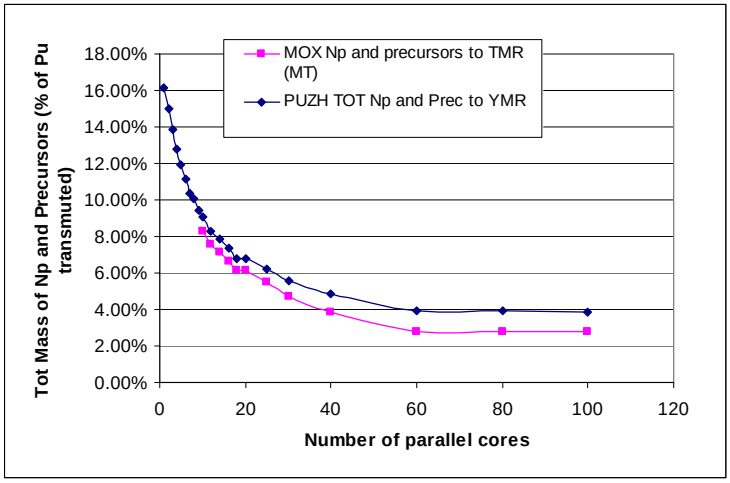

Figure 2.44 Total mass of ^{237}Np and its precursors (i.e. ^{241}Am and ^{245}Cm) (ton/ton of initial Pu) sent to YMR after the end of the recycling campaign as a function of the number of parallel PUZH and MOX cores

Table 2.33 Repository Impact of the Pu Stored at YMR Before the Recycling Campaign and of the TRU Stream After a Multi-Recycling Campaign in MOX and PUZH Fuels, for Selected Number of Parallel Cores

	LWR Pu	PUZH	MOX	PUZH	MOX	PUZH	MOX
	at YMR	1 core	1 core	6 cores**	6 cores	80 cores	80 cores
n/s	5.393E+08	2.658E+11	N/A	2.445E+11	N/A	1.414E+11	1.600E+11
Ci	1.057E+07	2.955E+06	N/A	3.533E+06	N/A	4.272E+06	5.374E+06
decay heat	21463	95395	N/A	85397	N/A	51841	58688
gamma heat	7.05	125.06	N/A	90.85	N/A	32.21	38.40
m^3 of Air	5.660E+19	1.079E+20	N/A	9.738E+19	N/A	6.586E+19	7.549E+19
m^3 of H_2O	1.068E+13	2.042E+13	N/A	1.843E+13	N/A	1.246E+13	1.429E+13

* All values are normalized per MT of LWR Pu transmuted; ** Recycling campaign with PUZH ~66 years.

2.7.5 Proliferation resistance

The total inventory of plutonium to be handled in the reprocessing plant is quite similar in the case of MOX and PUZH. However, the fissile fraction at the reprocessing facility (i.e. 10 years after download) − shown in Figure 2.45 as a function of the recycling number − shows that the PUZH stream is more proliferation resistant than that of MOX for the first 9-10 recycles.

Similarly, the neutron emission per gram of plutonium at the reprocessing plant − shown in Figure 2.46 as a function of the recycle number − is higher for PUZH than for MOX. Other important measures of proliferation resistance: 1) the neutron emission per gram of TRU at the reprocessing plant − shown in Figure 2.47 as a function of the recycle number − as well as the specific decay heat, are similar for the two fuel types.

It is concluded that multi-recycling in PuH_2-$ZrH_{1.6}$ appears more resistant to proliferation than multi-recycling in PuO_2-ZrO_2.

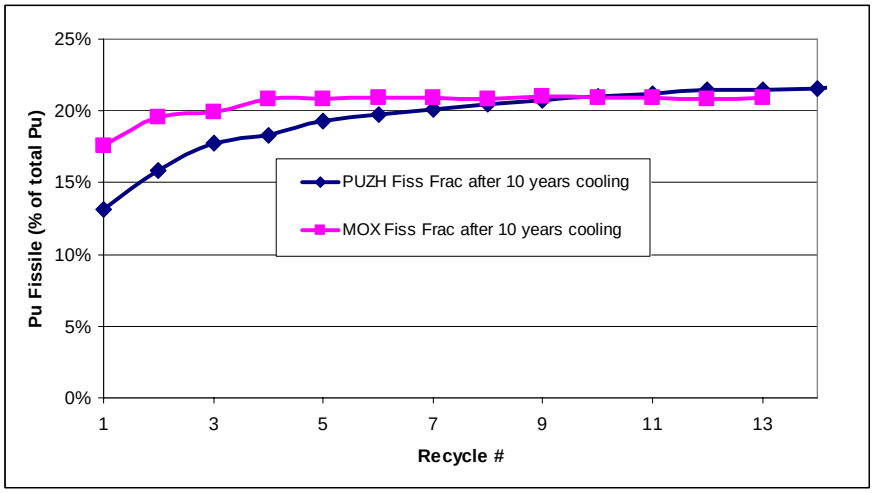

Figure 2.45 Plutonium fissile fraction for the first 13 recycles at the reprocessing plant (after 10 years of cooling), for PUZH and MOX fuelled system as a function of the recycle number

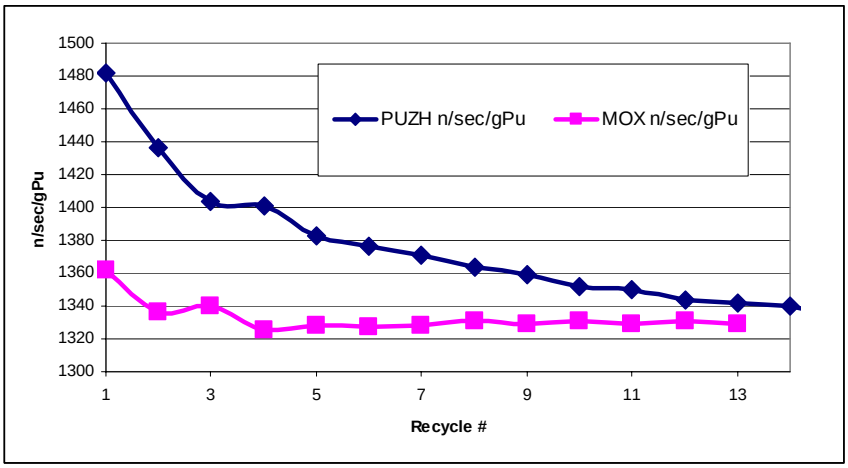

Figure 2.46 Neutron emission per gram of Pu at the reprocessing plant (after 10 years of cooling), for PUZH and MOX fuelled system as a function of the recycle number

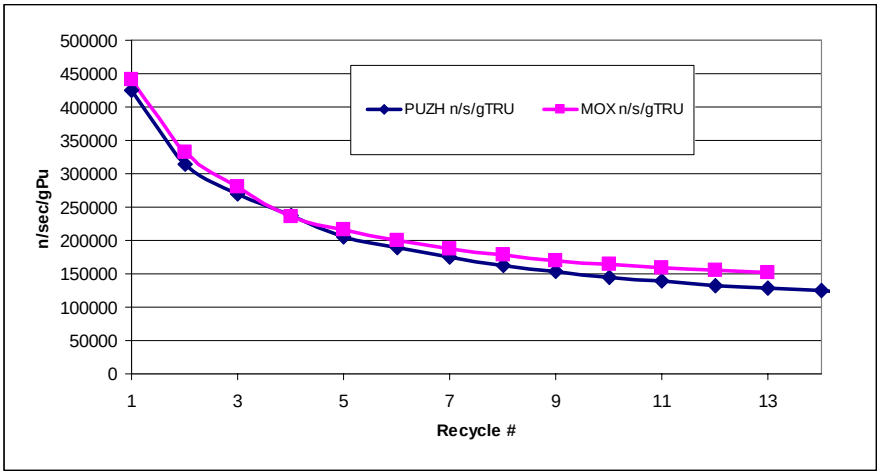

Figure 2.47 Neutron emission per gram of TRU at the at the reprocessing plant (after 10 years of cooling), for PUZH and MOX as a function of the recycle number

2.7.6 Fuel cycle costs

Since the mass of plutonium loaded in PuH_2-$ZrH_{1.6}$ and PuO_2-ZrO_2 is very similar (4.5% higher in case of PuO_2-ZrO_2), and the cost of reprocessing is mainly a factor of the total plutonium to be processed, it is expected that the cost of the two fuels will be similar, only slightly higher for MOX. However, hydrides have a slightly higher fabrication costs due to the cost of hydrating. Absent industry data, in previous studies on uranium-based hydrides [21, 22] it was assumed that the fabrication cost of hydrides is the same as oxide on a "per volume base", which would effectively double the cost on a "per heavy metal" base. The fabrication cost for a typical PWR assembly (for a fabrication cost of 275 $/kgHM, [23]) is about 130,000$. From industry estimate, it is known that the typical fabrication cost of a MOX assembly is ~550,000$ [24]. The inert matrix MOX and PUZH load ~10% less plutonium than standard MOX (i.e. PuO_2-UO_2). Conservatively, it is assumed here that the cost of fabrication of inert matrix MOX will be the same as of standard MOX, and that the cost of fabrication of PuH_2-$ZrH_{1.6}$ will be higher by 130,000$, effectively doubling the part of the cost not related to plutonium handling, for a total fabrication cost per assembly of 680,000$ for PuH_2-$ZrH_{1.6}$.

However, the main part of the recycling cost comes from the reprocessing of spent fuel, that were estimated in [24] at 1800 $/kgHM for the reprocessing, plus the cost of disposing the high level waste (253 $/kg) minus the cost of disposing the unprocessed spent fuel (500+200$/kg), resulting in a total cost of 0.63 million$ for a standard UO_2 PWR assembly. Considering that it is necessary to recycle 6.7 and 6.9 spent LWR assemblies to obtain the plutonium respectively for a PuH_2-$ZrH_{1.6}$ assembly and for a PuO_2-ZrO_2 assembly, the reprocessing part of the cost amounts respectively to 4.2 and 4.4 million$/assembly. Summing the respective fabrication costs of 0.55 and 0.68 million$/assembly, the final cost of PuH_2-$ZrH_{1.6}$ would only be ~1.2% lower than that of PuO_2-ZrO_2, not enough to justify the choice of this fuel based on this cost estimation.

2.7.7 System analysis: conclusions

It was found that, at equilibrium, the CORAIL system requires less natural resources and has a smaller repository impact than the coupled LWR+PUZH. For the purpose of Pu inventory reduction, PuH_2-$ZrH_{1.6}$, offers only a slightly smaller repository impact than PuO_2-ZrO_2 on most of the analyzed parameters, but is the preferred choice from the perspective of proliferation resistance, featuring a smaller fissile fraction and a higher plutonium specific neutron emission rate. The cost difference is likely not significant enough to justify the choice of one fuel type over the other.

2.8 Conclusions

The neutronic part of this project assessed the feasibility of multi-recycling plutonium and TRU in PWR using hydride rather than oxide fuel. The extra hydrogen in the fuel softens the neutron spectrum and thereby reduces the critical Pu concentration. First our neutronic computational capabilities have been benchmarked against heterogeneous, plutonium-containing (CORAIL [3,4]) and TRU-containing (CONFU [14]), fuel assemblies. The TRITON/NEWT sequence and associated cross section libraries of the SCALE 5.1 code package were found of satisfactory accuracy for modeling complex TRU-containing PWR fuel assemblies like the CORAIL and CONFU, provided that the ORIGEN default branching ratio for production of ^{242m}Am is changed to approximately 10-11%. A value of 10% for the branching ratio was found to provide good agreement with the calculated results of both APOLLO2 and WIMS8 in the case of CORAIL. In case of CONFU, the agreement between the TRITON and CASMO predictions is good for all the evaluated actinides with the exception of ^{242m}Am which shows a discrepancy of about 20%: CASMO, which likely uses a slightly different value for the branching ratio of ^{241}Am, predicts a higher concentration of ^{242m}Am. Since the TRU-containing hydride fuel assemblies analyzed feature a uniform composition, integral reactor physics characteristics, such as achievable burnup, actinide concentration evolution and reactivity coefficients can be estimated using an equivalent unit cell analysis. Modeling an equivalent unit cell enables using the 238 energy group cross-section library. Other characteristics, such as the assembly power peaking factors and control rods worth, were calculated using a full 2-D fuel assembly model using the 44 group library.

An equivalent Pu-hydride (PUZH) fuel assembly was compared with two oxide fuel assembly designs that were proposed to overcome the positive void coefficient of reactivity – CORAIL and MOX-UE. The CORAIL design offers ~30% natural uranium and Separating Working Unit (SWU) saving over conventional UO_2 fuelled cores, but it provides for Pu stabilization rather than net destruction (a complete Pu drawdown from the YMR would require ~300 CORAIL cores, three times the current LWR fleet).It was found that the equivalent PUZH fuel (i.e. with 45% uranium loading) offers twice as large a fractional transmutation as the equivalent MOX-UE oxide fuel. That is, a PWR loaded with these PUZH fuel assemblies will incinerate in the first recycle twice as much TRU (primarily Pu) as it will do when loaded with MOX fuel assemblies when both core designs are loaded with same amount of TRU and operate at the same power level for the same time. This equivalent PUZH core (i.e. with 45% uranium loading) will also be less expensive, since it uses depleted uranium versus significantly larger quantities of enriched uranium required for the equivalent MOX-UE core. Additionally, the equivalent PUZH fuel design has a lower power peaking factor than both MOX-UE and CORAIL fuel assemblies. The PUZH fuel with heavy plutonium loading (as in the case of MOX-UE-4) enables attaining the same cycle length of the MOX-UE fueled systems while the LVRC substantially more negative, which is an important safety feature.

An assessment of the feasibility of enhancing the fractional plutonium transmutation using hydride fuels with varying amounts of thorium and uranium was undertaken as well. These fuels are of the form ThH_2-$ZrH_{1.6}$-PuH_2 and U-$ZrH_{1.6}$-PuH_2 respectively. It was found that the fertile free hydride fuel (of the form PuH_2-$ZrH_{1.6}$), while offering the higher TRU destruction fraction of all the systems analyzed, also allows multi-recycling of Pu in PWR an unlimited number of times when uniformly loaded in all fuel assemblies in the core. This unique feature of hydride

fuels is due to the incorporation of a significant fraction of the hydrogen moderator in the fuel, thereby reducing the effect of spectrum hardening due to coolant voiding accidents; the large void reactivity coefficient remains negative. The fractional transmutation of PuH_2-$ZrH_{1.6}$ was found to be about 64% at the first recycle and gradually decreases to about 20% towards the equilibrium recycle. The FTC of this promising fuel was found positive in the third batch, thereby potentially limiting the practically achievable burnup, and therefore the transmutation effectiveness. The use of deuterium instead of hydrogen in PuH_2-$ZrH_{1.6}$ fuel was found an effective approach for obtaining a negative fuel temperature coefficient of reactivity during the first recycle, practically without penalizing the achievable burnup or TRU transmutation effectiveness. Addition of relatively small amount of either depleted U or Th offer two alternative approaches for providing a negative FTC over the entire first recycle, but slightly penalize the attainable fractional transmutation. An inert-matrix oxide fuel counterpart -- PuO_2-ZrO_2, was investigated as well. Although the TRU destruction fraction at first recycle is almost as high as that of PuH_2-$ZrH_{1.6}$ fuel, the practical applicability of this fuel for multi-recycling is limited − due to a positive reactivity effect introduced by large voiding the maximum possible number of recycles is limited to 10 despite of the fact that the leakage effect due to large core voiding was found significantly larger for oxide as compared to hydride fueled cores.

The feasibility of recycling Pu+MA in hydride fuels was also assessed: it was found that hydride fuels allow multi recycling of Pu+Np at least 6 times, before getting a positive large void reactivity feedback. This corresponds to approximately 86 years of recycling campaign. A number of approaches where investigated for making negative the large voiding reactivity coefficients beyond the 6^{th} recycle for NpH_2-PuH_2-$ZrH_{1.6}$ fuel[14]. Enlarging the fuel rod radius while conserving the pitch was found effective for substantial extension of the feasible number of recycles. This approach does not substantially change the neutronic behavior during normal operation, while it would result in a larger amount of hydrogen to remain in the core during large voiding. On the down side, this would penalize the maximum attainable power because of the larger friction losses associated with the reduction in the hydraulic diameter, unless an increase in the pressure drop is allowed. It was also found that if it is desired to recycle all the TRU in PWR using hydride fuel, the number of possible recycle would be limited to 3; the limit is imposed by a positive large void reactivity feedback.

Finally, a system analysis was performed to compare the fuel cycle characteristics of Pu multi-recycling in PWR using the promising hydride fuel assembly designs identified before versus Pu recycling in PWRs using the most promising oxide fuel assemblies. It was found that, at equilibrium, the CORAIL system requires less natural uranium and SWU and has a smaller repository impact than the coupled LWR+PUZH.

The investigation of the reduction in TRU inventory attainable by multi-recycling Pu in a given number of PWR cores using either the optimal hydride or the optimal oxide fuels found that a larger number of cores (i.e. smaller number of required plutonium recycles) results in a smaller accumulation of MA, but also in a larger residual inventory of plutonium at discharge. The net effect, somewhat surprisingly, is that the total TRU mass after the recycles is relatively constant with the number of parallel cores; slightly smaller for smaller number of cores (and more

[14] Based on physics considerations, it is expected that a similar concept would apply successfully also to the "all TRU" hydride fuel, but not to oxide fuels.

recycles), at about 30-35% of the initial inventory. It was also found that the residual TRU inventory is slightly higher for MOX cores than for PUZH cores.

The repository impact was evaluated through the estimate of the following parameters (normalized per ton of Pu transmuted) at the end of the campaign, as a function of the total number of best-performing PUZH and MOX cores: 1) total radioactivity of the TRU stream; 2) total neutron emission; 3) total decay heat; 4) total gamma decay heat; 5) total toxicity in air; 6)total toxicity in water; and 7) total mass of ^{237}Np and its precursors (i.e. ^{241}Am and ^{245}Cm). It was found that all these measures of repository impact, except for the mass of neptunium and its precursors, are slightly higher for MOX than for PUZH, more so for larger number of cores. It was also observed that the radioactivity is higher for larger number of cores, while all the other measures decrease with the use of higher number of parallel cores (i.e. with a smaller number of recyclings).

The proliferation resistance was evaluated through the estimate of the following parameters (normalized per ton of Pu transmuted) at the reprocessing plant: 1) total inventory of plutonium to be handled at the reprocessing plant; 2) Pu fissile fraction; 3) neutron emission per gram of plutonium and TRU; 4) specific decay heat for Pu and TRU. The total inventory of plutonium to be handled in the reprocessing plant is quite similar in the case of MOX and PUZH. However, the plutonium fissile fraction at the reprocessing facility, as well as the neutron emission per gram of plutonium, shows that the PUZH stream appears more proliferation resistant than that of MOX for the first 9-10 recycles. The neutron emission per gram of TRU and the specific decay heat are similar for the two fuel types. It is concluded that multi-recycling in PuH_2-$ZrH_{1.6}$ is more resistant to proliferation than multi-recycling in PuO_2-ZrO_2.

Based on costs estimates for fuel fabrication, reprocessing and fuel and waste disposal, it was found that the final cost of PuH_2-$ZrH_{1.6}$ would only be ~1.2% lower than that of PuO_2-ZrO_2, not enough to justify the choice of this fuel based on this cost.

It is concluded that PuH_2-$ZrH_{1.6}$, while offering an only slightly smaller repository impact than PuO_2-ZrO_2 on most of the analyzed parameters, is the preferred choice from the perspective of proliferation resistance, featuring a smaller fissile fraction after 10 years of cooling and a higher plutonium specific neutron emission. The cost difference is likely not significant enough to justify the choice of one fuel type over the other.

If desired to transmute plutonium in a 2-tier system (i.e. recycle once in thermal reactors for Pu inventory reduction and subsequently recycle all the leftover TRU in fast reactors), the number of core-passes (i.e. total parallel cores or equivalently fewer cores used in series) required to eliminate the entire Pu inventory originally planned to be disposed of at the YMR would be ~300 in case of using CORAIL fuel assemblies, ~70 for conventional MOX and ~100 in case of inert matrix hydrides or oxides. This implies that CORAIL would not be a practical option for that purpose with the current LWR fleet. Inert matrixes would provide the greatest inventory reduction in one pass (see Table 2.32), leaving only 30% of the initial plutonium after the campaign, while the conventional MOX would leave 77% of the initial plutonium mass. Inert matrixes would also leave a substantially more proliferation resistant discharged stream. Between oxide and hydride inert matrixes, it was found that hydride leaves a more proliferation resistant discharged stream (Section 2.7.5), while no substantial difference on other parameters was observed. It is also noted that inert matrixes are most likely the cheapest Pu recycling options, since they allow reaching the typical cycle length in PWR with a smaller Pu loading,

thereby providing the largest amount of electricity generated per unit of reprocessed LWR spent fuel.

2.9 References

[1] F. Ganda and E. Greenspan, "Plutonium Incineration Capability of Hydride Versus MOX Fuel in PWR", Proceedings of GLOBAL'05, Tsukuba, Japan, 2005.

[2] F. Ganda and E. Greenspan, "Physics Analysis of Hydride Fuel in PWR Cores," Submitted to Nuclear Science and Engineering, 2009.

[3] G. Youinou and A. Vasile, "Plutonium Multirecycling in Standard PWRs Loaded with Evolutionary Fuels", Nuclear Science and Engineering: 151, 25-45, 2005.

[4] F. Ganda, M. Milosevic, T. Taiwo and E. Greenspan, "TRITON/NEWT Calculation of the CORAIL Assembly for Plutonium Recycling in PWR", Joint International Topical Meeting on Mathematics & Computation and Supercomputing in Nuclear Applications MC2007, Monterey, California, 2007.

[5] M.D. DeHart, "TRITON: A Two Dimensional Depletion Sequence for Characterization of Spent Nuclear Fuel", Nuclear science and technology division (94), Oak Ridge National Laboratory, 2005.

[6] M.D. DeHart, "NEWT: a New Transport Algorithm for Two-Dimensional Discrete Ordinates Analysis in Non-Orthogonal Geometries", Nuclear science and technology division (94), Oak Ridge National Laboratory, 2005.

[7] D. Hamrin et al., "SCALE-5: A Modular Code System for Performing Standardized Computer Analyses for Licensing Evaluation", Oak Ridge National Laboratory Radiation Safety Information Computational Center Computer Code Package COO725, 2004.

[8] O.W. Hermann, and C.V. Parks, "SAS2H: A Coupled One-Dimensional Depletion and Shielding Analysis Module", NUREG-CR-0200, Rev. 6, Vol. 1, Section 2, Oak Ridge National Laboratory, 1998.

[9] T.K. Kim et al., "Benchmark Comparisons of Deterministic and Monte Carlo Codes for a PWR Heterogeneous Assembly Design", PHYSOR, Chicago, Ill, April 25-29, 2004.

[10] SCALE Newsletter, Number 35, January2007.

[11] CORAIL benchmark specifications-03, internal communication, Nov 2003.

[12] O. Bringer et al., "Detailed studies of Minor Actinide Transmutation-Incineration in High-Intensity Neutron Fluxes", PHYSOR-2006, Vancouver, BC, Canada, September 10-14, 2006.

[13] Nuclear Energy Agency, "Physics of Plutonium Recycling," Vol. II, OECD, Paris, 1995.

[14] E. Shwageraus, P. Hejzlar and M.S. Kazimi, "Feasibility of Multirecycling of Pu and MA in PWRs Using Combined Non-Fertile and UO_2 (CONFU) Fuel. Proc. GLOBAL'03, New Orleans, LA, 2003.

[15] E. Shwageraus, P. Hejzlar and M.S. Kazimi, "Use of Thorium for Transmutation of Plutonium and Minor Actinides in PWRs", Nuclear Technology, 147, 2004.

[16] E. Shwageraus, P. Hejzlar and M.S. Kazimi, "A Combined Non-fertile and UO_2 PWR Fuel Assembly for Actinide Waste Minimization," Nuclear Technology, Volume 149, Number 3, Pages 281-303, 2005.

[17] F. Ganda, D. Barnes and E. Greenspan, "OECD Benchmark A & B of MOX Fueled PWR Unit Cells using SAS2H," Proc. Int. Mtg. Mathematics and Computation – MC2005, Avignon, France, 2005.

[18] F. Ganda and E. Greenspan, "Plutonium Recycling in Hydride Fueled PWR Cores. Accepted for publication in Nuclear Engineering and Design, 2009.

[19] F. Ganda and E. Greenspan, "A Simplified Method for Multi-Batch PWR Core Analysis based on SAS2H Unit Cell Calculations," Proc. Int. Mtg. Mathematics and Computation – MC2005, Avignon, France, 2005.

[20] R.N. Hill et al., "Multiple Tier Fuel Cycle Studies for Waste Transmutation", ICONE-10-22575, Arlington, VA, April 14-18, 2002.

[21] C. Shuffler, J. Malen, P. Diller, F. Ganda, N. Todreas, E. Greenspan and B. Petrovic, "Economic analysis for PWRs" Accepted for publication in Nuclear Engineering and Design, 2009.

[22] F. Ganda and E. Greenspan, "Economic Analysis of Hydride-Fuelled BWR," Accepted for publication in Nuclear Engineering and Design, 2009.

[23] DOE RW 0533, 2001. Analysis of the total system life cycle cost of the civilian radioactive waste management program.

[24] M. Bunn, J.P. Holdren, S. Fetter and B. Van Der Zwaan, "The Economics of Reprocessing versus Direct Disposal of Spent Nuclear Fuel," Nuclear Technology, Vol. 150, June 2005.

[25] F. Ganda and E. Greenspan, "Neutronic Analysis of Hydride Fuelled PWR Cores". Accepted for publication in Nuclear Engineering and Design, 2009.

3. Thermal hydraulic analysis

This section is organized as follows:

- Section 3.1: objectives of the thermal hydraulic analysis;
- Section 3.2: reference plant;
- Section 3.3: fuel physical property database;
- Section 3.4: steady-state analysis;
- Section 3.5: Large Break Loss Of Coolant Accident (LBLOCA) analysis;
- Section 3.6: Main Steam Line Break (MSLB) analysis;
- Section 3.7: Complete Loss Of Coolant Accident (CLOFA) analysis;
- Section 3.8: conclusions;
- Appendix: the inverted core design.

While the first eight sections were part of the original project proposal, the appendix describes an innovative core design that was developed in parallel. Such design consists of hexagonal blocks of hydride fuel perforated with cooling channels. Although the investigation of this design was not part of the project scope requirement, a brief summary of the inverted core project is presented for completeness.

3.1 Objectives

The thermal hydraulic analysis was aimed at comparing the behavior of a PUZH-fueled PWR core with that of geometrically identical cores, but loaded with different assemblies, both during normal operation and during accident scenarios. These assemblies have the same geometry, but differ either because of the type of fuel with which they are loaded or because of the fuel arrangement in the lattice. The assemblies analyzed are the following:

- all-UO_2-assembly: the reference assembly; it uses UO_2 fuel pins only.
- CONFU-assembly: heterogeneous assembly made of standard UO_2 fuel pins and pins made of recycled transuranics in an inert matrix.
- CORAIL-assembly: heterogeneous assembly made of enriched UO_2 pins and MOX pins.
- PUZH-assembly: homogeneous assembly containing U-Pu-Th-$ZrH_{1.6}$ as fuel.

The corresponding cores are referred to as all-UO_2-, CONFU-, CORAIL- and PUZH-core. Their geometry is identical to that of the PWR core of Seabrook, which is the plant used as reference in the project. Key plant parameters are summarized in Table 3.1.

CONFU- and CORAIL- cores were analyzed since, like PUZH-core, are capable of recycling plutonium and Minor Actinides (MA). The all-UO_2-core, instead, cannot be used for that purpose but it was analyzed anyway for two reasons:

- the all-UO_2-core is the only core for which the behavior during normal operation and during accident scenarios is known. Plant response data found in [1] could therefore be used to benchmark the plant modeling technique used in this project;

- the safety margins characterizing the all-UO_2-core during various accident scenarios are known. They were used as metric of comparison of the core performance, in the sense that they were used to "rank" the core types examined against a core type, i.e. the Seabrook core, which has been licensed and is currently in operation.

3.2 Reference plant

The Seabrook plant, a Westinghouse 4-loop PWR, was used as reference plant for this project. Key plant parameters, referred to nominal operating conditions, are summarized in Table 3.1. While the geometry of the plant was kept fixed throughout the project, in some cases thermal hydraulic parameters used in the analyses deviated from those shown in the table, due to conservative margins, accident-specific, that were added in the modeling of steady-state and transient conditions. The new values are presented in the following sections whenever such margins are added.

Table 3.1 – Nominal parameters for the reference core[1]

Parameter	Unit	Value
Vessel		
Vessel inner diameter	m	4.394
Steam Generators		
Steam generator type		Westinghouse model F
Heat transfer area per SG	m^2	5109.7
Overall height	m	20.62 ([2])
Number of tubes per SG		5626
Tube outer diameter	mm	17.47
Tube inner diameter	mm	15.44
Tube pitch	mm	24.89 ([3])
Height of bundle	m	8.73 ([3])
Largest curvature radius for U-tubes	m	1.44 ([3])
Height of straight part of tubes (tubesheet excluded)	m	7.06 ([2])
Tubesheet thickness	m	0.539 ([3])
Inner diameter of SG main body (downcomer included)	m	3.59 ([2])
Inner diameter of SG secondary pool (downcomer excluded)	m	3.10 ([2])
Inner diameter of SG upper head	m	4.28 ([2])
Number of moisture separators per SG		16
Moisture separator height	m	3.13 ([2])
Moisture separator inner diameter (lower part)	m	~0.51 ([2])
Moisture separator inner diameter (upper part, inclusive of liquid return path)	m	~0.70 ([2])
Steam flow restrictor diameter at SG outlet nozzle	m	0.407
Main steam line inner diameter	m	0.703
Main Steam Line Isolation Valve (MSLIV) flow area	m^2	0.183
Length of main steam line between SG outlet nozzle and MSLIV	m	71
Steam flow per SG	kg/s	476.28

[1] All data are from [1] except otherwise specified.

Primary inlet temperature	ºC	325.7
Primary outlet temperature	ºC	292.6
Steam outlet temperature	ºC	284.8
Steam pressure	MPa	6.89
Feedwater temperature	ºC	226.67
Mass of each SG (dry)	kg	316154
Volume available for primary coolant in each SG	m^3	~27.3
Volume available for secondary coolant in each SG	m^3	~167.1
Weight of secondary coolant in each SG at HZP	kg	76205
Pressurizer		
Volume	m^3	50.97
Inner diameter	m	2.13
Core		
Active height	m	3.6576
Equivalent core diameter	m	3.3706
Pressure	MPa	15.513
Total primary flow rate	kg/s	18358
Effective flow rate for heat transfer	kg/s	17476
Core average mass flux	kg/s m^2	3675.4
Vessel inlet temperature	ºC	293.1
Vessel outlet temperature	ºC	325.7
Average void fraction in the hot subchannel	%	6
Maximum void fraction in the hot subchannel	%	20.6
UO_2 weight	kg	101034
Power		
Core thermal power	MW	3411
Average core power density	W/cm^3	104
Average Linear Heat Generation Rate (LHGR)	W/cm	178.6
Peak LHGR for normal operation	W/cm	446.2
Nuclear Enthalpy Rise Hot Channel Factor used in safety analyses		1.65
Total heat flux hot channel factor used in safety analyses		2.50
Assemblies		
Number of assemblies		193
Lattice type		17×17
Rods per assembly		264
Guide thimbles per assembly		24
Guide thimble inner/outer diameter (mm)	mm	11.430 / 12.243
Instrumentation tubes per assembly		1
Instrumentation tube inner/outer diameter (mm)	mm	11.379 / 12.294
Grids per assembly		8
Assembly side width	cm	21.40
Assembly pitch	cm	21.50
Total assembly length (nozzles included)	m	4.063
Fuel Rods		

Number of fuel rods in the core		50952
Active length	m	3.6576
Total rod length	m	3.8760
Fission gas plenum length	mm	188.7
Clad outer diameter	mm	9.500
Clad inner diameter	mm	8.357
Rod pitch	mm	12.6
Cladding thickness	mm	0.571
Cladding material		Zr alloy
Fuel-clad gap thickness	mm	0.0825
Pellet diameter	mm	8.19
Pellet height	mm	9.83
Form loss coefficients		
Bottom fuel nozzle		1.6992
Bottom grid spacer		0.389
Intermediate grid spacers		0.4822
Upper grid spacer		0.3834
Intermediate Flow Mixers		0.4154
Top fuel nozzle		0.5519

3.3 Fuel physical property database

Physical properties for PUZH fuel are not available in the literature. However, studies on similar fuels were performed by Prof. Yamawaki and Prof. Konashi and their colleagues, who measured the properties of U_x-Th_y-Zr_z-H_t fuels as a function of temperature. Even though these fuels do not contain plutonium, their physical properties can be considered reasonable estimates of PUZH properties. Among the fuels examined, $UTh_4Zr_{10}H_{27}$ was chosen to represent PUZH because, at the initial stage of the project:

- the optimized composition of PUZH was not known, and motivations based on chemical similarity could not be formulated;
- $UTh_4Zr_{10}H_{27}$ was the most documented fuel type within the U_x-Th_y-Zr_z-H_t family.

Density, thermal conductivity, specific heat and linear thermal expansion data are presented below.

3.3.1 Density

The correlation presented by Tsuchiya ([5]) for hydrogenated UTh_4Zr_{10} was used to get the density of UTh_4Zr10H_{27}:

$$\rho = 8440 - 29.9 \times t$$

where t is the ratio of H to U-Th_4-Zr_{10}. When applied to $UTh_4Zr_{10}H_{27}$, the formula gives a value of 7592.7 kg/m^3.

3.3.2 Thermal conductivity

Thermal conductivity of $UTh_4Zr_{10}H_{27}$ is shown in Figure 3.1.

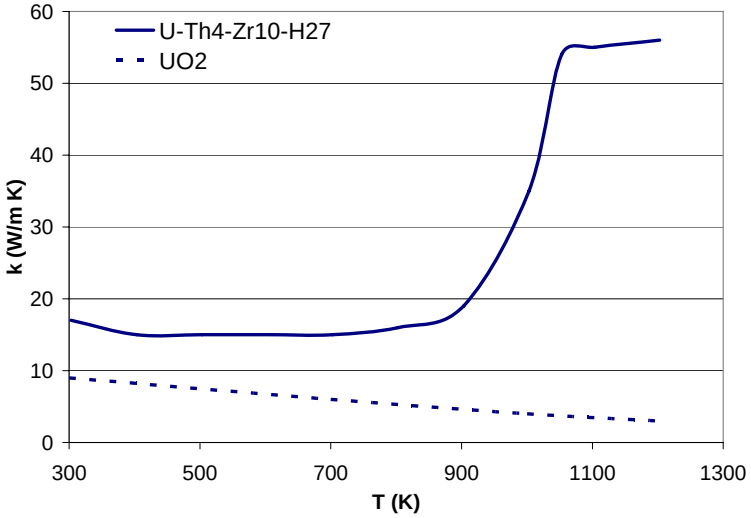

Figure 3.1 – $UTh_4Zr_{10}H_{27}$ thermal conductivity vs temperature ([5])

3.3.3 Specific heat

Specific heat of $UTh_4Zr_{10}H_{27}$ is shown in Figure 3.2.

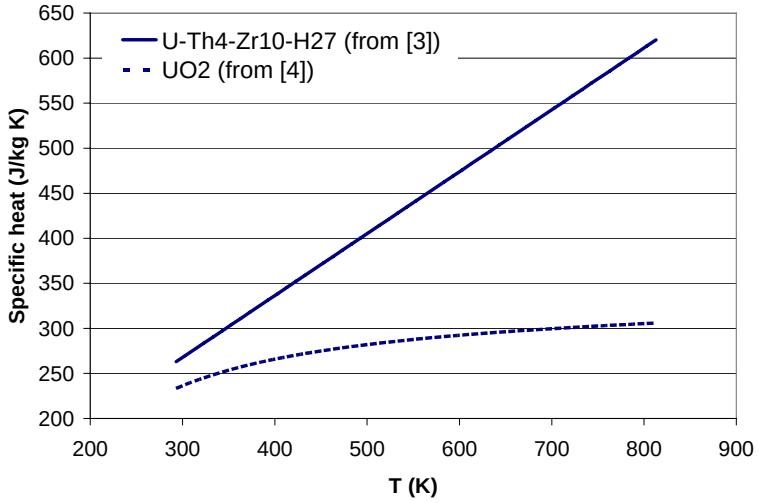

Figure 3.2 – $UTh_4Zr_{10}H_{27}$ specific heat vs temperature ([5], [6])

3.3.4 Linear thermal expansion coefficient

Linear thermal expansion coefficient of $UTh_4Zr_{10}H_{27}$ is shown in Figure 3.3.

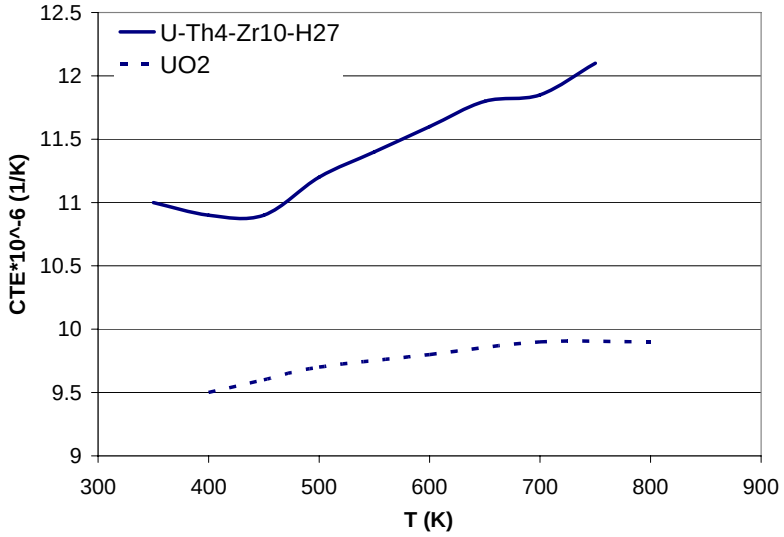

Figure 3.3 – $UTh_4Zr_{10}H_{27}$ coefficient of thermal exp. vs temperature ([4])

The discontinuity experienced by thermal conductivity of $UTh_4Zr_{10}H_{27}$ at about 900 K (Figure 3.1) is due to hydrogen release. In this regard it is important to note that after comparing ternary alloys (U-Th-Zr) to binary alloys (U-Zr, e.g. TRIGA fuel), Yamamoto stated: "*the ternary alloy can hold more hydrogen than U-Zr alloy at the same temperature. In other words, it can hold a certain amount of hydrogen at a higher temperature than the U-Zr alloy. This fact gives an attractive advantage if it is used as a nuclear fuel"* ([7]). From this observation, it can be concluded that PUZH fuel can operate at higher temperatures than the most well know hydride fuel, i.e. $U_{0.31}ZrH_{1.6}$, the latter being a binary hydride.

3.4 Steady-state analysis

3.4.1 Objectives of the analysis

The steady-state analysis was aimed at calculating the maximum steady-state power that a core can attain without breaching some thermal hydraulic constraints. The analysis was performed for each of the core types listed in Section 3.1, assumed to be at Beginning Of Life (BOL).

3.4.2 Code used and modeling approach

The steady-state analysis was performed using the VIPRE code ([8]). The main features of the code input file are:

- $1/8^{th}$ of the core was modeled, shown in Figure 3.4;
- the hot assembly was assumed to be located at the centre of the core (in red in Figure 3.4);
- the $1/8^{th}$ of core was modeled as composed by 6 pseudo-assemblies[2], identified with letters "a" to "f" in Figure 3.4:
  - $1/8^{th}$ of the hot assembly ("a" in Figure 3.4);
  - two halves of the two adjacent assemblies ("b" and "c" in Figure 3.4);

[2] The term "pseudo-assembly" is used to identify fractions of assemblies or multiple assemblies lumped together.

- a pseudo-assembly equivalent[3] to two assemblies ("d" in Figure 3.4);
- a pseudo-assembly equivalent to 7 assemblies ("e" in Figure 3.4);
- a pseudo-assembly equivalent to 14 assemblies ("f" in Figure 3.4);

The 1/8th fraction of the hot assembly was modeled in detail, i.e. by specifying geometry of each pin and subchannel, as well as the radial peaking factor of each pin. Pseudo-assemblies "b" through "f" were modeled using a lumping approach. The dashed lines shown in Figure 3.4, which do not have any correspondent meaning in the VIPRE model (because of lumping), indicate the location of the assemblies.

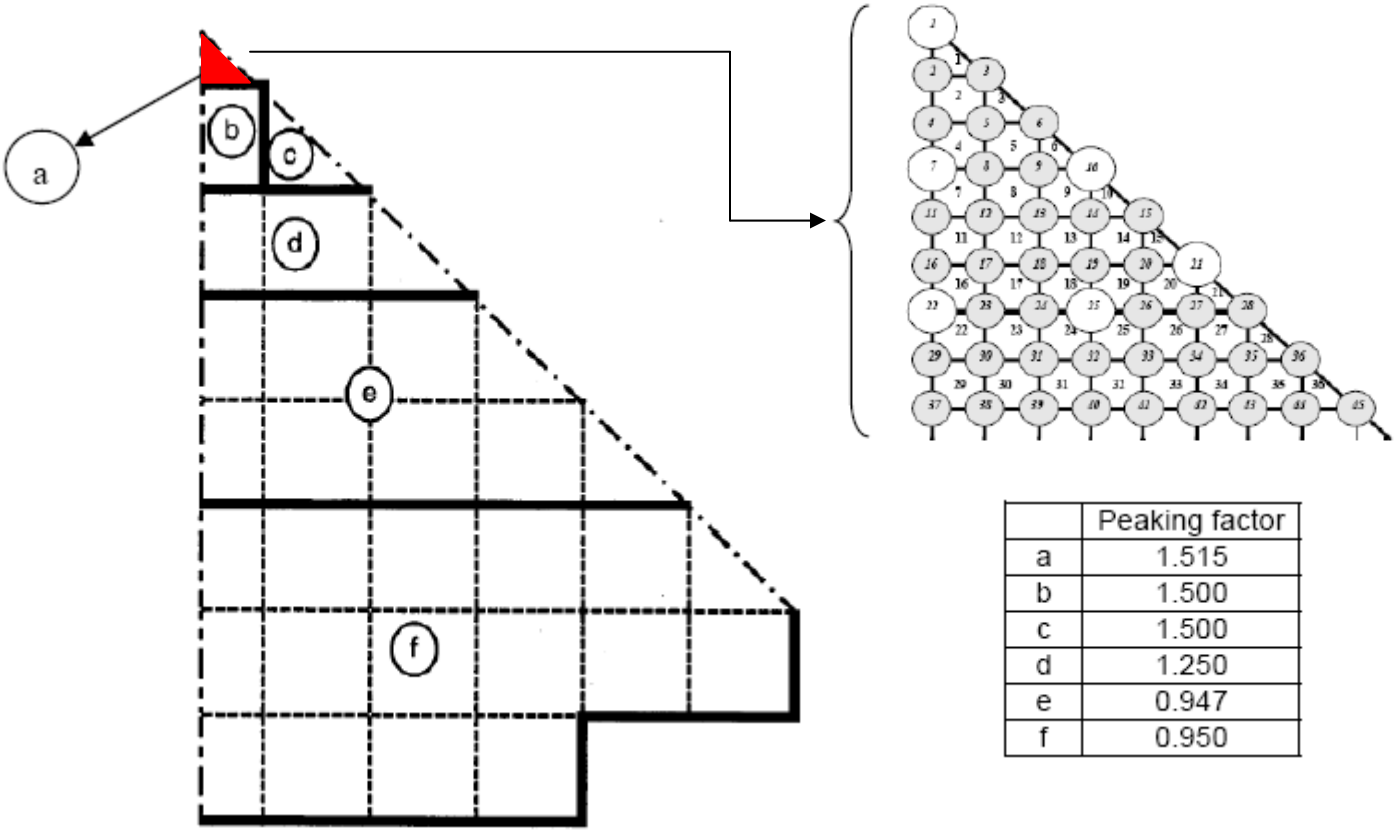

	Peaking factor
a	1.515
b	1.500
c	1.500
d	1.250
e	0.947
f	0.950

Figure 3.4 – Assembly lumping and radial peaking factors used in the steady-state analysis

The radial peaking factors corresponding to each pseudo-assembly are shown in Figure 3.4 and described in Section 3.4.4.

3.4.3 Thermal hydraulic constraints

The maximum attainable core power is defined as the maximum power that does not cause any of the thermal hydraulic constraints to be breached. These constraints are summarized in Table 3.2, and a brief description of each follows the table. The search for the maximum attainable

[3] Pseudo-assembly "d" is formed by 1 whole assembly and two halves of two separate assemblies. "Equivalent to two assemblies" means that the number of fuel rods, flow area etc. are equal to those characterizing two assemblies lumped together.

power is performed, for each core type, by increasing core power and coolant flow rate starting from low values, but maintaining their ratio fixed, till one[4] of the constraints is matched and none of the others is exceeded.

Table 3.2 – Thermal hydraulic constraints used in the steady-state analysis

Core type	MCHFR	Core pressure drop[5] (kPa)	Max. fuel T (ºC)	Max. fuel average T (ºC)	Max cladding surface T (ºC)	Core enthalpy rise (kJ/kg)
all-UO_2, CONFU and CORAIL	2.11	150	2805	1400	349	195
PUZH	2.11	150	850	Not applied	349	195

MCHFR (Minimum Critical Heat Flux Ratio): the limit value for this parameter was chosen using a reverse engineering approach, i.e. it is equal to the MCHFR calculated for the all-UO_2-core. The MCHFR limit ensures a margin from the critical heat transfer conditions.

Core pressure drop: again, a reverse engineering approach was used to fix the maximum allowed core pressure drop. The decision of not allowing the pressure drop to exceed the reference core value was made to avoid pump system upgrading. Should a higher pressure drop be allowed, a larger core power could be achieved, not only for PUZH but also for the other core designs.

Fuel temperature: for all-UO_2-, CONFU- and CORAIL-core, 2805°C and 1400°C are used to prevent fuel melting (2805ºC is the melting point of UO_2) and exceeding approximately 5% fission gas release ([9]). For PUZH, the temperature is limited to prevent excessive hydrogen release. The value of 850ºC was chosen as the temperature corresponding to the same hydrogen pressure as that characterizing U-$ZrH_{1.6}$ at 750ºC (~0.3 atm, [10]), which was the maximum allowed temperature fixed for U-$ZrH_{1.6}$ in the previous NERI project ([11]). Consistent with this data comparison, while comparing ternary alloys (U-Th-Zr, i.e. PUZH type) to binary alloys (U-Zr, i.e. TRIGA type) Yamamoto states: "*the ternary alloys can hold more hydrogen than U-Zr alloy at the same temperature. In other words, it can hold a certain amount of hydrogen at a higher temperature than the U-Zr alloy. This fact gives an attractive advantage if it is used as a nuclear fuel"* ([7]). The choice of the maximum allowed fuel temperature should account also for fission gas release. However, detailed investigations of this phenomenon for ternary hydrides have not been found in the public literature. So far, the only available source dealing with this phenomenon ([12]) discusses experiments performed on $UTh_4Zr_{10}H_{20}$ irradiated at low linear power (14 kW/m) and burnup of 1.1% FIMA (equivalent to about 17 GWD/ton), and states that: "*Released fission gas was not observed because of low burnup of pellet"*. For PUZH, the limit of 850ºC on maximum centerline temperature clearly prevents fuel melting.

Cladding surface temperature. 349°C was chosen to assure sufficient margin between the oxide corrosion layer thickness that unavoidably forms during steady state operation and the maximum oxide thickness allowed during LOCA severe accidents. According to the NRC Regulation 10 CFR 50.46, the maximum thickness shall nowhere exceed 17% of the total cladding thickness before oxidation.

[4] Actually, the status of the constraints when the maximum attainable power is reached is that two are matched: one among MCHFR, core pressure drop, maximum fuel temperature, maximum fuel average temperature and maximum cladding surface temperature, plus the core enthalpy rise. The latter, in fact, is kept constant throughout the analysis regardless of whether the core power is the maximum or a lower value.

[5] Core lower and upper plates excluded.

Core enthalpy rise. The value chosen is the core enthalpy rise for the reference core, under licensing conditions. This parameter is typically constrained to limit the temperature at the exit of the core, so that steam generator tube corrosion can be maintained within acceptable limits.

3.4.4 Analysis assumptions

The core types analyzed, i.e. all-UO_2-, CONFU-, CORAIL- and PUZH-core, have the same geometry, operating pressure, core inlet temperature, core enthalpy rise and coolant flow rate, which are fixed at the licensing values of the Seabrook Power Station ([1]). Table 3.3 summarizes the key assumptions that are common to all the core types analyzed. The geometric parameters, also common to all the core types, are shown in Table 3.1. Particularly, Table 3.3 highlights the difference between the nominal values (from Table 3.1) and the licensing values actually used in the steady-state analysis. Consistent with practice in Safety Analyses (Chapter 15 of [1]), the thermal hydraulic conditions of the analyzed cores are obtained by applying a conservative margin to the normal operation values.

Table 3.3 – Licensing values used for steady-state analysis (common to all the core types)

Parameter	Nominal values	Licensing values
Operating conditions		
Pressure (MPa)	15.513	15.513
Core inlet temperature (ºC)	293.1	296.3
Power and flow rates		
Core thermal power (MW)	3411	3479
Coolant enthalpy rise across the core (kJ/kg)	191	195
Coolant flow rate through the core (flow between peripheral assemblies and baffle not included) (kg/s)	17843	17843
Percentage of coolant flowing through guide thimbles	2	2

Important parameters missing from Table 3.3 are those related to the power distribution inside the core. In fact, while it was reasonable to fix the parameters of Table 3.3 to the same values regardless of the core type under examination, parameters related to the power distribution should be core-specific. These parameters are:

- pin radial peaking factor F_{pin} – ratio between the power of the hottest pin and that of the average pin in the same assembly;
- assembly radial peaking factor $F_{assembly}$ – ratio between the power of the hottest assembly and that of the average assembly;
- pin axial peaking factor F_{axial} – ratio between the maximum linear power along the hottest pin and the average linear power in the same pin.

Actually, only F_{pin} was set to core-specific values. This is because for CONFU- and PUZH-core only 2D neutronic analyses, at assembly-level, have been performed, and neither whole core data nor axial data were available. Therefore, it was decided to fix $F_{assembly}$ and F_{axial} for all the core types to the licensing values typically used for UO_2-cores. Table 3.4 summarizes the values used for $F_{assembly}$, F_{pin} and F_{axial} in the steady-state analysis of the cores analyzed. Values of the enthalpy rise hot channel factor ($F_{\Delta H} = F_{assembly} \times F_{pin}$) and of the total peaking factor ($F_Q = F_{\Delta H} \times F_{axial}$) are also shown.

Table 3.4 – Power peaking factors used in the steady-state analysis					
	$F_{assembly}$	F_{pin}	F_{axial}	$F_{\Delta H}$	F_{Q}
All-UO_2	1.515	1.089	1.515 (chopped cosine)	1.650	2.500
CONFU	1.515	1.241	1.515 (chopped cosine)	1.880	2.848
CORAIL	1.515	1.152	1.515 (chopped cosine)	1.745	2.644
PUZH	1.515	1.083	1.515 (chopped cosine)	1.641	2.486

Besides that for the hot assembly, the radial peaking factors used for the pseudo-assemblies shown in Figure 3.4 were arbitrarily chosen[6], with the constraint of power normalization across the whole core. The intra-assembly radial power distributions used for the hot assembly in the steady-state analysis are instead shown in Figures 3.5 through 3.8. Together with the radial peaking factor corresponding to the hottest pin, F_{pin}, these figures also show the pin location at which the MCHFR is detected.

0								
1.035	0.972							
0.992	1.012	0.978						
0	1.002	1.054	0					
0.999	1.018	0.986	1.064	1.008				
1.050	0.985	1.022	1.018	***+1.089**	0			
0	1.059	1.008	0	1.012	1.034	0.940		
0.999	1.028	1.019	0.992	1.001	0.935	0.916	0.960	
1.003	1.007	1.003	0.995	0.987	0.971	0.962	0.960	0.918

***Hot Pin** **+ MCHFR**

Figure 3.5 – Intra-assembly pin peaking factors for all-UO_2, Fresh Assembly, BOL, w/IFBA ([1])

0								
0.980	0.460							
1.071	0.985	0.471						
0	1.136	1.116	0					
1.179	1.145	1.141	**+1.187**	1.160				
1.144	1.112	1.111	1.146	1.134	0			
0	1.031	1.020	0	0.997	0.931	0.808		
0.434	0.802	0.431	0.824	0.423	***1.241**	1.137	1.003	
1.141	1.170	1.151	1.168	1.086	1.021	0.985	0.958	0.965

UO_2 Pins | Gd Pins

FFF Pins

***Hot Pin** **+ MCHFR**

Figure 3.6 – Intra-assembly pin peaking factors for CONFU, Recycle 01, BOL, w/Gd_2O_3 ([13])

[6] It was demonstrated that the radial peaking factors assumed for the assemblies surrounding the hot assembly do not appreciably affect the MCHFR of the core.

0							UO_2 Pins	
+*1.152	1.117							
1.147	1.111	1.104					MOX Pins	
0	1.133	1.130	0					
1.116	1.081	1.075	1.104	1.066			*Hot Pin	+ MCHFR
1.076	1.044	1.038	1.064	1.045	0			
0	1.012	1.004	0	0.962	0.876	0.747		
0.898	0.869	0.861	0.867	0.793	1.062	0.927	0.825	
1.120	1.111	1.098	1.081	1.014	0.911	0.839	0.803	0.811

Figure 3.7 – Intra-assembly pin peaking factors for CORAIL, Recycle 01, BOL, 8% Pu, 600 ppm B ([14])

0								
1.041	0.987							
1.039	0.985	0.982						
0	1.046	1.045	0					
1.040	0.985	0.985	1.056	1.026			*Hot Pin	+ MCHFR
1.042	0.988	0.988	1.062	*+1.083	0			
0	1.040	1.041	0	1.066	1.040	0.958		
1.030	0.978	0.976	1.035	0.975	0.949	0.930	0.926	
0.968	0.970	0.966	0.972	0.964	0.956	0.949	0.955	0.987

Figure 3.8 – Intra-assembly pin peaking factors for PUZH, Fresh Assembly, BOL, Recycle 01 (calculated in this project)

3.4.5 Results

The core configurations (core type plus operating conditions) characterized by the maximum attainable power are summarized in Table 3.5, together with the relevant results derived from the steady-state analysis. The cells containing the thermal hydraulic constraints are highlighted in grey.

Table 3.5 – Maximum attainable power comparison

	Units	All-UO2-core	CONFU-core	CORAIL-core	PUZH-core
Total peaking factor (F_Q)		2.5	2.848	2.644	2.486
Assembly radial peaking factor		1.515	1.515	1.515	1.515
Max. intra-assembly pin peaking factor		1.089	1.241	1.152	1.083
Axial peaking factor		1.515	1.515	1.515	1.515
MCHFR		2.11	2.11	2.11	2.11
Max. fuel temperature	ºC	2070	1799	1772	805
Max. average fuel temperature	ºC	1321	1161	1145	751
Max. pellet surface temperature	ºC	685	653	635	684
Max. cladding inside temperature	ºC	402	397	394	402
Max. average cladding temperature	ºC	374	372	370	374
Max. cladding outside temperature	ºC	348.5	348.4	348	348
Core pressure drop (Core plates excluded)	kPa	149.8	105.7	107.9	150.3

Max. subchannel exit quality	%	0.3	1.1	4.0	0.4
Hot assembly exit quality (subch. averaged)	%	0.09	0.19	0.74	0.10
Max. subchannel exit void fraction	%	1.88	6.27	19.66	2.56
Hot assembly exit void fraction (subch. averaged)	%	0.51	1.12	4.24	0.59
Core thermal power	**MW**	**3479**	**2761**	**2801**	**3487**
Core power difference percentage with respect to all-UO_2-core		**0**	**-20.6**	**-19.5**	**+0.2**

3.4.6 Conclusions

The most important conclusions arising from the steady-state analysis are:

- while CONFU and CORAIL can reach only about 80% of the power attainable by the all-UO_2-core, PUZH-core can operate at 100% of that power without exceeding any thermal hydraulic limit. This is due to the homogeneity of the fuel lattice, which yields a flatter intra-assembly power distribution.
- The weakness of PUZH, i.e. the inability to operate safely above 850ºC, is not the limiting constraint since the thermal conductivity assumed for this fuel, which is about 80% higher than that of UO_2 ([5]), prevents the fuel centerline temperature from reaching the 850ºC limit.
- The MCHFR is the limiting parameter for all the core configurations.

It must be pointed out that the first conclusion above is a consequence of having imposed, to all the core types, the same MCHFR limit. However, the licensing of reactors different from typical all-UO_2 reactors, aimed at plutonium-MA recycling other than electricity generation, may be performed using different safety limits than those applied to all-UO_2 reactors. If, for example, the MCHFR limit was reduced, CONFU- and CORAIL-core would be able to reach higher power levels than those shown in Table 3.5.

3.5 Large Break LOCA analysis

3.5.1 General event description

A Loss Of Coolant Accident (LOCA) is defined as a condition IV event, i.e. an event whose occurrence is not expected during the life of a plant, but that is however postulated since it may yield the release of significant amount of radioactive material. It is the result of a pipe rupture of the Reactor Coolant System (RCS) pressure boundary: if the rupture total cross-sectional area is equal or greater than 1 ft^2 the scenario is typically referred to as LBLOCA.

The LBLOCA analyzed here consists of a double-ended guillotine break of a cold leg, located between the RCS pump and the vessel inlet nozzle. The transient following the break occurrence can be divided in three consecutive phases:

- blowdown: it is the phase immediately after the break, characterized by a rapid depressurization of the RCS. Lasting about 10-30 seconds, this phase can be further divided in two subphases: an ultra-rapid cooling of the fuel rods, through forced convection caused by coolant flowing upward in the core and being released from the break, followed by a fuel rod isolation phase, during which fuel rods are practically

thermally isolated since only steam is left in the vessel. Core power is at decay power levels because of the large negative reactivity insertion due to coolant loss and vaporization.

- Refill: the Emergency Core Cooling System (ECCS) injects borated water into the RCS causing the vessel lower head and core lower plenum to be progressively filled with water. Fuel rod temperature in this phase increases monotonically.
- Reflood: the continuous water injection by the ECCS causes the liquid level to reach the bottom of the fuel rods which, because of their temperature higher than the Leidenfrost temperature, cause water to boil. Heat removal through boiling causes fuel rod temperature at the bottom of the core to progressively reduce, until it falls below the Leidenfrost value so that the rods, locally, can be quenched. The quenching front moves progressively upward both because of the cooling effect due to the steam released from lower axial locations and because of axial heat conduction, inside the rods, across the quenching front. During the reflood phase, cladding temperature at any axial location tends to increase and then, once the rod is quenched locally, decrease.

The maximum cladding temperature during the transient, typically reached during reflood, is referred to as Peak Cladding Temperature (PCT).

While that discussed above is the description of a general LBLOCA event, the description of the event actually analyzed requires specifying several assumptions made, both boundary conditions (mainly from the specifications dictated by Chapter 15 of any PWR Safety Analysis Report) and simplifying assumptions made to reasonably model the event accounting for the available computational tools. Such assumptions are presented in Section 3.5.4 and 3.5.5.

3.5.2 Objectives of the analysis

The analysis modeled the occurrence of a Large Break Loss Of Coolant Accident (LBLOCA) at the Seabrook plant, in which the core was assumed to be, alternatively, of all-UO_2-, CONFU-, CORAIL- or PUZH-type. The objectives of the analysis were:

- verify whether a steady-state core power of 3479 MW_t yields a PCT above the limit value established by 10CFR50.46, i.e. 2200ºF (1478 K), at any time during the LBLOCA;
- compare the PCT of the different core types during the LBLOCA.

As done in the steady-state analysis, the characteristics of the plant used for the LBLOCA analysis reflect those of Seabrook Power Station ([1]). Geometry of the plant (core included) and out-of-core thermal hydraulic parameters are summarized in Table 3.1. Table 3.6 shows instead the thermal hydraulic parameters used for the core.

3.5.3 Code used and modeling approach

The LBLOCA analysis was entirely performed using RELAP-3D version 2.3.6 ([15]).
The RELAP analysis consisted of two runs for each core type: a steady-state run aimed at finding the thermal hydraulic conditions characterizing the plant in the pre-accident state, and a transient run which actually modeled the LBLOCA starting from the state obtained through the steady-state run.

The plant nodalization implemented in the RELAP files is shown in Figure 3.9. It is worth noting that:

a) the break assumed was a double ended guillotine break located in the cold leg between the primary pump discharge and the vessel inlet nozzle;

b) the three intact loops are lumped together, while the broken loop is modeled separately;

c) the axial modeling of the core was performed using 16 axial zones: the bottom and the top zones are 45.3 cm long each, while the remaining 14 zones are 22.6 cm long each. The heated part of the core includes all the 14 central zones plus a fraction of the two outermost ones;

d) the radial modeling of the core consisted of three channels:

   - channel 335 represents the hot channel (hot assembly). Its flow area does not include the flow area of the guide thimbles, which however contribute in terms of wetted perimeter;
   - channel 333 represents the remaining 192 channels lumped together (193 are the assemblies contained in the core). Again, its flow area does not include the guide thimble flow area, while the region between the peripheral assemblies and the core baffle is included;
   - channel 320 contains the fraction of coolant that, after flowing down through the downcomer, bypasses the core by going through the guide thimbles and between the core baffle and the barrel;

e) other than the 2.5% of total primary flow bypassing the core through channel 320, about 2% of the same flow bypasses the core by flowing directly from the vessel inlet to the vessel outlet nozzle, and by going from the vessel inlet nozzle to the vessel head to cool it;

f) two heat structures are embedded in channel 335: the hottest pin and a dummy rod representing the remaining 263 rods contained in the hot assembly. Therefore, even though the subchannel-level modeling performed with VIPRE for the steady-state analysis (see Sections 3.4.2 and 3.4.4) was undoubtedly more detailed than the lumping approach used in RELAP, an hot pin is however modeled[7]. Mixing is allowed between channel 333 and channel 335.

[7] The good accuracy of the core thermal hydraulic model was proved by the MCHFR calculated by RELAP, which was only 10% larger than that predicted by VIPRE.

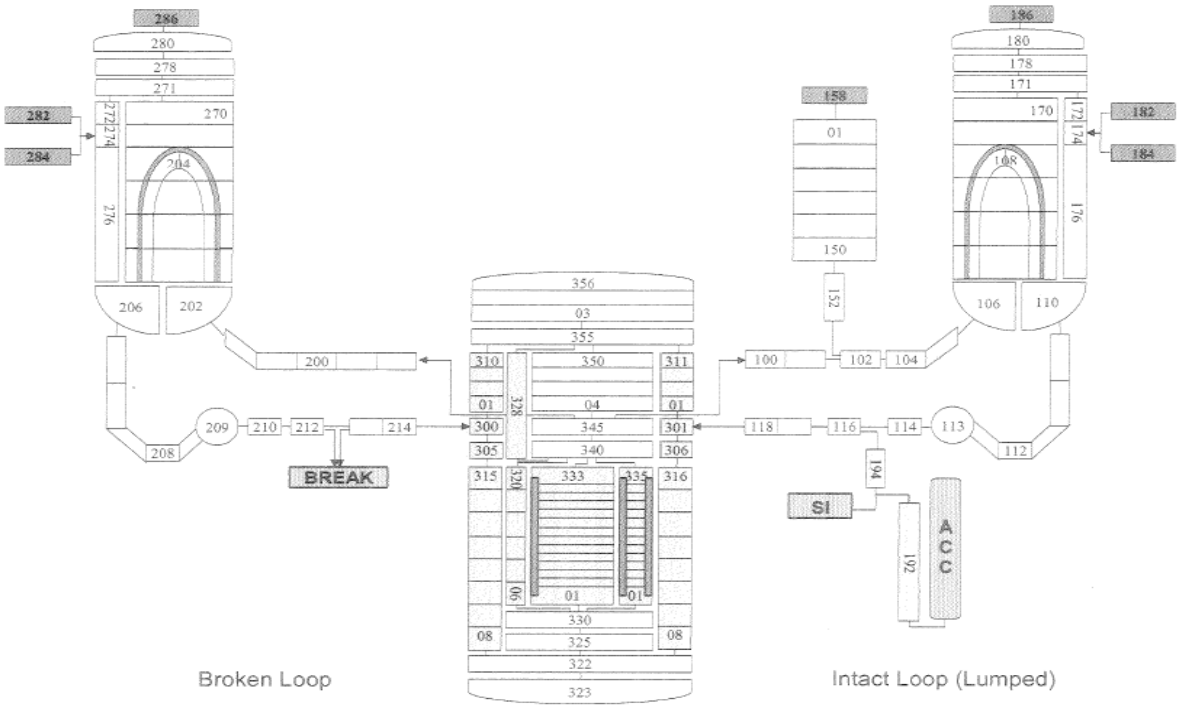

Figure 3.9 – RELAP plant nodalization used for LBLOCA analysis

3.5.4 RELAP model for steady-state

Table 3.6 shows the thermal hydraulic parameters characterizing the steady-state for the cores analyzed. Contrary to the methodology followed in the steady-state analysis, where a crucial parameter like the coolant flow rate through the core was input explicitly in the VIPRE input file, the more extended plant modeling performed with RELAP does not allow directly entering this flow rate, which is instead a consequence of the input primary pump characteristics and of the input form losses that are encountered by the coolant while flowing from the inlet to the outlet vessel nozzle. For this reason, for some of the key thermal hydraulic parameters used for transient initialization, Table 3.6 shows both the desired value (from [1]) and the simulated value. The agreement is quite good. Parameters for which the desired value is not displayed are input directly, and therefore it is understood that the simulated value coincides with the desired one. In order to highlight the conservatism implemented in the analysis, the nominal value of each variable is also shown.

Table 3.6 – Steady-state key thermal hydraulic parameters used for LBLOCA initialization, common to all core types

	Units	Nominal	Simulated
Operating conditions			
Core pressure	MPa	15.513	15.513 (desired) 15.709 (simulated)
Coolant temperature at core inlet	ºC	293.1	296.3 (desired) 296.4 (simulated)
Average coolant temperature at core outlet	ºC	326.2	329.3 (desired) 328.2 (simulated)
Power and flow rates			

Core thermal power	MW	3411	3479
Axial peaking factor		~1.40	1.515 (chopped cosine) and 1.515 (peaked at ~2.8 m)
Total primary circuit coolant flow rate	kg/s	18358	18358 (desired) 18363 (simulated)
Active flow rate through the core (guide thimble flow is not included, but flow between peripheral assemblies and baffle is included)	kg/s	17568	17568 (desired) 17558 (simulated)
Core bypass flow, contribution 1 (guide thimble flow + flow between baffle and barrel)	kg/s	448	448 (desired) 465 (simulated)
Core bypass flow, contribution 2 (flow from vessel inlet nozzle to outlet nozzle + flow from the inlet nozzle to the vessel head)	kg/s	342	342 (desired) 340 (simulated)
Plant geometry		See Table 3.1	See Table 3.1

As indicated in Table 3.6, the LBLOCA analysis considers two possible steady states to initialize the transient: one characterized by a typical chopped cosine axial power shape, which makes the power distribution in the core identical to that assumed in the steady-state analysis (Section 3.4), and one characterized by a top-skewed axial power shape. The choice of adding this last case was consistent with the LBLOCA analysis methodology described in Chapter 15 of [1], which states that the most limiting axial power profile for LBLOCA transient initialization is an 8.5-foot top-skewed profile. However, since reference [1] does not provide any graphic representation of this profile, the profile adopted in this analysis derives from [16]; it is peaked at about 9.2 feet (2.80 m) (see Figure 3.10). Although such a power profile is unusual for a PWR at steady-state, its adoption has been found to be very frequent in LBLOCA analyses. However, as mentioned in [17], "*this shape corresponds to a transient power condition that would not be sustained long enough for decay heat to assume this shape following trip*".

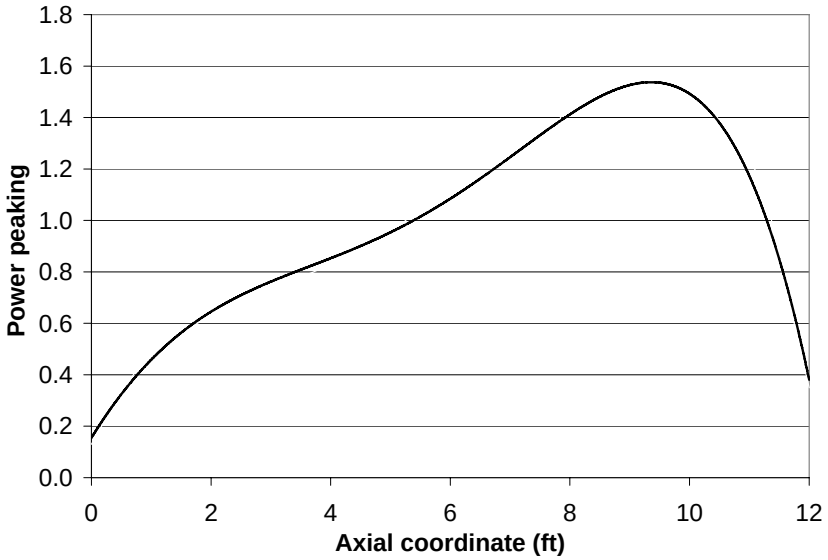

Figure 3.10 – Top-skewed axial power shape used, in addition to chopped-cosine, for LBLOCA transient initialization

The pin radial peaking factor F_{pin} and the assembly radial peaking factor $F_{assembly}$ entered in the REALP steady-state file were those assumed for the VIPRE steady-state analysis, which are shown in Table 3.4. These peaking factors, as well as the axial peaking factor, are assumed to remain constant during the whole transient scenario.

3.5.5 RELAP model for transient

The plant response to the LBLOCA event consists of a series of actions actuated with a certain delay time with respect to the first of the following two signals being detected:

- S1 (low pressurizer pressure): PRZ pressure drops below 1935 psia (13.34 MPa);
- S2 (low core flow): coolant flow rate at core inlet drops below 87% of the nominal value, i.e. below 15674 kg/s.

The protective actions are summarized in Table 3.7, together with the corresponding delay times which are consistent with those used in Chapter 15 of [1] for the LBLOCA analysis.

Table 3.7: Sequence of events following the occurrence of the break

	Delay with respect to S-signals (s), or actuation setpoint	Notes
Main Steam Line Isolation Valves start closing	2 s after S1 1 s after S2	5 s are needed for complete closure
RCP trip. Coastdown starts	2 s after S1	
Main Feedwater Isolation Valve start closing	2 s after S1	10 s are needed for complete closure
Auxiliary Feedwater Pumps start injecting	75 s after S1	
PRZ Power Operated Valves open	PRZ pressure > 2425 psia	They close after PRZ pressure has decreased below 2330 psia
Safety injection signal	31 s after PRZ pressure has dropped below 1867 psia	CCP, SIP and RHRP flow rates vary based on RCS pressure
Accumulators start injecting	Cold leg pressure < 600 psia	

Conservative assumptions that are also made to reduce the ECCS capability to mitigate the event are consistent with those used in Chapter 15 of [1]. They can be summarized as follows:

a) Reactor trip is not credited, i.e. control rods are assumed completely withdrawn during the whole transient.

b) Boron contained in ECCS water is not credited.

c) 1 out of 4 accumulators is not credited.

d) 1 out of 2 ECCS trains is assumed not available, i.e. 1 Centrifugal Charging Pump, 1 Safety Injection Pump and 1 Residual Heat Removal Pump are not credited. The capacity of the remaining train is 10% degraded.

In addition, the containment pressure variation assumed[8] during the LBLOCA corresponds to that of a transient in which the containment atmosphere cooling system is perfectly working. In this way, the backpressure is maintained quite low and the flow through the break, after the period when it is chocked, is higher. Figure 3.11 compares the containment pressure evolution assumed in the LBLOCA analysis to that used in [1] for containment design purposes. In spite of being different, they are both conservative since the ECCS cooling capability is challenged by a low backpressure, while the containment isolation is challenged by a high backpressure.

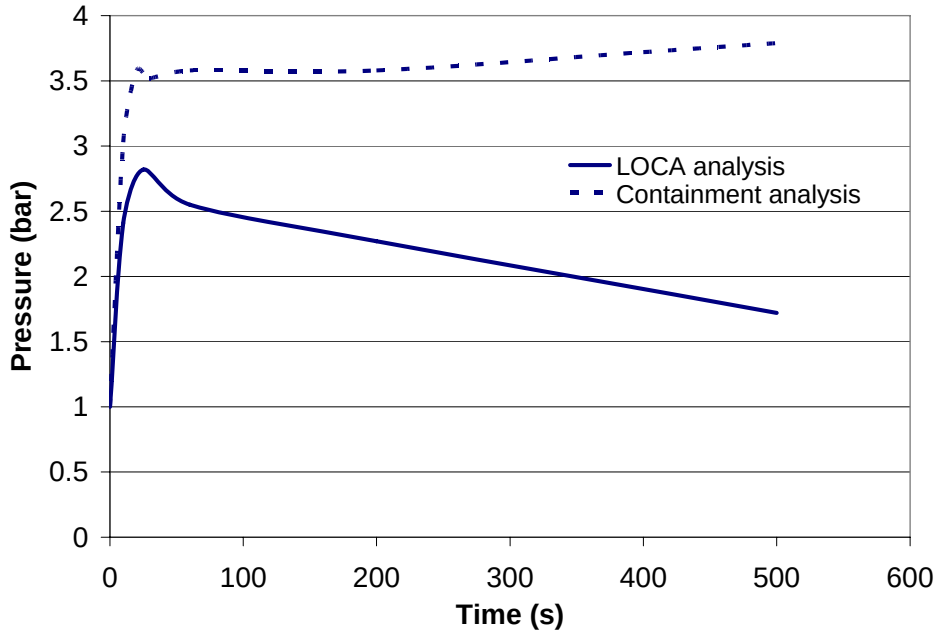

Figure 3.11 – Containment pressure evolution used for LOCA analysis compared to that used for containment design purposes

Technical specifications regarding the LBLOCA mitigation capability are shown in Table 3.8 and derive from [1].

[8] Since the containment atmosphere is not modeled explicitly but simply plays the role of a fixed boundary condition for the primary circuit after the break, the evolution of the containment backpressure is entered as input data.

Table 3.8 – Nominal and simulated ECCS capability to mitigate LOCA event ([1])			
	Units	**Nominal**	**Simulated**
Accumulators			
Number of units		4	3 (one is not credited)
Water volume in each unit	m^3	24.07	24.07
Nitrogen volume in each unit	m^3	14.16	14.16
Accumulator water temperature	ºC	38-65	52
Boron concentration	ppm	2600-2900	0 (boron not credited)
Injection pressure setpoint	MPa	4.83	4.14
Centrifugal Charging Pumps (CCPs)			
Number of units		2	1 (one is not credited)
Discharge head at shutoff	MPa	18.54	18.54
Discharge head at max flow rate	MPa	4.18	4.18
Max flow rate	m^3/s	0.03470	0.0312 (10% degraded)
High pressure Safety Injection Pumps (SIPs)			
Number of units		2	1 (one is not credited)
Discharge head at shutoff	MPa	10.60	10.60
Discharge head at max flow rate	MPa	5.08	5.08
Max flow rate	m^3/s	0.04164	0.03748 (10% degraded)
Residual Heat Removal Pumps (RHRPs)			
Number of units		2	1 (one is not credited)
Discharge head at shutoff	MPa	1.37	1.37
Discharge head at max flow rate	MPa	0.822	0.822
Max flow rate	m^3/s	0.2965	0.2668 (10% degraded)

3.5.6 Results

The output of the LOCA analysis consists of the time evolution of all the plant thermal hydraulic variables during the transient. In this section only the key parameters are shown, starting with "generic" plant variables like pressure, break flow, injected flow etc., and then focusing on the limiting variable for LBLOCA transients, i.e. the Peak Cladding Temperature (PCT). While the time evolution of the "generic" parameters is the same regardless of the type of fuel and of the axial power profile, PCT evolution depends both on the fuel and on the axial power profile assumed for the analysis.

In all the plots the break occurs at time t_0= 5 seconds.

3.5.6.1 Time evolution of "generic" plant parameters

The following plots show the time variation of several thermal hydraulic plant variables, most of which are referred to the primary system. Since they are very well known in the context of LOCA analysis and do not contain any atypical feature, they are not discussed further.

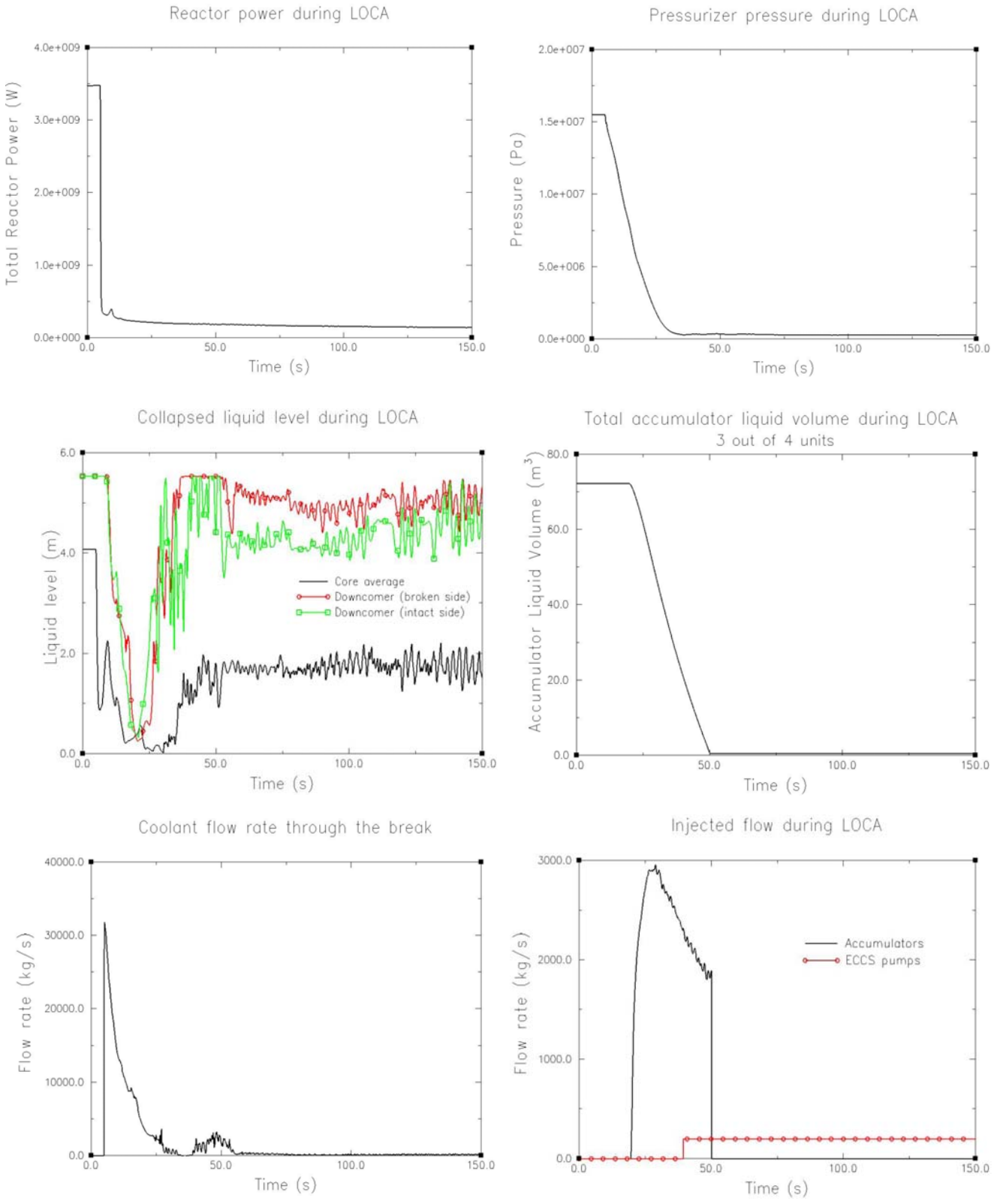

Figure 3.12 – Evolution of some plant parameters during LBLOCA (same for all core types)

3.5.6.2 PCT time evolution

The PCT has been found to depend on the assumed axial power profile (chopped cosine vs top skewed) only in terms of the shape of the curve PCT-vs-time and in terms of the axial location at which the maximum PCT is reached. The difference in numerical values between the axial power shapes investigated is instead quite small. Likewise, the fuel composition similarities between all-UO_2-, CONFU- and CORAIL-assembly cause the corresponding PCT profiles to be substantially the same, with only small differences of the order of 20ºC. For these reasons, regarding these assemblies, only for all-UO_2 and CONFU the PCT-vs-time plots are shown below (Figures 3.13 and 3.14). Figure 3.15 presents PUZH results.

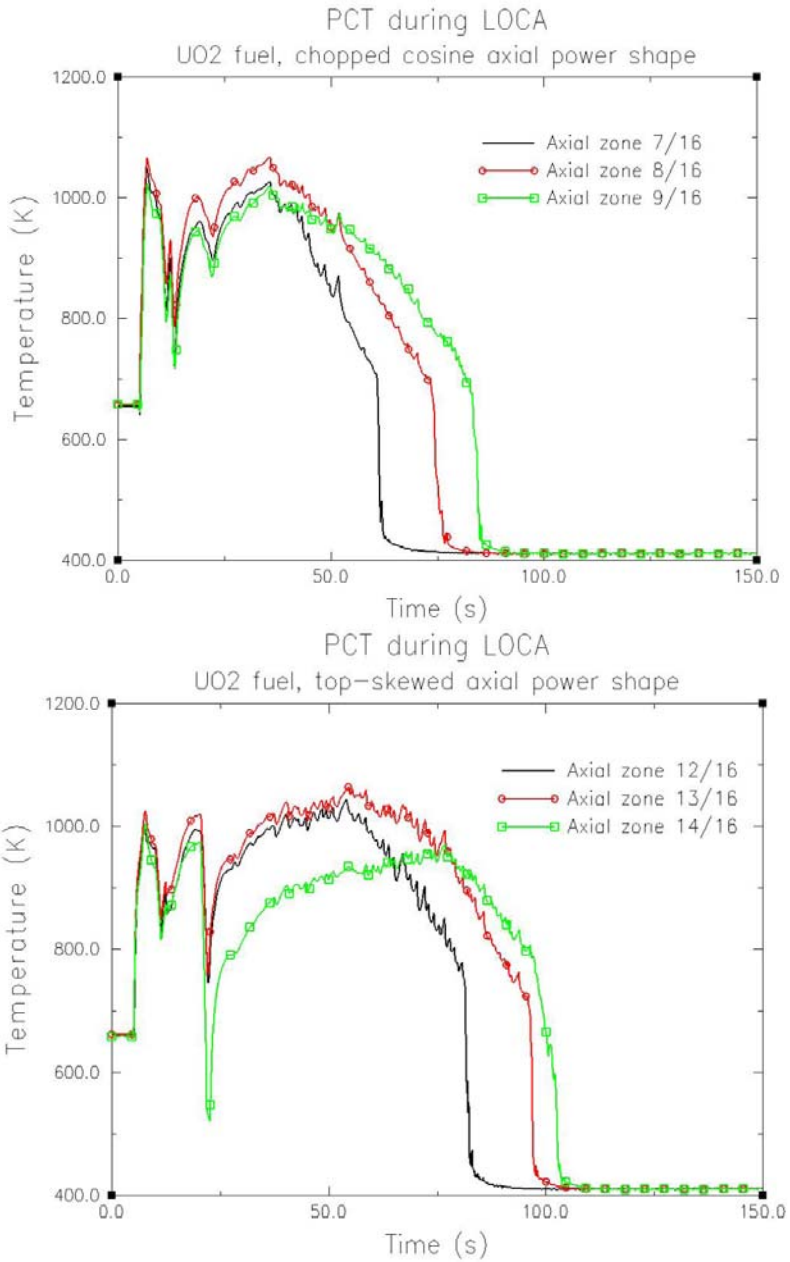

Figure 3.13 – Peak cladding temperature behavior for all-UO_2-core, for alternate axial power shapes. Steady-state core power: 3479 MW_t

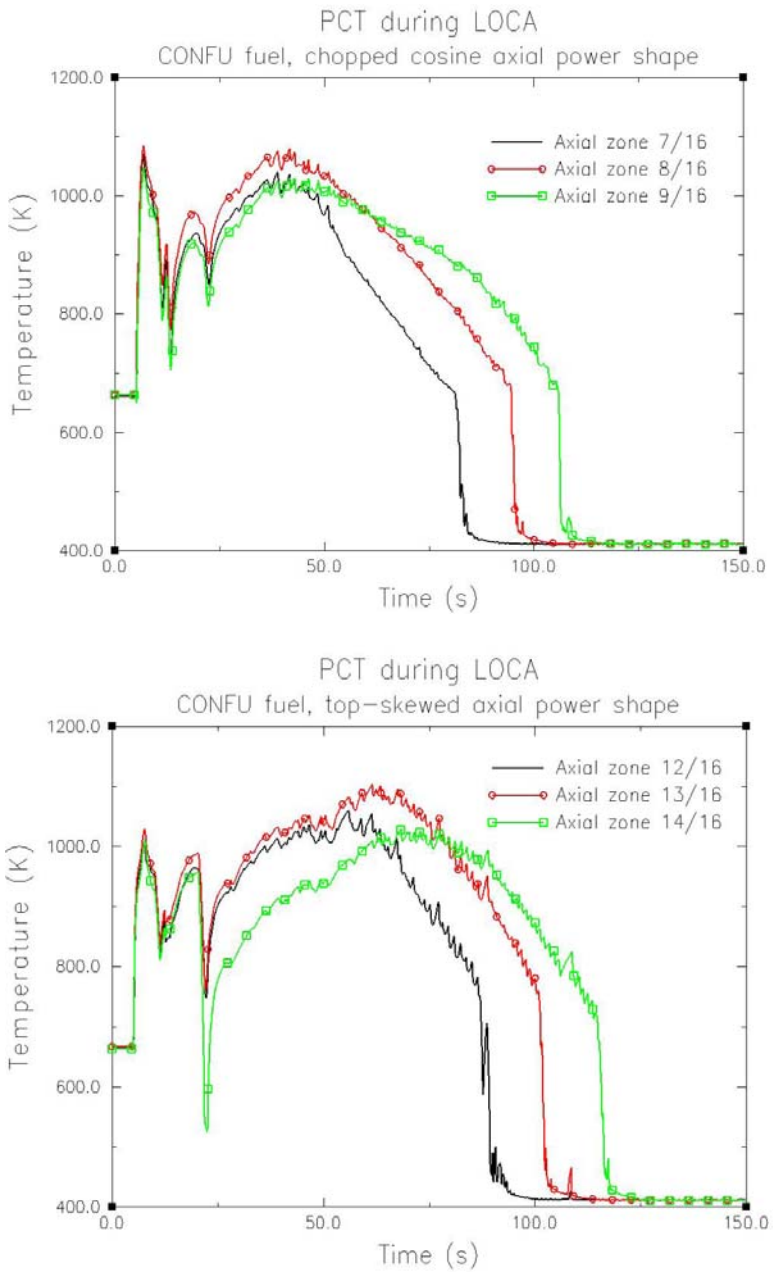

Figure 3.14 – Peak cladding temperature behavior for CONFU-core, for alternate axial power shapes. Steady-state core power: 3479 MW_t

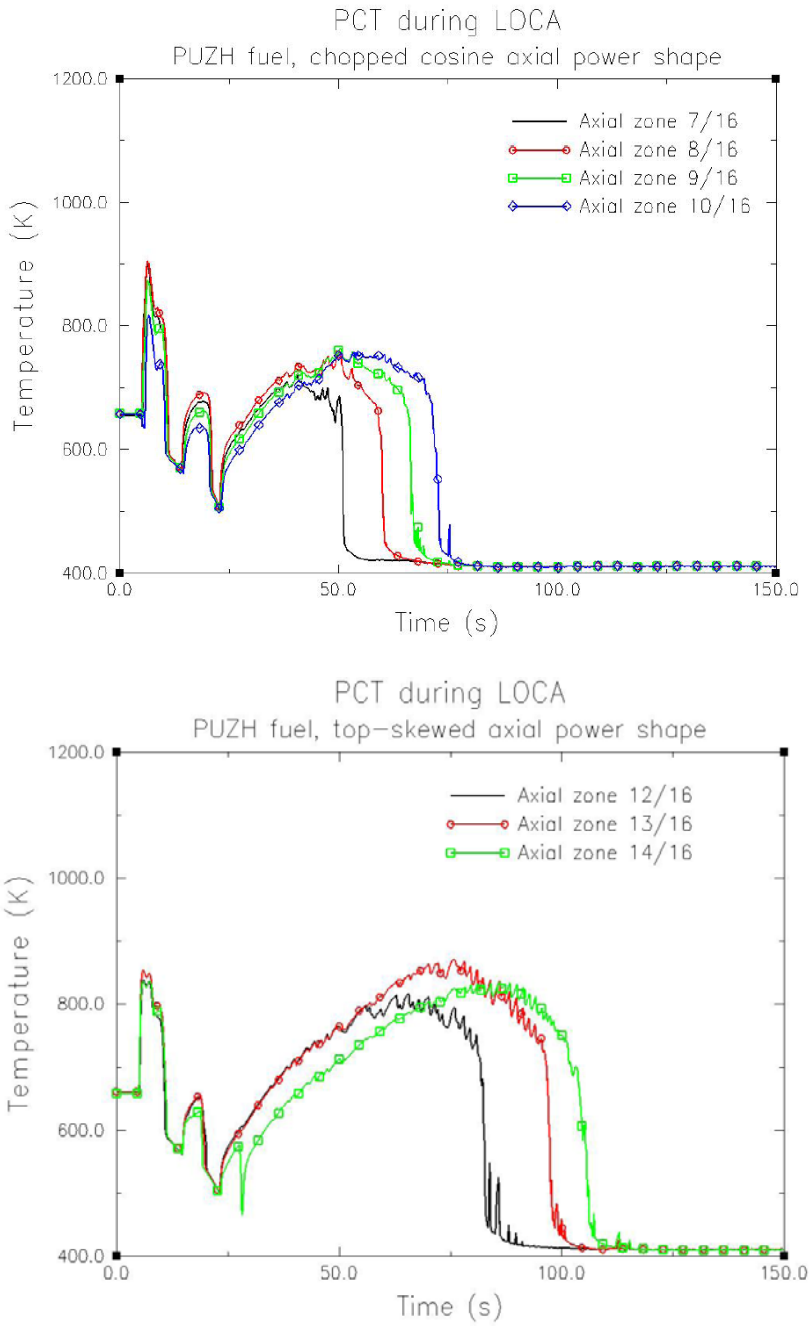

Figure 3.15 – Peak cladding temperature behavior for PUZH-core, for alternate axial power shapes. Steady-state core power: 3479 MW_t

Table 3.9 summarizes the maximum PCTs reached during blowdown and reflood phases by the assemblies investigated.

Table 3.9 – Summary of the maximum PCTs reached during LBLOCA (K)								
	All-UO_2-core		CONFU-core		CORAIL-core		PUZH-core	
Phase	Cosine	Top-skewed	Cosine	Top-skewed	Cosine	Top-skewed	Cosine	Top-skewed
Blowdown	1067	1026	1084	1029	1096	1052	906	854
Refill-reflood	1068	1066	1081	1104	1135	1117	759	872

3.5.7 Conclusions

The most important conclusions arising from the LBLOCA analysis are:

a) the 1478 K cladding temperature limit established by 10CFR50.46 is never reached by any of the assemblies investigated;

b) the maximum PCT for PUZH-core is much lower than those of the reference fuels. The reference fuels yield maximum PCTs between 1068 and 1135 K for both the axial power profile assumed for the core; after blowdown, the maximum PCT for PUZH-core is 759 K and 872 K for chopped cosine and top-skewed power profile respectively. The lower temperatures for PUZH-core are due to its higher thermal conductivity, which causes the maximum steady-state fuel centerline temperature to be about 1000 K lower than that of the other core types.

3.6 Main Steam Line Break analysis

3.6.1 General event description

A major Main Steam Line Break (MSLB) is defined as a condition IV event, i.e. an event whose occurrence is not expected during the life of a plant, but that is however postulated since it may yield the release of significant amount of radioactive material. In fact, the break causes a rapid depressurization of the secondary side and an increase in steam flow rate through the Steam Generator (SG) nozzles with a consequent overcooling of the RCS. Because of the negative moderator temperature reactivity coefficient, the reduction in primary coolant temperature results in reactivity insertion and, depending on the initial conditions, an increase in core power or, if the reactor was in shutdown at the time of break occurrence, in a possible return to criticality. In both cases Departure from Nucleate Boiling (DNB) may occur locally, with consequent fuel pin failure. The overcooling caused by the break is not radially uniform in the core, but is more significant in the sector which receives water mostly from the loop affected by the break. Control rod insertion and borated water injection by the Emergency Core Cooling System (ECCS) are aimed at preventing/limiting the power excursion.

While that discussed above is the description of a general MSLB event, the description of the MSLB event analyzed in this project requires specifying several assumptions made, which are both boundary conditions (mainly from the specifications dictated by Chapter 15 of any PWR Safety Analysis Report) and simplifying assumptions made to reasonably model the event accounting for the available computational tools. These assumptions are presented in Section 3.6.4.

3.6.2 Objectives of the analysis

The MSLB analysis was performed for the Seabrook plant ([1]) in which, alternatively, the core was assumed to be loaded with all-UO_2-, CONFU-, CORAIL- and PUZH-assemblies. The case of the all-UO_2-core was mainly used to validate the plant modeling technique, by comparing the results obtained with those given in [1]. The analysis of the other three core types was aimed at comparing their thermal hydraulic behavior during a MSLB, particularly the Minimum Critical Heat Flux Ratio (MCHFR) reached during the transient.

3.6.3 Code used and modeling approach

The analysis was performed using RELAP-3D ([15]) and VIPRE ([8]). RELAP was used to model the plant (primary and secondary circuits) response upon MSLB. Output data from RELAP were then used as input in VIPRE for a more detailed analysis of the core. This was done to better capture the core thermal hydraulics since the core model in the VIPRE input file was much more detailed than that in the RELAP input file.
The plant nodalization contained in the RELAP input file is shown in Figure 3.16. Important observations about such nodalization are as follows:

- the three intact loops are lumped together while the faulted loop is modeled individually.
- The secondary side is modeled up to the Main Steam Line Isolation Valves (MSLIVs, components 186 and 286 in Figure 3.16), i.e. all the components downstream the MSLIVs (common steam header, turbine etc.) are not modeled.
- The active core (in yellow in Figure 3.16) is modeled as composed of two channels and three Heat Structures (HS, not shown in Figure 3.16). Channel 333 lumps the subchannels contained in the $3/4^{th}$ core fraction fed mainly by the three intact SGs, while channel 335 lumps the subchannels contained in the $1/4^{th}$ core fraction mainly fed by the faulted SG. The three HSs are: HS1 represents the hot assembly (assumed to face channel 335), which is modeled by lumping all its rods; HS2 represents 47 assemblies lumped together, facing channel 335; HS3 represents 145 assemblies lumped together and facing channel 333.
- The valves marked in black (906 and 908) are used to model the break occurrence. During Hot Zero Power (HZP)-steady-state[9] they are fully closed and the path that would be followed by steam, in case it was produced in the SGs, is that through the MSLIVs 186 and 286. At time t = 5 s the break occurs and it is modeled by instantly opening valves 905 and 908. Starting from this time, the faulted SG blows down completely while the intact SGs depressurize only slightly since valve 906 closes upon MSL low-low pressure signal detection[10].

[9] The MSLB is assumed to occur when the plant is in HZP conditions: see Section 3.6.4 for details.
[10] For ease of programming, the modeling of the partial depressurization of the intact SGs upon MSLB is performed by using valve 906, which replaces the function of MSLIV 186 after break occurrence, i.e. at $t \geq 5s$. In fact, in spite of being open, during HZP-steady-state valve 906 does not affect the pre-accident scenario since valve 908 is closed and volume 907 is very small. Thus, the steam free path in the lumped loops is through MSL 185 and MSLIV 186. However, starting from t=5s:
- valve 905 and 908 open instantly (break occurs);
- valve 186 and 286 close instantly;
- 2 seconds after the low-low pressure signal in MSL 285 is generated, valve 906 starts to close, and take 6 seconds to complete closure. The closure of valve 906 stops the depressurization of the intact loops.

- Complete coolant mixing is assumed to occur both in the vessel lower plenum and in the vessel upper plenum[11].

- For ease of visualization, the nodalization of the SG boiling regions (components 170 and 270) and of the SG U-tubes (components 108 and 204) are shown with fewer subvolumes than those actually used in the RELAP plant model. Volumes 170 and 270 are divided in 13 axial subvolumes (instead of the six shown), while volumes 108 and 240 are divided in 22 subvolumes (from U-tube inlet to U-tube outlet).

After running RELAP, the time evolution of:

- total core power;
- coolant temperature and half flow rate at the inlet of channel 335;
- pressure at the inlet of channel 335;

are used as input for a detailed modeling, performed with the VIPRE code, of $1/8^{th}$ of the core. This core fraction was modeled in the same way as in the steady-state analysis discussed in Section 3.4. In particular, the core modeling (except for the peaking factors) was the same as that shown in Figure 3.4, which therefore reproduces half of channel 335 of the RELAP model, including half of HS2 and $1/8^{th}$ of HS1. As shown in Figure 3.4, the red region, which represents $1/8^{th}$ of HS1 plus the corresponding subchannels, was analyzed via subchannel mode, i.e. single rods and subchannels are modeled explicitly. In this way it was possible to accurately monitor the thermal-hydraulics of the hot assembly and particularly to predict the Minimum Critical Heat Flux Ratio (MCHFR).

[11] The importance of this assumption for the present analysis is not significant since coupling between neutronics and thermal hydraulic is not performed (see Section 3.6.4.5). It is instead a key assumption in any MSLB analysis modeling spatial coupling since the coolant mixing in the vessel lower plenum significantly influences the power distribution among the different sectors of the core. If no mixing is assumed to occur, the temperature at the inlet of the fourth of the core fed mostly by the faulted loop will be the same as that of the coolant entering the vessel through the "faulted" cold leg, which is the lowest temperature in the RCS during a MSLB. As a consequence, the power peaking corresponding to that fraction of the core will be very high. The prediction of whether this is the most conservative scenario is however not easy. In fact, while on one hand the power peaking corresponding to that sector of the core is overestimated, on the other the coolant temperature at the inlet of that sector is underestimated. In terms of MCHFR these two factors act in opposite directions since the high power has a detrimental effect while the low coolant temperature is beneficial. For the present analysis, since the power spatial distribution in the core was simply assumed (see Section 3.6.3.5), the choice of a complete mixing in the lower plenum can be considered conservative: in fact, the coolant at the inlet of the sector of the core generating more power is relatively hotter than that obtainable by assuming an incomplete coolant mixing. It is worth mentioning that none of the Seabrook reference documents consulted describes the assumptions made for the coolant mixing in the vessel lower and upper plenum.

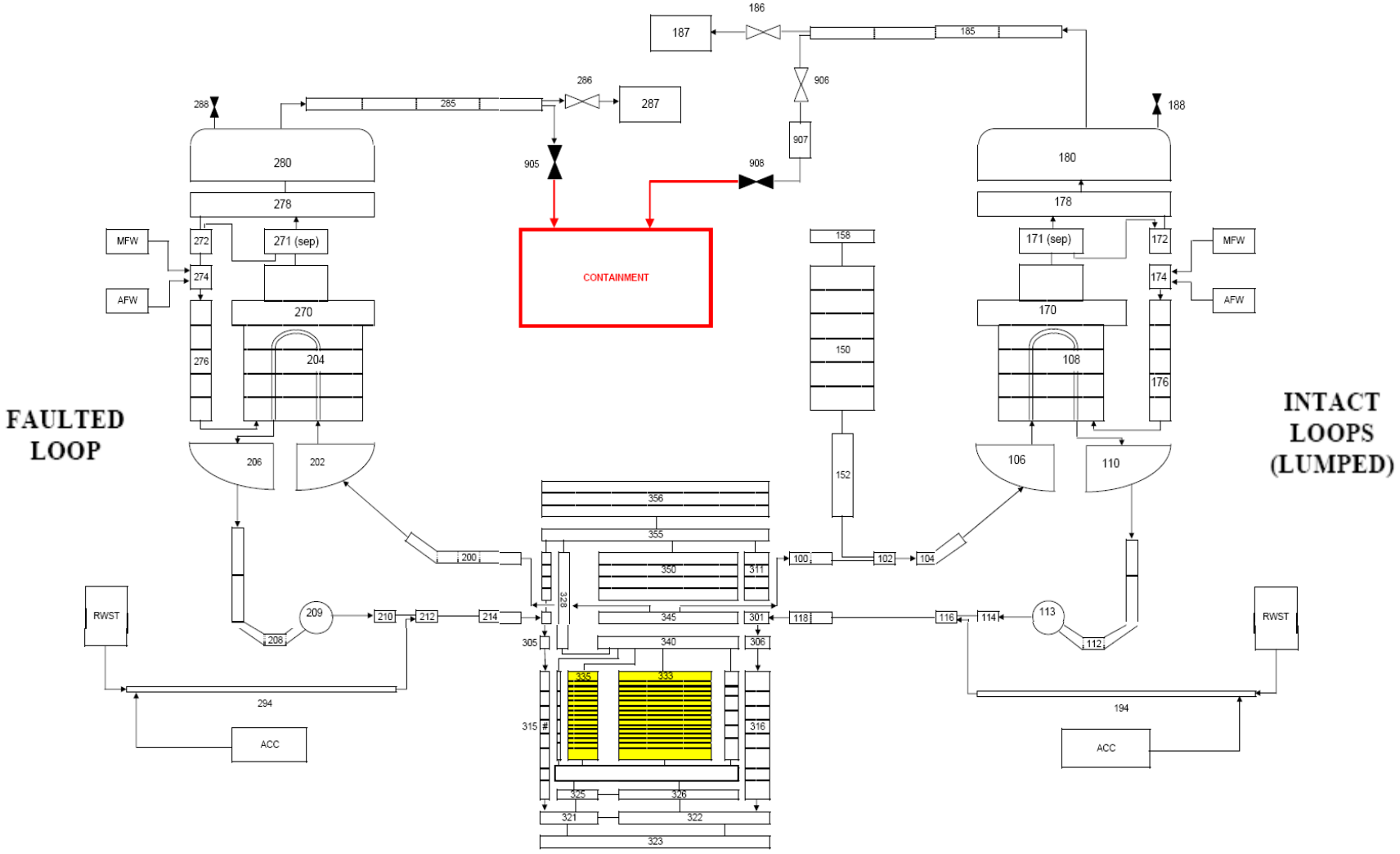

Figure 3.16 – RELAP-3D plant nodalization used for MSLB analysis

3.6.4 Detailed MSLB scenario description

The MSLB modeled in this study consists of a double-ended guillotine break of the Main Steam Line (MSL) that connects one of the four steam generators to the common steam header. The modeling of the whole scenario required several assumptions to be made, regarding both the status of the plant just before the accident occurrence (pre-accident assumptions) and the performance and timing of the various plant components that change their operational status upon MSLB (post-accident assumptions). Some assumptions are common to both the pre-accident and the post-accident condition (whole-scenario assumptions). Consistent with the common practice in safety analyses, conservative assumptions are made, i.e. they tend to overestimate the reactivity insertion and to underestimate the performance of the control and shutdown systems. Pre-accident, whole-scenario and post-accident assumptions are qualitatively described below. Assumptions on the reactivity coefficients and on the power distribution in the core are exceptions to this grouping: in spite of being post-scenario assumptions they are discussed in separate sections for clarity.

Table 3.11 summarizes the quantitative aspects of the assumptions made. Unless otherwise specified, the assumptions are from Section 15.1.5 of [1].

3.6.4.1 Pre-accident assumptions

1) The core pre-accident condition is Hot Zero Power (HZP) at End Of Cycle (EOC). All the control rods are fully inserted, except for the most reactive bank which is conservatively assumed to be stuck in its fully withdrawn position during the whole transient. The pre-accident shutdown margin is -1.3 % $\Delta k/k$ for all the cores analyzed ([19]). The combination HZP+EOC+stuck control bank is the worst scenario for the MSLB accident since RCS overcooling is maximized. In fact:
    - at HZP the secondary coolant inventory in each SG is maximum (~55% larger than that during Hot Full Power (HFP));
    - at HZP the RCS and the fuel contain less stored energy than that characterizing the system at reactor shutdown following operation at full power. If the pre-accident condition was HFP, the reactor would be tripped by overpower protection system and the additional stored energy characterizing this shutdown condition (with respect to that, lower, at HZP) would be removed via the cooldown caused by the MSLB before the no-load RCS temperature assumed in the present analysis is reached;
    - at EOC the delayed neutron fraction is the smallest, i.e. 0.0044 vs 0.0075 ([19]) characteristic of Beginning of Cycle (BOC); this clearly yields maximum neutronic feedback upon MSLB;
    - at EOC no boron is contained in the RCS;
    - because of the harder neutron spectrum characterizing the core at EOC, the injection of borated water into the RCS is less effective than at BOC.
2) The whole RCS is at a uniform temperature of 291.7 ºC.
3) The percentage of RCS flow not going through the core is assumed to be the same as that at HFP, i.e. ~5%. Reference [1], which refers this percentage to HFP, does not give the correspondent value at HZP.

4) Main Feedwater (MFW) flow to the SGs is zero, and no steam flows from the SG outlet nozzles[12].

3.6.4.2 Whole-scenario assumptions

1) RCS cooldown is maximized by neglecting decay heat and assuming offsite electric power available. Continued operation of the Reactor Coolant Pumps (RCPs) allows heat stored in the primary coolant to be removed through the secondary side.
2) Heat generated by RCPs is neglected. This assumption, in spite of not being mentioned in any of the literature sources consulted, was made for ease of plant modeling and to increase the extent of RCS cooling.
3) Containment pressure is 0.1 MPa ([20]). This is a conservative assumption since the actual containment pressure resulting from MSLB at HZP is much higher[13]: steam flow through the break is therefore maximized.
4) No SG tube plugging is assumed to maximize SG heat removal capability.

3.6.4.3 Post-accident assumptions

1) The break location is assumed to be just upstream the Main Steam Line Isolation Valve (MSLIV), so that MSLIV closure cannot prevent the faulted SG to blow down completely.
2) Spurious activation of the Auxiliary Feedwater (AFW) to the faulted SG is assumed to occur coincident with the postulated break and to be terminated by the operator after 30 minutes from the onset of the accident. AFW water is at a temperature of 10ºC and a flow rate of 145 kg/s.
3) Safety Injection Signal (SIS) is generated upon low-low pressure detection (3 MPa) in the affected Main Steam Line (MSL) ([19]).
4) A 2-second delay is assumed between SIS generation and actual SIS receipt by the plant control system. Upon SIS receipt:
    - MSLIV in the broken MSL starts closing; it takes 6 sec. to complete closure;
    - MSLIVs in the intact MSLs start closing and take 50 seconds to complete closure. In spite of the fact that [1] seems to assume same closure time for all the MSLIVs (6 s), the present analysis uses a longer time to artificially reproduce the partial blowdown of the unaffected SGs. The depressurization of the unaffected SGs resulting from using a closure time of 6 s was in fact found to be much less pronounced than that shown in [1].
    - Main Feedwater Isolation Valves (MFIVs) start closing and take 12 seconds to complete closure. Because of the depressurization of the secondary system, during the time interval between break occurrence and closure of the main feedwater lines MFW flow rate to all the SGs instantly increases from zero to 108% of the nominal value.

[12] In a real plant at HZP, MFW and steam flow rates are not zero. A small flow rate is in fact required in order to remove, from the primary coolant, the heat produced by fission product decay and by Reactor Coolant Pump (RCP) operation. In this analysis, however, these two heat sources are neglected and therefore pre-accident MFW and steam flow are both zero.

[13] Safety analysis of the containment assumes unavailability of one containment spray train. Under this assumption, a MSLB at HZP yields a containment peak pressure of about 0.35 MPa (chapter 6 of [1]).

- ECCS starts pumping borated water from the Refueling Water Storage Tank (RWST) into the RCS. Due to equipment delay and travel time through ECCS lines, 25 seconds are required for the borated water to actually reach the RCS.

5) ECCS performance is conservatively reduced by assuming the most restrictive single active failure, i.e. the unavailability of one of the two ECCS trains (one charging pump, one safety injection pump and one residual heat removal pump are assumed not working). The pumped[14] flow rate, as a function of the RCS pressure, is shown in Figure 3.17.

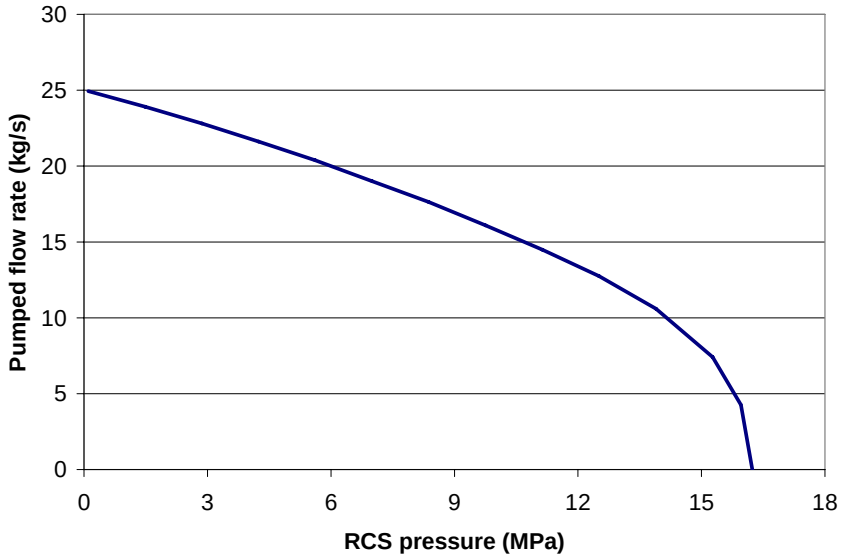

Figure 3.17 – ECCS flow performance assumed during MSLB ([21])

6) RWST water is assumed to be at 10ºC and to contain 2700 ppm of boron.

7) Accumulators are set to passively start injecting 2600 ppm borated water into the RCS when its pressure drops below 4.14 MPa ([1]). Water is injected at 0ºC ([19]).

3.6.3.4 Post-accident assumptions: reactivity coefficients

Common practice of safety analyses is to use conservative values of thermal hydraulic, neutronics and general plant parameters. As an example concerning reactivity coefficients, Table 4.3.2 of [1] provides two upper bounds for the rodded Moderator Density Coefficient (MDC) during the core life:

MDC≤ 28 pcm/(kg/m^3) (best estimate)

MDC≤ 50 pcm/(kg/m^3) (design limit)

For transients like the MSLB which requires, for conservatism, the use of the most positive MDC, reference [19] suggests using 54 pcm/(kg/m^3): a value much higher than the best estimate upper bound and even slightly higher than the design limit. Likewise, the delayed neutron fraction used for MSLB analysis of a typical UO_2-fueled PWR is 0.0044 ([1], [24]), which is more typical of discharged fuel than of core average EOC fuel (~0.0052, [25]). The present

[14] The term "pumped" is intentionally used to exclude the flow injected by accumulators.

analysis uses this conservative approach for all the input data not specifically associated with the type of fuel: valve closure times, safety injection flow rate, set-points for safety system actuation are examples of these parameters. Instead, the values chosen for reactivity coefficients and delayed neutron fractions are the best estimates calculated as part of this project or found in the open literature. This is because of two reasons:

- in spite of the well known temperature dependence of the reactivity coefficients, the reference documents (e.g. [1]) do not specify the dependence actually used in MSLB analysis. For example, reference [19] suggests using a MDC of 54 pcm/(kg/m^3) without however saying whether this coefficient is kept constant regardless of the coolant temperature or if a temperature dependence is instead implemented;
- a complete list of conservative estimates of plant parameters is available only for all-UO_2 cores; conversely, only best estimates are available for CONFU, CORAIL and PUZH assemblies.

Table 3.10 summarizes the reactivity coefficients, delayed neutron fraction (β) and boron worth (BW) used for the assembly types under consideration. All these values are referred to EOC conditions which correspond, in terms of core average burnup, to the value shown in the first to last row. Numerical values for which reference is not shown have been calculated in this project. The table is then followed by important considerations regarding the methodology used to determine the reactivity coefficients.

Table 3.10 – Neutronic parameters used in MSLB analysis

	All-UO_2	**CONFU**	**CORAIL**	**PUZH**
FTC (pcm/ºC)	-3.08 (Fig. 4.3-27 of [1])	-4.21	-5.17	-2.80
Rodded MTC (pcm/ºC)	-36.2 (Fig. 5-1 and 5-12 of [26])	-26.7	-31.0	-13.9
BW (pcm/ppm)	-9.2 (Fig. 5-20 of [26], consistent with Fig. 6.4.6 of [25])	-6.4 (Fig. 6.4.6 of [25])	-4.5 (Table VIII of [27]	-3.6
β	0.0052 (Fig. 5.4.1 of [25])	0.0048 (Fig. 5.4.1 of [25])	0.0041 (Table 4.3.I of [25])	0.0036
Rodded MDC (pcm/(kg/m^3))	24.2 (from MTC)	17.9 (from MTC)	20.8 (from MTC)	9.3 (from MTC)

Fuel Temperature Coefficient (FTC) and Moderator Temperature Coefficient (MTC): although the FTC and MTC vary with temperature, a single temperature-independent value was used for each of these coefficients and for each core type. The selection of these values was based on a common principle, regardless of the core type: the value selected is the one that, when assumed over the temperature ranges:

- 292-392ºC for the core average fuel temperature, for FTC;
- 292-230ºC for the coolant, for MTC;

gives approximately the same reactivity insertion as that actually due to temperature-dependent reactivity coefficients when coolant and/or fuel average temperature vary over the same temperature intervals[15]. The "sources" of data used to calculate what numerical value causes this

[15] The coolant temperature range used for MTC calculation, i.e. 292-230ºC, is a reasonable approximation of the RCS

condition to be met depends on whether the core is an all-UO_2-core or one of the remaining three. In fact, for the all-UO_2-core no neutronic analysis were performed, and the references shown in parentheses in Table 3.10 were used to calculate FTC and MTC. These references are in fact plots showing the reactivity coefficient variation with temperature, an example of which is shown in Figure 3.18. These plots were used to first calculate the reactivity insertion due to the mentioned temperature perturbations (from the HZP value of 292ºC) using the reactivity coefficient temperature dependence shown by the plot itself, and then the average FTC and MTC by dividing such reactivity insertions by the amplitude of the temperature perturbations. These average FTC and MTC are those shown in Table 3.10.

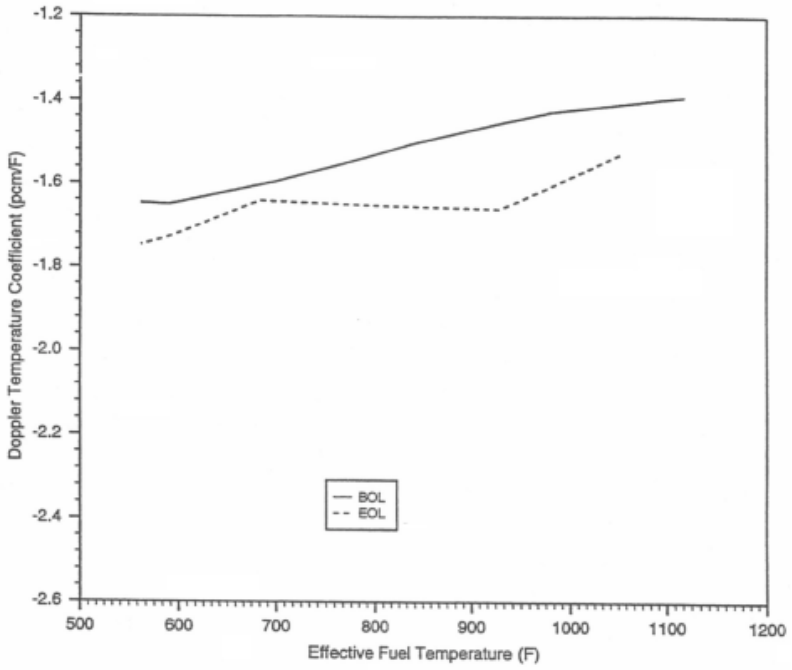

Figure 3.18 – Typical low leakage core design FTC vs fuel temperature ([1])

For the other core types, i.e. CONFU, CORAIL and PUZH, plots analogous to that shown in Figure 3.18 are not available. Therefore, the numerical values shown in Table 3.10 were obtained by running, for each assembly type a single assembly depletion analysis in which:

1) fuel and coolant temperature are separately perturbed by the amount previously mentioned (from 292 to 392ºC for the fuel, from 292 to 232ºC for the coolant) at three burnup values, corresponding to once burned, twice burned and discharged fuel;
2) the reactivity variations caused by the fuel temperature perturbation at the three burnup levels are calculated and averaged, thus obtaining a single reactivity variation $\Delta\rho_F$; the

overcooling occurring during MSLB, as shown in [1]. The choice of the fuel temperature perturbation, instead, was not based on data contained in the reference documents since they do not describe the core averaged fuel temperature variation occurring during MSLB. Therefore, since:

- FTC becomes less and less negative as the fuel temperature increases;
- MSLB safety analysis practice recommends using the most negative FTC and MTC ([19], [1]);

the temperature interval chosen is only 100ºC for conservativism. In this way, other than starting at a relatively low temperature (292ºC) the perturbed fuel temperature is itself quite low, guaranteeing a more negative FTC.

same is done for the reactivity variations due to coolant temperature perturbation, thus obtaining $\Delta\rho_C$;

3) the EOC equilibrium core FTC is calculated as $\Delta\rho_F/100$, while the EOC equilibrium core MTC is calculated as $\Delta\rho_C/60$; these are the values shown in Table 3.10.

The methodology summarized by means of points 1) through 3) was actually performed twice: one time for an assembly not having control rods inserted and a second time for an assembly in which control rods are inserted. In fact, an important consideration concerns the meaning of the word "Rodded", which is used in Table 3.10 both for MTC and for MDC. This term is important since the pre-accident steady state condition assumed for the MSLB analysis is HZP. For the present analysis the term "Rodded" is intended to refer to a situation in which Control Rod Banks C and D are fully inserted, while both Control Rod Banks A and B, as well as the Shutdown Banks, are withdrawn. This consideration is important since MTC becomes more and more negative as the number of control rods inserted increases (and consequently MDC becomes more and more positive). In fact, the insertion of control rods causes H/HM to decrease since they displace coolant. As a consequence, the operating point on the k_{eff} vs H/HM curve shifts to smaller H/HM, which is where the curve has a larger slope (negative). A larger (negative) slope means a more negative MTC. Unfortunately, reference documents ([19], [1]) do not specify how the EOC-HZP condition is achieved, i.e. how many control rods are actually inserted. Therefore, since graphs of Rodded MTC for the reference all-UO_2 core are available only for the cases:

- Control Rod Bank D inserted;
- Control Rod Banks C and D inserted;

it was decided to associate the Rodded MTC (and MDC) used to a situation in which Control Rod Banks C and D are inserted, while all the other banks are withdrawn. This assumption was extended to the other types of core, i.e. CONFU-, CORAIL- and PUZH-core, for which however average core Rodded MTC values can not be found in the public literature. Therefore, to account for control rod insertion, the depletion analyses mentioned above were performed not only for an assembly in which control rods are not inserted (leading to MTC_{out}) but also for an assembly in which control rods are inserted (leading to MTC_{in}). The EOC-HZP average core Rodded MTC was then determined by weighing MTC_{in} with the number of assemblies that are assumed to actually have control rods inserted (N_{in}), and MTC_{out} with the number of assemblies that do not (N_{out}). Since Control Rod Banks C and D have 8 and 5 control rods respectively ([1]), the EOC-HZP average core MTC shown in Table 3.10 was calculated as:

$$\text{Rodded MTC} = \frac{N_{in} \times MTC_{in} + N_{out} \times MTC_{out}}{193} = \frac{13 \times MTC_{in} + (193 - 13) \times MTC_{out}}{193}$$

At equilibrium EOC, MTC_{in} was found to be about 1.4 times MTC_{out}, while FTC_{in} was found to be about 0.7 times FTC_{out}.

Moderator Density Coefficient (MDC): the MDC shown in Table 3.10 is calculated by dividing the reactivity insertion due to the coolant temperature perturbation (obtained through the MTC) by the coolant density variation caused by the perturbation itself, calculated at a constant pressure of 15.513 MPa.

Boron Worth (BW) and delayed neutron fraction (β): BW and β are simply extracted from the references indicated in parentheses in Table 3.10.

3.6.4.5 Post-accident assumptions: power distribution

Although the total core power excursion upon MSLB is calculated by RELAP as a function of the RCS overcooling caused by the break, the power distribution among the four core sectors (corresponding to the four loops) is:

- uniform in the RELAP analysis, in order to be consistent with the 100% coolant mixing assumed in the vessel lower plenum;
- non-uniform in the VIPRE analysis, in order to account for the different degrees of overcooling affecting the four RCS loops. From the quantitative viewpoint, the radial power distribution used in the VIPRE analysis was assumed based on data found in the literature ([18]). In particular, the fourth of the core fed mostly by the faulted loop is assumed to generate half of the total core power, at any time during the transient. The hot assembly, which is assumed to be located in this sector of the core, is assumed to have a radial peaking factor of 4.25 (with respect to the core average assembly). For the VIPRE analysis, the radial power distribution in the core can therefore be expressed by means of the following assembly radial peaking factors:
    - hot assembly: 4.25;
    - 8 assemblies surrounding hot assembly: 3.8;
    - each of the remaining 47 assemblies located in the "affected" fourth of the core: 1.9095;
    - each of the 145 assemblies located in the "unaffected" sector of the core: 0.4731.

Both in the RELAP and in the VIPRE analysis:

- the pin-by-pin power distribution is uniform in all the assemblies[16]. This is consistent with a typical EOC power distribution;
- the axial power distribution, shown in Figure 3.19, is assumed to be top-peaked with a maximum peaking factor of 1.85. It has a peak of 1.85 and coincides with the mean of several core-averaged axial profiles obtained in the extensive benchmark analysis described in [18]. Consequence of this assumption is that the hot spot modeled in the final VIPRE analysis generates a linear power $4.25 \times 1.85 \times 1.0 = 7.86$ times higher than the core average linear power.

[16] Because of the lumping approach used in the RELAP model, i.e. single rods are lumped together, the uniform pin-by-pin power distribution was an input of the VIPRE model only.

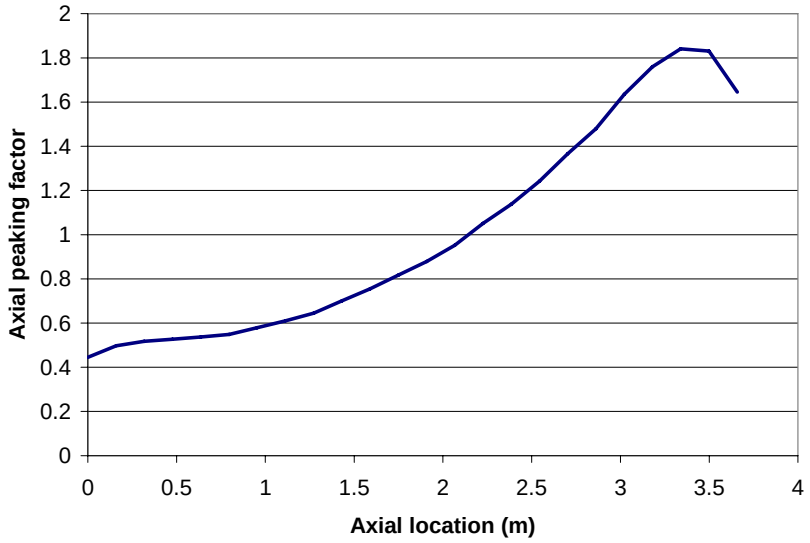

Figure 3.19 – Axial power profile assumed during the MSLB transient ([18])

Quantitative assumptions used for MSLB analysis are summarized in Table 3.11.

Table 3.11 – Quantitative assumptions made for MSLB scenario modeling

Parameter	Value[17]	Reference
Core and RCS		
Pressure in the vessel (MPa)	15.513	[1]
Primary coolant temperature (ºC)	291.7	[1]
Total coolant flow rate through RCS (kg/s)	17999 (17946)	Using volumetric flow from [19] and [28]
Active coolant flow rate through the core as % of RCS flow rate, at HFP (guide thimble flow not included)	95	[1]
Coolant flow rate through the core (kg/s)	17087	[1]
Delayed neutron fraction	See Table 3.10	
Shutdown margin	-1.3 % Δk/k	[1]
Reactivity coefficients	See Table 3.10	
Pin-by-pin power distribution	uniform	Assumed in this analysis
1/4th core sector power multiplier (ratio between power produced by the "affected" fourth of the core and the power that it would produce if power distribution was uniform through the core)	1 (RELAP) 2 (VIPRE)	Assumed in this analysis
Hot assembly radial peaking factor	1.0 (RELAP) 4.25 (VIPRE)	Assumed in this analysis
Axial peaking factor	1.85	Assumed in this analysis

[17] At EOC-HZP, unless otherwise specified.

Coolant mixing in vessel lower and upper plenum	100%	Assumed in this analysis
Secondary side		
Steam pressure in the SG dome (at HFP) (MPa)	6.895	[1]
Steam pressure in the SG dome (at HZP) (MPa)	7.543	Calculated to satisfy RCS temperature of 292ºC
Secondary coolant inventory per SG (kg)	76194 (76205)	[1], [21]
SG tube plugging	0%	[19]
AFW flow to faulted SG (kg/s)	144.8	[19]
Time of AFW actuation	At break occurrence	[19]
ECCS		
Steam line low-low pressure setpoint used for Safety Injection Signal (SIS) (MPa)	3	[19]
Delay between SIS and SIS reception (s)	2	[19]
Actions at SIS reception	MSLIVs and MFIVs start closing	[19]
MSLIV closure time (s)	6	[19]
Main feedwater valve closure time (s)	12	[19]
Delay between SIS reception and ECCS actuation (s)	25	[19]
RWST boron concentration (ppm)	2700	[1]
RWST water temperature (ºC)	10	[19]
Accumulator boron concentration	2600	[1]
Accumulator setpoint pressure (MPa)	4.14	[1]
Accumulator water temperature (ºC)	0	[19]
ECCS injection flow rate	Minimum flow (see Figure 3.17)	[21]
Miscellaneous		
Decay power (MW_t)	0	[1]
Containment pressure (MPa)	0.1 for the whole transient	[20]

3.6.5 Validation of the plant modeling technique

This section compares the results obtained for the reference all-UO_2-core with those presented, for the same core, in the reference documents ([1] and [19]). Even though the reactivity coefficients used are probably not the same as those used in the reference documents, the comparison is useful to verify the accuracy of the analysis and the correctness of the RELAP plant model. This comparison is made by means of plots showing the time variation of key plant parameters during the transient. In each figure, the plot on the left is that obtained here while that on the right derives from the reference documents (mainly [1] and [19]). It needs to be stated that while the present analysis assumes the MSLB to occur instantaneously at t = 5 s, the reference documents model the break as an instantaneous event occurring at t = 0 s. This does not affect the results, but only the way the two time scales need to be compared: a generic time instant *t'* on

the present analysis time-axis corresponds to the time instant *t'*+5 s on the reference document time-axis.

The first two sets of plots, presented in Figure 3.20, show the reactivity and power excursions resulting from the RCS overcooling occurring after MSLB. Even though the general trend is the same, some differences can be noted:

1) In spite of starting with approximately the same shutdown margin, i.e. -1.3% Δk/k equivalent to -2.5 $ in this analysis and -2.95 $ in the reference documents[18], the reactivity insertion calculated here is slower, with a consequent delay in return to criticality (after about 90 s here, after 20 s in the reference documents). This is probably due to two reasons:
    - the smaller MDC used: by assuming that the reactivity coefficients mentioned in the reference documents have been used as temperature independent parameters, the comparison of the MDCs would be: 24.2 pcm/(kg/m^3) in this analysis versus 54 pcm/(kg/m^3) in reference document [19]. The lower MDC assumed here resulted in a slower return to criticality.
    - The significant liquid carryover through the break, which is predicted here but not in the reference documents[19]. Such carryover causes the faulted SG to depressurize more slowly, resulting in a milder RCS overcooling.
2) The peak power predicted in this analysis is about 858 MW_t, with a plateau at about 700 MW_t. The reference documents instead show a peak power of about 520 MW_t. This is due, among others minor reasons, to the different FTC used. Assuming again that the reactivity coefficients mentioned in the reference documents have been used as temperature-independent parameters, the comparison would be: -3.08 pcm/K in this analysis versus -5.76 pcm/K used in reference document [19].

[18] The difference in dollars is due to the delayed neutron fraction assumed in the two analyses: 0.0044 in the reference documents, 0.0052 here.

[19] The tendency of RELAP to predict an excessive liquid carryover through the faulted steam line during SG blowdown is a problem frequently encountered by RELAP users, and detailed investigations have been performed to understand the reasons ([29]). Reference [29] states: "*In the past, a tendency to over-predict liquid entrainment to the break in steam line break transients have been attributed to shortcoming in interphase drag modeling. Recent studies however, have indicated that this is not the case, and the most likely explanation is the failure to model the accumulation of liquid on structures in the upper SG*". In the present RELAP model, in fact, the liquid-steam separation is performed by a single component located above the riser of the U-tube boiling region, which reproduces the effect of steam separators and steam dryers combined. The liquid-steam separation performed by this component is not modeled mechanicistically, i.e. by means of hydraulic laws governing the separation process actually occurring in the swirl vane zone of the separators and in the corrugated plates of the dryers, but simply by entering, as input, the component inlet flow steam quality above which the outlet flow must have a certain steam quality, the latter to be specified as well. MSLB tests performed on a 1/125 scale model reproducing a SG of the Seabrook type showed little liquid carryover through the faulted steam line. In this regard, Reference [29] authors state: "*Although the present authors and their colleagues do not believe that the dryers themselves could have such a significant effect, it is suggested that liquid carryover to the break in the experiment may have been reduced by the accumulation of liquid on other structures in the upper part of the SG, as a result of eddies in the local vapor flow*". It is likely that the break flow rate plots shown in the reference documents have been obtained by forcing the code to use a break flow rate table, rather than to let it calculate the break flow as a function of the upstream pressure. Alternatively, an artificial distortion of the SG dome geometry, coupled with the addition of components/flow paths not existing in the actual SG, might have been used to prevent liquid carryover through the faulted steam line. These tricks have been tried, however without success. The liquid carryover was therefore maintained as part of the MSLB transient.

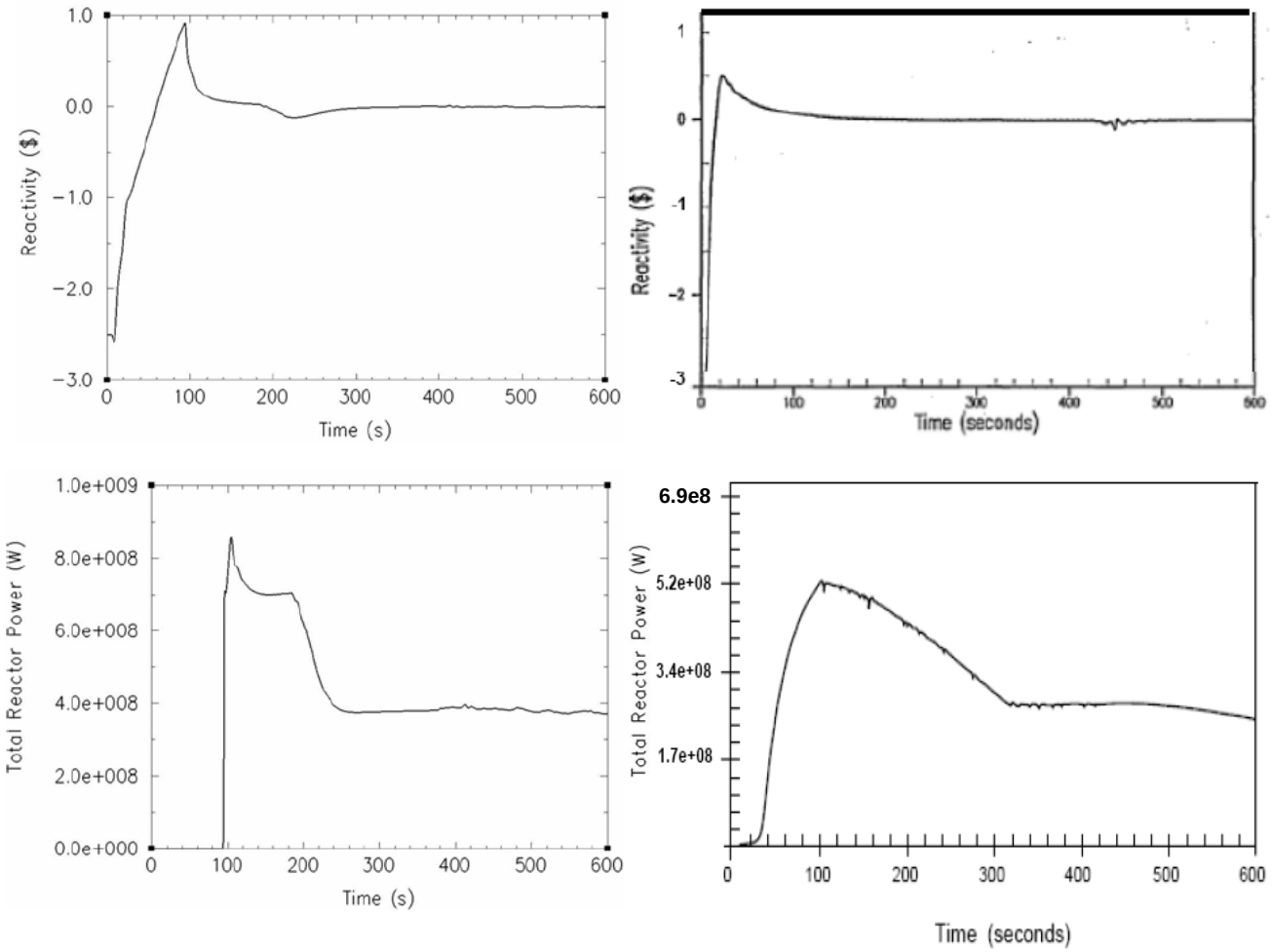

Figure 3.20 – Reactivity and core power during MSLB (left: this analysis; right: [1] and [19])

The role played by the MDC in determining the time at which criticality is achieved was also verified by running a MSLB analysis with the same MDC, FTC and β presumably used in the reference documents. As it can be seen from Figure B.6, the time of return to criticality coincides with that shown on the top right plot of Figure 3.21, i.e. about 20 s. However, the power peak is still overestimated, i.e. 850 MW_t vs 520 MW_t, which means that factors other than reactivity coefficients differ in the two analyses.

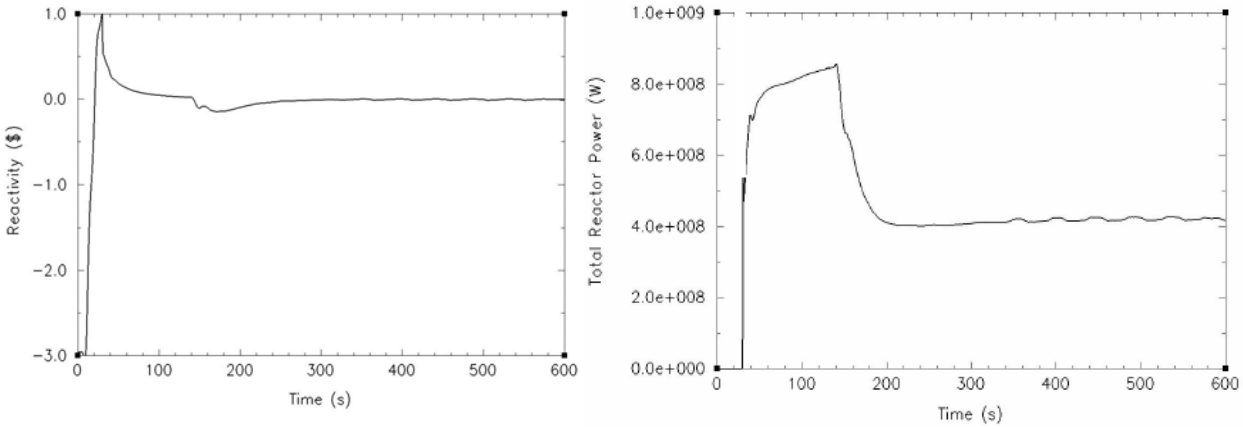

Figure 3.21 – Reactivity and core power during MSLB (obtained by using conservative reactivity coefficients probably used in the reference documents)

Figure 3.22 compares the SG dome pressure evolution predicted in this analysis to that shown in [1]. It can be noticed that the present analysis predicts a slightly slower SG depressurization during the first seconds of the transient: about 35-40 s are needed for the faulted SG to depressurize to 400 psia, while about 20 s are needed according to the reference documents. This phenomenon, together with the higher pressure at which the depressurization curve tends to change slope, are due to the liquid carryover previously discussed. Since liquid is lost through the break instead of steam, the rate of depressurization is lower. Another notable difference is the faulted SG pressure evolution at t > 100 s. While the plot on the right shows a very regular reduction in pressure, this analysis delivered an irregular behavior characterized by a pressure plateau in the time interval 100-180 s and a pressure constancy from 220 s to the end of the transient. The first anomaly is probably a consequence of the overestimation of the core power, which instead of causing the depressurization curve to simply bend at t~50 s (see right plot of Figure 3.22), causes the SG pressure to even stall. The constancy of the faulted SG pressure is instead due to an equilibrium between the AFW flow injected into the faulted SG and the break flow.

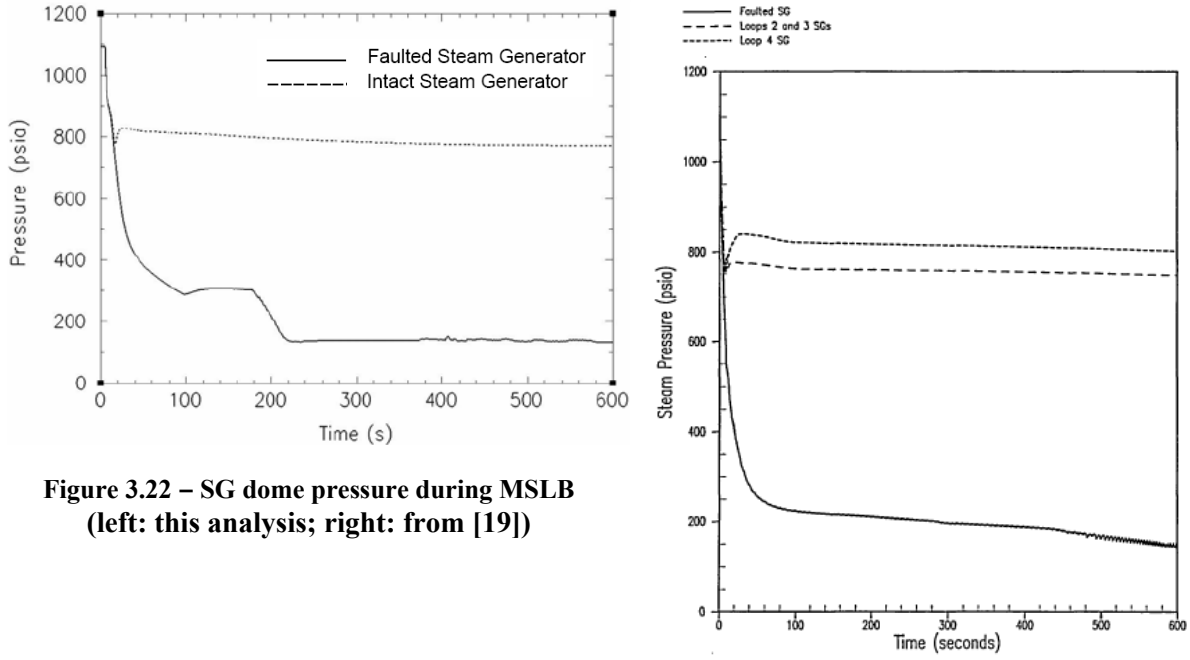

Figure 3.22 – SG dome pressure during MSLB (left: this analysis; right: from [19])

Figure 3.23 shows on the right the break flow rate evolution according to the reference documents, throughout the whole transient duration, while on the left the flow rate evolution predicted by the present analysis, but only up to 100 s[20]. It can be noticed that, while the reference document shows a regular steam-only break flow rate, the present analysis predicts a liquid carryover spike in the time interval, from the MSLB occurrence, 2-20 s. Besides such liquid spike, however, the steam flow rate predicted by the present analysis (see first 2 post-MSLB seconds as well as at t > 25 s) reproduces exactly that shown by the reference document. Unfortunately, as discussed earlier, the liquid carryover could not be eliminated or reduced.

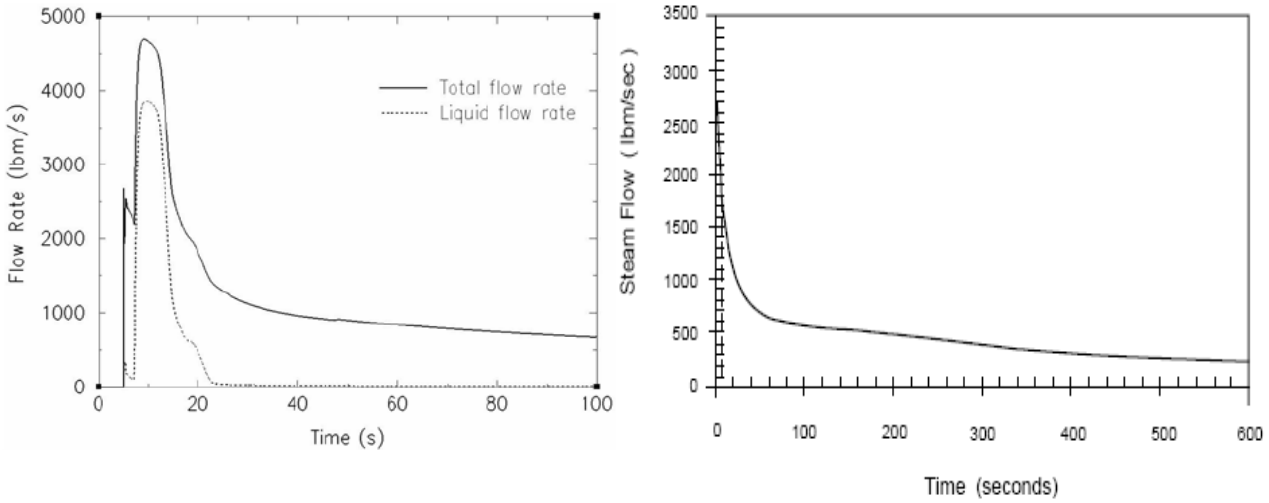

Figure 3.23 – Break flow rate evolution after MSLB (left: detail from this analysis; right: from [1])

Figure 3.24 shows the time evolution of the core average coolant temperature, which regulates the core power evolution by means of the MDC. The time profile in the first 50 s is similar in the two analyses. In the time interval 50-90 s the present analysis predicts a more rapid RCS cooling than that shown by the reference documents. This is because of the late return to criticality predicted by the present analysis, which implies that the core power is zero up to about 90 s, versus 25 s of the reference documents. During the interval 105-200 s the coolant temperature evolution predicted by the present analysis shows a plateau, due to the overestimation of the peak core power. This is a common feature with Figure 3.222, where also the SG pressure remains constant. The overestimation of the coolant temperature during the rest of the transient is both due to the difficulty to accurately model the heat transfer coefficient in the U-tube region[21], and

[20] The interruption at 100 s was only made to more clearly show the liquid carryover phenomenon.

[21] Reference [30] states: "*It often is difficult to obtain a satisfactory agreement with steam generator full-power conditions. The difficulty arises because the heat transfer coefficient calculated on the outside surface of the steam generator tubes is based on general vertical-pipe correlations rather than correlations that account for the swirling flows present within the tube bundle region. (...) resulting in excessively high calculated primary coolant temperatures*". It can be inferred that such difficulty characterizes even more the operation during a transient like a MSLB. Even though the suggestion given in the RELAP manual to solve this problem, i.e. instead of using the U-tube region hydraulic diameter as the heated diameter that the minimum tube-to-tube spacing be used, a satisfactory reproduction of the temperature evolution predicted by the reference documents was not achieved.

to the higher RCS pressure predicted by the present analysis, as shown in Figure 3.25. In fact, the lower RCS pressure estimated in the reference documents allows the accumulators to inject cold water in the primary system. The accumulator pressure injection setpoint is 600 psia, which is never reached in the present analysis, whereas it is reached at about 140 s in the reference documents.

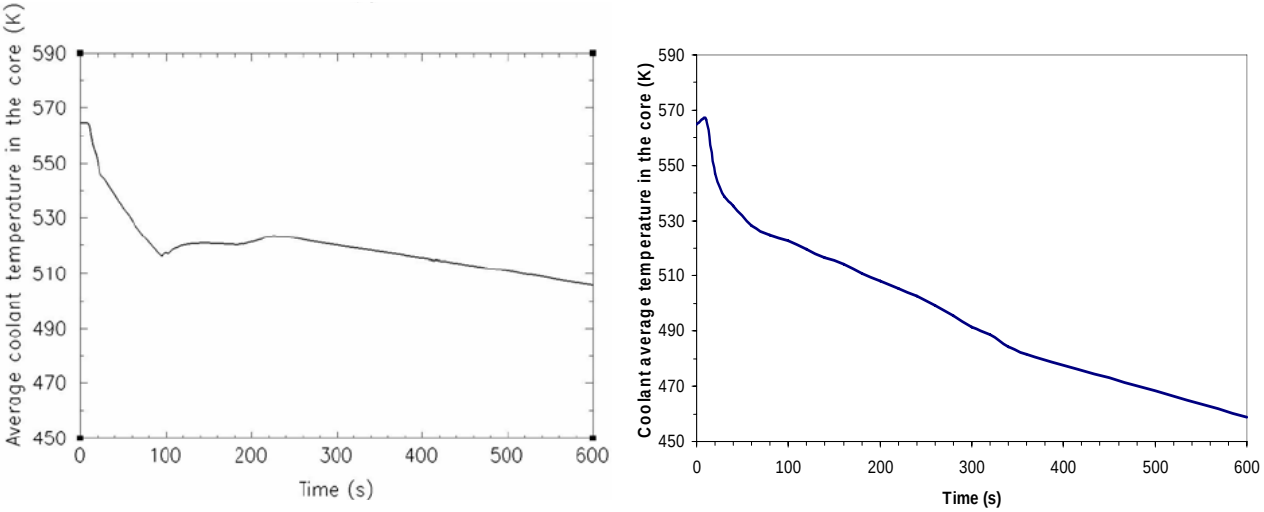

Figure 3.24 – Average coolant temperature in the core after MSLB (left: this analysis; right: from [1])

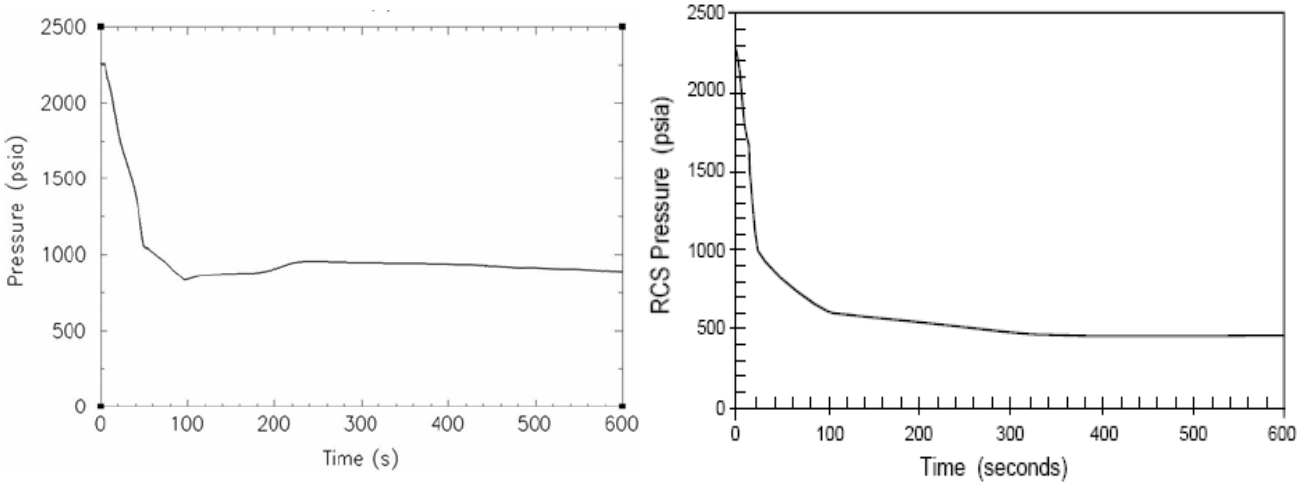

Figure 3.25 – RCS pressure evolution during MSLB (left: this analysis; right: from [1])

The limiting parameter typically calculated in MSLB analyses is, as mentioned in Section 3.6.2, the MCHFR. Figure 3.26 shows the time evolution of this parameter, up to t = 400 s, predicted by the present analysis using the Westinghouse W-3L correlation implemented in the VIPRE code ([8]). The minimum value reached, i.e. 2.3, should be compared to that mentioned in reference document [19], i.e. 1.79. However, this comparison is not particularly useful since the MCHFR is very sensitive to power level, core pressure, coolant flow rate and temperature, i.e. parameters whose time evolution was not found to be always in agreement with that shown by the reference documents [1] and [19]. This is not only because of a non optimal plant modeling,

but also because of different assumptions, driven both by lack of data and by judgment. Although MCHFR is the "final" output parameter upon which designers base their judgment of the plant capability to safely respond to a MSLB, its comparison with the value 1.79 can not be used to establish the accuracy of the analysis presented here. In fact, if this was the case, the hot assembly peaking factor assumed here, 4.25, could have been increased until the minimum MCHFR matched 1.79. The accuracy of the analysis should instead be judged based on the plant parameter comparison performed by means of Figure 3.20 through Figure 3.25. Conversely, the minimum MCHFR must be used as comparative parameter of the different core types analyzed, i.e. all-UO_2-, CONFU-, CORAIL- and PUZH-core.

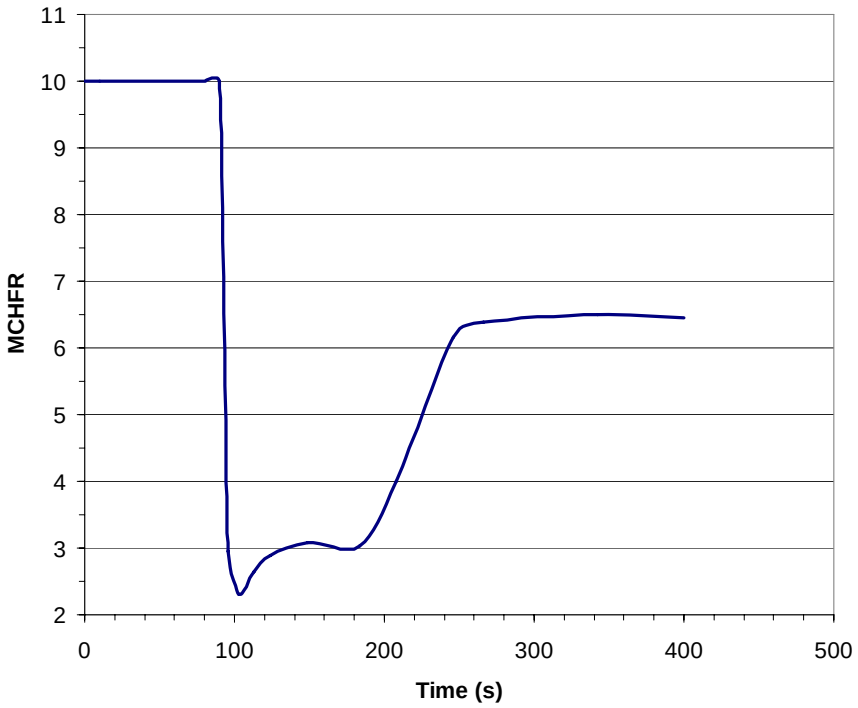

Figure 3.26 – MCHFR evolution for all-UO_2 core during the first 400 seconds of MSLB transient

3.6.6 Results

CONFU-, CORAIL- and PUZH- cores were analyzed in the same way as the all-UO_2-core. The only differences concern the fuel thermo-physical properties and the neutronic parameters listed in Table 3.10. Figure 3.27 shows the power excursion of each core, whereas Table 3.12 compares the minimum MCHFRs obtained.

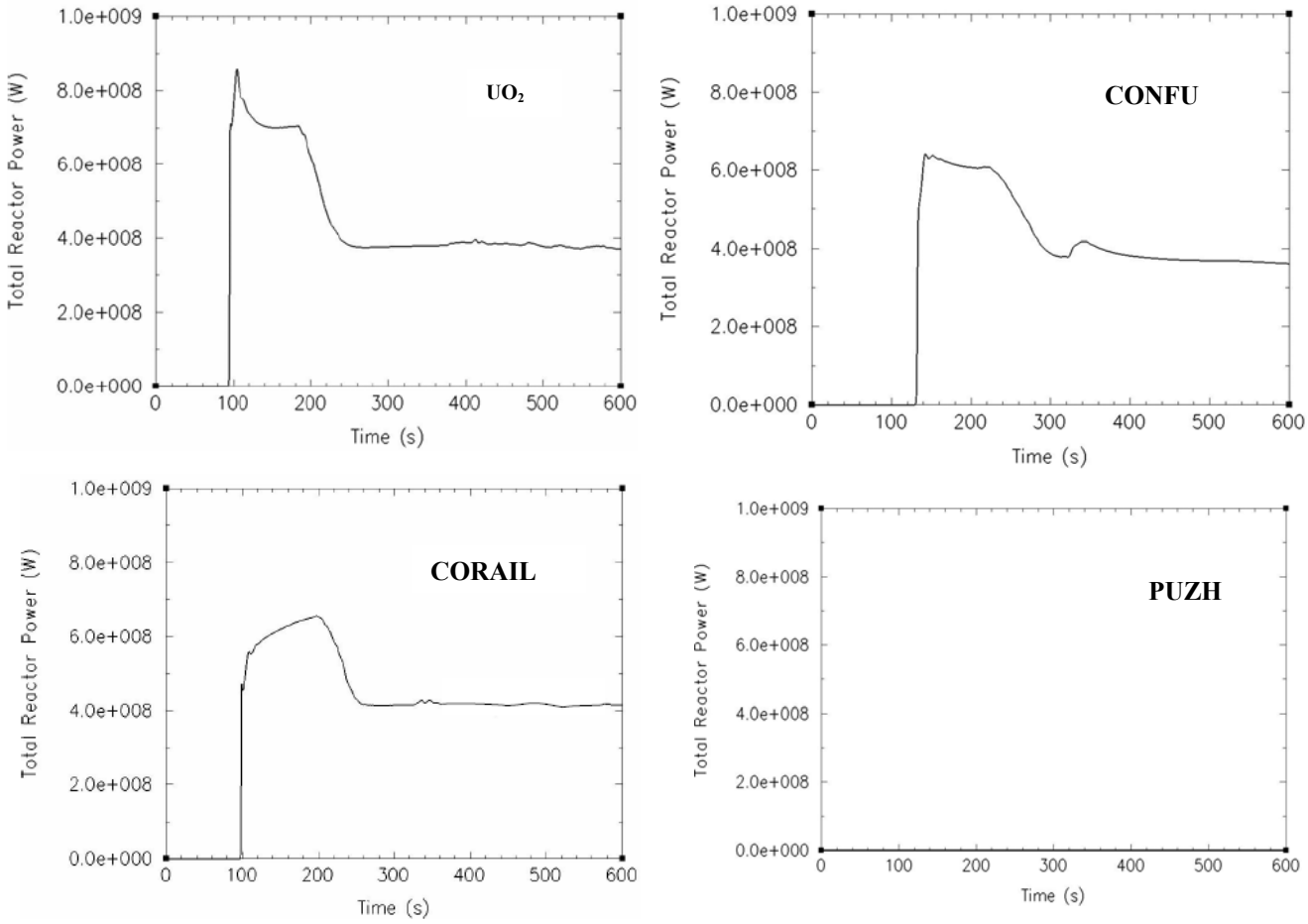

Figure 3.27: core power evolution during MSLB

Table 3.12 – Peak power and MCHFR during MSLB				
	All-UO_2	**CONFU**	**CORAIL**	**PUZH**
Peak core power (MW_t)	858	643	656	0
MCHFR	2.3	2.9	3.3	>10

3.6.7 Conclusions

A MSLB event occurring at HZP-EOC conditions was modeled. Four core types, loaded with all-UO_2-, CONFU-, CORAIL- and PUZH- assemblies respectively were analyzed. RELAP-3D and VIPRE were used for this purpose. The analysis did not model a spatial coupling between thermal hydraulics and neutronics, i.e. the total core power excursion is calculated by RELAP as a function of the global RCS overcooling caused by the break, but the non-uniform power distribution in the core was assumed based on data found in the literature. Such power distribution was used as input for the thermal hydraulic analysis performed with the VIPRE code. The quality of the RELAP plant model was assessed by comparing the time evolution of RELAP output parameters referred to the all-UO_2-core with those shown in the reference

documents analyzing MSLB ([1], [19]). Conclusions arising from the MSLB analysis are the following:

1) the accuracy of the RELAP plant modeling was found to be satisfactory. This is true in spite of some discrepancies between the time evolution of the plant parameters used to assess the adequateness of the plant model and that shown in the reference documents. These discrepancies are due to two reasons:
    - the use of different assumptions (due to lack of information or because of particular needs characterizing the present analysis);
    - the overestimation of the break flow rate during the first 20 s after the event initiation. This problem, related to the erroneous prediction of liquid carryover through the faulted main steam line, is due to the present inability to model the SG so that liquid from the inside the SG is prevented from flowing to the break.
2) PUZH-core was found to have better post-MSLB performance with respect to the other core types analyzed since it does not reach criticality after MSLB. The other core types, instead, do. This is because the reactivity excursion before criticality is more significant for high values of the Moderator Density Coefficient (MDC) which was found to be, for PUZH-assemblies in the HZP-EOC conditions, about half that of all-UO_2-, CONFU- and CORAIL- assemblies.
3) Like the other assembly types analyzed, PUZH-assemblies were found to have a negative Fuel Temperature Coefficient (FTC). This is beneficial, in terms of safety, for any event leading to the reaching of criticality and subsequent increase in power. However, in terms of comparison between the various core types, PUZH-assemblies were found to have a FTC less negative than the other assembly types, i.e. about 33 and 46% lower than that of CONFU and CORAIL respectively, and about 9% lower than that of all-UO_2 assemblies. For the MSLB analysis performed here, however, such less negative FTC does not affect the PUZH-core performance since criticality is not reached.

3.7 Complete Loss of Flow Accident analysis

3.7.1 General event description

CLOFA is defined as a Condition III incident ([1]) consisting of the complete loss of forced reactor coolant flow, which may result from a simultaneous loss of electrical supplies to all Reactor Coolant Pumps (RCPs). Following this loss, RCPs start coastdown causing the coolant flow rate through the core to decrease, with consequent reduction of its own heat removal capabilities. In case this event was not followed by immediate reactor scram, the increasing incapability of the coolant to remove heat would yield fuel pin failure and thus core damage. Protection against CLOFA is however provided by reactor scram, which initiates upon reception of one of the following two signals:

- RCP power supply undervoltage/underfrequency signal (not used in this analysis);
- low reactor coolant loop flow signal.

As a consequence of reactor scram, core power rapidly decreases to decay power level, and this terminates the accident scenario.

3.7.2 Objectives

The objective of the analysis was to compare the response, and in particular the Minimum Critical Heat Flux Ratio (MCHFR), of a PUZH-core with that characterizing other core types aimed at Pu/Minor Actinides incineration, i.e. CONFU- and CORAIL-core, during a CLOFA scenario. In spite of not being aimed at Pu/Minor Actinides recycling, the all-UO_2-core is analyzed in order to validate the plant modeling technique.

3.7.3 Code used and modeling approach

The CLOFA analysis was performed using two codes: RELAP 3D© ([15]) and VIPRE ([8]). RELAP was used to model the time evolution of the plant parameters during the accident (both in the primary and secondary system), focusing in particular on core power, core pressure, coolant flow rate through the core and coolant temperature at core inlet. These parameters were then entered as input in the VIPRE code which, relative to RELAP, models the core more in detail. The strategy of using two codes is motivated by the fact that the RELAP input file used in this analysis does not model the core with a sufficiently high spatial resolution: the active[22] core is in fact modeled by means of only two channels, as done for the MSLB analysis (the plant nodalization is in fact the same as that shown in Figure 3.16):

- channel 333: a single channel formed by the subchannels of 145 assemblies lumped together;
- channel 335: a single channel formed by the subchannels of 48 assemblies lumped together;

and three heat structures:

- heat structure 1: a single rod formed by the fuel rods of 145 assemblies lumped together, facing channel 333;
- heat structure 2: a single rod formed by the fuel rods of 47 assemblies lumped together, facing channel 335;
- heat structure 3: a single rods formed by the fuel rods of the hot assembly lumped together, facing channel 335.

The VIPRE input file used for the CLOFA analysis is again the same as that used for the steady state analysis (see Section 3.4): it models $1/8^{th}$ sector of the core, in which all the subchannels contained in the hot assembly are modeled individually. This allows performing a more detailed thermal hydraulic analysis than that obtainable using RELAP only.

3.7.4 Detailed event description and assumptions made

The assumptions made to model CLOFA are grouped in four categories:

- pre-accident thermal hydraulic condition assumptions;
- scenario evolution assumptions;
- reactivity coefficient assumptions;
- power distribution assumptions;

[22] The term “active” is used to identify the thermal hydraulic structures actually involved in the heat generation and removal. A core bypass channel, which is not “active”, is modeled separately.

and are described as follows.

3.7.4.1 Pre-accident thermal hydraulic condition assumptions

The main plant thermal hydraulic parameters characterizing the reactor before the accident occurrence are summarized in Table 3.12. Since some parameters, e.g. primary coolant flow rate, can not be entered into RELAP as input but are calculated by the code based on specified boundary conditions, e.g. pump performance, the value actually used is shown together with the target value (in parenthesis), i.e. with the value prescribed by the literature source used as reference. In case no target value is shown, the two coincide.

Table 3.12 – Pre-accident thermal hydraulic operating conditions used for CLOFA analysis (all from [1])

Parameter	Value	Notes
Core thermal power (MW_t)	3479	102% of nominal reactor power
RCS pressure (MPa)	15.51	Nominal pressure
RCS coolant flow rate (kg/s)	18336 (18358)	Nominal flow rate
Core active coolant flow rate (kg/s)	17388 (17476)	
Core inlet temperature (ºC)	296.3	+3.2ºC with respect to nominal value

3.7.4.2 Scenario evolution assumptions

In the present analysis electrical equipment is not modeled and thus the low flow signal is the only signal used to initiate reactor scram. In particular, the reactor scram is assumed to start one second after the coolant flow rate has dropped below 87% of the nominal value in any of the primary circuit loops ([1]).

3.7.4.3 Reactivity coefficient assumptions

Two assumptions were made about reactivity coefficients: the pre-accident values, i.e. the steady-state normal operation values, and their evolution with temperature during the transient. They are discussed as follows.

Steady-state: Since, for a fixed coolant flow rate, the severity of core overheating due to RCP coastdown increases with core power, CLOFA is assumed to occur when the reactor is at Beginning Of Cycle (BOC) ([1]). This is because of the need of minimizing the moderator negative feedback upon temperature increase. In fact, the Moderator Temperature Coefficient of Reactivity (MTC) has its least negative value at BOC, when the concentration of soluble boron in the primary circuit is maximum (~1400 ppm for a typical PWR [1]). Although the best estimate of the core average MTC at Hot Full Power (HFP)-BOC is -19.6 pcm/K (Figure 4.3-33 of [1]), reference [1] analyzes CLOFA assuming conservatively a very large MTC, i.e. +9 pcm/K. This value is even larger than that corresponding to Hot Zero Power-BOC (~-1 pcm/K) and may be close to that characterizing HFP operation at a boron concentration around 2700 ppm. In fact, reference [31] shows that at HFP-BOC the AP1000 design would reach a MTC of about 5 pcm/K if the boron concentration was 2500 ppm.

Although the practice of using conservative estimates of reactivity coefficients is a feature common to all the safety analyses, the present analysis uses best-estimate values for the

reactivity coefficients. This is because the achievement of the same level of conservativism, in terms of reactivity coefficients, as that used in [1] for an all-UO_2 core, is difficult to preserve when analyzing reactors different than an all-UO_2 type. In other words, the level of conservativism resulting from increasing, for an all-UO_2 core, the moderator temperature coefficient from -19.6 pcm/K (best-estimate) to +9 pcm/K (conservative value) is difficult to translate to another type of core, for which the increase of MTC by 28.6 units (9+19.6) from its best-estimate HFP-BOC value may yield an overconservative/unreasonable value.

Consistent with the choice of the MTC, the values used for Fuel Temperature Coefficient (FTC), Boron Worth (BW) and delayed neutron fraction (β) are also best-estimate values for each type of core. They are summarized in Table 3.13. Numerical values for which reference is not shown have been calculated in this project and do not derive from external sources.

Transient evolution: Among the parameters shown in Table 3.13, FTC, BW and β were assumed to remain fixed during the transient and equal to their pre-accident values[23]. The MTC dependence on coolant temperature is instead accounted for, and it is shown in Figure 3.28. The polynomial function used to plot the curves allows reproducing, for the all-UO_2 core, the MTC variation with temperature shown in [1] whereas, for the other core types, it yields an MTC vs temperature curve having the same shape as that for the all-UO_2 core but translated to lower or higher values of MTC to allow matching the pre-accident values shown in Table 3.13.

Table 3.13 – Reactivity coefficients and neutronic parameters used in pre-CLOFA operation (core-average values referred to HZP-BOC conditions)

	All-UO_2	**CORAIL**	**CONFU**	**PUZH**
FTC (pcm/ºC)	-2.5 (Fig. 4.3-27 in [1])	-2.5	-2.1	-3.4 (Fig. A.9 of [32])
MTC (pcm/ºC)	-19.6 (Fig. 4.3-33 in [1])	-6.1	-8.4	-13[24] (Fig. A.10 in [32])
BW (pcm/ppm)	-6.3 (Fig. 5-18 in [26])	-4.9	-5.1	-2.8
β	0.0075 (Table 4.3-2 in [1])	0.006 (Fig. 5.4.1 of [33])	0.006 (Table 4.3.III of [13])	0.00342

[23] This assumption is reasonable since: β depends only on the fuel composition (which does not change appreciably during the transient); FTC varies only slightly as the average fuel temperature decreases (e.g. from -2.5 pcm/K at 630ºC to -2.9 pcm/K at 292ºC for an all-all-UO_2 core); BW is not supposed to play any role since the high pressure of the RCS during the transient prevents injection of borated water.

[24] The MTC value used for PUZH-core refers to a burnable poison-free design: from the MTC viewpoint this is a conservative assumption since the presence of burnable poisons, needed to reduce the critical boron concentration, would make MTC more negative thus yielding a milder core power reduction soon after CLOFA occurrence. The detrimental effect caused by burnable poison addition on thermal hydraulics, i.e. the increase in pin-by-pin power distribution non-uniformity, was accounted for by analyzing the power distribution shown in Figure 3.5 other than that shown in Figure 3.8.

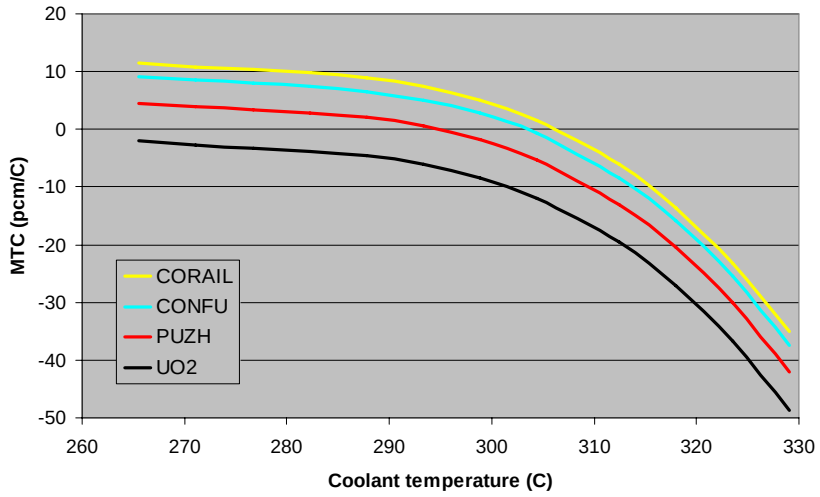

Figure 3.28 – MTC variation with coolant temperature assumed in this analysis

Power distribution assumptions: the axial power distribution in the core as well as the radial power distribution among the assemblies are the same for all the core types. The former is a chopped-cosine power profile having a maximum peaking factor of 1.515. The latter features a hot assembly peaking factor[25] of 1.515. These are conservative values typically used in the safety analyses of all-UO_2 PWRs ([1]).

The pin-by-pin power distribution is instead different depending on the assembly type under consideration, as shown in Figures 3.5 through 3.8. It is important to note that, while for the all-UO_2-, CONFU- and CORAIL-type assemblies only one power distribution was considered, two pin-by-pin power distributions were analyzed for the PUZH-type assembly. The first, shown in Figure 3.8, refers to a burnable poison-free assembly which was proved to yield a negative core average MTC at BOC in spite of being characterized by a very high Critical Boron Concentration (2750 ppm ([32])). Because of the need to prevent boron-assisted corrosion phenomena, this concentration must be reduced, and therefore burnable poisons (BP) need to be loaded in the fresh assemblies. The BP loading, which significantly affects CBC and less significantly the pin-by-pin power distribution, has not been fixed yet and it is therefore a design variable. For the CLOFA analysis it is assumed that the addition of a reasonable amount of BP would cause the PUZH-assembly power distribution to resemble that of the IFBA-containing all-UO_2 assembly shown in Figure 3.5, which is therefore the second pin-by-pin power distribution analyzed for PUZH-type assemblies.

It is important to note that all the power distributions used are assumed to be fixed during the accident, i.e. while the core power varies, its axial and radial profiles remain constant.

3.7.5 Validation of the plant modeling technique

This section compares the results obtained for the all-UO_2-core with those presented, for the same core, in [1]. Even though the reactivity coefficients used here are not the same as those used in [1][26], the comparison is useful to verify the accuracy of the analysis and the correctness

[25] The assembly peaking factor is defined as the ratio between the power of the assembly to which it is referred and the power of the average assembly.

[26] Except for MTC, reference [1] does not specify the numerical values of the reactivity coefficients actually used to perform the

of the RELAP plant model. This comparison is made by means of plots showing the time variation of key plant parameters during the transient. In each figure, the plot on the left is that obtained here while that on the right derives from [1].

Figure 3.29 shows the variation of core power during CLOFA. The trend predicted in this analysis is very similar to that shown in the reference document ([1]). Reactor scram occurs after about 3 seconds from the accident initiation, causing the core power to drop to about 15% of nominal power in less than 2 seconds. Subsequently, core power slowly decreases.

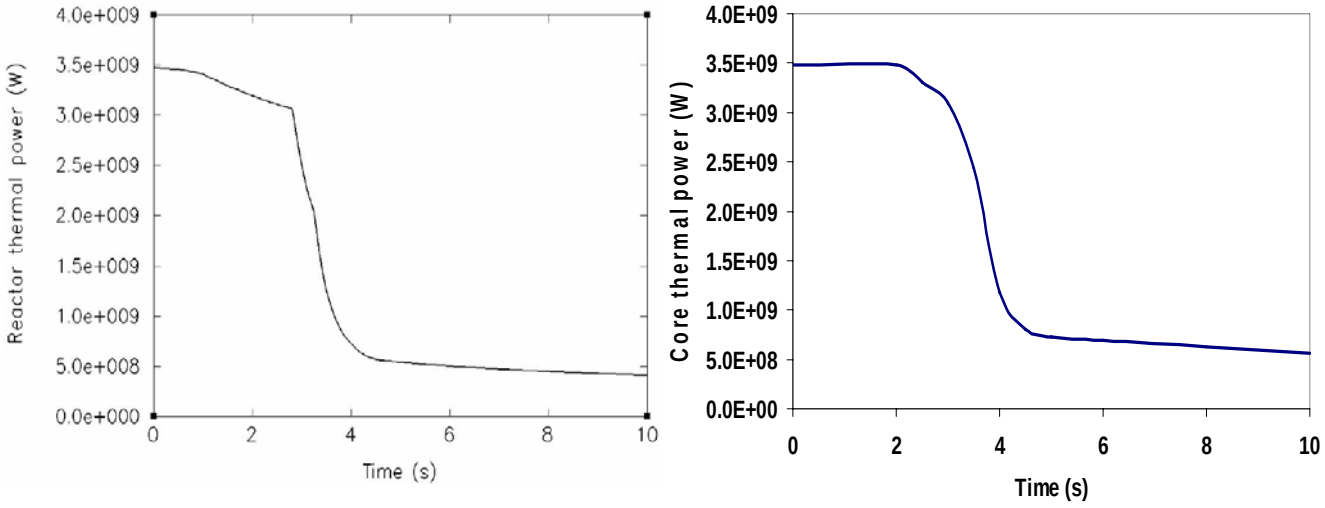

Figure 3.29 – Core power evolution during CLOFA for all-UO_2 core (left: this analysis; right: [1])

The core power profiles in the pre-scram period, i.e. the first 3 seconds after the accident initiation, do exhibit a slight difference: while [1] does not show any power variation, a power reduction from 3479 MW_t to about 3080 MW_t is obtained in the present analysis. This is due to the large negative MTC which, as the coolant average temperature in the core increases from about 315ºC to about 318ºC (see Figure 3.30[27]), causes an insertion of negative reactivity which adds to that due to FTC. It has been separately verified that the use of a positive MTC equal to that used in [1], i.e. +9 pcm/K, would have caused the core power to decrease of only 100 MW_t instead of the 400 MW_t reduction (3479-3080) shown in the left plot of Figure 3.29. Therefore, while in the present analysis the negative feedback due to MTC is coupled with that due to the FTC, causing a significant (400 MW_t) reduction in core power, in reference document [1] the positive feedback due to MTC overwhelms the negative feedback due to FTC, resulting in a substantially flat pre-scram power profile.

CLOFA analysis.

[27] Reference document [1] does not show the variation of the coolant average temperature during CLOFA. For this reason, Figure 3.30 does not have a plot with which being compared.

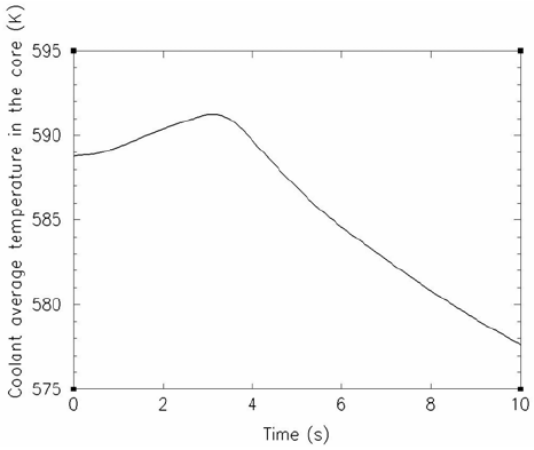

Figure 3.30 – Coolant average temperature in the core during CLOFA for all-UO_2 core

Figure 3.31 shows the variation of the coolant flow rate through the core during CLOFA. It can be seen that the present analysis well reproduces the flow rate profile shown in [1], with a slight overestimation (3-5%) over the whole transient.

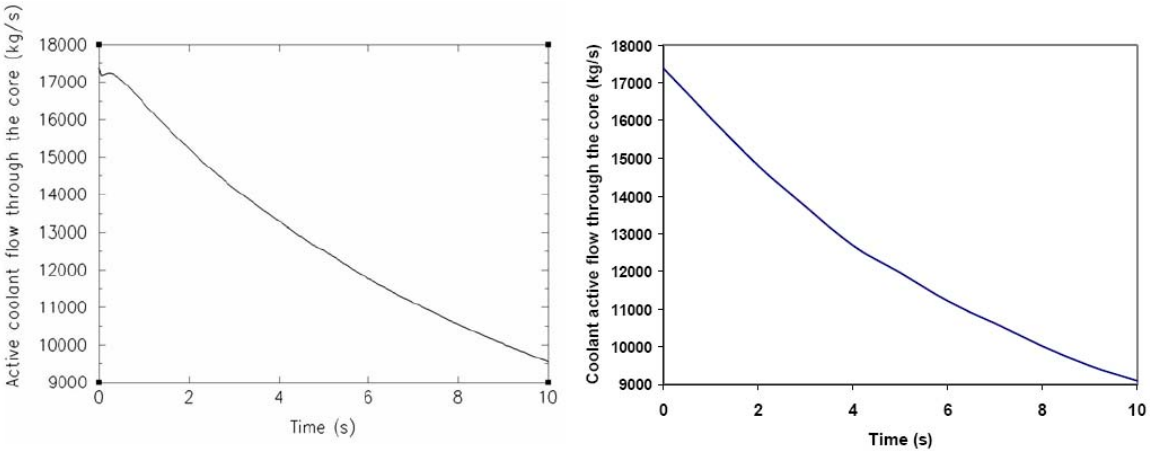

Figure 3.31 – Evolution of coolant flow rate through the core for all-UO_2 core (left: this analysis; right: [1])

Figure 3.32 shows the variation of the Minimum Critical Heat Flux Ratio (MCHFR) during CLOFA. Both the present analysis and reference [1] predict a reduction of MCHFR followed by a sharp increase after reactor scram. However, two main differences can be noticed:

- the present analysis underestimates the MCHFR with respect to that calculated in [1] (2.073 vs 2.17);
- in the first 3 seconds after the accident initiation, the present analysis predicts a very small reduction in MCHFR, i.e. from 2.138 to 2.073, while reference [1] shows a MCHFR reduction from 2.7 to 2.17.

The use of a different correlation might be the main reason for these differences. In fact, the present analysis computes the critical heat flux (CHF) by means of the W-3L correlation available in the VIPRE code. Reference [1], instead, does not explicitly state what CHF

correlation was used in CLOFA analysis. However, in a chapter not dedicated to safety analysis, i.e. Chapter 4 "Reactor" of [1], it is stated that: "*For conditions outside the range of applicability of WRB-1 or WRB-2, the W-3 correlation is used*" ([1]). Because of the mildness characterizing CLOFA scenario it is likely that one of the two WRB correlations were actually used. These two correlations are specific for Westinghouse-design assemblies provided (WRB-2) or not provided (WRB-1) with Intermediate Flow Mixers ([33])[28].

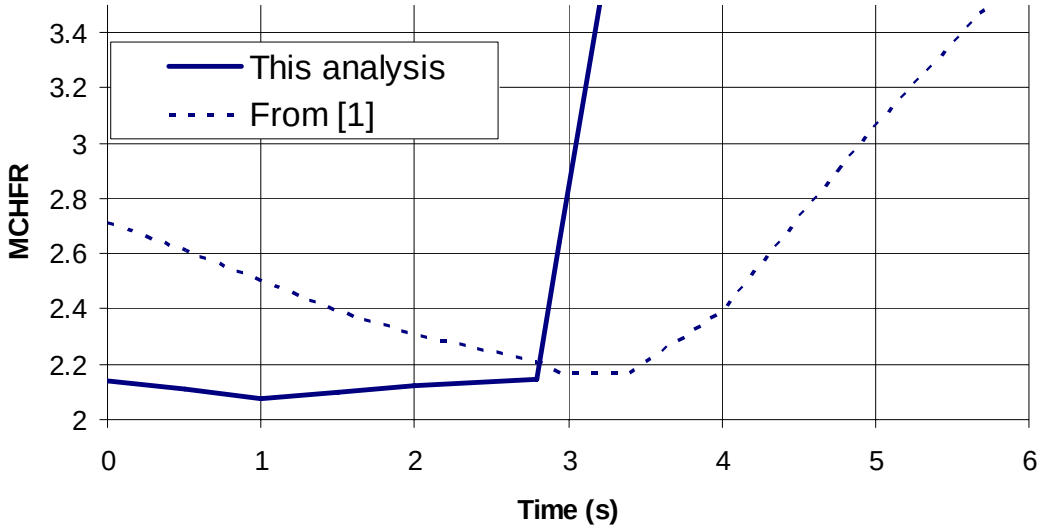

Figure 3.32 – Evolution of MCHFR during CLOFA for all-UO_2 core

It must be pointed out, however, that the scarcity of information given in [1] about the modeling of the CLOFA scenario does not allow the exclusion of other factors, like a different time variation of the core inlet coolant temperature, as causes of the differences between the two MCHFR profiles shown in Figure 3.32.

3.7.6 Results

Figure 3.33 shows the time variation of the core power for the four core types analyzed. Only the pre-scram evolution is shown since it is the most critical for CLOFA scenario. Because of the negative MTC characterizing all core types at normal operating conditions, they all experience a reduction in power soon after the accident initiation, i.e. when the operating conditions do not differ substantially from the nominal ones. In particular, the power reduction is maximum for the PUZH-core while it is minimum for the CORAIL-core. This is because the ratio MTC/β, which controls the reactivity insertion upon coolant temperature variation, is maximum (in absolute value) for PUZH (-0.038 \$/ºC) while it minimum for CORAIL (-0.010 \$/ºC).

[28] The WRB correlations are more accurate than the W-3L correlation. As a consequence, their use allows less margin from the failure limit, i.e. from CHFR=1: the minimum CHFR typically allowed in safety analyses is in fact 1.3 if the W-3 correlation is used, while it is 1.17 if one of the two WRB is used ([34]).

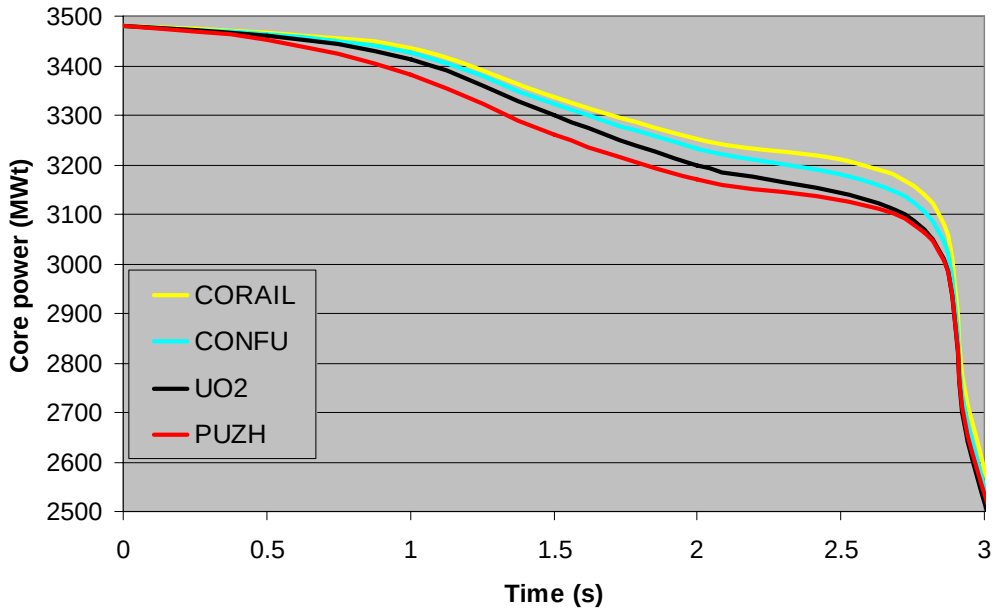

Figure 3.33 – Evolution of core power during CLOFA

Figure 3.34 shows the MCHFR time variation during CLOFA for the four core types analyzed. While two cases for the PUZH-core[29] were evaluated, only that referred to a burnable poison-free pin-by-pin power distribution is shown: this is because the MCHFR time variation obtained in the other case, i.e. using the all-UO_2 assembly power distribution to the PUZH-assembly, does not differ appreciably from that shown in Figure 3.34. The minimum MCHFR reached by each core type during CLOFA is shown in Table 3.14.

[29] The two cases analyzed differ only for the pin-by-pin power distribution assumed for the assemblies. Since the RELAP input file models the hot assembly by lumping all its subchannels and rods, the pin-by-pin power distribution does not affect the output parameters (e.g the core power evolution) obtained by running the RELAP plant model. For this reason, no mention to two PUZH-core cases was done while commenting Figure 3.33. Conversely, the VIPRE output parameters (e.g. the MCHFR) depends on the pin-by-pin power distribution since the VIPRE file models individually each rod and subchannel contained in the hot assembly.

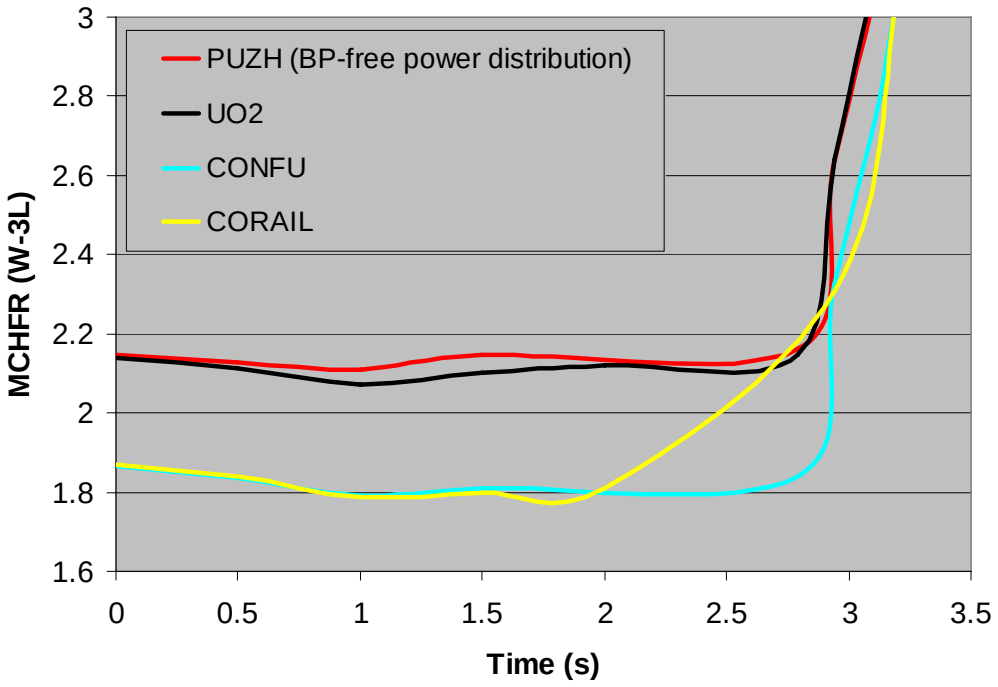

Figure 3.34 – Evolution of MCHFR during CLOFA

Table 3.14 – MCHFR during CLOFA scenario			
Core type	**MCHFR (W-3l correlation)**		**MCHFR variation % with respect to steady state value**
	At steady-state	**Minimum during CLOFA**	
All-UO_2	2.138	2.073	-3.0
CONFU	1.866	1.791	-4.0
CORAIL	1.870	1.788	-4.4
PUZH (BP-free pin-by-pin power distribution)	2.146	2.110	-1.7
PUZH (all-UO_2 pin-by-pin power distribution)	2.143	2.106	-1.7

From the results shown in Figure 3.34 and Table 3.14 it can be concluded that CLOFA causes all core types to experience a slight reduction in MCHFR with respect to their steady state values. However, while the absolute value of the minimum MCHFR during the CLOFA scenario of each core type mainly depends on the starting MCHFR, i.e. the steady state MCHFR, the severity of MCHFR reduction depends on the extent by which core power decreases soon after the accident initiation[30]. Since CONFU- and CORAIL-cores have not only the most non-uniform pin-by-pin power distribution but also the least negative MTC/β ratio, they experience the smallest MCHFR during the transient (1.791 and 1.788 respectively) and the largest MCHFR reduction from the

[30] Since 1) all core types are geometrically identical and 2) they have same steady-state coolant flow rate, the coolant flow rate reduction experienced by the four core types is the same. Thus, the differences in average coolant temperature in the core depend on the core power only.

pre-accident value (-4% and -4.4% respectively). Conversely, the homogeneity of the pin-by-pin power distribution characterizing PUZH-type assembly together with the large negative value of the MTC/β ratio cause the MCHFR to start from a relatively high MCHFR (~2.14) and to experience a small MCHFR reduction during the transient (-1.7%).

3.7.7 Conclusions

The following conclusions arise from the CLOFA analysis:

- the level of accuracy of the modeling of the CLOFA plant response can be considered acceptable for the preliminary stage characterizing this project. For the all-UO_2-core used for the model validation, the time evolution of the main plant parameters was found to be consistent with that shown in the reference document ([1]), with only small differences due to the scarcity of input data specifications in [1] and to simplifying assumptions made in this analysis.
- CLOFA was found to be a mild accident scenario for all the core types analyzed, during which the core experiences a slight reduction in MCHFR with respect to the steady-state value. This reduction was found to be smaller for the PUZH-core compared to the other core types aimed at Pu/Minor Actinides incineration, i.e. CONFU- and CORAIL-core. The reason lies in the more negative MTC/β ratio characterizing the PUZH-core, which causes the core power to decrease more significantly after CLOFA initiation for the PUZH-core than for the CONFU- or CORAIL-core.
- Given the mildness charactering the CLOFA scenario and the short time interval to reach the most limiting conditions (<5 seconds), the thermal hydraulic margin of safety of a core during CLOFA, i.e. the minimum value reached by the MCHFR, does not depend much on the post-accident evolution of the plant parameters, but on the MCHFR characterizing the core before the accident initiation. From this viewpoint, the homogeneity of the PUZH-assembly lattice allows the PUZH-core to perform better than the CONFU- and CORAIL-cores, and to resemble the performance of an all-UO_2 core. Even though a preliminary estimate of the PUZH-core safety margin during CLOFA was done in this analysis, a more accurate evaluation can be done once the pin-by-pin power distribution of a PUZH-type fresh assembly is finalized, i.e. when the burnable poison loading, so far still a design variable, is fixed.

3.8 Conclusions of the thermal hydraulic analysis

Steady state and transient analyses were performed for a PWR plant having the same geometry as that of Seabrook power station ([1]). The reactor core was alternatively assumed to be loaded with four types of assembly, having identical geometry but different fuel and/or fuel arrangement:

- all-UO_2-assembly: homogeneous assembly containing UO_2 fuel pins only.
- CONFU-assembly: heterogeneous assembly made of standard UO_2 fuel pins and pins made of recycled transuranics in an inert matrix.
- CORAIL-assembly: heterogeneous assembly made of enriched UO_2 pins and MOX pins.
- PUZH-assembly: homogeneous assembly containing U-Pu-Th-$ZrH_{1.6}$ as fuel.

The steady state analysis demonstrated that, under the constraint of the same safety limits for all the core types, a PUZH-core can operate at the same power level as the all-UO_2-core while CONFU- and CORAIL-core can only operate at about 80% of that power. This is due to the flat pin-by-pin radial power distribution characterizing the PUZH-assembly.

The transient analyses performed were: Large Break Loss Of Coolant Accident (LBLOCA), Main Steam Line Break (MSLB) and Complete Loss Of Forced Flow Accident. (CLOFA). For all three scenarios, the PUZH-core was demonstrated to perform better than the other two core types aimed at Pu/MA incineration, i.e. CONFU- and CORAIL-core. Particularly:

- the peak cladding temperature for PUZH-core during LBLOCA was found to be about 300 K lower than that of all-UO_2-, CONFU- and CORAIL-cores. This is mainly due to the lower operating temperature characterizing the highly conductive PUZH fuel relative to UO_2-based fuels;
- unlike all-UO_2-, CONFU- and CORAIL-cores, PUZH-core showed no return to criticality in the event of a MSLB. This is due to the moderator temperature coefficient of PUZH-core, which was found to be the least negative among the core analyzed;
- in the event of a CLOFA, the PUZH-core was found to reach a MCHFR larger than that of the CONFU- and CORAIL-cores, and similar to that of the all-UO_2-core. This is due both to a larger pre-accident MCHFR (due to the flat pin-by-pin power distribution characterizing the PUZH-assembly) than CONFU and CORAIL, and to the larger (negative) value of the MTC/β ratio (which controls the reactivity insertion upon coolant temperature variation) which caused a more rapid reduction in power upon the accident.

Appendix A: inverted core design

A.1 Description of the design

Although the idea of an inverted fuel design is not new (see Pope [35] for Gas Cooled Fast Reactors), Malen was the first to propose a variation of such a design for PWR applications ([36]). Malen's design consisted of vertically-oriented hexagonal blocks of hydride (U-$ZrH_{1.6}$) fuel (referred as "assemblies"), perforated by coolant channels arranged in a triangular lattice. A cylindrical Zircaloy clad forms the walls of each coolant channel, and a certain gap separates the outer clad surface from the inner surface of the fuel. Each channel is provided with multiple short-length twisted tapes (TTs) aimed at critical heat flux (CHF) enhancement. The TT pitch, which strongly affects the CHF performance, is designated as y and is defined as the axial distance, in units of coolant channel diameter, traveled by the tape to complete a 180º rotation around the coolant channel axis.

Although the fuel contained in each assembly is a single block, it can be imagined as composed of a number of smaller hexagonal units, called fuel subprisms, each having a coolant channel at the centre (see Figure A.1). The combination: coolant channel + channel clad + fuel-clad gap + fuel subprisms is referred as "unit cell". Figure A.1 shows a subchannel view of the inverted design (left) and of the typical rodded design (right). The latter is referred to as "standard design", and the corresponding core as "standard core" (SC).

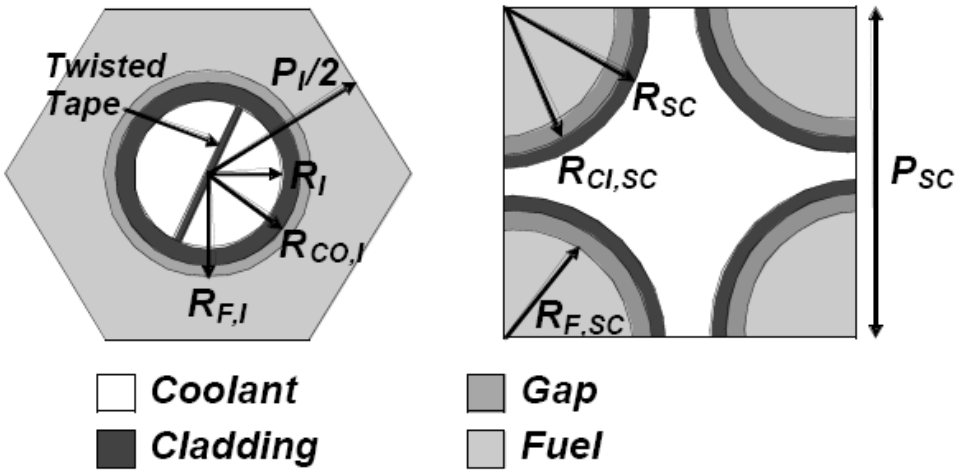

Figure A.1 – Inverted (left) vs standard (right) unit cell design ([36])

The innovative nature of the inverted design is twofold: hydride is used in place of UO_2 and an inverted configuration is used instead of the more common standard configuration. The inverted configuration is made possible by the more favorable workability properties of hydrides with respect to those of UO_2: hexagonal U-Zr blocks can be easily drilled to create cooling channels and then hydrated to obtain the final fuel composition (e.g. U-$ZrH_{1.6}$).

A.2 Motivations

Two factors motivated interest in the inverted design:

- in his preliminary study, Malen ([36]) found the inverted design to have the potential to allow an increase in power density, with a consequent reduction in the cost of nuclear-generated electricity;
- based on the findings of the plutonium incineration project, the inherent hydrogen content of hydride fuel makes it an advantageous alternative fuel for Plutonium and Minor Actinides burning.

It was therefore decided to investigate further this novel design.

A.3 Objectives

The inverted design project is aimed at determining the economic competitiveness of an inverted PWR with respect to other PWR core designs referred to as "competitor designs" and presented in Section A.6. To achieve this objective, the calculation of the maximum power density attainable by an inverted PWR, together with cost estimates for the new design, need to be performed.

A.4 Project status

The tasks performed in the period April 2007-August 2008 mainly concerned:

- the establishment of the design constraints;
- the estimate of the maximum power attainable by a "point design" core configuration, i.e. by a single inverted core geometry, which is shown in Figure A.2.

The objectives presented in Section A.3, which have not been reached yet, will require switching from a point design methodology to a spectrum design methodology, meaning that the

computation of the maximum attainable power density will need to be performed over a wide range of inverted core geometries, and not only for a single geometry as done with the point design core configuration.

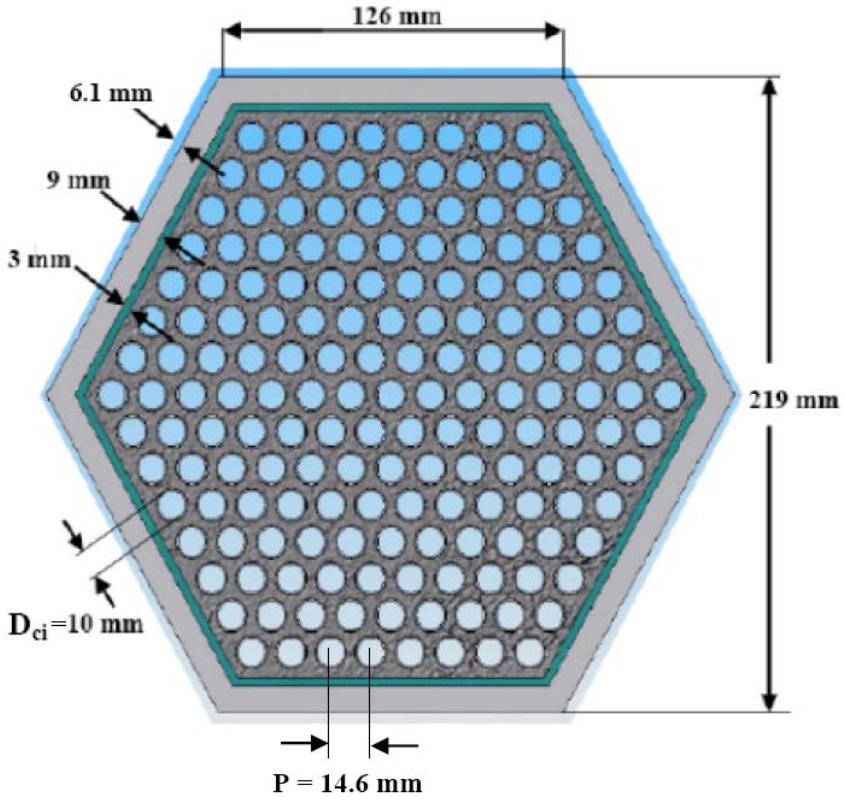

Figure A.2 – Point design investigated for the inverted core (TTs not whosn)

A.5 Analysis methodology

The analysis methodology planned for this project is the same as that used by Malen in his preliminary investigation ([36]), i.e. power-limiting constraints need to be fixed and used to compute the maximum power density attainable by an inverted PWR core. What actually differs from Malen's approach is the level of detail with which such constraints are chosen and examined. Because of the preliminary nature of his work, Malen did not account for all the possible design constraints, and some of them were neglected:

- constraints related to the manufacturability of the inverted assembly;
- constraints related to the structural integrity of the inverted assembly during operation;
- constraints related to the physical separation between adjacent fuel assemblies (Malen assumed an infinite array of unit cells);
- coolant pressure drop across the core;
- fuel performance constraints (sizing of gaps to accommodate fuel swelling);
- neutronic constraints (void reactivity coefficient);

- enrichment and cycle length.

A.5 Competitor core designs

Competitor core designs are PWR core designs with which the inverted design will need to be finally compared, in order to have a complete understanding of the potentials that such design has for future deployment. Competitor core designs, which have been investigated in previous research project at MIT and UCB, are summarized in Table A.1 together with the inverted point design discussed in Section A.4. In this table, the core designs are grouped according to the type of fuel and according to their geometric configuration (standard, annular, inverted). The table shows, for each competitor design, its main geometric characteristics and, most importantly:

- the attainable power uprate relative to the reference UO_2 core described in [1];
- the type of analysis performed to compute the power uprate (point design analysis or spectrum analysis).

Tabel A.1 – PWR competitor designs

	UO_2			HYDRIDE (U-Th-Zr-hydride)		
Configuration →	**Standard**		**Annular**	**Standard**		**Inverted**
Type of analysis	Point design (from [1])	Spectrum design	Spectrum design	Spectrum design		Point design
Power uprate relative to reference pin oxide (%)	0	+26%	+50%	+50% (w/o neutronics)	+24% (estimate accounting for neutronics)	up to +55%
D[31] (mm)	9.5	6.5	8.63(i); 15.37(o)	5.9	8	10
P/D	1.33	1.39	1.07	1.4	1.3-1.4	1.46
Neutronic constraints?	Met	Met	Met	Not applied	Met	Met
Cycle length (months)	18	~14	18	~10	~12	18
Enrichment	5%	5%	8-9%	12.5%	12.5%	17.5%

A.6 Design constraints

Design constraints used for the inverted point design shown in Figure A.2 are summarized in Table A.2. Some of them were used in the estimate of the maximum attainable power of the inverted point design, while others are still under investigation and will be added next.

[31] Diameter and pitch are defined as follows:
- *D*: fuel rod diameter for standard and annular geometries (for annular geometry an inner and an outer diameter are presented); cooling channel diameter for inverted geometry;
- *P*: fuel rod pitch for standard and annular geometries; cooling channel pitch for inverted geometry;

Table A.2 – Design constraints used for inverted point design		
Already in use		**Will be added**
Geometric	**Non-geometric**	
Duct thickness, 9 mm	Peak fuel T, 650ºC	CHF
Duct-fuel gap thickness, 3 mm	Peak clad T, 350°C	Core pressure drop
Clad thickness, 0.6 mm	PCT during LOCA, 1204°C	Maximum coolant velocity
Cladding-fuel gap thickness, 0.2 mm	Void react coefficient ,<0	
Fuel web thickness, 2 and 3 mm	Cycle length, 18 months	
Fuel block height, 20 cm		

The main reason why some constraints have not been used in the computation of the maximum attainable power is that the TT design has not been finalized yet. The geometry of the TTs, particularly the twist ratio and the spacing between successive TTs, strongly affect the CHF and pressure drop performance of the inverted core. Likewise, the maximum coolant velocity limit, which is imposed to protect the TTs from excessive mechanical stresses, will be fixed once the investigation on TTs design is performed.

A.7 Preliminary result

Figure A.3 shows the variation of the peak fuel temperature with the cooling channel pitch, for different core power levels. Besides the main x-axis, a secondary x-axis is shown: it contains the fuel web thickness which, being defined as the thickness of fuel comprised between two adjacent cooling channels, is function of the cooling channel pitch (main x-axis), cooling channel diameter (fixed to 10 mm), cladding wall thickness (fixed to 0.6 mm per Table A.2) and fuel-clad gap width (fixed to 0.2 mm per Table A.2).

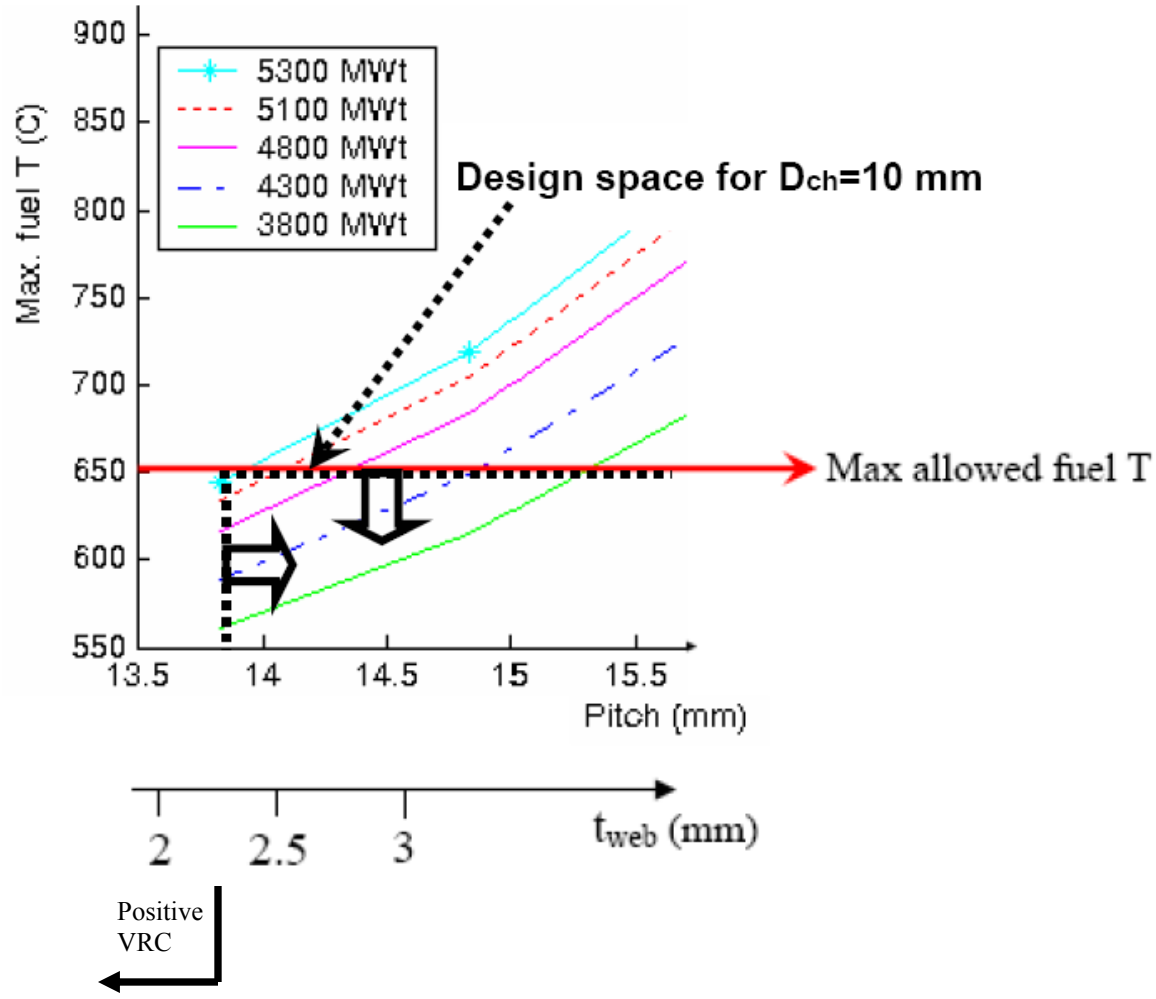

Figure A.3 – Graphic representation of maximum core power attainable by the inverted point design of Figure A.2

It can be seen that the maximum power attainable by a core fueled with inverted assemblies having the point design geometry shown in Figure A.2 is about 5300 MW_t. This value is however a preliminary result since the constraints shown in the last column of Table A.2 are still to be applied and they may reduce such power.

The big arrows in Figure A.3 define the allowed design space for the point design investigated: such design space is delimited by a minimum allowed pitch and a maximum allowed fuel temperature. The minimum pitch, equal to 13.8 mm, prevents the inverted design under investigation to have a positive void reactivity coefficient (VRC), which affects designs having high H/HM ratios[32]. In fact, for a fixed cooling channel diameter, when the pitch becomes too small the amount of heavy metal per unit cell is insufficient to guarantee a small H/HM ratio, resulting in a positive void reactivity coefficient.

[32] H and HM are the hydrogen and heavy metal atom density respectively.

Beside the VRC, also the fuel web thickness imposes a lower limit to the cooling channel pitch. In fact, if the fuel web thickness is too small, the strength of the resulting fuel block may be insufficient to sustain the mechanical stresses arising during manufacture, transport and assembly. For this reason, based on structural strength considerations, the fuel web thickness was limited to 3 mm (conservative limit) and 2 mm (optimistic limit). As explained above, however, the VRC constraint was found to be more limiting than the fuel web thickness constraint.

A.8 Work being performed

The inverted core design effort is currently focused on the following tasks:

- elaboration of pressure drop and CHF calculation techniques in order to use these parameters as power limiting constraints;
- TT design optimization;
- development of a code able to automatically perform the calculation of the maximum attainable power for multiple inverted geometries.

References

[1] Seabrook Power Station Updated Safety Analysis Report, Revision 8, 2002.

[2] Personal communication: R.E. White (FPL) to P. Ferroni (MIT). September 2006.

[3] B. Corder, "Westinghouse Model F Steam Generator General Information", Attachment 1 of "Callaway Plant, Engineering Technical Procedure, ETP-BB-01309 Steam Generator Eddy Current Testing Acquisition and Analysis Guidelines". January 2003. Available at NRC electronic library. ADAMS No. ML032320341.

[4] M. Yamawaki et al., Development of U-Th-Zr Alloy Hydrides as Alternative Thorium-base Fuel and MA Burning Target Fuel. Proc. Of the Int. Conference on Future Nuclear Systems, GLOBAL'99, Jackson Hole, WY, August 29-September 3, 1999.

[5] B. Tsuchiya et al., Thermal Diffusivity Measurements of Uranium-Thorium-Zirconium Hydride. Journal of Alloys and Compounds 312 (2000), 104-110.

[6] NUREG/CR-6150, SCDAP/RELAP5/MOD3.1 Code Manual Volume IV: MATPRO - A Library of Materials Properties for Light Water Reactor Accident Analysis. Idaho National Engineering Laboratory, November 1993.

[7] T. Yamamoto et al., Development of new reactor fuel materials: hydrogenation properties of U-Th-Zr alloys and neutron irradiation effects on their hydrides. Journal of Nuclear Materials 247 (1997) 339-344.

[8] C. Stewart, VIPRE-01: A Thermal Hydraulic Code for Reactor Cores. Vol.2: User's Manual. 1989.

[9] M.S. Kazimi, N.E. Todreas, "Nuclear Systems I, Thermal Hydraulic Fundamentals", Taylor & Francis, third printing, 1993.

[10] K. Konashi et al., "Thermodynamic Stability of $ThZr_2H_x$ at High Temperature", Journal of Physics and Chemistry of Solids 66 (2005) 625-628.

[11] P. Ferroni, N.E. Todreas, "Steady State Thermal Hydraulic Analysis of Hydride Fueled BWRs". Center of Advanced Nuclear Engineering Systems (CANES), MIT-NFC-PR-079. 2006.

[12] K. Konashi, M. Yamawaki, "The Development of Thorium Hydride Fuel", Characterization and Quality Control of Nuclear Fuels, edited by C. Ganguly and R.N. Jayaraj, (Allied Publishers Pvt. Ltd. 2004) 92-106.

[13] M. Visosky, M. S. Kazimi, P. Hejzlar, "Actinide Minimization Using Pressurized Water Reactors", Center of Advanced Nuclear Engineering Systems (CANES), MIT-NFC-PR-085, June 2006.

[14] T. K. Kim et al. "Benchmark Comparisons of Deterministic and Monte Carlo Codes for a PWR Heterogeneous Assembly Design", PHYSOR 2004, Chicago, IL, April 25-29, 2004.

[15] RELAP 3D© Code Manual. Volume 1: Code Structure, System Models, and Solution Methods. Idaho National Laboratory. Revision 2.3. Idaho Falls, ID, 2003.

[16] L. Heins, Framatome ANP GmbH, "Core Damage Extent Analysis to Fulfill an Additional LOCA Requirement", SEG FSM Topical Meeting on LOCA Issues, Argonne National Laboratory, May 25-26, 2004.

[17] NUREG-1793, "Final Safety Evaluation Report Related to Certification of the AP1000 Standard Design", September 2004.

[18] N. Todorova, K. Ivanov, B. Taylor, "Pressurised Water Reactor Main Steam Line Break (MSLB) Benchmark". Nuclear Engineering Program, Pennsylvania State University. NEA/NSC/DOC(2003)21.

[19] Seabrook Station Facility Operating License NPF-86 License Amendment Request 04-03, Application for Stretch Power Uprate. March 17, 2004. Available at NRC electronic library. ADAMS No. ML040860307.

[20] Personal communication: G. Myers (FPL) to P. Ferroni (MIT). July 2007.

[21] Seabrook Station Response to Request for Additional Information Regarding License Amendment Request 04-03, Application for Stretch Power Uprate. October 12, 2004. Available at NRC electronic library. ADAMS No. ML042890281.

[22] Seabrook Power Station Updated Final Safety Analysis Report. Revision 7, 2001. Available at NRC electronic library. ADAMS No. ML012180289.

[23] Personal communication: P.A. Bergeron (AREVA) to P. Ferroni (MIT). July 2007.

[24] Attachment 1 of "Callaway Plant, Engineering Technical Procedure, ETP-BB-01309 Steam Generator Eddy Current Testing Acquisition and Analysis Guidelines". Attachment titled:

"Westinghouse Model F Steam Generator General Information", by Brad Corder, January 2003. Available at NRC electronic library, ADAMS No. ML032320341.

[25] E. Shwageraus, "Rethinking the Light Water Reactors Fuel Cycle", PhD thesis, Massachusetts Institute of Technology. September 2003.

[26] M.A. Tremblay, J.P. Gorski, "Seabrook Station Cycle 5 Nuclear Design Report", YAEC-1927, Yankee Atomic Electric Company, Auburn, MA, November 1995.

[27] G. Youinou, A. Vasile, "Plutonium Multirecycling in Standard PWRs Loaded with Evolutionary Fuels", Nuclear Science and Engineering 151 (2005) 25-45.

[28] FPL Energy-NRC meeting, "Seabrook Station Stretch Power Uprate", March 3, 2004. Available at NRC electronic library. ADAMS No. ML040630431.

[29] NUREG/IA-0106 TEC/L/0471/R91, "Assessment of PWR Steam Generator Modelling in RELAP5/MOD2. Prepared by J.M. Putney, R.J. Preece, national Power Technology and Environmental Centre, United Kingdom. Published by US NRC. June 1993.

[30] RELAP 3D© Code Manual. Volume 5: User's Guidelines. Idaho National Laboratory. Revision 2.3. Idaho Falls, ID, 2003.

[31] AP1000 Design Control Document, Revision 14, 2004. Available at NRC electronic library, ADAMS No. ML050750282.

[32] E. Greenspan et al., "Feasibility of Recycling Plutonium and Minor Actinides in Light Water Reactors Using Hydride Fuel". NERI-Project No. 2006-065. Quarter 4 Report. April 30, 2007.

[33] Fuel safety Criteria in NEA Member Countries, Compilation of Responses Received from Member Countries. Nuclear Energy Agency. NEA/CSNI/R(2003)10. March 2003. Available online at: http://www.nea.fr/html/nsd/docs/2003/csni-r2003-10.pdf

[34] P. Hejzlar, N. Todreas, "Response to Letter to the Editor on the round table discussion on reactor power margins published in Nuclear Engineering and Design 163 (1–2) 1996". Nuclear Engineering and Design 201 (2000) 347-352.

[35] Pope, M.A., Yarsky P.J., Driscoll M.J., Hejzlar P. and Saha P., "An Advanced Vented Fuel Assembly Design for GFR Application," ANS Trans., Vol. 92, p. 211, San Diego, USA, June 5-9, 2005.

[36] J. Malen, N. Todreas, P. Hejzlar, P. Ferroni, A. Bergles, "Thermal Hydraulic Design of a Hydride-fueled Inverted PWR Core", accepted for publication in Nuclear Engineering and Design, 2009.

4. Materials Analysis

This section is organized as follows:

- Section 4.1: Objectives of the materials analysis;
- Section 4.2: Fabrication and characterization of uranium thorium zirconium hydrides;
- Section 4.3: Transient hydride fuel behavior in LWRs;
- Section 4.4: Kinetics of hydrogen desorption from zirconium hydride;
- Section 4.5: Zircaloy cladding compatibility with hydride fuel;
- Section 4.6: Oxidation behavior of hydride fuel in high temperature steam;
- Section 4.7: Irradiation plans for liquid metal bonded hydride fuel rod.

Each of these sections is self-contained – has its own equations, figures, tables and references numbering.

4.1 Introduction

The primary objective of the material analysis, as originally defined, was to investigate the compatibility of hydride fuel with Zircaloy clad and with water under typical PWR operating conditions. For this purpose we have located a damaged unused TRIGA fuel at the University of California campuses at both Irvine and Davis and received DOE agreement to transfer the fuel element from Davis to Berkeley. Unfortunately, we encountered numerous administrative hurdles first by DOE and later by Davis and Berkeley and did not succeed getting the fuel to this date. Consequently, we have modified the plan for the material analysis as reported below.

Initially two uranium-thorium-zirconium hydride fuel samples were fabricated in our lab based on recommendations from the neutronics study. The fabricated fuels were further characterized through multiple techniques to develop a deep understanding of the material systems and extract parameters and information that would govern its behavior during reactor operation.

Also a coupled transient heat transfer and hydrogen diffusion study was performed at the fuel level in order to characterize the behavior of the material under power transients. The analysis maps the temperature, hydrogen concentration and stress across the fuel during the power transient. The major differences between the oxide and hydride type fuels and the advantages of the latter are pointed out.

Another set of experiments was aimed at determining the kinetics of hydrogen desorption from the hydride fuel. This is an important phenomenon that needs to be understood in order to be able to predict the fuel behavior and cladding pressure buildup during transient scenarios.

Compatibility of liquid metal bonded hydride fuel with Zircaloy cladding is an essential component of this feasibility study. Zirconium getters hydrogen very aggressively and current LWR cladding failures are related to hydrogen pickup of cladding from the hydrogen produced during the waterside corrosion. Therefore an alloy of lead-tin-bismuth (Pb-33wt%Sn-33wt%Bi) was proposed as the gap filling material in order to retard the kinetics of hydrogen transfer from hydride fuel to the cladding. An experimental setup is built to test the effectiveness of this approach.

An investigation of the kinetics of oxidation of the hydride fuel exposed to high temperature steam in case of severe accident has been initiated but not completed. A plan for irradiation and post irradiation examination of the liquid metal bonded hydride fuel was also developed.

4.2 Fabrication and Characterization of Uranium Thorium Zirconium Hydrides

3.2.1 Introduction

Hydride nuclear fuels consist of metallic uranium particles dispersed in a hydride matrix. In the case of TRIGA fuel, the matrix consists solely of the δ-zirconium hydride ($ZrH_{1.6}$) phase. Hydride matrices have higher hydrogen atomic densities when compared to PWR or BWR coolants, and act as effective moderators to enhance the thermalization of neutrons in fission reactors. This allows more compact core designs with high power density, since a considerable fraction of the water moderator can be replaced with hydrogen within the fuel. In addition to higher thermal conductivity compared to the oxide fuels, hydride fuels also exhibit thermally-induced hydrogen up-scattering that accompanies Doppler feedback, which in turn provides a negative prompt temperature coefficient of reactivity [1].

Uranium-thorium-zirconium hydride fuel has been proposed as an optimized matrix for the deep burn of plutonium and minor actinides [2-5]. The proposed fuel could achieve TRU (transuranic elements) destruction fractions as high as twice those realized with MOX (mixed oxide) fuel. Unlike MOX fuel, it is also possible to realize infinite cycles of partitioning and transmutation with the hydride fuel without the risk of large positive reactivity coefficients as the cycles progress [6].

3.2.2 Fuel fabrication

Two uranium-thorium-zirconium hydride fuels of the overall chemical formulae $(UTh_4Zr_{10})H_{1.9}$ and $(U_4Th_2Zr_9)H_{1.5}$ have been fabricated in order to investigate and characterize the microstructure and the corresponding phases forming the material. Fuel fabrication was performed in Idaho National Laboratory's (INL) Materials and Fuels Complex (MFC). All the fabrication activities were performed either inside fume hoods with continuous air monitoring or in negative-pressure gloveboxes.

Two alloys of uranium-thorium-zirconium were prepared by arc melting of high-purity metal feedstock (>99%) in an argon glovebox under 4 ppm oxygen. The metals were initially acid treated so that any impurities and scaling on the surface were removed. Arc melting was done through the arc-lift process where the solidified buttons were turned 5 times and re-melted to achieve good homogeneity. Between each melting step, the surface of the button was abraded to remove impurities agglomerated at the surface. Arc melting resulted in melt temperatures in excess of 4000 °C. The melt was then quickly solidified in a copper hearth, resulting in a quenched microstructure with dendrite formation. According to the ternary phase diagram of the U-Th-Zr system [7], both of the alloys at equilibrium are in the γ(U+Zr) + α-Th two phase region. The γ phase is a solid solution of uranium and zirconium with a body-centered cubic unit cell, whereas the α-thorium phase has a face-centered cubic unit cell.

The arc-melted alloys were cut into disks of 2 mm thickness prior to hydriding in order to reduce the diffusion path length of hydrogen atom (diffusion-limited hydriding kinetics are assumed).

The metal disks underwent hydriding in a conventional tube furnace under 1 atm of hydrogen gas for 4 hours. Furnace temperature was initially set at 900 °C and was gradually reduced to 500 °C over the hydriding period. Since the hydriding process is diffusion-limited high temperatures were advantageous. Also, the material was able to better withstand the increase in volume at higher temperatures while maintaining its physical integrity. On the other hand, the furnace temperature had to be reduced eventually in order to increase the activity of hydrogen in the solid phase, and thus achieve higher hydrogen-to-metal (H/M) ratios. Figure 1 illustrates two of the hydride discs thus fabricated.

Figure 1. $(UTh_4Zr_{10})H_{1.9}$ fuel disks fabricated at INL. The disk to the left has experienced cracking due to severe volume expansion.

The detailed composition of the fuels is presented in Table 1. Actual H/M ratios were determined by weighing the samples prior to and after the hydriding process. The theoretical H/M ratios are calculated based on the assumption that the two hydride phases forming the fuels are δ-$ZrH_{1.6+x}$ and $ThZr_2H_{7-x}$ while uranium remains metallic (α-U). Volume fractions of each phase and the fuel density are all calculated based on the crystal structure of the aforementioned three different phases in the fuel. The theoretical density of the $(UTh_4Zr_{10})H_{1.9}$ is in good agreement with the experimental value of 7.55 gr/cm^3 determined by Tsuchiya et al. [8].

Table 1. Detailed Composition and Calculated Densities for $(UTh_4Zr_{10})H_{1.9}$ and $(U_4Th_2Zr_9)H_{1.5}$ Fuels.

	$(UTh_4Zr_{10})H_{1.9}$	$(U_4Th_2Zr_9)H_{1.5}$
Theoretical H/M† ratio	2.08	1.47
Theoretical H/(Zr+Th) ratio	2.23	2.00
Actual H/M ratio	1.93	1.55
Actual H/(Zr+Th) ratio	2.07	2.11
Vol% α-U	4.49	20.14
Vol% δ-$ZrH_{1.6}$	11.75	32.92
Vol% $ThZr_2H_{7-x}$	83.76	46.93
Fuel Density [gr/cm^3]	7.57	9.10

† M=U+Th+Zr

3.2.3 Characterization

3.2.3.1 X-ray diffractometry

XRD samples were prepared by depositing fuel powder on a low background silicon single-crystal sample holder using slurry of powder and ethanol. Samples were also mixed with lanthanum hexaboride (LaB_6 SRM 660a) powder to be used as internal standard during pattern refinement. High-resolution diffraction patterns were obtained using a Phillips PANalytical X'Pert Pro instrument with a Cu K_α source.

Rietveld refinement was performed on the experimental patterns for the two fuels. Formation of $ThZr_2H_{7-x}$, δ-$ZrH_{1.6+x}$, α-U, and minute amounts of ε-UH_3 was confirmed. Detailed results are presented in Table 2. The lattice parameter of α-U and ε-UH_3 phases could not be accurately determined for the $(UTh_4Zr_{10})H_{1.9}$ fuel due to the small volume fraction of these phases in this fuel. None of the following phases (accompanied by the corresponding space group) were detected in either of the fuels: ε-$ZrH_{1.8-x}$ (*I4/mmm*); δ-UH_3 (*Pm-3n*); δ-UZr_2 (*P6/mmm*); ZrH (*P42/n*); ThH_2 (*I4/mmm*); Th_4H_{15} (*I-43d*).

Table 2. Lattice Parameter of Phases Present in the $(UTh_4Zr_{10})H_{1.9}$ and $(U_4Th_2Zr_9)H_{1.5}$ Fuels Determined through Rietveld Refinement.

Phase	Space Group	$(UTh_4Zr_{10})H_{1.9}$	$(U_4Th_2Zr_9)H_{1.5}$	Reference
$ThZr_2H_{7-x}$	*Fd-3m*	a = 9.186(2) Å	a = 9.184(4) Å	a = 9.154 Å [9]
δ-$ZrH_{1.6}$	*Fm-3m*	a = 4.783(1) Å	a = 4.762(2) Å	a = 4.777 Å [10]
α-U	*Cmcm*	N/A	a = 2.855(4) Å	a = 2.854 Å [11]
		N/A	b = 5.862(4) Å	b = 5.869 Å
		N/A	c = 4.956(7) Å	a = 4.955 Å
ε-UH_3	*Pm-3n*	N/A	a = 6.655(1) Å	a = 6.627 Å [12]

The experimental powder patterns along with the results of the refinement fit are shown in Figure 2 for both fuels. Structure factor calculation (SFC) could be performed to match the experimental XRD intensities from different phases to the calculated volume fractions presented in Table 1. SFC was done specifically comparing the 022 type reflection from the $ThZr_2H_{7-x}$ phase and the 021 and 110 reflections from the α-U phase in the $(U_4Th_2Zr_9)H_{1.5}$ fuel. Scattering from hydrogen atoms was neglected in this calculation since the atomic scattering factor from this element is negligible compared to that of the other species. The resulting normalized intensities agree well with the experimental values (Table 3).

Table 3. Comparison of Peak Intensities between Experimental Results and Structure Factor Calculations.

Phase	Reflection	Experimental	SFC
$ThZr_2H_{7-x}$	022	1	1
α-U	021	0.75	0.79
	110	0.32	0.27

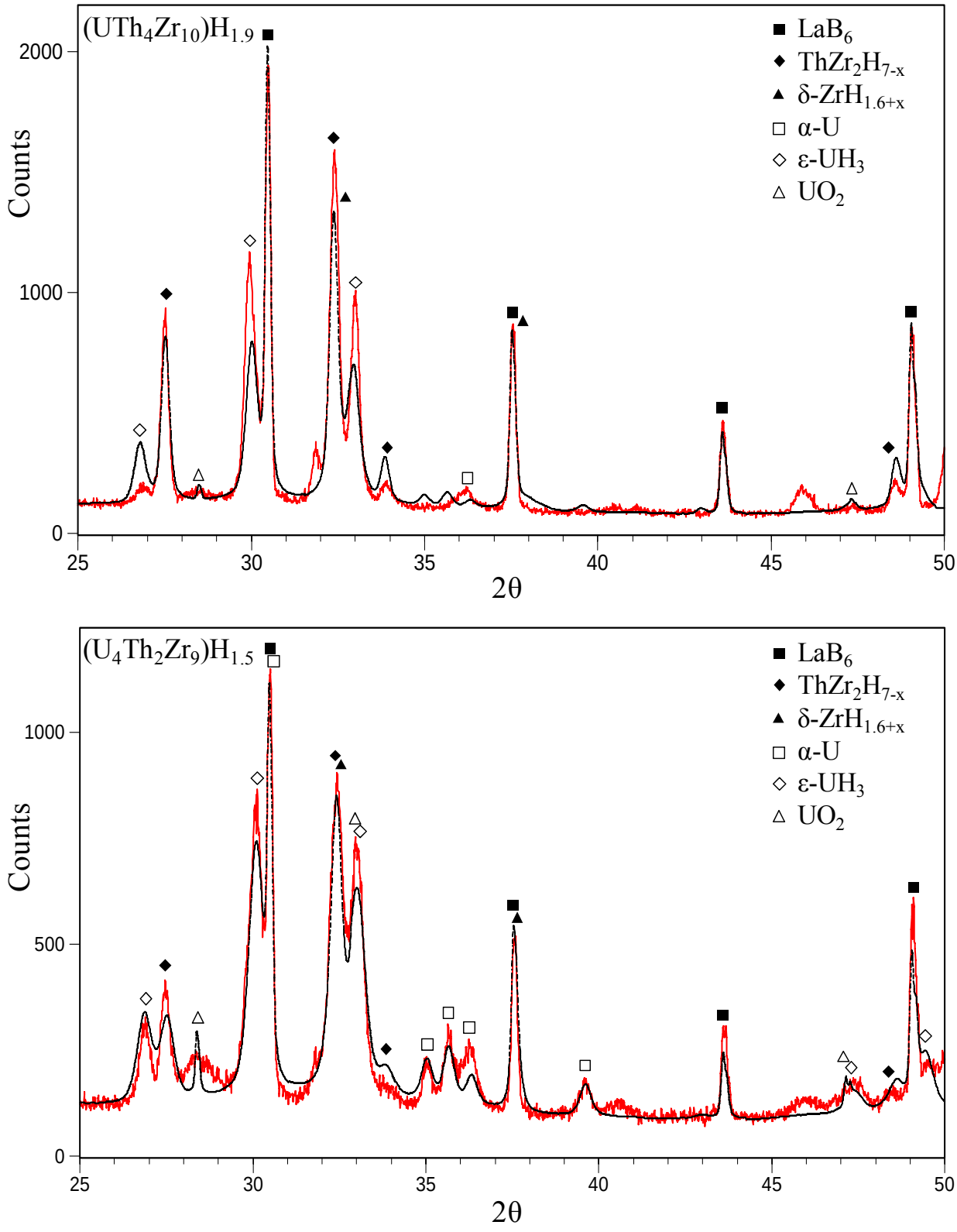

Figure 2. Powder x-ray diffraction patterns for $(UTh_4Zr_{10})H_{1.9}$ and $(U_4Th_2Zr_9)H_{1.5}$ fuels along with Rietveld refinement fit.

3.2.3.2 Scanning electron microscopy

Scanning electron microscopy was performed on a JEOL instrument model JSM-5610 equipped with secondary and backscatter electron detectors and an Oxford ISIS EDS (energy dispersive x-ray spectroscopy) system. The accelerating potential during operation was 15 kV. Figure 3 shows the backscattered electron image of the two fuels. The morphology of both fuels showed three distinct phases present. Each region corresponds to the one of the structures identified in the previous section, where the phases from brightest to darkest are α-U, $ThZr_2H_{7-x}$, and δ-$ZrH_{1.6+x}$ respectively. This is the case since the intensity of the backscattered image is proportional to the average atomic number in each phase. This is also in agreement with the corresponding EDS spectra.

Severe microcracking is observed in the microstructure of the $(UTh_4Zr_{10})H_{1.9}$ fuel, a result of volume expansion during processing. The cracks are both transgranular and intergranular, forming a network that expands across the microstructure. However, no sign of cracking is observed in the microstructure of $(U_4Th_2Zr_9)H_{1.5}$. This is in agreement with the calculated percent volume expansions of 22.4% and 17.7% upon hydriding for $(UTh_4Zr_{10})H_{1.9}$ and $(U_4Th_2Zr_9)H_{1.5}$ fuels, respectively. Solubility of thorium in the γ(U+Zr) phase and zirconium and uranium in the α-Th phase are assumed to be zero in this analysis. The volume expansion is then calculated based on the change in the molar volume of the phase prior to and after hydriding. The extent of cracking for $(UTh_4Zr_{10})H_{1.9}$ fuel significantly worsened over time after hydriding when the material was stored at room temperature. This is due to residual stresses in the material. However no such behavior was observed in case of the $(U_4Th_2Zr_9)H_{1.5}$ fuel.

The morphology of both fuels shows elongated grains, but this feature is much more noticeable in the $(U_4Th_2Zr_9)H_{1.5}$ fuel. This morphology is due to the formation of dendrites during the solidification of metal alloys. Uranium particles are evenly dispersed in small scale in $(UTh_4Zr_{10})H_{1.9}$ fuel (≤1 μm in diameter) while in $(U_4Th_2Zr_9)H_{1.5}$ fuel the uranium particle distribution is random with large particle size. Similar characteristics can be seen for δ-$ZrH_{1.6+x}$ grains of different sizes with an average diameter in the range of a few micrometers. These micrographs further show that the ternary $ThZr_2H_{7-x}$ phase is the dominant phase in both fuels. This major chemical phase resides approximately 85 vol% of the $(UTh_4Zr_{10})H_{1.9}$ sample where it is continuous. On the other hand only ~46 vol% of the $(U_4Th_2Zr_9)H_{1.5}$ sample constitutes this phase.

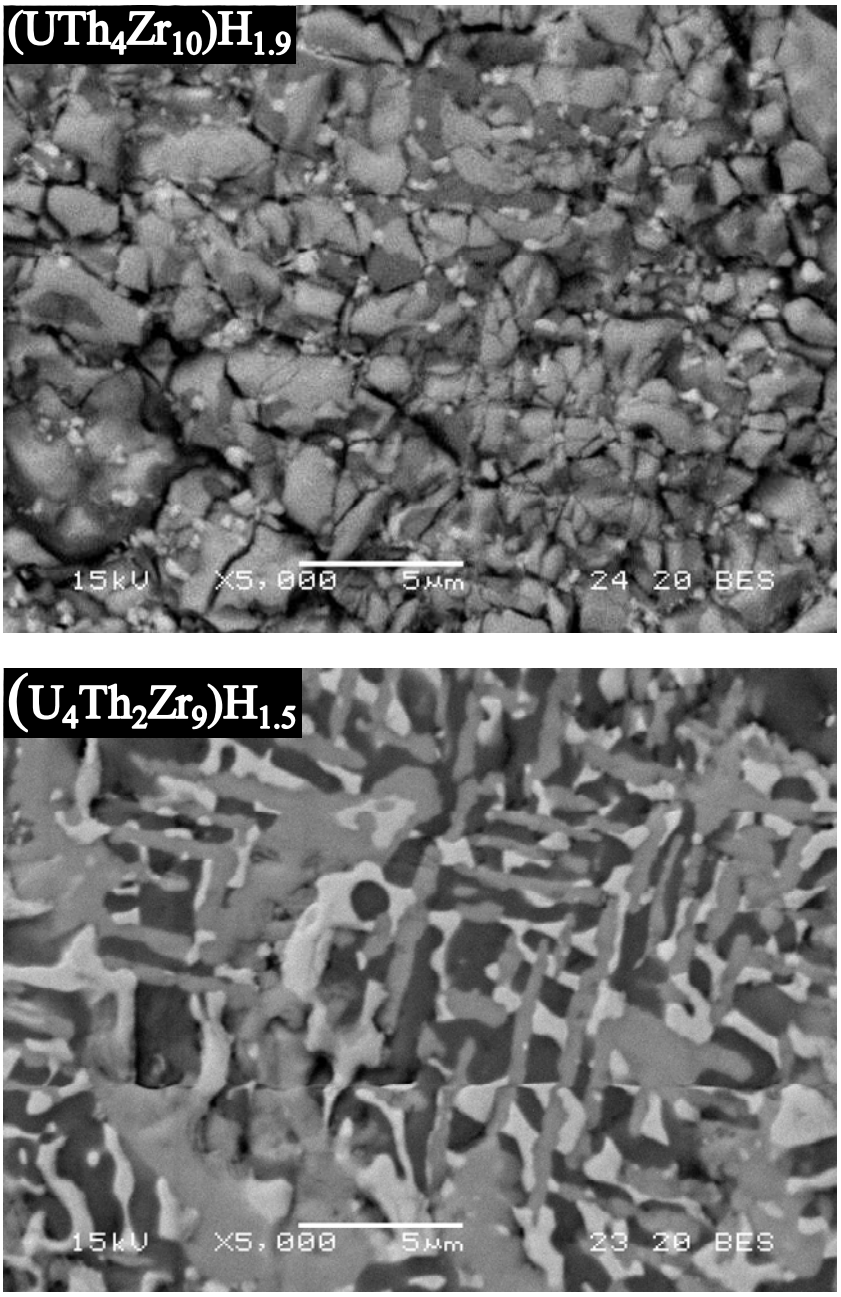

Figure 3. Backscattered electron image of $(UTh_4Zr_{10})H_{1.9}$ and $(U_4Th_2Zr_9)H_{1.5}$ fuels.

3.2.3.3 Transmission electron microscopy

Transmission electron microscopy was performed using a TECNAI-G2-F30 microscope with a 300 keV field emission gun. TEM images were recorded using a low scan CCD camera attached to a Gatan GIF 2000 image filter. Four TEM specimens were prepared through microtome cutting at thicknesses of 25 and 50 nm for each fuel. Thin samples are essential because of the significant electron beam attenuation by samples consisting of high atomic number elements. Powderized fuel was initially embedded in spur-resin in a micro-vial, which was then solidified

at 60 °C overnight. The microtome specimens were cut using the diamond blade of a Leica EM UC6rt instrument and were then placed on a 3mm copper grid supported by thin carbon film.

A bright field image of $(U_4Th_2Zr_9)H_{1.5}$ is presented in Figure 4. This image lacks any morphological information since the specimens were prepared starting from fine powder, and during microtomy further cracking occurred. Dislocation-free grains of $ThZr_2H_{7-x}$ and δ-$ZrH_{1.6+x}$ phase are shown with good coherence at the grain boundary. EDS was performed by the TEM in scanning mode, confirming the composition of the grains shown in the image.

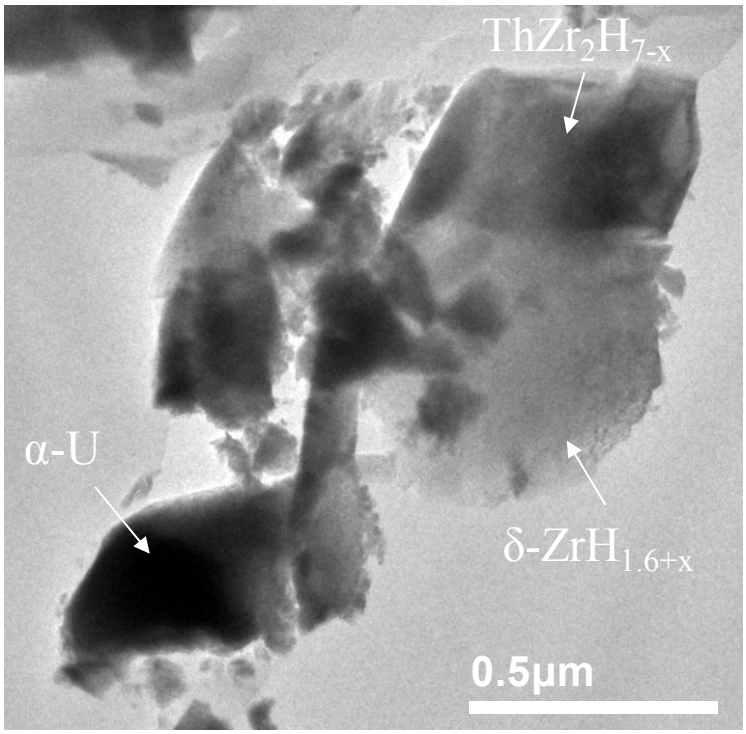

Figure 4. Bright field image of $(U_4Th_2Zr_9)H_{1.5}$ fuel.

High-resolution (HRTEM) images of $ThZr_2H_{7-x}$, δ-$ZrH_{1.6+x}$, and α-U phases were generated through phase contrast imaging. The microscope's spherical and chromatic aberration coefficients were reported as 1.2 mm and 1.4 mm by the manufacturer. Figure 5 shows the phase contrast image of the three phases forming the fuels along with the fast Fourier transformation of each image into reciprocal space. The extent of defocus for the $ThZr_2H_{7-x}$ phase contrast image is determined through analysis of contrast transfer function contours based on scattering from an amorphous region of the sample. No amorphous region was present during imaging of the δ-$ZrH_{1.6+x}$ or α-U phase, and Bloch wave computer simulation [13] was used instead to estimate the defocus value. This approach is shown in the middle section of Figure 5 where the phase contrast image of δ-$ZrH_{1.6+x}$ is matched by computer simulation at 25 nm sample thickness and -40 nm defocus.

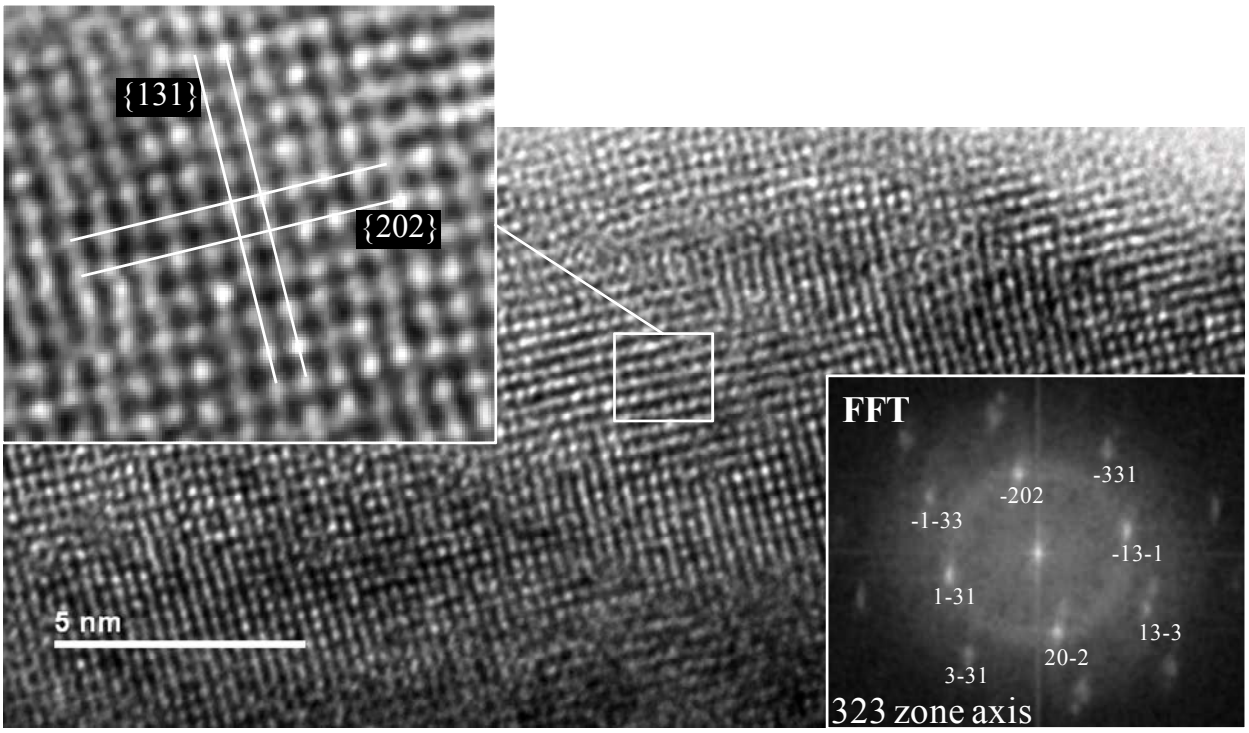
{131}
{202}
5 nm
FFT
-331
-202
-1-33
-13-1
1-31
13-3
20-2
3-31
323 zone axis

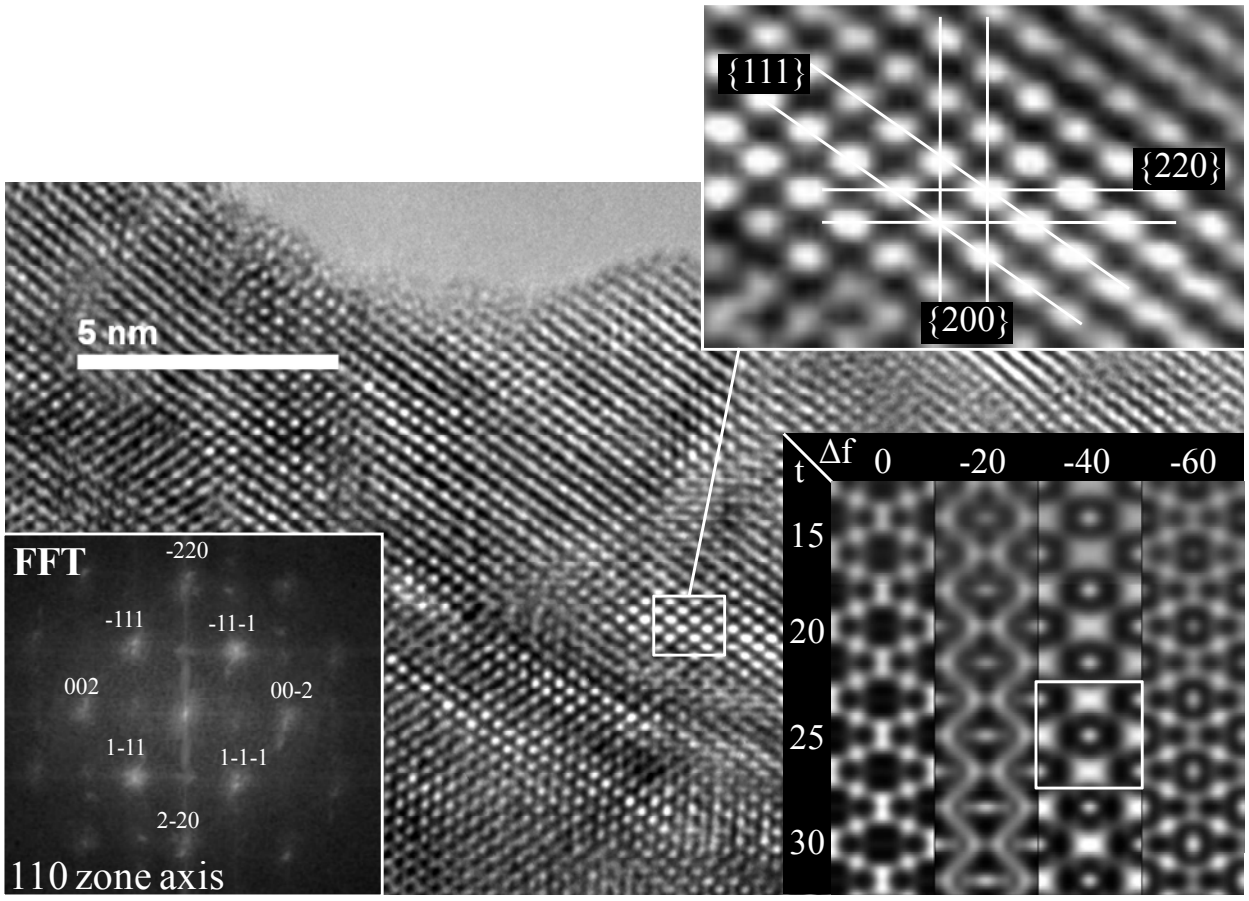
{111}
{220}
{200}
5 nm
FFT
-220
-111
-11-1
002
00-2
1-11
1-1-1
2-20
110 zone axis
t
Δf
0
-20
-40
-60
15
20
25
30

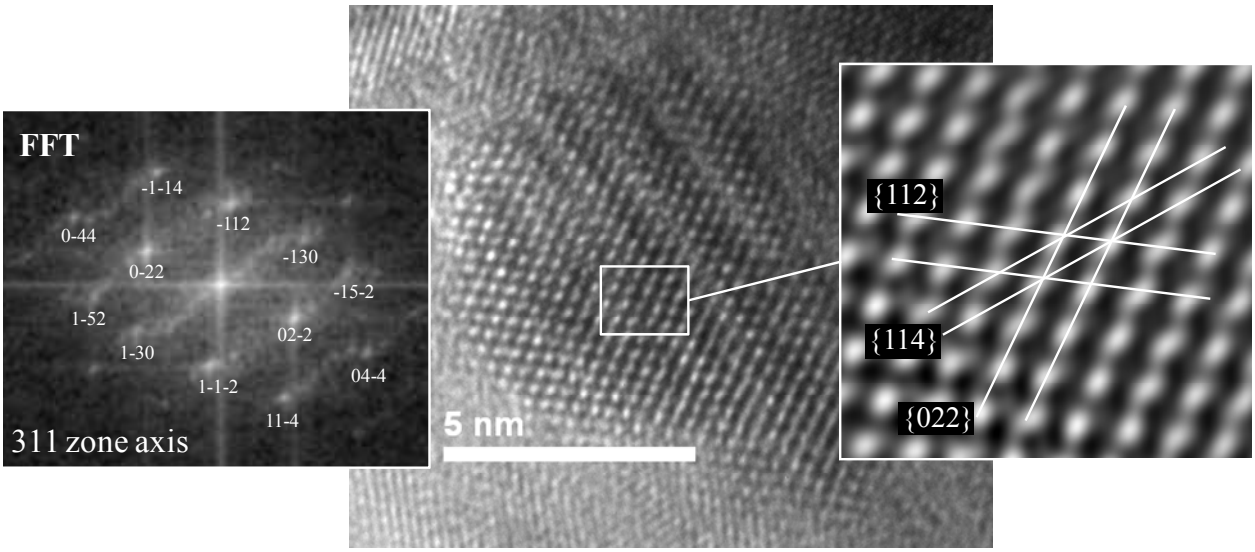

Figure 5. Phase contrast imaging on $(U_4Th_2Zr_9)H_{1.5}$ fuel. Top: 323 zone axis of $ThZr_2H_{7-x}$ phase (Δf=-100nm). Middle: 110 zone axis of δ-$ZrH_{1.6+x}$ along with Bloch wave computer simulation (Δf=-40nm). Bottom: 311 zone axis of α-U (Δf=-60nm).

The observations from HRTEM are in agreement with the XRD results, confirming the formation of $ThZr_2H_{7-x}$ and δ-$ZrH_{1.6+x}$. No sign of formation of tetragonal ε-$ZrH_{1.8}$ phase is observed. The FFT of the image corresponding to the uranium phase is representative of diffraction from an orthorhombic phase. This result rules out formation of significant amounts of cubic ε-UH_3.

3.2.3.4 Nanoscale dynamic stiffness mapping (DSM)

DSM (TriboScope nanoindenter, Hysitron, Minneapolis, MN) coupled with an atomic force microscopy controller (NanoScope IIIa, Veeco, Santa Barbara, CA) was used to determine the elastic modulus of the phases forming the uranium-thorium-zirconium hydride fuels. The technique provides topography as well as viscoelastic properties through storage and loss moduli mapping across the fuel microstructure at nanometer length scales. This was done by applying a sinusoidal electrostatic force acting on the spring-suspended center of the force-displacement transducer of the nanoindenter while contact mode imaging was conducted. A cube-corner diamond tip was attached to this transducer. The amplitude and the phase of the resulting transducer displacement signal were measured with a dual-channel lock-in amplifier, and this information was used to determine the local indentation moduli of the sample at each pixel of the imaging process. In the present case only the storage modulus (designated as elastic modulus) is reported due to negligible magnitudes of loss modulus found for the samples studied. The diamond tip radius used for imaging was calibrated by a standard quartz sample with an elastic modulus of 69.7 GPa. Balooch et al [14] provide detailed description of the instrument and the technique.

Two areal regions of 3.5x3.5 μm^2 and 10x10 μm^2 in size were investigated in the $(U_4Th_2Zr_9)H_{1.5}$ fuel, and the results are presented in Figure 6. The elastic modulus values are represented by the false color in the images. The variation of the elastic modulus (black spots) along the black

horizontal lines superimposed on the images is also shown for further clarification. Three distinct regions, corresponding to α-U, $ThZr_2H_{7-x}$, and δ-$ZrH_{1.6+x}$, are apparent from brightest to darkest, respectively. The microstructure in this set of images is directly comparable to what was previously characterized during backscattered scanning electron microscopy.

The elastic moduli of α-U and δ-$ZrH_{1.6+x}$ are reported as 202 GPa [15] and 130 GPa [16], respectively. The results of this study are in good agreement with the values reported previously for these two phases. The elastic modulus of the ternary $ThZr_2H_{7-x}$ phase has not been reported previously and the mean value is determined here as 172 GPa.

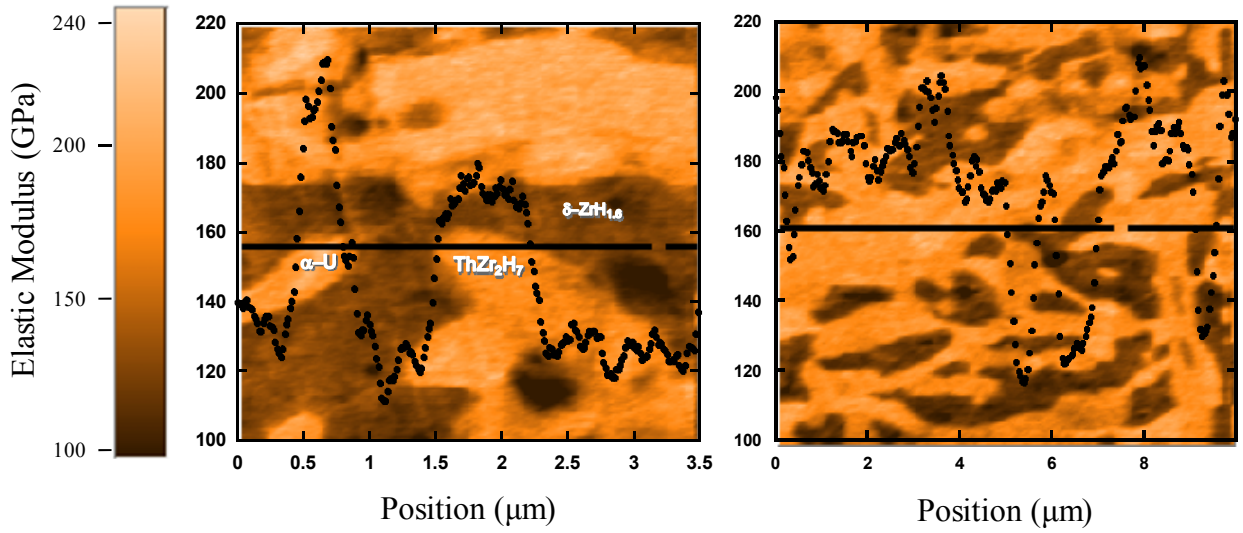

Figure 6. Elastic modulus mapping across the microstructure of $(U_4Th_2Zr_9)H_{1.5}$ fuel.

3.2.4 Discussion

Fuel fabrication could be improved by homogenization of the arc-melted metal alloys prior to hydriding in order to remove the dendritic structure. The hydriding process could also be greatly improved if the desired H/M ratio is initially established at high temperature and then maintained during the cool down. The diffusion-limited process takes place relatively quickly at high temperature under high pressure of hydrogen gas while the material is ductile enough to accommodate the large volume expansion. During the cool-down step, the hydrogen partial pressure should be continuously reduced to correspond to the desired H/M ratio. This inhibits formation of hydrogen concentration gradients that would in turn induce stress across the material. The equilibrium partial pressure of hydrogen with zirconium hydride and thorium-zirconium hydride is known [17, 18] as a function of temperature. At equilibrium, the activity of hydrogen in the gas and the two hydride phases is identical; therefore the exact H/M ratio in each phase could be determined. However, the equilibrium partial pressure of hydrogen changes by four orders of magnitude over the processing temperatures of these hydrides. Therefore, sophisticated instrumentation and control systems are necessary to execute this procedure.

The thermodynamic stability of the possible metal hydrides in this system increases as follows: UH_3, ThH_2, δ-$ZrH_{1.6+x}$, $ThZr_2H_{7-x}$ [19,20,21,22,23]. However, the thermodynamic stability changes as a function of H/M ratio. This result is in agreement with the characterization

observations, where only the latter two hydrides were observed. Uranium hydride is unstable above 420 °C (under 1 atm of H_2 gas). The residual uranium hydride formation, as detected by XRD analysis, is due to the presence of hydrogen in the furnace during the cool-down.

The actual H/M ratio in the $ThZr_2H_{7-x}$ phase is unknown. Bartscher et al. [9] have studied the $ThZr_2D_x$ system using neutron scattering and report the lattice parameter for the cubic unit cell as a function of different deuterium to metal ratios up to x = 6.3. Linear extrapolation of these results matches the determined lattice parameter of this phase to hydrogen stoichiometry of 7 (as in $ThZr_2H_7$) in both fuels.

The density of hydrogen in hydride nuclear fuels is of great importance since it replaces a part of the moderator and thus significantly affects the neutronic properties. Figure 7 shows the hydrogen and uranium atomic densities in different hydride fuels as a function of atomic percent uranium dispersed in the hydride matrix. Uranium-thorium-zirconium hydride fuels are superior to uranium-zirconium hydride fuels since similar uranium atomic densities could be achieved with higher hydrogen atomic densities.

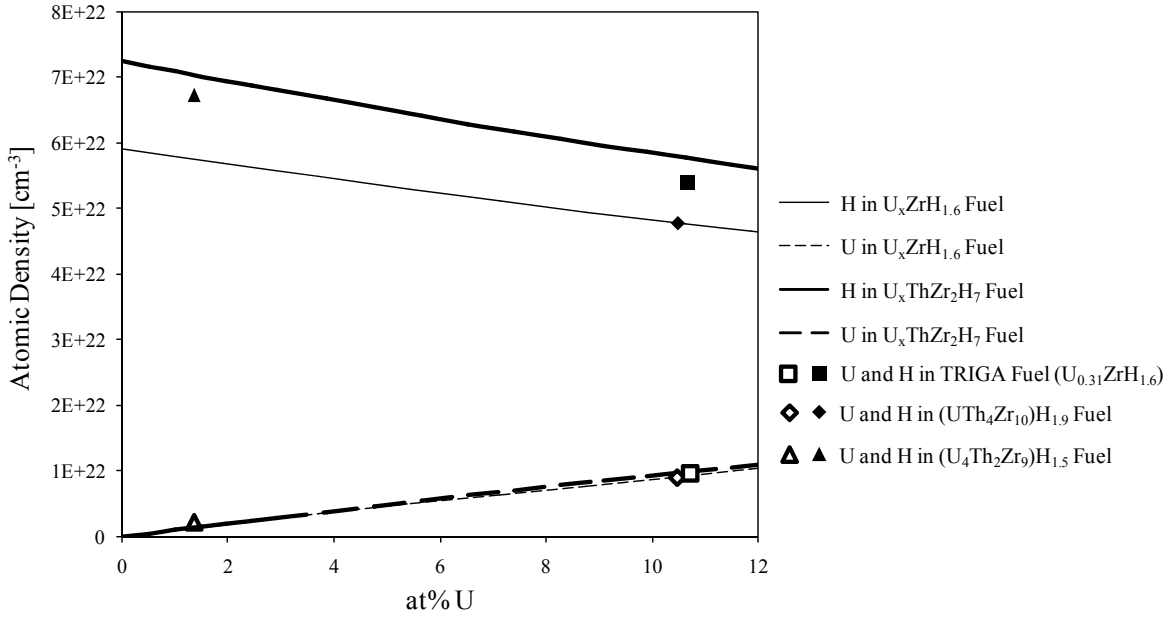

Figure 7. Hydrogen and uranium atomic density as a function of at% uranium metal in different hydride matrices.

3.2.5 Conclusions

Two uranium-thorium-zirconium alloys were arc-melted and then hydrided to form fuels with the nominal compositions of $(UTh_4Zr_{10})H_{1.9}$ and $(U_4Th_2Zr_9)H_{1.5}$. Powder XRD analysis showed both these fuels consisted of the α-U, δ-$ZrH_{1.6+x}$, and $ThZr_2H_{7-x}$ chemical phases with the last being the dominant in both. SEM and TEM (in bright-field and high-resolution mode) imaging confirmed the presence of these three phases. Atomic force microscopy along with nanoscale dynamic stiffness analysis performed on fuel specimens to map the Young's modulus across the microstructure revealed the elastic modulus of $ThZr_2H_{7-x}$ to be 172 GPa.

Uranium-thorium-zirconium hydride fuels appear to be superior to TRIGA fuel for power reactor

use since the hydride matrix is more stable with respect to dehydriding. Also, high uranium and hydrogen atomic densities are achieved in fuels containing thorium. Extensive study of the effects of irradiation on these fuels under typical light water reactor conditions is necessary in order to adequately understand their performance compared to TRIGA fuel and oxide fuels.

3.2.6 Acknowledgement

The aid and valuable technical insight of Dr. Mitchell Meyer and all the Fuels and Applied Science Building personnel at the Materials and Fuels Complex of Idaho National Laboratory is gratefully acknowledged.

3.2.7 References

1. F. Ganda, E. Greenspan, "Physics analysis of hydride fuel in PWR cores," *submitted to Nuclear Science and Engineering*, (2008).
2. F. Ganda, E. Greenspan, "Plutonium Incineration Capability of Hydride Versus MOX Fuel in PWR," *Procd. Global '05*, Tsukuba, Japan (Oct. 2005).
3. F. Ganda and E. Greenspan, "Incineration of Plutonium in PWR Using Hydride Fuel," *Proc. 2005 International Conference on Advances in Nuclear Power Plants ICAPP–2005*, Seoul, Korea (May 2005).
4. F. Ganda, E. Greenspan, "Plutonium Recycling in Hydride Fueled PWR Cores," *accepted for publication in Nuclear Engineering and Design*, (2008).
5. F. Ganda, E. Greenspan, "Neutronic Analysis of Hydride Fuelled PWR Cores," a*ccepted for publication in Nuclear Engineering and Design*, (2008).
6. F. Ganda, E. Greenspan, "Plutonium and Neptunium multi-recycling in PWR using hydride fuels," *Physor 2008, Interlachen, CH.* (2008).
7. T.A. Badaeva, G.K. Alekseenko, "Structure of Alloys of the Thorium-Uranium-Zirconium System," *Struct. Alloys Certain Systems Cont. Uranium Thorium*, pp.376-394, (1963).
8. B. Tsuchiya, J. Huang, K. Konashi, W. Saiki, T. Onoue, M. Yamawaki., "Thermal Diffusivity Measurement of Uranium-Thorium-Zirconium Hydride," *J. Alloy and Compounds*, **312**, pp.104-110, (2000).
9. W. Bartscher, J. Rebizant, A. Boeuf, R. Caciuffo, F. Rustichelli, J. Fournier, W. Kuhs, "Distribution of Deuterium in the Cubic Laves Phase $ThZr_2D_x$," *Journal of Less Common Metals*, **121**, pp.455-460 (1986).
10. R. Beck, "Zirconium-Hydrogen Phase System," *Trans. Am. Soc. Metals*, **55**, pp.542-555 (1962).
11. Sturken, Post., *Acta Crystallogr.*, **13**, 852, (1960).
12. W. Bartscher, A. Boeuf, R. Caciuffo, J. Fournier, W. Kuhs, J. Rebizant, F. Rustichelli, "Neutron Diffraction Study of Beta-UD_3 and Beta-UH_3," *Solid State Communications*, **53** (4), pp.423-426, (1985).

13. J.M. Zuo and J.C. Mabon, Web-based Electron Microscopy Application Software: Web-EMAPS, Microsc Microanal 10(Suppl 2), 2004; URL: http://emaps.mrl.uiuc.edu/.
14. G. Balooch, G. Marshall, S. Marshall, O. Warren, S. Asif, M. Balooch, "Evaluation of a New Modulus Mapping Technique to Investigate Microstructural Features of Human Teeth," *Journal of Biomechanics*, **37**, pp.1223-1232, (2004).
15. ASM Handbooks, Vol 2., Properties and Selection: Nonferrous Alloys and Special-Purpose Materials.
16. S. Yamanaka, K. Yoshioka, M. Uno, M. Katsura, H. Anada, T. Matsuda, S. Kobayashi, "Thermal and Mechanical Properties of Zirconium Hydride," *J. Alloys and Compounds*, **293-295**, pp.23-29, (1999).
17. M. Simnad, "The U-ZrH_x Alloy: Its Properties and Use in TRIGA Fuel," *Nuclear Eng. Design*, **64**, pp.403-422 (1981).
18. K. Konashi, B. Pudjanto, T. Terai, M. Yamawaki, "Thermodynamic stability of $ThZr2H_x$ at high temperature," *Journal of Physics and Chemistry of Solids*, **66**, pp.625-628, (2005).
19. C.J.M. Northrup, Jr., "The Hydrogen-Uranium System," *Journal of Physical Chemistry*, **79**, pp.726-731 (1975).
20. E. Wicke, K. Otto, "The Uranium Hydrogen System and the Kinetics of Hydride Formation," *Z. Phys. Chem., Neue Folge*, **31**, pp.222-248 (1962)
21. M. W. Mallett, I. E. Campbell, "The Dissociation Pressure of Thorium Dihydride in the Thorium-Thorium Dihydride System," *Journal of the American Chemical Society*, **73**, pp.4850-52, (1951).
22. 'W. Wang, D.R. Olander, "Thermodynamics of the Zr-H System," *Journal of American Ceramic Society*, **78** [12], pp.3323-28 (1995).
23. W. Bartscher, J. Rebizant, "Equilibrium and Thermodynamics Properties of The $ThZr_2$-H System," *Journal of the Less Common Metals,* **136**, pp.385-394, (1988).

4.3 Transient Hydride Fuel Behavior in LWRs

3.3.1 Introduction

Hydride nuclear fuels (uranium-zirconium hydride) have been successfully utilized in many research and test reactors as well as space programs. The added presence of hydrogen in the fuel provides neutron moderation within the fuel in addition to the traditional moderator. This allows displacement of moderator with fuel, effectively increasing power density. Hydride fuels also have a higher thermal conductivity than oxide fuels and feature a fuel-temperature-driven reactivity feedback due to fuel hydrogen neutron scattering; the latter effect accompanies Doppler feedback. Hydride fuel has also been proposed as an optimized matrix for the deep burn of plutonium and minor actinides. The proposed fuel could achieve TRU (transuranic elements) destruction fractions as high as twice that realized within MOX (mixed oxide) fuels [1].

Uranium - zirconium hydride fuel consists of metallic α-U phase dispersed in a δ-$ZrH_{1.6}$ matrix. The fuel is typically fabricated by massive hydriding of uranium zirconium alloys formed by arc melting of the metal components. Uranium inside the fuel remains metallic since the equilibrium partial pressure of the UH_3 phase at fuel processing temperatures is very high (pH_2 = 1atm for UH_3 at ~700K, where hydriding temperatures range from 800K – 1200K). Maximum heavy metal loading inside the fuel is limited to 45 vol% uranium which corresponds to the fuel composition of $U_{0.31}ZrH_{1.6}$. During operation of the reactor, the temperature gradient across the fuel drives the hydrogen to the cooler regions due to the large heat of transport of hydrogen in the δ-$ZrH_{1.6}$ phase (T_Q = 640K) [2]. Thermal conductivity of the fuel is a function of both temperature and hydrogen concentration, with a stronger dependence on the latter. The volumetric heat capacity has the same dependencies; however its dependence on the temperature is more marked. Hydrogen diffusivity is an exponential function of temperature with a small dependence on hydrogen concentration (site blocking by other hydrogen atoms during stochastic jumps).

It is therefore necessary to couple the heat conduction to the hydrogen diffusion in order to achieve accurate results in predicting the temperature and hydrogen concentration profiles both under steady state and transient operating conditions. Accurate modeling of the coupled transient behavior will provide detailed information of the stress across the fuel as well as the necessary information for predicting the possibility of excessive hydrogen release from the fuel during accidents.

3.3.2 Methodology

3.3.2.1 Hydride fuel properties

3.3.2.1.1 Thermal conductivity and volumetric heat capacity

The fuel is a composite structure of metallic α-uranium dispersed in a δ-zirconium hydride matrix. The thermal conductivity of the fuel can be calculated as the product of thermal diffusivity, density, and specific heat capacity of the composite material. These properties can be estimated using the rule of mixtures where thermal diffusivity and density are estimated on volume fraction basis and heat capacity on mass fraction basis, respectively. Therefore the overall thermal conductivity of the fuel can be estimated using the thermal properties of uranium as a function of temperature and zirconium hydride as a function of both temperature and H/Zr

ratio [3,4,5,6] as shown in Equation 1[1] (Fig. 1a). A similar approach can be used to determine the volumetric heat capacity of the fuel as function of temperature and H/Zr ratio in the composite fuel (Fig. 1b). The influence of burnup on these properties is unknown and therefore this analysis is applicable only to fresh fuel. Thermal conductivity is however expected to decrease as function of burnup since hydride fuel experiences large swelling rates, especially at low burnups. Hydride fuel also has good fission gas retention properties indicating that voids containing noble gases are form during operation. This is related to swelling and will further deteriorate the thermal conductivity.

$$k_{Fuel} = k_U \left(v_U + \frac{\kappa_{ZrH_{1.6}}}{\kappa_U}(1 - v_U) \right) \left(v_U + \frac{\rho_{ZrH_{1.6}}}{\rho_U}(1 - v_U) \right) \left(w_U + \frac{C_{p,ZrH_{1.6}}}{C_{p,U}}(1 - w_U) \right) \quad (1)$$

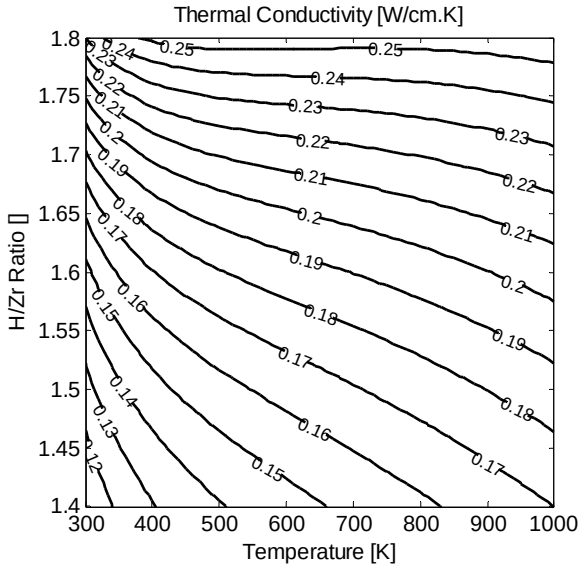

[1] Refer to the Table of notations in Section 6 for a description and respective units of all the variables discussed in the Equations throughout this paper.

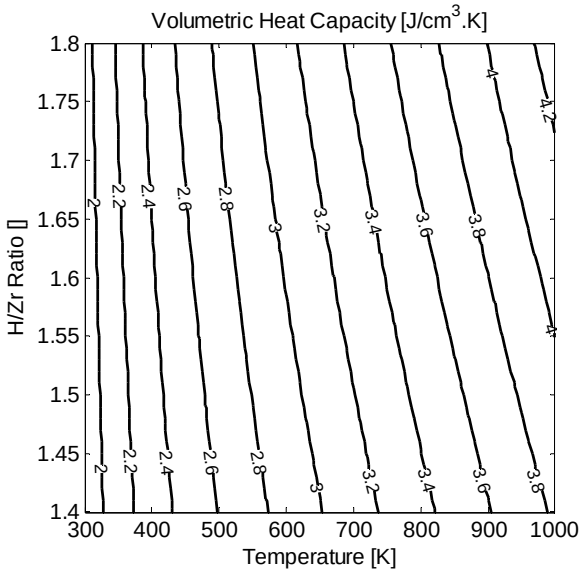

Figure 1. Thermal conductivity and volumetric heat capacity of the $U_{0.31}ZrH_x$ fuel as functions of temperature and H/Zr ratio.

3.3.2.1.2 Hydrogen diffusivity

The diffusivity of hydrogen in zirconium hydride has been measured over a relatively large range of temperatures and hydrogen concentrations by Majer et al. [7]. The only set of data corresponding to δ phase zirconium hydride (H/Zr ratio = 1.58) yields the diffusion coefficient as:

$$D = 1.53 \times 10^{-3} \exp\left(\frac{-58.8}{RT}\right) \qquad (2)$$

The Einstein diffusion model describes the diffusion coefficient as the following:

$$D = \frac{1}{6}\frac{\lambda^2}{\tau} \qquad (3)$$

where λ is the jump distance of the diffusing species and τ is the mean residence time in each site before a jump. The mean residence time is inversely proportional to the product of the number of available adjacent jump sites (η) and the jump frequency. The jump frequency is the product of vibration frequency of the species in that site (υ) with an Arrhenius factor that determines the probability of each vibration leading to a successful jump. Therefore, the pre-exponential factor in the diffusion coefficient can be expressed as:

$$D_\circ = \frac{1}{6}\lambda^2 \eta \upsilon \qquad (4)$$

η is the product of the number of adjacent jump sites (6, since hydrogen is on a simple cubic lattice inside the face centered cubic Zr unit cell where the overall structure corresponds to a Fd-3m space group) with the probability that the site is not currently occupied by another hydrogen atom. This probability can be determined from the stoichiometry and structure of the system; the pre-exponential term can therefore be estimated as:

$$D_{\circ} = \frac{1}{6}\lambda^2 6\left(1-\frac{C}{2}\right)\upsilon \qquad (5)$$

Activation energy for diffusion is essentially independent of hydrogen concentration, assuming the mechanism of diffusion doesn't change in the range of interest (H/Zr ratio from 1.5 to 1.7). The final expression that is used for the diffusion coefficient of hydrogen in δ-ZrH_x is the following:

$$D = 7.29\times10^{-3}\left(1-\frac{C}{2}\right)\exp\left(\frac{\text{-58.8}}{RT}\right) \qquad (6)$$

3.3.2.2 Heat conduction model

The transient radial heat equation for an axial slice of fuel with internal heat generation and variable properties is shown below:

$$\frac{\partial}{\partial t}\left(\rho C_p T\right) = \frac{1}{r}\frac{\partial}{\partial r}\left(kr\frac{\partial T}{\partial r}\right) + \dot{q}''' \quad (7)$$

All terms are treated as radially and temporally variant except for the internal heat generation which is approximated as spatially uniform. The validity of this assumption is addressed in detail in the discussion section 4.3. The steady-state solution defines the initial condition and the time-dependant heat generation drives the model. The two necessary boundary conditions are zero heat flux at the fuel centerline and a fuel surface temperature that depends on the coolant temperature and the conductance between. This second relation is shown below.

$$T_{R_f}(t) = -\frac{k_{R_f}(t)}{h}\left(\frac{\partial T}{\partial r}\right)\Bigg|_{R_f,t} + T_{\infty} \qquad (8)$$

where the heat conductance, h, is defined as:

$$\frac{1}{h} = R_f\frac{\ln\left(1+\frac{\delta_{gap}}{R_f}\right)}{k_{gap}} + \left(R_f+\delta_{gap}\right)\frac{\ln\left(1+\frac{\delta_{clad}}{R_f+\delta_{gap}}\right)}{k_{clad}} + \frac{1}{h_{hyd}} \qquad (9)$$

A semi-implicit Crank-Nicolson scheme is used for discretization [8] whereby time is discretized with the trapezoid rule and space with the central difference formula, obtaining inherent stability and second order accuracy. At first glance, the solution might require an iterative predictor-corrector algorithm since the unknown iterate is not known explicitly. However, if the extra effort is made to form the relation into a linear system, the problem is transformed into solving a sparse linear system of equations at each time-step. Fortunately, MATLAB® contains LAPACK, a library of linear algebra subroutines that solves linear systems such as these quickly and accurately. The full discretization of the heat equation can be found in Appendix A.

3.3.2.3 Hydrogen diffusion model

The driving force for flux of hydrogen atoms across the fuel exists due to temperature and concentration gradients across the pellet. The radial flux is equal to:

$$J_r = -DN_{Zr}\left(\frac{dC}{dr}+\frac{T_Q C}{T^2}\frac{dT}{dr}\right) \qquad (10)$$

After relating the flux and concentration in a conservation equation such as in Huang et al. [9], an explicit time-discretization scheme is used since the rate of change of the concentration is small and linearization introduces only small errors. Flux at the surface of the fuel is approximated to be zero; the accuracy of this simplification is addressed in section 4. In the conservation equation, the fluxes are multiplied by a ratio of surface area and volume which correspond to the surface through which the flux is passing and the volume of fuel in which hydrogen resides. Since hydrogen exists only in the δ-ZrH_x phase (the flux of hydrogen atoms in the α-U phase is negligible [9]), this area to volume ratio is weighted by the fraction of this phase (~0.9). The fully-expanded discretized diffusion equation and its derivation can be found in Appendix B.

3.3.2.4 Coupling Algorithm

As mentioned earlier, there is a high degree of interdependency of the pertinent variables. The heat equation for temperature depends on thermal conductivity and volumetric heat capacity. The hydrogen diffusion equation depends on temperature, hydrogen concentration, and diffusivity. The diffusivity, thermal conductivity, and volumetric heat capacity all depend on temperature and hydrogen concentration.

The following operator splitting algorithm is used for each time-step. The heat equation is semi-implicitly solved for the current temperature using properties from the previous time-step and extrapolated properties for the current time step (see Appendix A). Next, the hydrogen concentration is explicitly calculated for the current time-step using parameters only at the previous time-step (see Appendix B). Third, the diffusivity, thermal conductivity, and volumetric heat capacity are updated with the current temperature and hydrogen concentration. This process is shown in Figure 2 where arrows denote inputs, circles are variables (dashed lines denote the previous time step), rectangles are equations, pentagons are boundary conditions, and the hexagon is power density (assumed independent of other variables).

Before the transient solution algorithm is run, the steady-state equations are solved using a similar process with a relative error tolerance for convergence of 10^3 times machine precision.

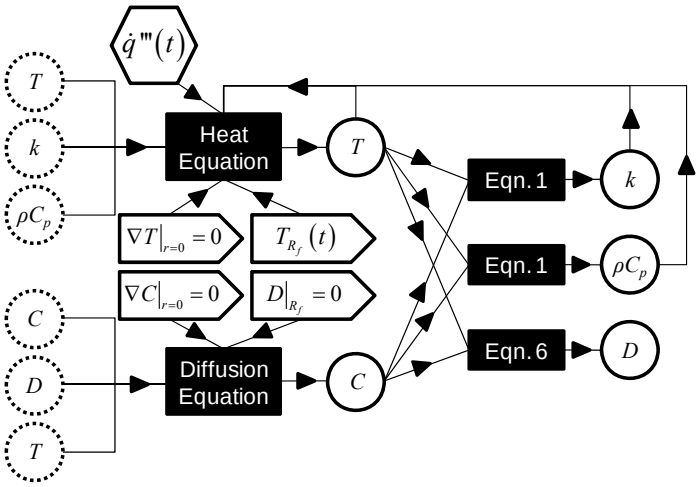

Figure 2. A single time-step in the solution algorithm.

3.3.2.5 Stress Calculation

The two sources of strain in the material arise from temperature and hydrogen concentration gradients across the fuel. Olander [10] reported the linear coefficient of expansion of hydrogen as $\beta=0.027$ per unit change of H/Zr ratio in ZrH_x. The temperature dependent coefficient of thermal expansion of the zirconium hydride has been reported as $\alpha = 3.36\times10^{-6}\left[1+4.40\times10^{-3}T\right]$ per unit change of temperature in Kelvin [11]. The elastic modulus of zirconium hydride is approximately 130 GPa in the temperature range of interest [12]. The elastic modulus of the composite fuel is obtained using the rule of mixtures as 145GPa (vol% α-U = 19.4). With a similar analysis, the Poisson ratio for the composite is 0.3 ($\nu_{\alpha\text{-U}} = 0.23$, $\nu_{ZrH1.6} = 0.32$ [12]). Total strain in the fuel is the sum of elastic, thermal and hydrogen strains. The constitutive equations in the axi-symmetric cylindrical coordinates are then presented as:

$$\varepsilon_r = \frac{1}{E}\left[\sigma_r - \nu\left(\sigma_\theta + \sigma_z\right)\right] + \alpha\left(\Delta T\right) + \beta\left(\Delta C\right) \qquad (11)$$

$$\varepsilon_\theta = \frac{1}{E}\left[\sigma_\theta - \nu\left(\sigma_r + \sigma_z\right)\right] + \alpha\left(\Delta T\right) + \beta\left(\Delta C\right) \qquad (12)$$

$$\varepsilon_z = \frac{1}{E}\left[\sigma_z - \nu\left(\sigma_\theta + \sigma_r\right)\right] + \alpha\left(\Delta T\right) + \beta\left(\Delta C\right) \qquad (13)$$

Eliminating the displacement vectors in the definition of cylindrical strains, the relationship in Equation 14 is obtained. Using the constitutive equations coupled with this condition and also assuming a plane strain scenario in the axial direction, a differential equation governing the radial stress across the fuel is determined (Eqn. 15). The fuel is assumed initially restrained in the axial direction (the plain strain assumption); later by application of Saint Venant's principle the unrestrained axial stress is determined [13]. The two necessary boundary conditions are a zero stress gradient at the fuel centerline and zero radial stress at the fuel surface.

$$\frac{d\varepsilon_\theta}{dr} + \frac{\varepsilon_\theta - \varepsilon_r}{r} = 0 \qquad (14)$$

$$\frac{1}{r^2}\frac{d}{dr}\left(r^3\frac{d\sigma_r}{dr}\right) = \frac{-E}{1-\nu}\left[\frac{d}{dr}\left(\alpha T\right) + \beta\frac{dC}{dr}\right] \qquad (15)$$

The radial equilibrium condition in cylindrical coordinates (Eqn. 16) is used to calculate the azimuthal stress across the fuel based on the radial stress.

$$\sigma_\theta = \frac{\partial}{\partial r}\left(r\sigma_r\right) \qquad (16)$$

To determine the distribution of axial stress across the fuel, the axial stress is first calculated assuming complete restraint in the axial direction ($\varepsilon_z = 0$). Then the difference from the average of this quantity across the fuel is denoted as the actual magnitude of axial stress (Saint Venant's principle). For complete set of calculations showing the derivation of different stress components please refer to Appendix C.

Simpson and Cann [14] report the mode I fracture toughness of δ-zirconium hydride as 3 $MPa.m^{½}$ at 573 K. Ductile phase toughening in the fuel due to the presence of uranium particles is expected by crack bridging and process zone toughening mechanisms. By conservatively ignoring such effects, linear elastic fracture mechanics can be applied. However finite element methods are necessary to predict the evolution of flaw size in the material due to the complex state and distribution of stress and are beyond the scope of this work. An adequate scheme would

be to artificially assign cracks to different regions of the material that would in turn correspond to dissimilar states of stress. The progression in flaw size and geometry that correspondingly depends on the evolution of the changing stress state can then be studied.

3.3.2.6 Model physical parameters

The model was composed of a fuel element 1 cm in diameter, housed inside a Zircaloy cladding of 0.9 mm in thickness, with a 70 μm molten lead-tin-bismuth (Pb-33.3wt%Sn-33.3wt%Bi) gap in between. The gap and cladding were not modeled explicitly but instead were introduced as the outer boundary condition along with the hydraulic conditions. The conductivities used for the liquid-metal (LM) gap and clad were 0.20 W/cm.K [15] and 0.16 W/cm.K [16], respectively. The thermal-hydraulic heat transfer coefficient was estimated using the Presser correlation for the Nusselt number with the typical geometry and operating parameters of a PWR, resulting in an approximate value of 1 W/cm^2.K. The bulk coolant temperature was 575 K and the pitch to diameter ratio was 1.2. The fuel-averaged H/Zr ratio was 1.6.

3.3.3 Results

3.3.3.1 Steady state results

The steady-state calculations were conducted with 500 spatial nodes at linear heat rates (LHR) of 100, 200, and 300 W/cm. The results of the steady state temperatures, H/Zr ratios, and axial stress distributions are shown in Figures 3a, 3b, and 3c respectively.

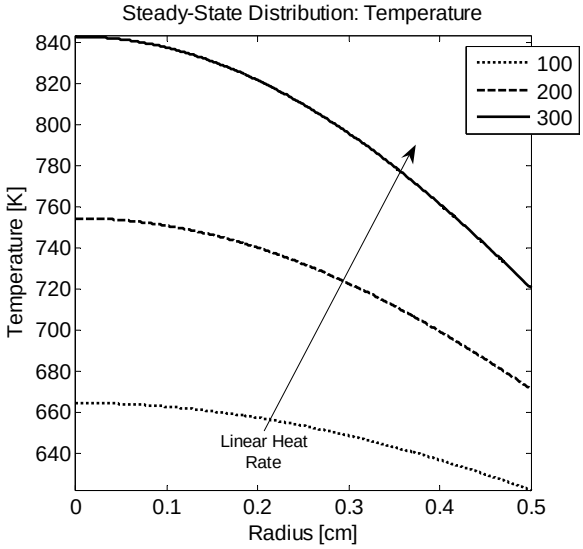

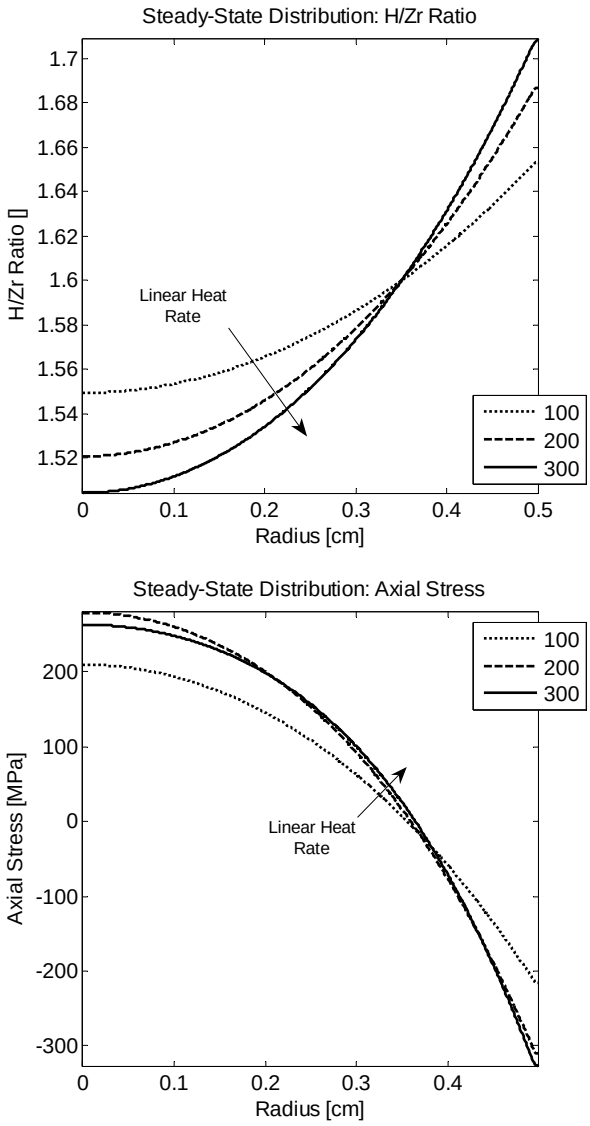

Figure 3. Top to Bottom: steady-state temperature, H/Zr ratio, and axial stress distributions at LHRs of 100, 200, and 300 W/cm.

As expected, the fuel temperature gradient and outer fuel temperature increase with LHR. The hydrogen concentration gradients are also steeper with increasing LHR. With a LM bonded fuel, even though the average temperature is lower when compared to the conventional He gap fuel, the extent of hydrogen redistribution is more severe (as reported by Olander [10]). This has been confirmed by the model but is not shown in this paper. This trend is justified by inspection of the flux governing equation where the T^{-2} dependence of the temperature gradient term enhances its impact at lower temperatures.

The largest component of stress is the axial stress, whose value is influenced by the temperature and hydrogen concentration gradients in an opposing manner. However, hydrogen-induced stresses are the dominant component, as is evident from the steady state results. Generally, the fuel surface experiences severe compression from axial and azimuthal components of stress, while all three components of stress are tensile at the central region of the fuel. Even though the

hydrogen redistribution is larger with increasing LHR, the magnitude of stress might not increase due to larger thermally induced strains.

3.3.3.2 Transient results

A parametric transient case study was completed with a nominal LHR and coolant temperature of 300 W/cm and 575K, respectively. The power was pulsed to twice the nominal value for 2.5s and then dropped to 5% while the coolant temperature and fuel-to-coolant conductance remained constant. This represents a simplified and exaggerated reactivity insertion accident (RIA) with a large pulse height, a long pulse width, and a subsequent SCRAM. The hydrogen redistribution, although present, is miniscule since the hydrogen diffusivity is orders of magnitude smaller than the thermal diffusivity (~$2x10^{-8}$ cm^2/s compared to ~$6x10^{-2}$ cm^2/s). Consequently, only the resultant spatial fuel temperature and axial stress distributions are shown in Figure 4a and 4b respectively.

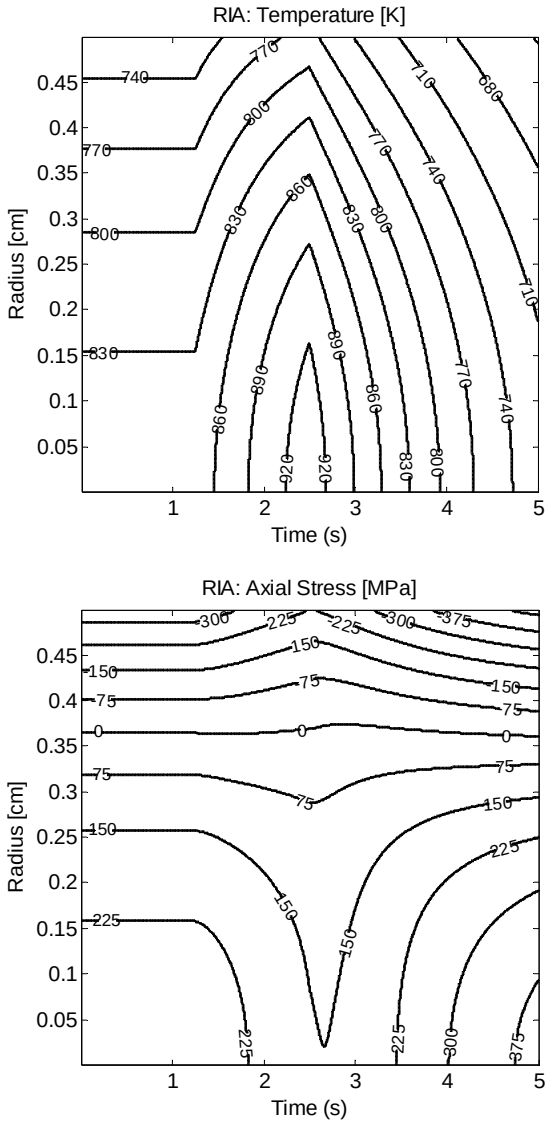

Figure 4. Fuel temperature and axial stress response to RIA

The fuel temperature directly follows the power pulse, rapidly peaking as the power jumps and then relaxing down after the SCRAM. The stress response of the fuel is interesting in that the axial stress is actually lowered and flattened during the power pulse. This is caused by the increased thermal stresses that counteract the dominating stresses created by the hydrogen concentration gradient. As the fuel cools during the SCRAM portion, the hydrogen-induced stresses remain unopposed and the overall stress increases. Figure 5 shows the maximum fuel temperature for various pulse heights and durations induced on a fuel operating with nominal linear heat rate of 300 W/cm.

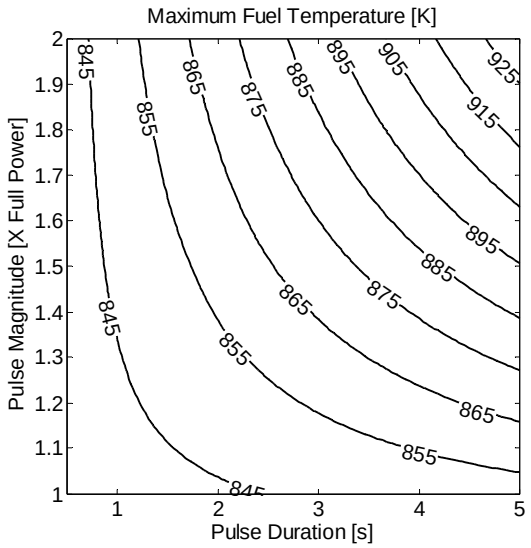

Figure 5. Maximum fuel temperature during power pulse.

3.3.4 Discussion

3.3.4.1 Comparison of constant to variable properties

Table 1 summarizes the relative percent error one would accrue by using material properties that are independent of temperature and hydrogen concentration for a steady-state solution. The constant values used for thermal conductivity and volumetric heat capacity were 0.16 W/cm.K and 2.3 J/cm^3.K. Results are shown for LHRs of 100, 200, and 300 W/cm.

Although the relative percent errors may seem small, a 3% relative difference amounts to 30 K at a temperature of 1000 K. Also, at 100 W/cm, the overshoot in temperature and undershoot in H/Zr ratio at the fuel centerline would bring about a significant error in the axial stress. A moderate discrepancy in any of these terms may have a significant effect on the overall fuel behavior.

3.3.4.2 Extent and effect of hydrogen desorption

The extent of hydrogen release from the LM bonded fuel is unknown. However, it is believed to be smaller when compared to the case of fuel gap filled with helium (He), since the hydrogen is readily released from the surface into a much larger volume and the gas phase solubility is infinite. For perspective, it is appropriate to study fuel with a He filled gap. The extent of release can then be estimated by the equilibrium partial pressure of hydrogen inside the cladding, which

can be expressed as a function of temperature and fuel surface hydrogen concentration according to Wang et al. [17] as:

$$P\,[\text{atm}] = \left(\frac{C_{eq}}{2 - C_{eq}}\right)^2 \exp\left(8.01 + 5.21 C_{eq} - \frac{2.07 \times 10^4}{T[\text{K}]}\right) \qquad (17)$$

The free volume inside the cladding due to the plenum volume and gap is approximately 40 cm^3. Assuming a pre-pressurization to 1 MPa of He, the total pressure in the cladding can be calculated as the sum of partial pressures of hydrogen and helium that in turn obey the ideal gas law. Therefore equilibrium pressure inside the cladding as function of temperature and H/Zr ratio at the fuel surface could be estimated as shown in Figure 6a. The plenum and gap are conservatively assumed to be at the fuel surface temperature. The amount of hydrogen within each fuel rod is approximately 25 moles. The equilibrium fractional loss of this amount as function of fuel surface temperature and H/Zr ratio at the fuel surface is also shown in Figure 6b. Adsorption of hydrogen on the inner surface of cladding and its subsequent diffusion into the cladding is ignored. Over time however, this will result in a larger fractional release of hydrogen into the cladding.

3.3.4.3 Magnitude and effect of power depression

A pin cell model was built in MCNP (Monte Carlo N-Particle Transport Code) to determine the steady state power profile during the reactor operation so the accuracy of the uniform power approximation could be addressed. The steady state temperature and hydrogen concentration results with the uniform power LHR of 300 W/cm were used as input for the cross-sections and number densities of the MCNP model. The power was tallied in 10 radial shells of the fuel. The resultant power profile was used to update the heat and Hydrogen diffusion model and the process was iterated until convergence.

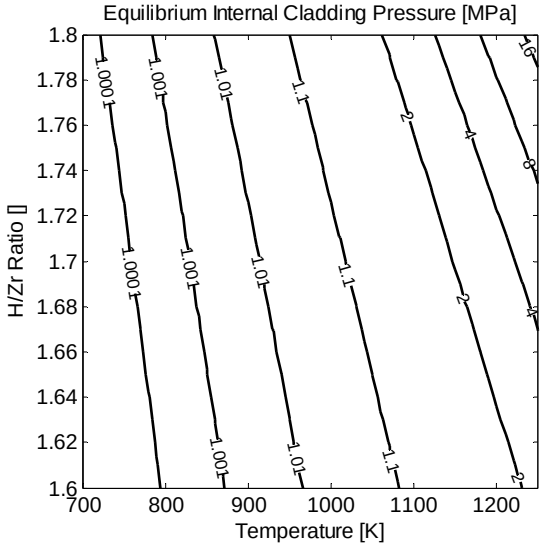

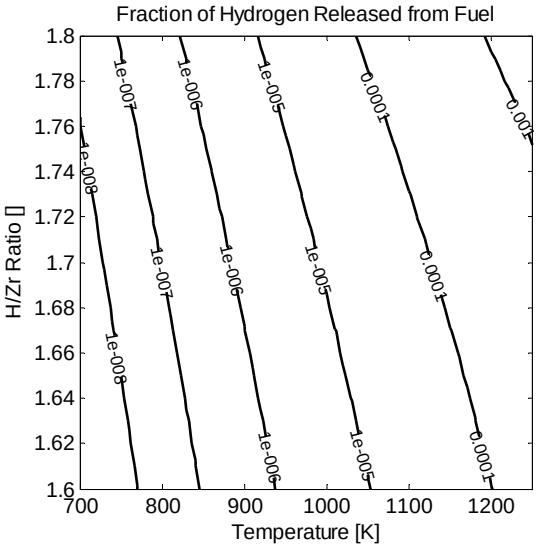

Figure 6. Top: equilibrium total pressure inside the cladding [MPa]. Bottom: total fraction of hydrogen inside the fuel lost to the gaseous phase inside the cladding in equilibrium.

The normalized power profile for the first iteration is shown in Figure 70. The maximum difference between the uniform and depressed power profiles is around 2% and it changes the centerline temperature by 2.25 K, or ~0.8% of the fuel centerline to coolant temperature drop. Its effects on the Hydrogen concentration and stresses are even smaller, leaving one to conclude that the uniform power profile is a good assumption.

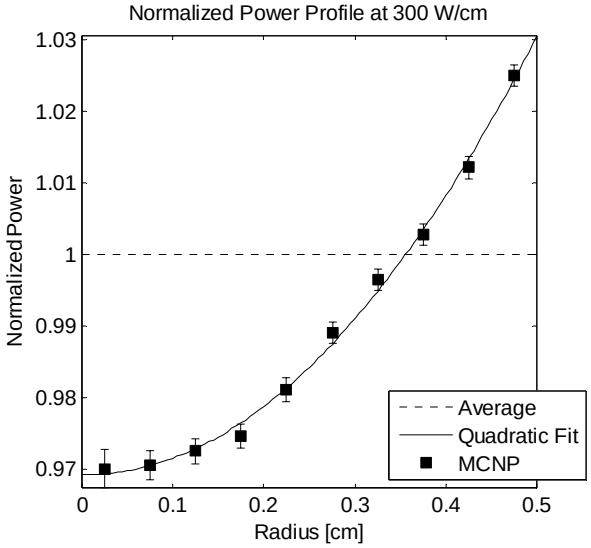

Figure 7. Distribution of the power profile across the fuel operated at 300 W/cm linear heat rate

3.3.5 Conclusions

Steady state and transient behavior of several aspects of the fuel operating performance have been investigated, taking into account the temperature and hydrogen concentration dependence of the fuel properties.

Steady state temperature, hydrogen concentration, and stress profiles of the hydride fuel operated at various linear heat rates have been calculated. The extent of hydrogen redistribution, driven by the gradient in temperature, becomes more severe as the power increases. Strains in the fuel occur from thermal and hydrogen concentration gradients, with the latter being the dominant contributor. Axial and azimuthal stresses are both compressive at the surface and tensile at the fuel centerline. These results are in agreement with what was previously shown by Olander, where the dependence of fuel properties (except the coefficient of thermal expansion) on temperature and hydrogen concentration were ignored [10]. The fuel fracture criterion is unknown and needs be determined through finite element methods.

The transient response of hydride fuel to a reactivity insertion accident scenario was studied by artificially pulsing power in a square wave. The thermal response of the fuel to the changing boundary conditions is very rapid (on order of few seconds) due to the small fuel rod and large thermal diffusivity. There is no discernable alteration in the transient hydrogen profile, since the characteristic diffusion time for these length scales is many orders of magnitude larger than the transient durations. However, it is necessary to model the hydrogen diffusion since it is important to know the steady-state distribution for the initial conditions. Surprisingly, the stress across the fuel is actually reduced during the power pulse. The temperature-induced stresses counteract the hydrogen-induced stresses, so the fuel is in its most relaxed state during this stage of the transient. The fuel experiences maximum stress when temperature gradients diminish but the hydrogen displacement remains at the pre-transient distribution.

The flux of hydrogen atoms, in a fuel assembly with a He filled gap, out of the fuel during steady state and transient operation of the fuel is very small since the net rate (desorption – adsorption) quickly becomes zero when the equilibrium hydrogen partial pressure is established. The pressure buildup inside the cladding and the total fraction of hydrogen lost from the solid state to the cladding volume are negligible even at very high fuel surface temperatures. The extent of dehydriding is expected to be even less for LM bonded fuels.

3.3.6 Acknowledgements

The authors wish to thank Professor Per Peterson for helpful discussions and comments.

3.3.7 Notation

Symbol	Quantity (Units)
k	Thermal conductivity (W/cm.K)
v	Volume fraction
w	Mass fraction
κ	Thermal diffusivity (cm^2/s)
ρ	Mass density (kg/cm^3)
C_p	Specific heat capacity (J/gr.K)
T	Temperature (K)
$\dot{q}'''$	Volumetric heat generation rate (W/cm^3)

T_{Rf}	Fuel surface temperature (K)
h	Heat transfer coefficient (W/cm^2.K)
T_∞	Coolant temperature (K)
δ	Cladding/gap thickness (cm)
J	Radial flux (cm^{-2}/s)
D	Macroscopic diffusion coefficient (cm^2/s)
λ	Jump distance during diffusion (cm)
τ	mean residence time in each lattice site(s)
η	number of available adjacent jump sites
υ	Vibrational frequency inside lattice (s^{-1})
N_{Zr}	Zirconium number density in δ-$ZrH_{1.6}$ Phase (atoms/cm^3)
C	H/Zr ratio in ZrH_x
T_Q	Heat of transport of H in δ-$ZrH_{1.6}$ (K)
S	surface area/volume of shell (cm^{-1})
β	coefficient of expansion of hydrogen
α	coefficient of thermal expansion (K^{-1})
ε_r, ε_θ, ε_z	radial, azimuthal, and axial strain
σ_r, σ_θ, σ_z	radial, azimuthal, and axial stress (MPa)
E	Elastic (Young's) modulus (GPa)
ν	Poisson's ratio
R	Gas constant (kJ/mole.K)
k_{DH}	Dehydriding rate (mole/cm^2.s)

4.3.8 APPENDIX A

The radial heat equation with variable properties is a non-linear partial differential equation (Eqn. 7), so discretization must be done carefully. A well known procedure is that of Crank and Nicolson [8], in which time is discretized with the trapezoid rule and space with central difference. This first step is shown below:

$$\frac{1}{\Delta t}\left(\left(\rho C_p T\right)_i^{j+1}-\left(\rho C_p T\right)_i^{j}\right)=\frac{1}{2}\left(\dot{q}_i'''^{j+1}+\dot{q}_i'''^{j}\right)+\frac{1}{2}\frac{1}{r_i\Delta r}\left[\left(rk\frac{\partial T}{\partial r}\right)_{r_{i+\frac{1}{2}}}^{j+1}-\left(rk\frac{\partial T}{\partial r}\right)_{r_{i-\frac{1}{2}}}^{j+1}+\left(rk\frac{\partial T}{\partial r}\right)_{r_{i+\frac{1}{2}}}^{j}-\left(rk\frac{\partial T}{\partial r}\right)_{r_{i-\frac{1}{2}}}^{j}\right] \quad \text{(A1)}$$

where i and j indicate the radial node and time step, respectively. All terms are considered as node-centered. The equation is expanded and shuffled more:

$$\left(\left(\rho C_p\right)_i^{j+1}T_i^{j+1}-\left(\rho C_p\right)_i^{j}T_i^{j}\right)=Q\Delta t+\omega\left[\frac{r_{i+\frac{1}{2}}}{r_i}k_{i+\frac{1}{2}}^{j+1}\left(T_{i+1}^{j+1}-T_i^{j+1}\right)-\frac{r_{i-\frac{1}{2}}}{r_i}k_{i-\frac{1}{2}}^{j+1}\left(T_i^{j+1}-T_{i-1}^{j+1}\right)+\frac{r_{i+\frac{1}{2}}}{r_i}k_{i+\frac{1}{2}}^{j}\left(T_{i+1}^{j}-T_i^{j}\right)-\frac{r_{i-\frac{1}{2}}}{r_i}k_{i-\frac{1}{2}}^{j}\left(T_i^{j}-T_{i-1}^{j}\right)\right] \quad \text{(A2)}$$

where the following terms and notations are defined and used for convenience:

$$Q=\frac{1}{2}\left(\dot{q}_i'''^{j+1}+\dot{q}_i'''^{j}\right) \quad \text{(A3)}$$

$$\omega=\frac{\Delta t}{2\Delta r^2} \quad \text{(A4)}$$

$$k_{i\pm\frac{1}{2}}=\frac{1}{2}\left(k_{i\pm1}+k_i\right) \quad \text{(A5)}$$

Since a marching procedure is performed with time, solving for the $j+1^{st}$ iterate from the known j^{th} iterate, the thermal conductivity and volumetric heat capacity at the $j+1^{st}$ time step are not known as they depend on both temperature and hydrogen concentration. Further, the functional dependencies are highly non-linear. Initially, predictor-corrector iterations were performed at each time step, requiring substantial increases in run-time. Newton-Raphson methods were also

considered but were deemed too laborious. A final, simpler method that produces results with essentially no difference is a first-order Taylor extrapolation of the material properties using the j^{th} and $j\text{-}1^{st}$ values. This procedure is outlined below:

$$k^{j+1} \approx k^j + \Delta t \frac{\partial k^j}{\partial t} \approx k^j + \Delta t \frac{k^j - k^{j-1}}{\Delta t} = 2k^j - k^{j-1} \quad \text{(A6)}$$

$$\left(\rho c_p\right)^{j+1} \approx 2\left(\rho c_p\right)^j - \left(\rho c_p\right)^{j-1} \quad \text{(A7)}$$

The node-centered radius terms are also expanded accordingly:

$$r_i = \Delta r\left(i - 1/2\right) \quad \text{(A8)}$$

$$\frac{r_{i\pm 1/2}}{r_i} = \frac{r_i \pm \Delta r/2}{r_i} = 1 \pm \frac{\Delta r}{2r_i} = 1 \pm \frac{\Delta r}{2\Delta r\left(i - 1/2\right)} = 1 \pm \frac{1}{2i-1} \quad \text{(A9)}$$

Utilizing these enhancements, the final form of the semi-implicitly discretized heat equation is acquired:

$$\begin{Bmatrix} T_i^{j+1}\left[\frac{\left(\rho c_p\right)_i^{j+1}}{\omega} + \left(1 + \frac{1}{2i-1}\right)k_{i+1/2}^{j+1} + \left(1 - \frac{1}{2i-1}\right)k_{i-1/2}^{j+1}\right] \\ +T_{i+1}^{j+1}\left[-\left(1 + \frac{1}{2i-1}\right)k_{i+1/2}^{j+1}\right] + T_{i-1}^{j+1}\left[-\left(1 - \frac{1}{2i-1}\right)k_{i-1/2}^{j+1}\right] \end{Bmatrix} = \begin{Bmatrix} T_i^{j}\left[\frac{\left(\rho c_p\right)_i^{j}}{\omega} - \left(1 + \frac{1}{2i-1}\right)k_{i+1/2}^{j} - \left(1 - \frac{1}{2i-1}\right)k_{i-1/2}^{j}\right] \\ +T_{i+1}^{j}\left[\left(1 + \frac{1}{2i-1}\right)k_{i+1/2}^{j}\right] + T_{i-1}^{j}\left[\left(1 - \frac{1}{2i-1}\right)k_{i-1/2}^{j}\right] \end{Bmatrix} + \frac{Q\Delta t}{\omega} \quad \text{(A10)}$$

4.3.9 APPENDIX B

The hydrogen mass balance equation can be written for a differential radial shell in terms of the flux within the fuel as the following:

$$c_i^{j+1} = c_i^j + \left[J_{i-1/2}^j S_{i-1/2} - J_{i+1/2}^j S_{i+1/2}\right]\Delta t \quad \text{(B1)}$$

where c is the molar concentration of hydrogen in mole H/cm^3; J is the hydrogen atom flux specified earlier in equation 10. S is the ratio of inner/outer surface of each radial shell to its volume with units of cm^{-1}:

$$S_{i\pm 1/2} = \frac{2\pi r_{i\pm 1/2} l}{\pi\left(r_{i+1/2}^2 - r_{i-1/2}^2\right)l} = \frac{2\left(r_i \pm \Delta r/2\right)}{\left(\left[r_i + \Delta r/2\right]^2 - \left[r_i - \Delta r/2\right]^2\right)} \quad \text{(B2)}$$

After substituting Eqn. A9 and simplifying, B2 becomes:

$$S_{i\pm 1/2} = \frac{2\left(r_i \pm \Delta r/2\right)}{\left(2r_i \Delta r\right)} = \frac{r_i \pm \Delta r/2}{r_i \Delta r} \xrightarrow{r_i = \Delta r\left(i - 1/2\right)} \begin{cases} - \rightarrow \frac{i-1}{\Delta r\left(i - 1/2\right)} \\ + \rightarrow \frac{i}{\Delta r\left(i - 1/2\right)} \end{cases} \quad \text{(B3)}$$

The atomic ratio of hydrogen to zirconium is:

$$C_i^j = \frac{M_{Zr}}{\rho_{Zr}} c_i^j \quad \text{(B4)}$$

Substituting for Equations B3, B4, and 10, Equation B1 generates the following result:

$$C_i^{j+1}\frac{\rho_{Zr}}{M_{Zr}}=C_i^j\frac{\rho_{Zr}}{M_{Zr}}+\left[-D_{i-\frac{1}{2}}^j\frac{\rho_{Zr}}{M_{Zr}}\left\{\frac{C_i^j-C_{i-1}^j}{r_i-r_{i-1}}+\frac{T_Q C_{i-\frac{1}{2}}^j}{T_{i-\frac{1}{2}}^2}\cdot\frac{T_i-T_{i-1}}{r_i-r_{i-1}}\right\}\frac{i-1}{\Delta r\left(i-\frac{1}{2}\right)}+D_{i+\frac{1}{2}}^j\frac{\rho_{Zr}}{M_{Zr}}\left\{\frac{C_{i+1}^j-C_i^j}{r_{i+1}-r_i}+\frac{T_Q C_{i+\frac{1}{2}}^j}{T_{i+\frac{1}{2}}^2}\cdot\frac{T_{i+1}-T_i}{r_{i+1}-r_i}\right\}\frac{i}{\left(i+\frac{1}{2}\right)\Delta r}\right]\Delta t \quad \text{(B5)}$$

Further simplification of the above results in the fully explicit discretization for H/Zr ratio as:

$$C_i^{j+1}=C_i^j\left[\begin{array}{l}1-0.9\frac{\Delta t}{\Delta r^2}D_{i+\frac{1}{2}}^j\frac{i}{\left(i+\frac{1}{2}\right)}\left\{1-\frac{T_Q\left(T_{i+1}^j-T_i^j\right)}{2\left(T_{i+\frac{1}{2}}^j\right)^2}\right\}\\ -0.9\frac{\Delta t}{\Delta r^2}D_{i-\frac{1}{2}}^j\frac{i-1}{\left(i-\frac{1}{2}\right)}\left\{1+\frac{T_Q\left(T_i^j-T_{i-1}^j\right)}{2\left(T_{i-\frac{1}{2}}^j\right)^2}\right\}\end{array}\right]+C_{i+1}^j\left[0.9\frac{\Delta t}{\Delta r^2}D_{i+\frac{1}{2}}^j\frac{i}{\left(i+\frac{1}{2}\right)}\left\{1+\frac{T_Q\left(T_{i+1}^j-T_i^j\right)}{2\left(T_{i+\frac{1}{2}}^j\right)^2}\right\}\right] \quad \text{(B6)}$$

$$+C_{i-1}^j\left[0.9\frac{\Delta t}{\Delta r^2}D_{i-\frac{1}{2}}^j\frac{i-1}{\left(i-\frac{1}{2}\right)}\left\{1-\frac{T_Q\left(T_i^j-T_{i-1}^j\right)}{2\left(T_{i-\frac{1}{2}}^j\right)^2}\right\}\right]$$

4.3.10 APPENDIX C

Equation 15 for the radial stress is first discretized with central difference:

$$\frac{1}{r_i^2}\frac{1}{\Delta r}\left(r^3\frac{d\sigma_r}{dr}\bigg|_{r_{i+\frac{1}{2}}}-r^3\frac{d\sigma_r}{dr}\bigg|_{r_{i-\frac{1}{2}}}\right)=\frac{-E}{1-\nu}\left[\frac{1}{\Delta r}\left(\alpha T\big|_{r_{i+\frac{1}{2}}}-\alpha T\big|_{r_{i-\frac{1}{2}}}\right)+\beta\frac{C_{i+\frac{1}{2}}-C_{i-\frac{1}{2}}}{\Delta r}\right] \quad \text{(C1)}$$

Utilizing Eqn. A8 and Eqn. A9 and taking into account the linearly temperature dependant coefficient of thermal expansion Equation C1 becomes:

$$\begin{aligned}&\sigma_{r,i}\left(-i\left[1+\frac{1}{2i-1}\right]^2-(i-1)\left[1-\frac{1}{2i-1}\right]^2\right)+\sigma_{r,i+1}\left(i\left[1+\frac{1}{2i-1}\right]^2\right)+\sigma_{r,i-1}\left((i-1)\left[1-\frac{1}{2i-1}\right]^2\right) \quad \text{(C2)}\\ &=\frac{-E}{1-\nu}\left[\alpha_\circ\left(\left[T_{i+\frac{1}{2}}-T_{i-\frac{1}{2}}\right]+a\left[T_{i+\frac{1}{2}}^2-T_{i-\frac{1}{2}}^2\right]\right)+\frac{\beta}{2}\left(C_{i+1}-C_{i-1}\right)\right]\end{aligned}$$

With the boundary conditions described in section 2.5, Equation C2 can be solved in the matrix form, obtaining the radial stress across the fuel. The azimuthal stress across the fuel is then determined through Equation 16 as the following, where the condition of radially symmetric stress is again applied:

$$\sigma_{\theta,i}=\frac{1}{2}\left(i\left(\sigma_{r,i+1}+\sigma_{r,i}\right)-(i-1)\left(\sigma_{r,i}+\sigma_{r,i-1}\right)\right) \quad \text{(C3)}$$

As discussed in section 2.5 the axial stress is defined as the difference between the actual to the mean of the restrained axial stress (such that $\varepsilon_z = 0$), as shown in Equation C4.

$$\sigma_{z,i}=\sigma_{z,i}^R-\bar{\sigma}_{z,i}^R \quad \text{(C4)}$$

The actual and mean of the restrained axial stress are found as shown in Equations C5 and C6. The reference temperature was taken as 750K, corresponding to the typical fuel processing temperatures, during which the material is assumed to be free of residual stresses. The reference value of H/Zr ratio is 1.6.

$$\sigma_{z,i}^R=\nu\left(\sigma_{\theta,i}+\sigma_{r,i}\right)-E\left[\left(\alpha_\circ\left[T_i+aT_i^2\right]-\alpha_\circ\left[T_{ref}+aT_{ref}^2\right]\right)+\beta\left(C_i-C_{ref}\right)\right] \quad \text{(C5)}$$

$$\bar{\sigma}_{z,i}^{R} = \frac{2}{R^2}\int_0^R r\sigma_{z,r}^{R}dr = \frac{2}{R^2}\sum_{i=1}^{m}\left(i - 1/2\right)\sigma_{z,i}^{R}\Delta r^2 \quad \text{(C6)}$$

4.3.11 References

1. F. Ganda, E. Greenspan, "Plutonium Incineration Capability of Hydride Versus MOX Fuel in PWR," *Procd. Global '05*, Tsukuba, Japan (Oct. 2005).
2. A. Sommer, W. Dennison, *NAA-SR-5066*, (1960).
3. S. Yamanaka, K. Yamada, K. Kurosaki, M. Uno, K. Takeda, H. Anada, T. Matsuda, S. Kobayashi, "Thermal Properties of Zirconium Hydride," *J. Nuclear Materials*, **294**, pp.94-98 (2001).
4. Y. Takahashi, M. Yamawaki, K. Yamamoto, "Thermophysical Properties of Uranium-Zirconium Alloy," *J. Nuclear Materials*, **154**, pp.141-144 (1988).
5. I. Grenthe, J. Fuger, R. Konings, R. Lemire, A. Muller, C. Nguyen-Trung, H. Wanner, *Chemical Thermodynamics of Uranium*, OECD Publications, Paris, France (2004).
6. B. Tsuchiya, J. Huang, K. Konashi, M. Teshigawara, M. Yamawaki, "Thermophysical Properties of Zirconium Hydride and Uranium-Zirconium Hydride," *J. Nuclear Materials*, **289**, pp.329-333 (2001).
7. G. Majer, W. Renz, R. Barnes, "The Mechanism of Hydrogen Diffusion in Zirconium Dihydrides," *J.Phys.: Condens. Matter*, **6**, pp.2935-2942 (1994).
8. J. Crank, P. Nicolson, "A Practical Method for Numerical Evaluation of Solutions of Partial Differential Equations of the Heat Conduction Type," *Proceedings of the Cambridge Philosophical Society*, **43**, pp.50–64. (1947).
9. J. Huang, B. Tsuchiya, K. Konashi, M. Yamawaki, "Estimation of Hydrogen Redistribution in Zirconium Hydride under Temperature Gradient," *J. Nuclear Sci. and Tech.*, **37**, No. 10, pp 887-892 (2000).
10. D. Olander, M. Ng, "Hydride Fuel Behavior in LWRs," *J. Nuclear Materials*, **346**, pp.98-108 (2005).
11. M. Simnad, "The U-ZrH_x Alloy: Its Properties and Use in TRIGA Fuel," *Nuclear Eng. Design*, **64**, pp.403-422 (1981).
12. S. Yamanaka, K. Yoshioka, M. Uno, M. Katsura, H. Anada, T. Matsuda, S. Kobayashi, "Thermal and Mechanical Properties of Zirconium Hydride," *J. Alloys. Comp.*, **293-295**, pp.23-29 (1999).
13. H. Rust, *Nuclear Power Plant Eng.*, (1979), 393.
14. L. Simpson, C. Cann, "Fracture Toughness of Zirconium Hydride and Its Influence on The Crack Resistance of Zirconium Alloys," *J. Nuclear Materials*, **87**, pp.303-316 (1979).
15. Y. Kim, D. Olander, S. Yagnik, "Liquid-Metal-Bonded Gap for Light Water Reactor Fuel Rods," *Nuclear Tech*., **128**, pp. 300-312 (1999).
16. J. Fink, "Zircaloy Thermal Conductivity: Preliminary Recommendation," *International Nuclear Safety Center, Argonne National Laboratory*: Available from: http://www.insc.anl .gov/matprop/zircaloy/zirck.pdf, (2000).
17. W. Wang, D. Olander, "Thermodynamics of the Zr-H System," *J. Am. Ceram. Soc.*, **78** [12], pp.3323-28 (1995).

4.4 Kinetics of Hydrogen Desorption from Zirconium Hydride

4.4.1 Introduction

Hydride nuclear fuels conventionally consist of metallic uranium particles dispersed in a matrix of zirconium hydride as demonstrated by fuels utilized in the SNAP program and currently used in GA's TRIGA reactors. Hydride fuels offer much superior thermal conductivity and fission gas retention while suffering from larger extent of swelling. Hydrogen is bound to the fuel that acts as the moderator and could effectively replace the coolant for this purpose resulting in more compact core designs with higher power density. Thermally-induced hydrogen up-scattering that accompanies Doppler feedback provides a negative prompt temperature coefficient of reactivity that makes the fuel very attractive.

Hydride fuels are processed through bulk hydriding of the uranium-zirconium alloys where the uranium-zirconium alloy is exposed to hydrogen gas at high temperatures. The stoichiometry of the hydride matrix is customized by controlling the pressure and temperature during the process. During the early stages of the hydriding process the kinetics are surface reaction limited (soon to become limited by diffusion) and are controlled through the hydrogen adsorption and desorption rates. However more importantly the kinetics of the surface reaction are of concern during reactor operation where dehydring from the fuel causes hydrogen buildup and permeation through the cladding.

3.4.2 Thermodynamics

Hydrogen dissolves in zirconium metal and undergoes reaction to form two distinct hydrides of zirconium, the cubic δ-ZrHx (Fm-3m) [1] and tetragonal ε-ZrHx (I4/mmm) [2] at lower and higher hydrogen to metal ratios, respectively. Both of the hydrides span a large range of hydrogen stoichiometries as depicted in Figure 1 [3].

The pressure-temperature-composition relationship for the hydrogen gas in equilibrium with δ-ZrH_x has been developed by Wang et al. [4] and is presented in Equation 1, where C is the H/Zr ratio.

$$P\ [\text{atm}] = \left(\frac{C}{2-C}\right)^2 \exp\left(8.01 + 5.21C - \frac{172[\text{kJ}]}{RT[\text{K}]}\right) \quad (1)$$

3.4.3 Kinetics

In a closed system the net rate of desorption of hydrogen from the surface of the hydride is the difference between the rates of desorption and adsorption. The adsorption process involves two steps where initially a hydrogen molecule from the gas (H_2) dissociates on the surface to hydrogen atoms (H^S). The surface hydrogen atom then diffuses to the bulk into the hydrogen sublattice (H^I). The first step of the desorption process involves the interstitial hydrogen atom (H^I) diffusing to the surface, leaving behind a vacancy in the hydrogen sublattice (V^I). The next step involves reaction of two hydrogen atoms on the surface of the hydride to from a hydrogen molecule which immediately desorbs. All the above reactions are summarized in Table 1.

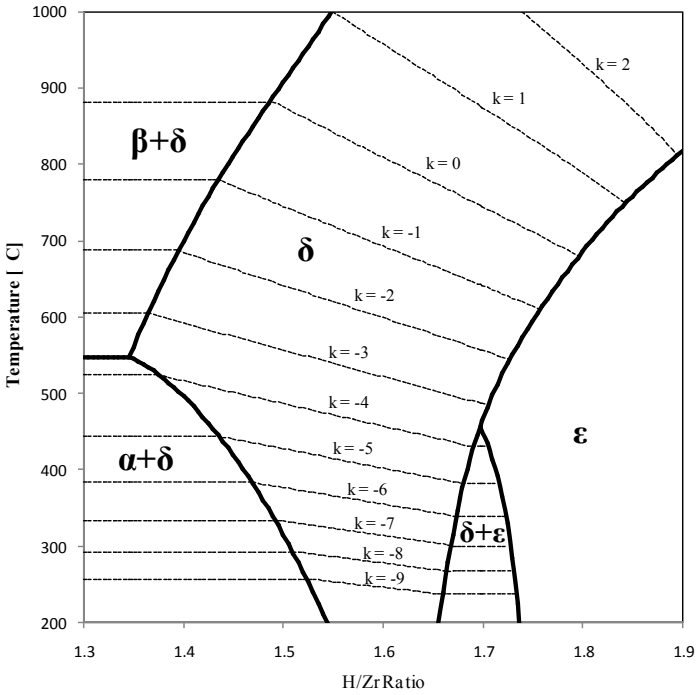

Figure 1. Phase Diagram for Zirconium-Hydrogen System [3] with equilibrium H_2 isobars labeled as $P_{H2}=10^k$ atm.

Table 1. Reaction Steps Involving the Desorption and Adsorption of Hydrogen form Hydride Surface.

Description	***Reaction***
1) Adsorption – Gas to Surface	$H_{2(g)} + 2V^S \rightarrow 2H^S$
2) Adsorption – Surface to Bulk	$H^S + V^I \rightarrow H^I$
3) Desorption – Bulk To Surface	$H^I \rightarrow H^S + V^I$
4) Desorption – Surface to Gas	$2H^S \rightarrow H_{2(g)} + 2V^S$

For the gas to surface adsorption reaction (reaction 1), the overall rate is the product of the rate at which the hydrogen molecules collide with the hydride surface (derived from kinetic theory of gases), the probability that the collision site is unoccupied, the probably that the adjacent site to the collision site is also unoccupied, and the sticking probability. Therefore rate of the first reaction is presented in Equation 2 as:

$$R_1 = \left(2\pi mkT\right)^{-1/2} p_{H_2} \beta \left(1 - y_s\right)^2 \eta_0 e^{-Ha/kT} \qquad (2)$$

p_{H_2} is the pressure of the hydrogen gas. y_s is the fraction of occupied sites by hydrogen atoms on the surface. β is the 2-D coordination number of the surface sites for the hydrogen atoms and is dependent on the specific crystallographic plane exposed to the gas.

For the reaction of hydrogen atom going from the surface to bulk (reaction 2), the overall rate is proportional to the product of the fraction of sites occupied with hydrogen atoms on the surface with the fraction of vacancies on the hydrogen sublattice in the bulk (Equation 3).

$$R_2 = k_2 y_s \left(1 - \xi_s\right) \qquad (3)$$

ξ_s is the fraction of occupied hydrogen sublattice sites by hydrogen atoms in the bulk. k_2 is a rate constants with an Arrhenius dependence on temperature.

The rate for the first step involving desorption (reaction 3) is proportional to the hydrogen atom concentration in the bulk adjacent to the surface and the portion of vacant site at the surface (Equation 4). k_3 is a rate constants with an Arrhenius dependence on temperature.

$$R_3 = k_3 \xi_s \left(1 - y_s\right) \qquad (4)$$

The rate of the surface to gas desorption reaction (reaction 4), is proportional to the hydrogen atom concentration at the surface and the probability of another surface hydrogen atom jumping into and adjacent site of a particular hydrogen atom on the surface. The later is the product of jumping frequency (I), hydrogen atom concentration and a combinatorial number (depending on the positioning and coordination number of the surface atoms). Einstein equation predicts the 2-D (surface) diffusion coefficient proportional to the product of the square of jumping distance (λ) and jumping frequency as:

$$D_S = \frac{1}{4}\lambda^2 I \qquad (5)$$

Substituting for jumping frequency using Equation 5, it is possible to determine the surface to gas desorption rate as:

$$R_4 = \frac{zND_S}{\lambda^2} y_s^{\,2} \qquad (6)$$

Where z is the combinatorial number and N is the aerial density of the total surface sites.

3.4.4 Experimental setup

An experiment has been set up to determine the rates of hydrogen desorption and adsorption on hydride samples. The experimental setup is shown in Figure 2. The sample is placed in a 316 stainless steel vessel that is enclosed in a furnace. The gas pressure is continuously monitored through a high pressure transducer connected to the vessel. The volume of the vessel and the connecting pipes up to the V1 valve and the interior of the pressure transducer is 19.5 cm^3. The system has been designed with minimal volume in order to record changes in molar gas content with higher accuracy through measuring pressure changes.

The sample is placed inside the stainless steel vessel through an opening in the bottom and the cavity is then welded with a stainless steel cap. Utilization of conventional flange and gasket was not possible since the copper gasket was unable to withstand the experimental temperatures inside the furnace.

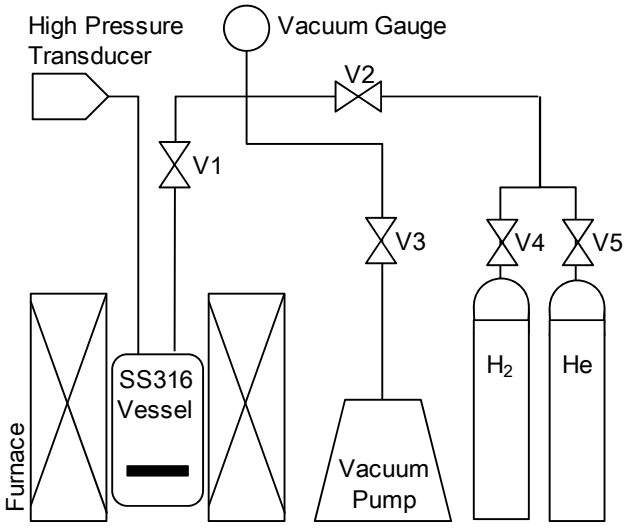

Fig 2. Experimental setup

3.4.5 Hydriding and diffusion

The hydride samples are processed with control over stoichiometry of the hydride by control of temperature and hydrogen pressure required by Equation 1. The samples start out as thin disks of zirconium at 1mm thickness and 1.35 cm in diameter. Upon hydriding however significant volume expansion takes place (~16%) that would increase the dimensions of the specimen accordingly. The hydrogen diffusion path to establish uniform concentration across the hydride is the half thickness of the specimen (l) and the characteristic diffusion time (l^2/D) for this process is relatively short. The diffusion coefficient of hydrogen in the δ-zirconium hydride has been reported by Majer et al. [5] as:

$$D\left[\mathrm{cm^2 s^{-1}}\right] = 1.53\times10^{-3}\exp\left(\frac{\text{-}58.8\left[\mathrm{kJ}\right]}{RT\left[\mathrm{K}\right]}\right) \qquad (7)$$

Therefore for instance at 900 °C and 800 °C the characteristic diffusion time for this process is 11 and 20 minutes respectively. These times were used to process hydrides of uniform hydrogen concentration at each experimental temperature.

3.4.6 Hydrogen loss through the vessel wall

The hydriding and dehydriding processes do not take place in a closed system because of the permeability of stainless steel vessel to hydrogen. The leakage rate of hydrogen from the vessel (flux) could be written in terms of the parameters shown in Equation 8, where Φ_o, δ, and H_Φ are the pre-exponential term in permeability, thickness of the vessel, and the activation energy associated with the permeation process respectively.

$$R_{leakage} = \Phi_o \frac{1}{\delta}\sqrt{p}\exp\left(\frac{-H_\Phi}{RT}\right) \qquad (8)$$

Permeation of hydrogen through stainless steel has been extensively studied [6] and the activation energy is reported as 60 KJ/mole. Measuring the rate of pressure drop, using an empty vessel filled with hydrogen gas at different temperatures, the permeation rate of the vessel has

been calculated. The pre-exponential term and activation energy were determined as 1.14×10^{-4} mole H^2/m.s.$MPa^{½}$ and 53.2 KJ/mole respectively that are in great agreement with literature. The leakage rate as a function of temperature is shown in Figure 4.

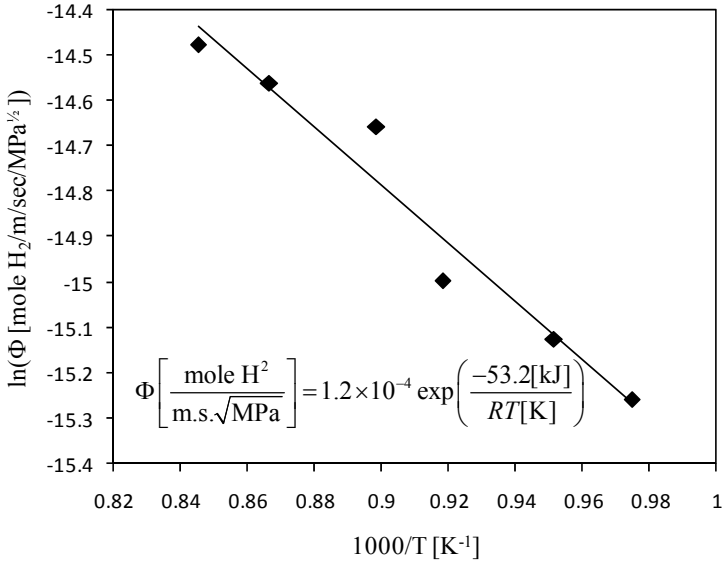

Fig 3. Leakage rate of hydrogen (permeation) from the stainless steel vessel as function of temperature.

3.4.7 Experimental method and results

After the uniform hydriding is achieved across the sample, the system is quickly pumped down to vacuum, isolated and the rise in pressure due to dehydriding is monitored. The hydriding and dehydrding are done in sequence at constant temperature. This allows pinpointing the hydrogen concentration at the hydride surface at the beginning of the dehydriding process based on the equilibrium condition during the hydriding.

A typical graph showing the rise in pressure as a function of time during dehydriding is presented in Figure 4. The rise in pressure is very fast and equilibrium conditions are quickly established. The zirconium hydride disk used for the dehydriding experiments was 14.04 mm in diameter and 1.04 mm in thickness. The dehydridng experiment was performed at 14 different temperatures and starting H/Zr ratios (Table 2).

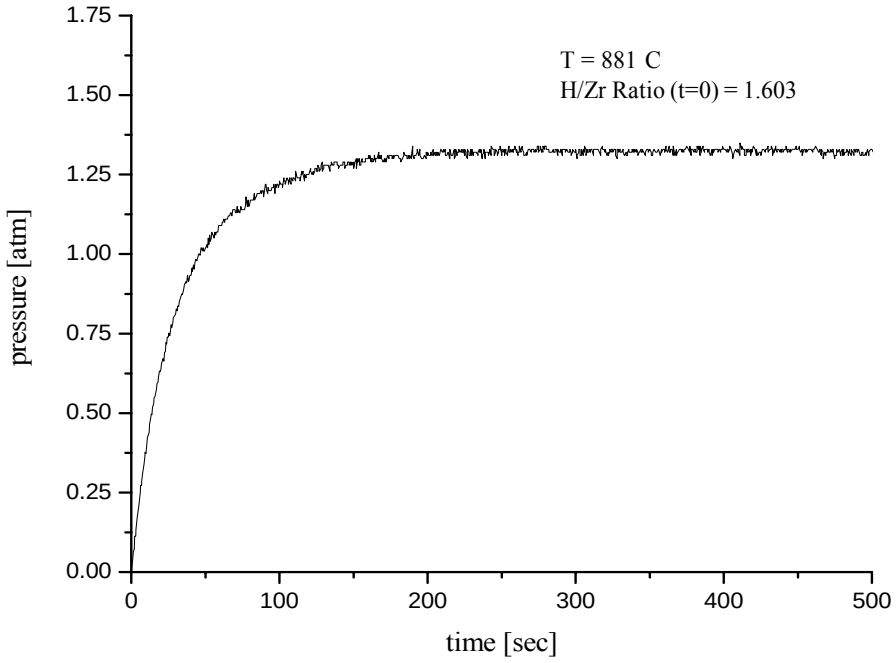

Fig 4. Typical rise in pressure as function of time during dehydriding from zirconium hydride disk.

3.4.8 Interpretation of pressure rise

The rate of change in the hydrogen gas pressure accumulated in the vessel is due to rates of hydrogen gas adsorption and desorption from the hydride and the rate at which the hydrogen leaks from the vessel. Conservation of mass can be applied at the surface of the hydride disk and the vessel boundary as shown in Figure 5 (Equations 9 and 10).

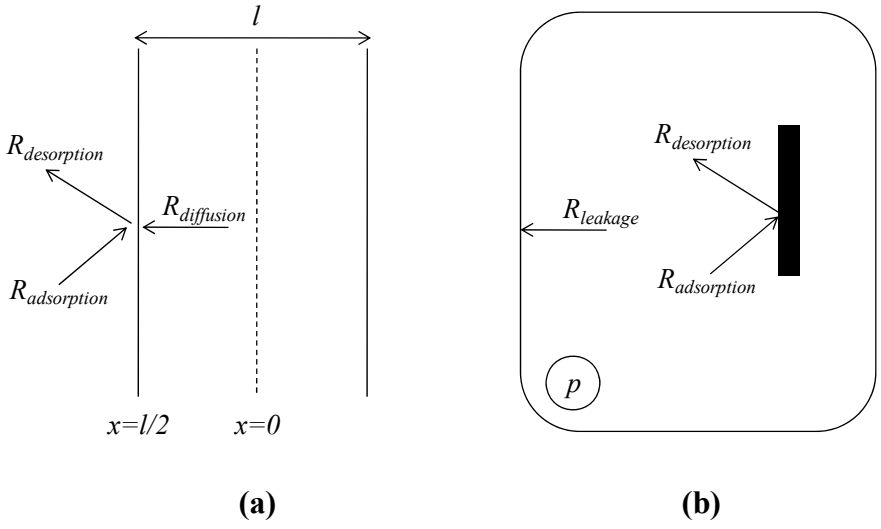

Fig 5. (a) Conservation of hydrogen mass at the hydride surface. (b) Conservation of hydrogen gas inside the vessel.

$$\frac{1}{2} R_{diffusion}\Big|_{x=l/2} = R_{desorption} - R_{adsorption} \qquad (9)$$

$$\frac{V}{RT}\frac{dp}{dt} = \left(R_{desorption} - R_{adsorption}\right) S_d - \frac{1}{2} R_{leakage} S_v \qquad (10)$$

The rate of diffusion and leakage are divided by a factor of 2 since they correspond to flux of hydrogen atoms and the rates of adsorption and desorption correspond to that of hydrogen gas. V, R, T, S_d, and S_v are vessel volume (19.5 cm^3), gas constant, temperature, disk surface area (3.561 cm^2), and vessel surface area respectively. By applying Fick's first law the rate of diffusion into the surface of the hydride is determined as:

$$R_{diffusion} = -2DN_{Zr}\left.\frac{\partial \xi}{\partial x}\right|_{x=l/2} \qquad (11)$$

where N_{zr} is the zirconium number density in δ-zirconium hydride (the number density of hydrogen lattice sites is twice that of zirconium atoms, hence N_{zr} is multiplied by 2). Substituting for the difference between rates of desorption and adsorption from Equations 9 and 11 into 10, the following is formulated:

$$\frac{V}{RTS_d}\frac{dp}{dt} + \frac{S_v}{2S_d} R_{leakage} = -DN_{Zr}\left.\frac{\partial \xi}{\partial x}\right|_{x=l/2} \qquad (12)$$

Equation 12, employing the experimental results, could serve as the boundary condition in order to solve the transient diffusion equation (Fick's second law) across the hydride disk.

3.4.9 Solution to the diffusion equation

The disks are assumed to have uniform hydrogen concentration across the thickness at the beginning of the dehydriding process that is determined by the pressure at which the disks were processed (initial condition). The boundary condition at the surface of the disk is provided using the experimental results using Equations 8 and 12. Diffusion equation is solved (for details of the semi-implicit numerical solution refer to appendix A) for a disk of zirconium hydride with half-thickness of 0.52 mm and starting uniform H/Zr ratio of 1.603 at 881°C (the dehydriding results are shown in Figure 4) and the evolution in the hydrogen concentration is shown in Figures 6 and 7.

The details of the different dehydriding experiments are summarized in Table 2. Steady state surface H/Zr ratio is calculated by plugging the steady state hydrogen pressure (the constant pressure reached at the end of the dehydriding experiment) into Equation 1. The calculated surface and average H/Zr ratios are generated through the results of the solution of diffusion equation.

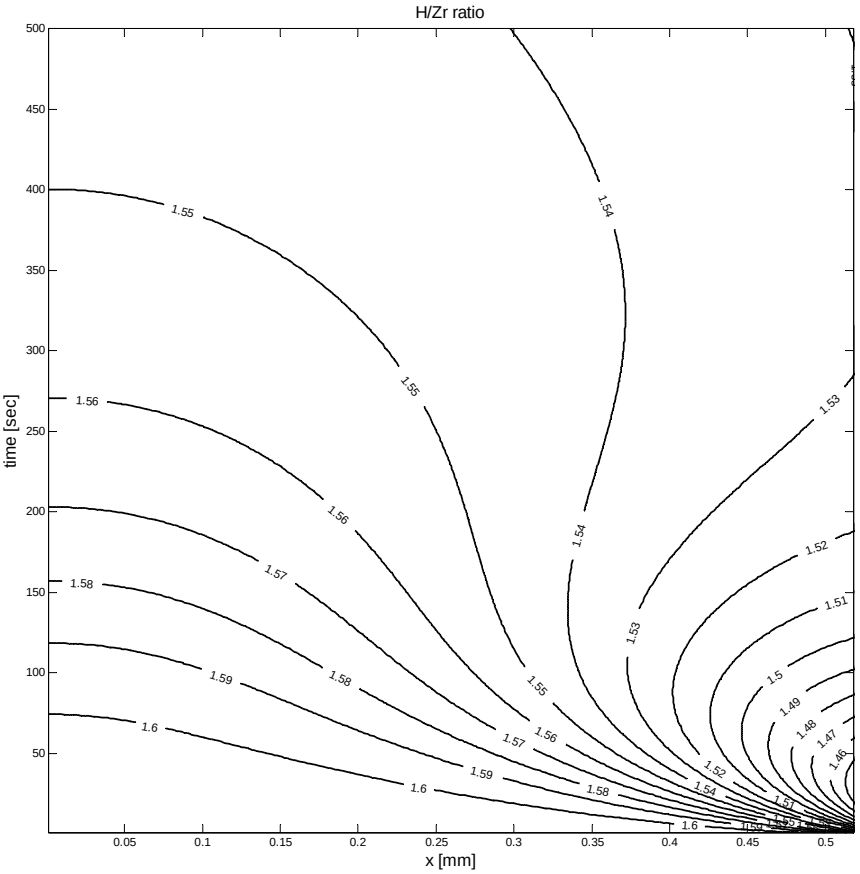

Figure 6. Evolution in the hydrogen concentration profile as a result of dehydriding

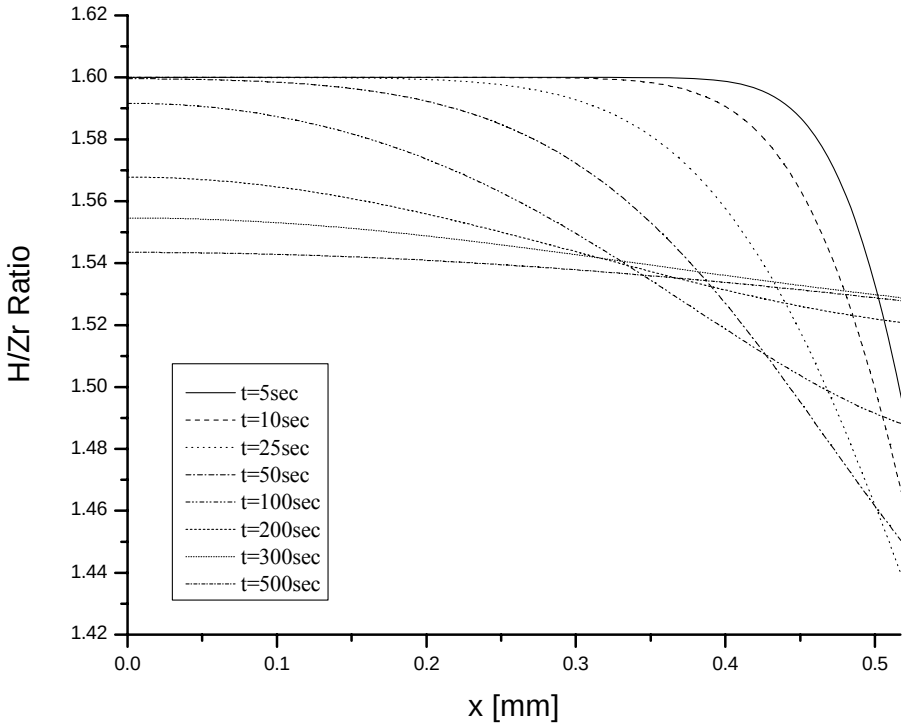

Figure 7. Evolution in the hydrogen concentration profile as a result of dehydriding

Table 2. Complete Set of Experimental Conditions and Details

Temperature [°C]	Processing H_2 pressure [atm]	As processed H/Zr ratio	Steady state H_2 pressure [atm]	Steady state surface H/Zr ratio	Calculated surface H/Zr ratio	Calculated average H/Zr ratio	Percent loss of hydrogen from hydride
743	0.41	1.632	0.16	1.546	1.616	1.621	0.6
770	0.91	1.654	0.38	1.579	1.622	1.630	1.5
798	2.90	1.704	0.65	1.581	1.664	1.674	1.8
800	4.58	1.735	0.74	1.589	1.682	1.696	2.3
829	2.19	1.639	0.82	1.553	1.591	1.600	2.4
830	4.48	1.694	0.90	1.560	1.637	1.649	2.7
852	4.07	1.658	1.16	1.550	1.562	1.573	5.1
859	1.45	1.560	0.88	1.512	1.506	1.517	2.8
861	2.33	1.599	1.19	1.538	1.538	1.552	2.9
863	4.27	1.648	1.22	1.538	1.582	1.590	3.5
880	4.51	1.630	1.35	1.522	1.555	1.566	3.9
881	3.37	1.603	1.40	1.524	1.528	1.544	3.7
902	4.41	1.599	1.64	1.508	1.517	1.533	4.1
920	4.51	1.578	2.14	1.508	1.469	1.480	6.2

4.4.10 Determination of the reaction order

In order to determine the dependence of the flux on the surface hydrogen concentration (and therefore test the applicability of the second order kinetics earlier discussed), the surface hydrogen flux is plotted against hydrogen gas pressure in Figure 8.

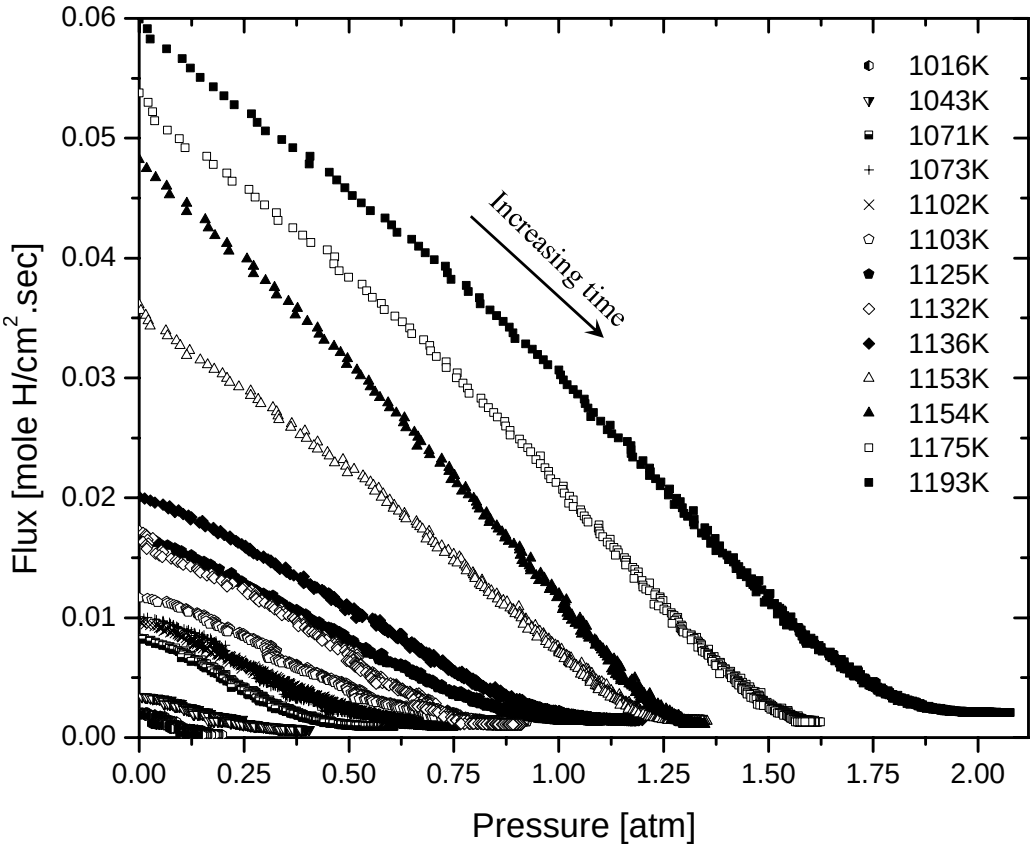

Figure 8. Dependence of surface hydrogen flux on hydrogen gas pressure inside the chamber

As appears on the figure, the flux is linearly dependent on the hydrogen gas pressure and no correlation with the evolving hydrogen surface concentration is observed. At the beginning of the desorption process, the hydrogen gas pressure inside the chamber is zero. Therefore the adsorption rate, that is directly dependent on the gas pressure, is also zero, and the intercept of the flux curve with the y axis is the absolute desorption rate. The slope of the flux curve then corresponds to the absolute rate of desorption per unit of hydrogen gas pressure. This relationship is mathematically developed as the following:

$$f(t) = k_d - k_a p_{H_2}(t) \quad (13)$$

This relationship suggests zero order kinetics similar to what has been discussed by Venables et al. [7]. Assuming zero order kinetics the absolute rates of hydrogen adsorption and desorption are plotted as a function of temperature, to determine the Arrhenius dependence. Desorption data also include thermogravimetry data from set of experiments performed under vacuum.

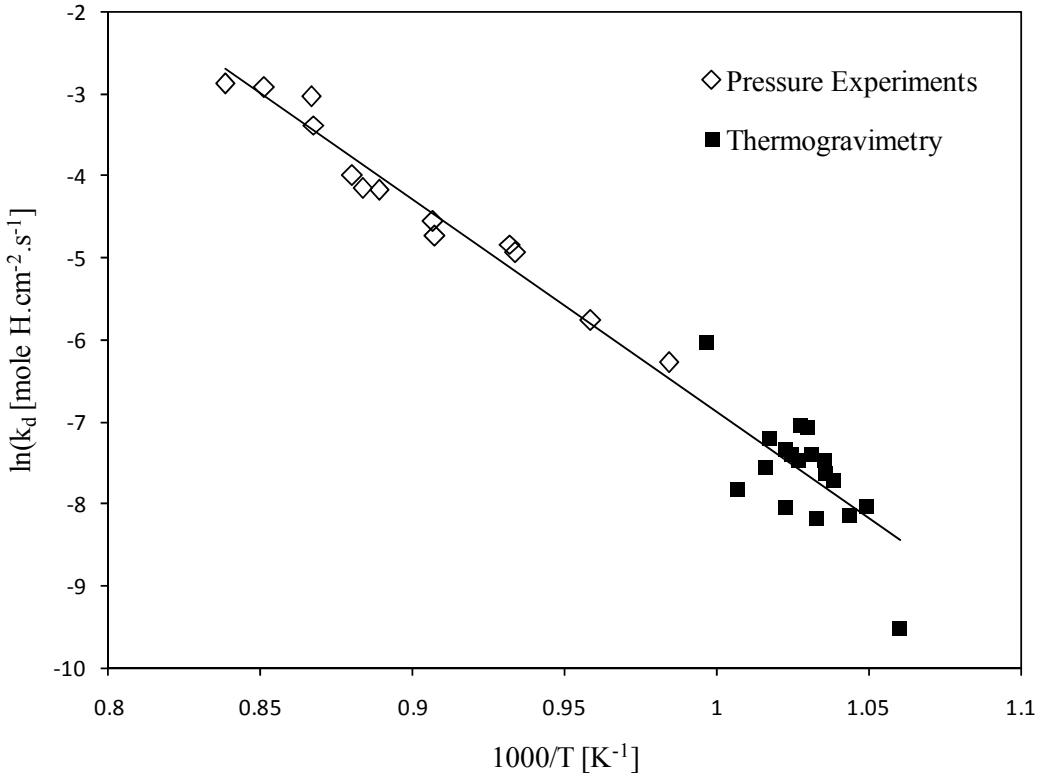

Figure 9. Arrhenius dependence of the hydrogen desorption rate from zirconium hydride

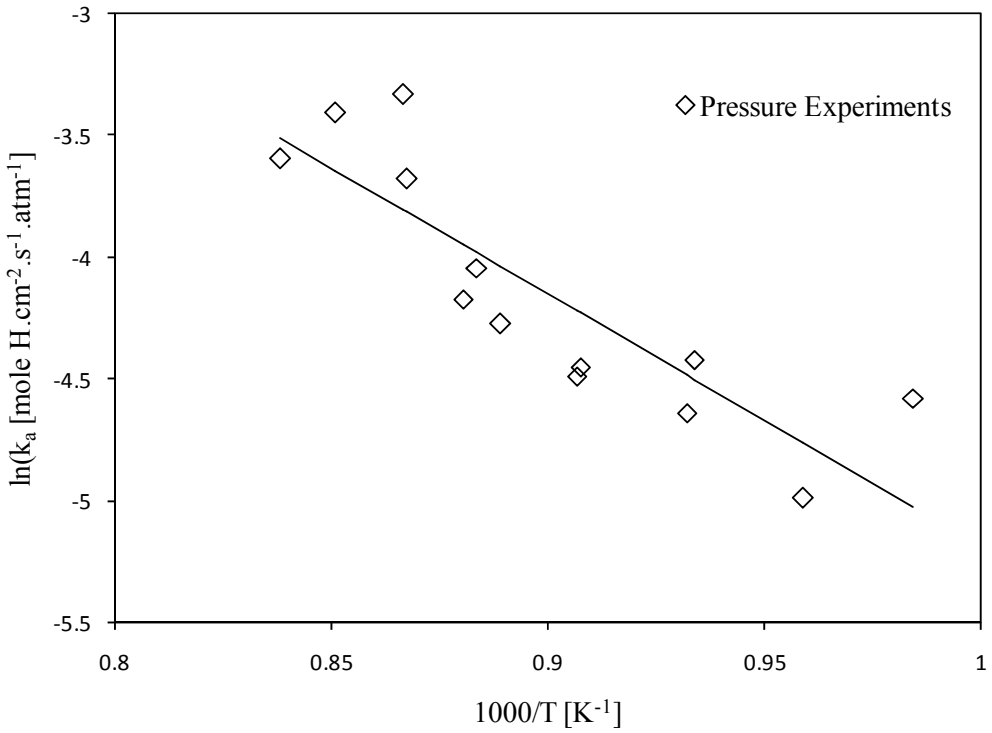

Figure 10. Arrhenius dependence of the hydrogen adsorption rate from zirconium hydride

The zero order rate equations for hydrogen desorption and adsorption processes are presented in Equations 14 and 15 respectively. The reproducibility of the pressure buildup curves through utilization of the below equations is examined in Figure 11, where somewhat poor results are shown.

$$k_d\left[\frac{\text{mole H}_2}{\text{cm}^2.\text{sec}}\right] = 1.73\times10^8 \exp\left(\frac{-215[kJ]}{RT}\right) \qquad (14)$$

$$k_a\left[\frac{\text{mole H}_2}{\text{cm}^2.\text{sec.atm}}\right] = 1.75\times10^2 \exp\left(\frac{-86[kJ]}{RT}\right) \qquad (15)$$

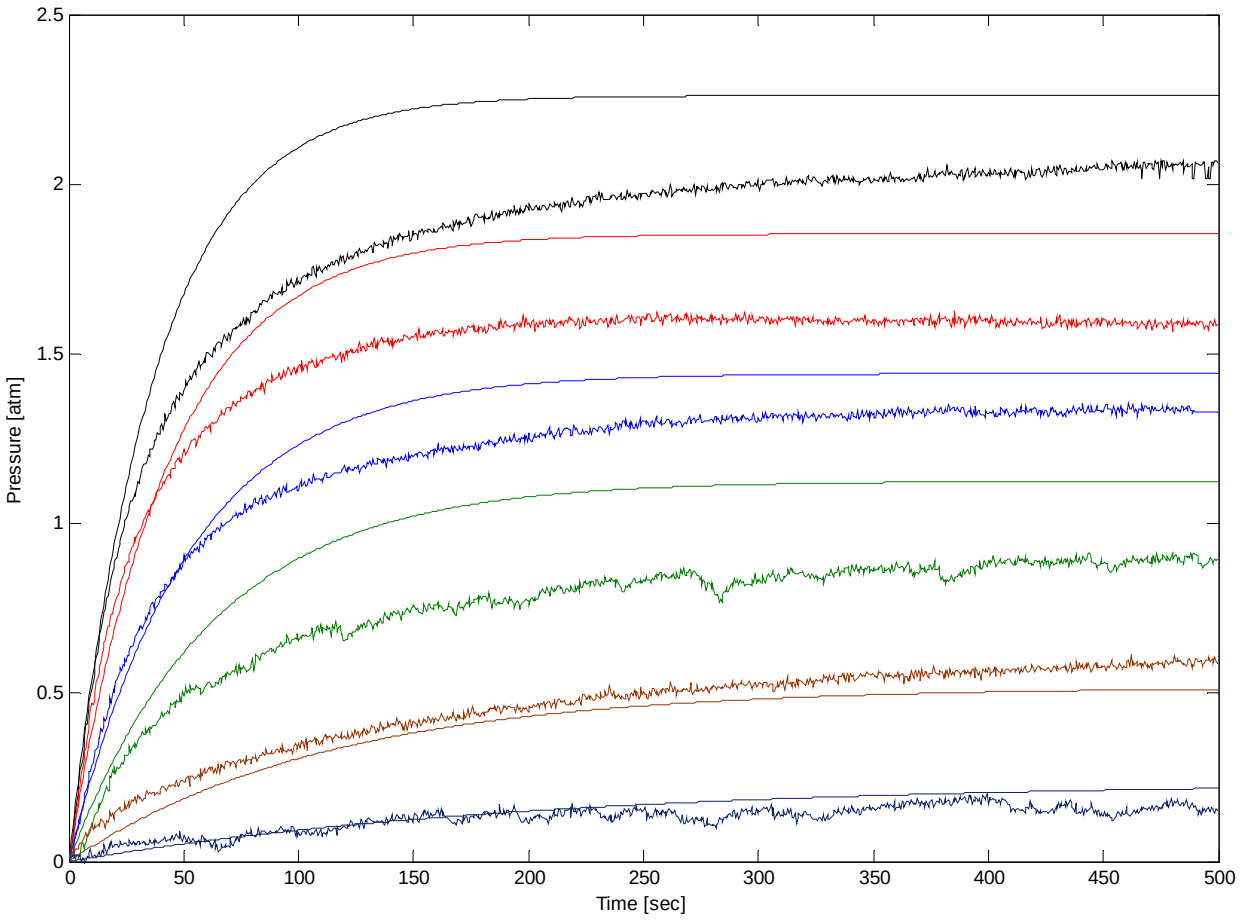

Figure 11. Reproduction of pressure buildup curves through utilization of the zero order kinetics parameters. The smooth lines represent the model

3.4.10 Discussion and conclusion

Although zero order kinetics is apparent, it does not agree with the thermodynamics governing the binary system. The mismatch between the model and experimental pressure buildup curves is precisely due to this reason, since the equilibrium hydrogen pressure at large times that coexists with the hydride after the desorption process stops, corresponds to the relationship discussed in Equation 1. Therefore the relationships developed above are missing some component of surface hydrogen concentration dependence and further scrutiny and analysis of the results is required to determine the mechanism governing the kinetics.

With respect to the applicability of the above study to the overall applicability of hydride nuclear fuels in LWRs the following could be concluded. The rates of hydrogen desorption and adsorption are sufficiently fast at high temperatures (i.e. during power transients) such that thermodynamic equilibrium is quickly established. Therefore for the purpose of safety analyses assuming instantaneous equilibrium conditions is a conservative and relatively accurate assumption.

4.2.17 References

1. R. Beck, “Zirconium-Hydrogen Phase System,” *Trans. Am. Soc. Metals*, **55**, pp.542-555 (1962).
2. S. Sidhu, N. Satya Murthy, F. Campos, D. Zauberis, “Neutron and X-ray Diffraction Studies of Nonstoichiometric Metal Hydrides,” *Advances in Chemistry Series, Washington D.C.*, **39**, pp.87-98, (1963).
3. K. Moore, W. Young, “Phase Studies of Zr-H System at High Hydrogen Concentrations,” *J. Nuc. Mat.*, **27**, pp.316-324 (1968).
4. W. Wang, D. Olander, “Thermodynamics of the Zr-H System,” *J. Am. Ceram. Soc.*, **78** [12], pp.3323-28 (1995).
5. G. Majer, W. Renz, R. Barnes, “The Mechanism of Hydrogen Diffusion in Zirconium Dihydrides,” *J.Phys.: Condens. Matter*, **6**, pp.2935-2942 (1994).
6. C. San Marchi, B. Somerday, S. Robinson, ”Permeability, solubility and diffusivity of hydrogen isotopes in stainless steels at high gas pressures,” *International Journal of Hydrogen Energy*, **32**, pp.100-116 (2007).
7. J.A. Venables, M. Bienfait, *Surf. Sci.*, **61**, (1970) 667.

3.5 Zircaloy Cladding Compatibility with Hydride Fuel

Compatibility of Zircaoly, conventionally used as the fuel cladding for LWR fuels, with hydride fuel has significant impact on the outcome of the feasibility study. Currently the oxide fuel cycle length inside the reactor is limited by the cladding performance. Zirconium is an effective getter of hydrogen and readily undergoes hydriding. Therefore the susceptibility of Zircaoly cladding to hydride formation and damage is obvious from the thermodynamic standpoint. However the fuel could be engineered such that the kinetics of hydrogen transfer from the fuel to cladding is limited and effectively becomes insignificant during the lifetime of the fuel inside the reactor.

The proposed design for such fuel rod is to substitute helium as the gap filling material between the cladding and the fuel, with a liquid metal alloy. A ternary alloy of lead-tin-bismuth (Pb-33wt%Sn-33wt%Bi) is proposed to be used for this purpose. The alloy is chemically compatible with both the fuel and the cladding. Also hydrogen solubility in any of the components of the alloy is very limited at the operating temperatures of the fuel assembly.

To further investigate the compatibility of the liquid metal bonded hydride fuel with the cladding a set of experiments are currently being conducted where the fuel is exposed to the cladding, submerged in liquid metal, at different times, temperatures, and contact pressures. Figure 1 shows the setup of the experiment, were the contact is made inside an open stainless steel pressure cell. The contact pressure between the fuel and the cladding is controlled through the application of torque over the screw that pushes the fuel and cladding together. In case that a certain thickness of a gap is top be maintained between the fuel and the cladding, platinum wires are used. The stainless steel pressure cells are heated inside an argon environment.

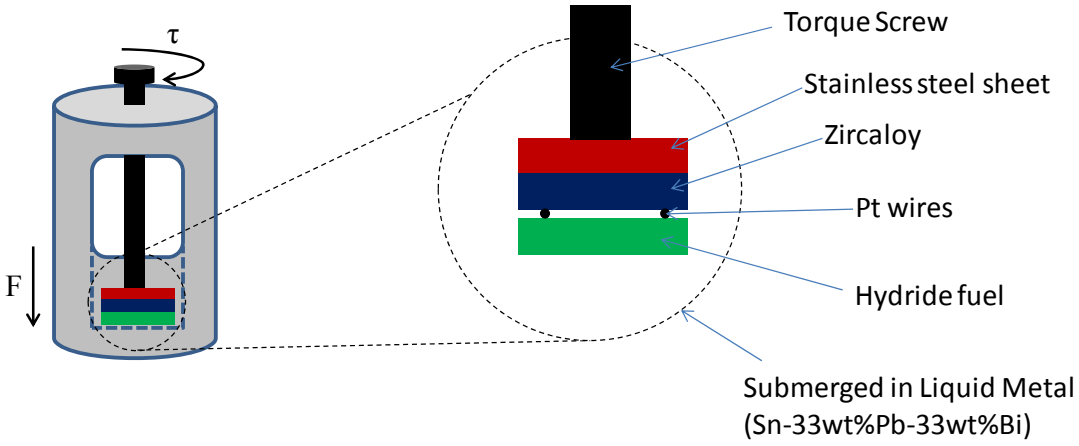

Figure 1. Experimental setup for the liquid metal bonded fuel – Zircaoly cladding compatibility test.

The temperatures of the experiment are in the range of what is expected for steady state LWR operation (i.e. 450°C and 500°C). After the fuel is exposed to the cladding, the cladding is mounted and metallography followed by optical and scanning electron microscopy will be performed in order to investigate formation of any hydride in the cladding. The work is done with Zircaloy 4 cladding, and $(U_4Th_2Zr_9)H_{1.5}$ hydride fuel. Originally the experiment was expected to be conducted using commercial TRIGA fuel, however such fuel could not be obtained due to multiple administrative hurdles from different organizations involved in the process.

4.6 Oxidation Behavior of Hydride Fuel in High Temperature Steam

During sever accident conditions the fuel cladding could burst and result in introduction of water into the cladding. The water in turn evaporates into high temperature steam that could react with the fuel and the inner wall of the cladding. To determine the susceptibility of hydride type fuels an experiment was performed using a thermogravimetry (TGA) setup. The goal was to determine the kinetics of steam reaction with the fuel based on the mass gain as a function of time. Typically such analysis yields rate information that then could be analyzed in order to determine the mechanism of the phenomenon examined. A very preliminary experiment has been performed. The sample used was a small piece of $(U_4Th_2Zr_9)H_{1.5}$ hydride fuel exposed to a mixture of steam and helium at 900 °C. The oxide scale forming on the surface of the fuel however was not adherent and quickly spalled and fractured away from the surface. Therefore due to the severe reaction rates no kinetic data could be deduced from the steam reaction with the hydride fuel. This result appears to be in some contradiction with that reported by Dr. Simnad,[1] — the developer of TRIGA fuel, that exposing small and large samples of TRIGA fuel heated to 900^oC to water caused no damage except surface discoloration [1].

The exposition of hydride fuel samples to steam experiments need be continued. It should be noted that the steam temperature expected in operating LWR will be on the order of only 400^oC rather than 900^oC used in this single experiment. Moreover, the outcome of the oxidation reaction could significantly change based on the composition of the fuel – in case of TRIGA fuel an outer oxide layer could be protective where no thorium is present. Therefore further investigation is required before sound conclusions could be drawn.

Reference

1. M.T. Simnad, “The U-ZrH_x Alloy: Its Properties and Use in TRIGA Fuel,” General Atomics publication GA-A16029, August 1980.

4.7 Irradiation Plans for Liquid Metal Bonded Hydride Fuel

4.7.1 Introduction

The experimental data available in the open literature on the swelling of hydride fuel and on the fission gas released from hydride fuel is very limited [1-6]. Moreover, there is no data available at all on the feasibility of using liquid metal bonding instead of helium for hydride fuel. The liquid-metal bonding will enable to provide a sufficiently large gap between the initially loaded hydride fuel and the clad to accommodate the relatively large swelling of hydride fuel without increasing the fuel temperature. The liquid metal bonding will also eliminate a large temperature gradient between the fuel surface and the cladding ID and, possibly, will protect the Zircaloy clad from the fuel hydrogen. An irradiation test of a hydride fuel specimen in the ATR irradiation test reactor at the Idaho National Laboratory was planned in order to investigate all the above mentioned issues. A brief description of the proposed experiment follows.

4.7.2 Brief description of the proposed ATR experiment

The objective of ATR experiment is to perform a realistic irradiation test of combined innovative uranium hydride fuel with a low-melting liquid metal (Sn,Bi,Pb) as the gap filler [7]. The test will utilize a Zircaloy-clad mini-fuel element instrumented for continuous recording of fuel-centerline and cladding outside temperatures and evolved-gas composition. The mini-fuel fabrication steps and assembly into ATR capsule are shown in Figure 1.

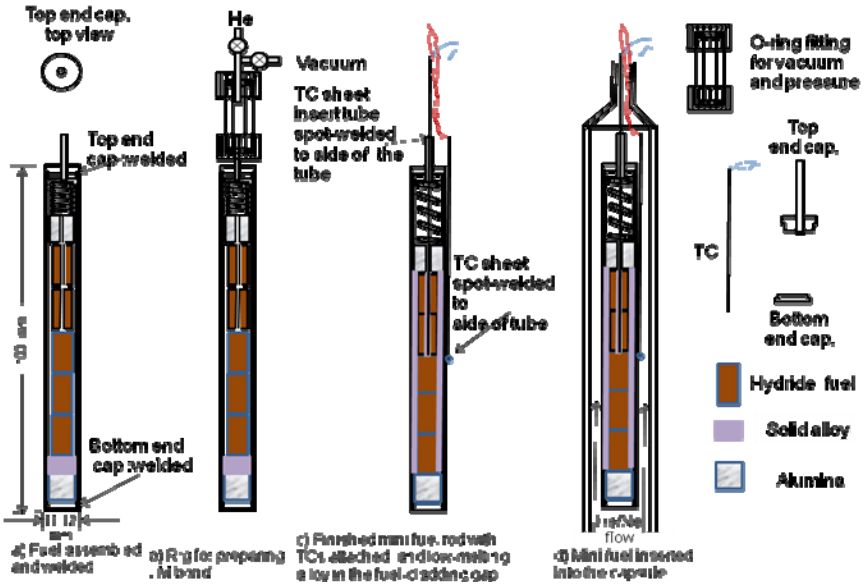

Figure 1. Mini-fuel fabrication steps

Since TRIGA Uranium/Zr hydride fuel has yet to be delivered to Berkeley campus, a mock up of mini-fuel has been assembled with Cu pellets instead of the actual fuel. From large ingot, Cu pellets have been drilled out using the diamond core drilling technique to an approximate size followed by an in-house designed centerless grinder to the precise diameter equal to the LWR UO_2 pellets. The actual U-Zr hydride pellets production for mini-fuel will be accomplished in a

glove box. The partially assembled mini fuel rod consisting of Cu pellets, Zircaloy clad and liquid metal filled gap in between is shown in Figure 2.

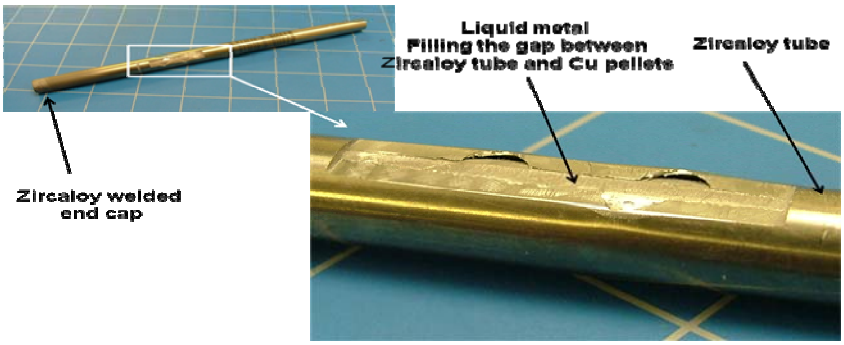

Figure. 2 Mini-fuel cladding with Cu pellets, Zircaloy cladding and LM filled gap

The initial thickness of the fuel-cladding gap is chosen so as to achieve closure prior to the end of irradiation at ATR. During irradiation, fuel-centerline and outside cladding as well as composition of gaseous fission products are monitored at the ATR facilities. The post-irradiation examination at UC Berkeley include: possible fuel cracking, gas bubbles formation in the frozen alloy, hydrogen distribution in fuel, hydride precipitation in cladding, void around uranium particles, dimensional changes of cladding and second-phase particles generation in the fuel.

The mini-fuel rodt will be instrumented for continuous recording of fuel- centerline and cladding-OD temperatures as well as of gas composition. A constant fuel-centerline temperature is maintained for an irradiation period of one year, which corresponds to ~50% burnup of the U-235. The initial thickness of the fuel-cladding gap is chosen to achieve closure prior to the end of irradiation.

The mini-fuel rod ("rodlet") will be inserted into an ATR capsule equipped for gas flow in the annulus between the specimen and the capsule wall. Varying the He/Ne ratio of the flowing gas controls the fuel-centerline temperature. The upper end-cap of the rodlet contains a space to allow fission gases to escape. The He/Ne gas, containing any released fission gases, will enter an instrument that will measure the gas composition.

The Post-Irradiation-Experiments (PIE) planned include the determination of:

- the state of fission gases: remaining in the fuel, or collected as bubbles in the liquid-metal in the gap
- behavior of hydrogen: redistribution in the fuel; hydriding of the cladding
- morphology of the fuel: cracking; second-phase particles; voids around uranium particles
- diametral expansion of the cladding
- pellet-cladding mechanical interaction.

Information such as the above will help determine whether this fuel concept is suitable for commercial use. A list of specific experiments planned is given in Table 1.

Table 1. Post-Irradiation-Experiments Planned

Phenomenon	Instrumentation
Fuel cracking	OM, SEM
Xe in the plenum gas	On-line
Gas bubbles in the frozen alloy	OM
Hydride precipitates in cladding	OM, SEM
Uranium particles	SEM
Voids around U Particles	TEM
Diametral expansion of the cladding	micrometer
Second-phase particles in the fuel	SEM

4.7.3 Irradiation conditions

Three requirements must be met by the irradiation regime:

- For the entire irradiation time the fuel-centerline temperature remains at ~ 650°C[2].
- A burnup of ~50% of the U-235 should be achieved in ~1 year of irradiation
- The fuel-cladding gap should close before the end of irradiation

The most desirable irradiation condition would be to maintain constant both the fuel-centerline and cladding OD temperatures. However, in the ATR, the neutron flux and the coolant temperature are fixed. These conditions do not result in constant fuel-centerline and cladding OD temperatures because of the burnup of U-235, which continually reduces the fission rate and hence the linear heat rate. The compromise condition for the proposed test is to maintain the fuel-centerline temperature (T_o) constant by allowing the cladding OD temperature (T_{CO}) to rise during irradiation. These two temperatures are related by:

$$T_o = T_{coolant} + \Delta T_{hyd} + \Delta T_{Cap} + \Delta T_{gap2} + \Delta T_C + \Delta T_{gap1} + \Delta T_f \quad (1)$$

where $T_{coolant}$ = ATR coolant temperature, ~ 60°C

T_o = fuel centerline temperature = 650 - 700°C

the intervening temperature drops are across:

ΔT_{hyd} = hydraulic boundary layer

ΔT_{cap} = ATR capsule wall

ΔT_{gap2} = helium/neon flush gas

ΔT_C = Zircaloy cladding

ΔT_{gap1} = liquid metal gap filler

ΔT_f = fuel

Dimensions of the specimen are given in Table 2 and thermal conductivities are given in Table 3.

[2] This centerline-temperature is higher than required of the hydride fuel in commercial LWRs, but it tests the performance limits of the fuel.

Table 2. Specimen & Capsule Radial Dimensions

COMPONENT	SYMBOL	CM
Fuel-pellet radius	R_f	0.467
Cladding ID/2	R_{CI}	0.487
Cladding OD/2	R_{CO}	0.557
Capsule ID/2	R_{capI}	0.571
Capsule OD/2	R_{capO}	0.730*

* assumes a 1/16 " wall thickness

Table 3 Thermal Conductivities (W/cm-K)

MATERIAL	SYMBOL	W/CM-K
Zr hydride	k_f	0.18*
Zircaloy	k_C	0.17*
Liquid metal	k_{gap1}	0.3*
Helium/neon	k_{gap2}	Table B1
Capsule wall	k_{cap}	0.17[#]

* temperature-independent
[#] depends on alloy; stainless steel assumed

4.7.4 Summary

Design and performance of a mini fuel element consisting of a 5-pellet stack of (U,Zr) hydride fuel, Zircaloy cladding and a Bi-Sn-Pb liquid metal alloy in the fuel-cladding gap were analyzed with the objective of an irradiation test in the ATR. A thermal-neutron flux of ~ $3x10^{13}$ n/cm^2-s is estimated required in order that the fuel-centerline temperature remains constant at ~ 650°C. At this flux, 50% burnup of the U-235 is attained in 1 year of irradiation. An initial gap thickness of ~100 μm is required for gap closure at the end of the irradiation. The specialized machining and welding techniques required for fabrication of the mini-fuel element have been developed.

4.7.5 References

1. J. D. Gylfe et al*, "Evaluation of Zirconium Hydride as Moderator in Integral Boiling –Water Superheat Reactors",* NAA-SR-5943 (1960)
2. A. Lillie et al, "*Zirconium Hydride Fuel Element Performance Characteristics",* Atomics International/USAEC Rept. AI-AEC-13084 (1973)
3. M. T. Simnad, "*The U-ZrH_x alloy: its properties and use in TRIGA fuel",* Nucl. Engin. & Design **64** (1981) 403
6. D. Olander and O. Ng, "*Hydride Fuel Behavior in LWRs*" J. Nucl. Mater, **346** (2005) 98
7. D. Olander & D. Wongsawaeng "A Liquid-metal bond for improved LWR fuel performance", Nucl. Technol., 15**9** (2007) 279